University College London

Allele-specific siRNA Therapy for Keratitis-Ichthyosis-Deafness Syndrome

Ming Yang Lee

A thesis submitted to University College London for the degree of

Doctor of Philosophy

Great Ormond Street Institute of Child Health

University College London

2018

Declaration

I, Ming Yang Lee, confirm that the work presented in this thesis is my own. Where information has been derived from other sources, I confirm that this has been indicated in the thesis

Abstract

Dominant mutations in the gene *GJB2* cause keratitis-ichthyosis-deafness (KID) syndrome, a severe condition affecting the skin, cornea and inner ear. *GJB2* encodes the protein connexin-26 (Cx26) which forms hemichannels or gap junction channels allowing the passage of signalling molecules. Approximately 80% of KID syndrome patients carry a c.148G>A (p.D50N) mutation in *GJB2*, which results in aberrant channel function. We hypothesised that silencing of the mutant allele in patient keratinocytes using allele-specific siRNA could correct the channel function.

First, to confirm whether patient keratinocytes with only one wildtype *GJB2* allele formed functional channels following allele-specific siRNA treatment, $GJB2^{+/-}$ keratinocytes were generated using CRISPR/Cas9. The scrape-loading dye transfer (SLDT) assay showed no distinguishable difference in gap junction intercellular communication (GJIC) between $GJB2^{+/-}$ and $GJB2^{+/+}$ cells, suggesting normal GJIC in $GJB2^{+/-}$ keratinocytes.

Nineteen siRNAs were designed and tested in HeLa cells expressing wildtype or mutant *GJB2-GFP* transgene. A lead siRNA, was discovered, which potently inhibited the mutant mRNA and protein without affecting wildtype *GJB2* expression. The efficacy of the lead siRNA was assessed using keratinocytes derived from a KID syndrome patient (KID-KC) harbouring heterozygous c.148G>A mutation. These cells displayed pathological features of KID syndrome, with reduced gap junction plaque formation, impaired GJIC and hyperactive hemichannels confirmed by immunostaining, SLDT, patch clamp and neurobiotin uptake assays.

Following treatment with the siRNA, selective silencing of mutant *GJB2* allele in KID-KCs was confirmed at mRNA and protein levels. Significant improvement of GJIC and reversal of hemichannel activity were detected, with the latter corrected to a level comparable to that recorded in normal keratinocytes. Furthermore, RNA-Seq analysis showed that only six genes in the KID-KC transcriptome were significantly altered by the siRNA treatment, suggesting low-level off-target effects.

In conclusion, allele-specific siRNA silencing of pathogenic dominant *GJB2* mutation could be a potential therapeutic intervention for KID syndrome.

Impact Statement

This study has utilised the allele-specific siRNA technique to effectively silence the mutant *GJB2* allele in KID syndrome patient-derived keratinocytes. The silencing led to reversal of aberrant channel function in the cells, including improvement of gap junction intercellular communication and correction of hyperactive hemichannels. Strikingly, the therapeutic siRNA caused a very low level of genome-wide off-target effects in the patient cells, as detected by RNA-Seq.

The data presented in this thesis could be beneficial to multiple fields of research. First of all, the cell model used in this work is the first published immortalised, patient-derived keratinocyte cell line. The cell line, harbouring the most common KID syndrome mutation, are of great research values for elucidating the pathomechanism of the condition; meanwhile, it would benefit pre-clinical assessment of any new treatment developed for the condition. Also useful are the *GJB2*-knockout cell lines generated alongside the study by CRISPR/Cas9 genome editing. These cell lines would also be essential for future research into biological processes and signalling pathways related to the gene.

KID syndrome is an incurable, life-long condition with multi-systemic defects, thus posing a tremendous burden on affected patients, families and healthcare systems. This study provides an important proof-of-concept for the use of the allele-specific siRNA strategy in targeted therapy for the condition. The successful *in vitro* outcomes have been presented in five national or international conferences, and a manuscript (in preparation) will soon be submitted to a peer-reviewed journal. The data will form strong basis for further research and optimisation of strategies regarding the siRNA treatment, such as routes of administration, a critical step towards its potential clinical translation. Our laboratory has also established a human-murine chimeric mouse model for further *in vivo* studies. If successful, the siRNA strategy can enter a phase 1 clinical trial, which could potentially bring in long-term clinical benefits to patients with the debilitating condition. Furthermore, this strategy can be adapted to other human conditions associated with dominant mutations, therefore having additional impact to a broad range of research.

Acknowledgements

First of all, I would like to express my gratitude to my principal supervisor Wei-Li Di for her guidance, time and support throughout my PhD. Wei-Li is a passionate researcher who has never said no when I am in need of work discussion and troubleshooting. The opportunities she gave me to present my work in many national and international conferences, as well as her advice on grant/fellowship applications have been invaluable training experience towards my career in medical science.

I am also extremely grateful to my subsidiary supervisors Veronica Kinsler and Steve Hart. Veronica is a supportive supervisor, quick thinker and excellent communicator. She has expanded my professional skills and network, and provided me with all support needed, particularly in my times of desperation. Steve is my role model, from whom I have experienced his good sense of humour, ability to manage a big lab (in my vision) and of course, considerable knowledge in the fancy nanotechnology. All above has made them fantastic supervisors.

I also wish to thank my U.S. host, Thomas White, who accepted me as a visiting fellow to carry out my research there. Numerous inspirational beer or non-beer chats with Tom (and other connexin experts) always effectively resolved my connexin issues. Outside my work, I can clearly remember some lifts and a MTX bike Tom offered/lent in my first week in Stony Brook, without which I probably would not have survived. All the U.S. experience has certainly been the highlight of my PhD.

I would like to acknowledge the financial support from the UCL Overseas Scholarship, the CHRAT Studentship, the Bogue Fellowship, the NIHR GOSH BRC Doctoral Training Support Fund, the SLMS Student Conference Fund and the ICH Travel Award. All allowed me to complete this project in London and New York, and took me to six cities to share my research, making my PhD fairly rewarding.

Despite my countless nights finishing at 11:01 pm making me one of the most remembered ICH workers, friendships have been an indispensable part of my PhD. I wish to thank Farhatullah Syed, Anastasia Petrova, Christos Georgiadis, Yanan Zhu and Wenjie Chen for being my fabulous colleagues, not only passing down lab

techniques, but also tolerating my endless questions. I also wish to thank Dale Moulding, Ayad Eddaoudi, Stephanie Canning, Aris Tagalakis, Ruhina Maeshima, Ahmad Aldossary, William Baird, Maanasa Polubothu, Anna Thomas, and Kwan Hau for your support on my work. Thank you to Cristina Tommasi, Sakinah Hassan, Ching-In Lau for being my wonderful friends, sharing my usually-funny jokes. Special thanks to my other lovely office mates for constant provision of delicious cakes and pizzas. Thank you to founders and members of the London Taiwanese Biomedical Society for those interdisciplinary scientific topics. Furthermore, my sincere thanks go to my non-science friends Nigel, Johnnie, Yun-Hui and others who have added much spice to my arduous PhD journey.

Finally, but most importantly, I owe an enormous thanks to my family, especially my wife and parents, for their love and support all these years. My thanks also go to my daughter, who is probably too small to read this line. I owe a debt of gratitude to my grandmother, who passed away much too soon, but had been extraordinarily concerned in all facets of my life, raised and shaped me into the man I am today. They all have been the driving force in my life, and I dedicate this thesis to them.

Table of Contents

List of Figures

Chapter 1

Chapter 2

Chapter 3, Section 3.1

Chapter 3, Section 3.2

Chapter 3, Section 3.3

Chapter 3, Section 3.4

Chapter 3, Section 3.5

List of Tables

Chapter 1

Chapter 2

Chapter 3

Abbreviations

aa	Amino acid
ANOVA	Analysis of variance
ATP	Adenosine triphosphate
BPS	Bart-Pumphrey syndrome
cAMP	Cyclic adenosine monophosphate
Cas9	CRISPR associated protein 9
CB	Cascade Blue
CBX	Carbenoxolone
cDNA	Complementary DNA
cGMP	Cyclic guanosine monophosphate
CL	Cytoplasmic loop domain (of connexin)
CMV	Cytomegalovirus
Control-FB	Healthy control-derived fibroblast
Control-KC	Healthy control-derived keratinocyte cell line
COX-2	Cyclooxygenase 2
cPPT	Central polypurine tract
CRISPR	Clustered regularly interspaced short palindromic repeats
CT	Carboxyl-terminal domain (of connexin)
Cx	Connexin
DAPI	4,6-diamino-2-phenylindole
DEG	Differentially expressed genes
DEG-2	The set of differentially expressed genes given by a lower threshold
DMEM	Dulbecco's modified Eagle's medium
dNTP	Deoxynucleotide
dT	Deoxythymine
DTT	Dithiothreitol
dTTP	Deoxythymidine Triphosphate
dUTP	Deoxyuridine Triphosphate
E1	The first extracellular loop domain (of connexin)
E2	The second extracellular loop domain (of connexin)
EC1	First extracellular loop of connexin

EDTA	Ethylenediaminetetraacetic acid
EGF	Epidermal growth factor
EGTA	Ethylene glycol tetraacetic acid
EKV-P	Erythrokeratodermia variabilis et progressive
EMT	Epithelial-mesenchymal transformation
FACS	Florescence-activated cell sorting
FB	Fibroblast
FBS	Foetal bovine serum
FSC	Forward scatter
GAPDH	Glyceraldehyde 3-phosphate dehydrogenase
GESS	Genome-wide Enrichment of Seed Sequence matches
GFP	Green fluorescence protein
GJIC	Gap junction intercellular communication
GO	Gene ontology
H&E staining	Haematoxylin and eosin staining
HB-EGF	Heparin binding EGF like growth factor
HBSS	Hank's balanced salt solution
HDR	Homology-directed repair
HDR	Homology-directed repair
HeLa-M1	HeLa clone expressing c.148G>A mutant *GJB2-GFP* transgene #1
HeLa-W1	HeLa clone expressing wildtype *GJB2-GFP* transgene #1
HID	Hystrix-like ichthyosis with deafness
HIV-1	Human immunodeficiency virus type 1
Indel	Insertion and delection
IP_3	Inositol 1,4,5-triphosphate
IPA®	Ingenuity® Pathway Analysis
IPTG	Isopropyl β-D-1-thiogalactopyranoside
IRES	Internal ribosome entry site
KC	Keratinocyte
kDa	kilodalton
KHLS	Keratoderma hypotrichosis leukonychia totalis syndrome
KID syndrome	Keratitis-ichthyosis-deafness syndrome
KID-1 patient	The first recruited patient with KID syndrome

KID-FB	KID-1 patient-derived fibroblast
KID-KC	KID-1 patient-derived keratinocyte cell line
L2K	Lipofectamine® 2000
LTR	Longer terminal repeat
mAb	Monoclonal antibody
MMP	Matrix metalloproteinase
mRNA	Messenger RNA
MUT	Mutant
N.S.	Not significant
N/TERT-MUT	(non-clonal) N/TERT cells expressing mutant *GJB2-GFP* transgene
N/TERT-WT	(non-clonal) N/TERT cells expressing wildtype *GJB2-GFP* transgene
NB	Neurobiotin
NF-κB	Nuclear factor-kappa B
NHEJ	Non-homologous end joining
NSHL	Non-syndromic hearing loss
nt	Nucleotide
NT	Amino-terminal domain (of connexin)
ODDD	Oculodentodigital dysplasia
OMIM	Online Mendelian Inheritance in Man
P2X	P2X purinergic receptors
pAb	Polyclonal antibody
p-adj	*P*-value adjusted using the Benjamini-Hochberg method
PAM	Protospacer adjacent motif
PBS	Phosphate-buffered saline
PCR	Polymerase chain reaction
PMSF	henylmethanesulfonyl fluoride
PPK	Palmoplantar keratoderma
PPKD	Palmoplantar keratoderma with deafness
PVDF	Polyvinylidene difluoride
qPCR	Real-time quantitative polymerase chain reaction
RIN	RNA integrity number
RISC	RNA-induced silencing complex
RLU	Relative light unit

RNAi	RNA interference
RNAiMAX	Lipofectamine® RNAiMAX
RNA-Seq	RNA-sequencing transcriptomic analysis
ROI	Region of interest
RT	Room temperature
RT-PCR	Reverse transcription polymerase chain reaction
SCC	Squamous cell carcinoma
SD	Standard deviation
SDS	Sodium dodecyl sulfate
SDS-PAGE	Sodium dodecyl sulfate polyacrylamide gel electrophoresis
SEM	Standard error of the mean
SFFV	Spleen focus-forming virus
sgRNA	Single guide RNA
SHL	Syndromic hearing loss
shRNA	Small-hairpin RNA
si-cont	Control small interference RNA against hHAS2 gene
si-GFP	Small interference RNA against green fluorescence protein (GFP)
siRNA	Small interference RNA
SLDT	Scrape-loading dye transfer
SSC	Side scatter
STRING	Search Tool for the Retrieval of Interacting Genes/Proteins
TIMP	Tissue inhibitors of metalloproteinases
TLR	Toll-like receptor
TM1	Transmembrane domain-1 (of connexin)
VS	Vohwinkel syndrome
VSV-G	The G glycoprotein of vesicular stomatitis virus
WT	Wildtype

CHAPTER 1. INTRODUCTION

1.1 KID syndrome

1.1.1 Clinical overview

Keratitis-Ichthyosis-Deafness (KID) syndrome (MIM 148210) is a rare, autosomal dominant genetic condition characterised by corneal inflammation, hearing loss and ichthyosis (Coggshall et al., 2013; Richard et al., 2002). The condition was first described in 1915 (Burns, 1915) and was subsequently classified as a specific ectodermal disorder which affects the epidermis, corneal epithelium and inner ear (Caceres-Rios et al., 1996; de Berker et al., 1993; Tsuzuku et al., 1992; Wilson et al., 1973). In 1981, the acronym 'KID' was first proposed. To date, there have been just over 100 cases with KID syndrome reported in the literature, with an estimated incidence ranging from 1 in 100,000 (Levit and White, 2015) to 1 in 1,000,000 (Al Fahaad, 2014). Although KID syndrome is rare, the clinical manifestations are debilitating, progressive, and difficult to treat.

Ocular involvement in KID syndrome is often bilateral and progressive, reported as neovascularisation, conjunctivitis, keratoconjunctivitis sicca and pannus formation (Brown et al., 2016; Kim et al., 2008; Messmer et al., 2005; Sonoda et al., 2004; Walcott et al., 2002), with histopathology showing thickened corneal epithelium with poorly differentiated epithelial cells (Djalilian et al., 2010). Patients often have photophobia, tearing and visual disturbance. Recurrent corneal erosions, corneal opacity and trichiasis have also been reported in the literature (Caceres-Rios et al., 1996; Haruna et al., 2010; Messmer et al., 2005; Serrano-Ahumada et al., 2017). The corneal findings are progressive and may lead to diminished visual acuity and blindness (Coggshall et al., 2013).

Sensorineural hearing loss is often profound and occurs in nearly all reported cases with KID syndrome (Patel et al., 2015). Unlike ocular impairment, the auditory impairment is usually non-progressive; however, due to its prelingual onset (average age of onset of 23 months) (Szymko-Bennett et al., 2002), it may affect speech development severely. A previous post-mortem histological study of temporal bone samples from a patient revealed dysplasia of cochlear and saccular neuroepithelium (Griffith et al., 2006). The dual sensory defect, combining ocular and auditory impairment, often leads to profound disability which is hard to rehabilitate (Coggshall

et al., 2013; Griffith et al., 2006).

The cutaneous involvement of KID syndrome usually develops as early as in the neonatal stage, despite the reported age of onset ranging from birth to 15 years (Alvarez et al., 2003; Arita et al., 2006; Bygum et al., 2005; Maintz et al., 2005; van Steensel et al., 2002; Werchau et al., 2011). The cutaneous features include erythrokeratodermic or verrucous plaques, follicular hyperkeratosis, and/or palmoplantar keratoderma with characteristic coarse-grained appearance (Coggshall et al., 2013). Other reported cutaneous features include, but not limited to, porokeratotic eccrine ostial and dermal duct nevus (Criscione et al., 2010; Lazic et al., 2012), follicular occlusion triad, featuring dissecting folliculitis, hidradenitis suppurativa and cystic acne (Maintz et al., 2005; Montgomery et al., 2004). Nail dystrophy and loss of hair and nails have been frequently documented (Alvarez et al., 2003; Binder et al., 2005; Coggshall et al., 2013), with loss of scalp hair, eyebrows or eyelashes occurring in 79% of cases (Caceres-Rios et al., 1996).

Chronic cutaneous infection and tumours are common complications of KID syndrome (Coggshall et al., 2013). Patients are prone to opportunistic infections, with bacterial pathogens including *Staphylococcus* and *Streptococcus* species, *Escherichia coli*, *Serratia marcescens, Pseudomonas aeruginosa and Proteus mirabillis* (Binder et al., 2005; Jonard et al., 2008; Lazic et al., 2008) and fungal pathogens including *Trichophyton rubrum* and the *Candida* species (Conrado et al., 2007; Gilliam and Williams, 2002; Ma et al., 2017). The infection issues often cause failure to thrive (Janecke et al., 2005; Lazic et al., 2008; Sbidian et al., 2010). In severe cases, septicaemia occurs in the first year of life (Gilliam and Williams, 2002; Haruna et al., 2010; Janecke et al., 2005; Jonard et al., 2008; Sbidian et al., 2010), and this complication was reported to be the major cause of premature death in patients with KID syndrome (Martin and van Steensel, 2015). Susceptibility to infection has led to the proposal that KID syndrome should be viewed as an immunodeficiency resulting from altered innate immunity (Donnelly et al., 2012; Ma et al., 2017) and/or from an imperfect epidermal barrier (Maintz et al., 2005).

Tumours are a clear feature of KID syndrome (Coggshall et al., 2013; Natsuga et al., 2011). Trichilemmal tumours, ranging from benign trichilemmal cyst to malignant

proliferating trichilemmal tumour (Kim et al., 2002; Nyquist et al., 2007), as well as squamous cell carcinoma (SCC) (Bergman et al., 2012; Mayama et al., 2013; Mazereeuw-Hautier et al., 2007; Sakabe et al., 2012) have been documented. Strikingly, in some cases, widespread metastasis can occur as early as in the third decade of life (Nyquist et al., 2007). Thus, careful, lifelong monitoring is warranted and a lower threshold for diagnostic biopsy and surgical excision of suspicious lesions is recommended (Coggshall et al., 2013).

1.1.2 *GJB2*: the causative gene of KID syndrome

In 2002, Richard et al. identified germline mutations in the *GJB2* gene in nine families with KID syndrome, providing the earliest genetic basis of the disorder (Richard et al., 2002). A single case of KID syndrome caused by a mutation in the *GJB6* gene has since been reported (Jan et al., 2004); however, *GJB2* remains the major causative gene for the condition. *GJB2*, located on chromosome 13q12, encodes a transmembrane, channel-forming protein known as connexin-26 (Cx26) (Richard et al., 2002). This gene has two exons, with the first exon encoding only an untranslated region and the second exon containing the entire protein-coding sequence (Sohl and Willecke, 2004). *GJB2* is expressed in multiple organs throughout the human body, including epithelial and connective tissues of the cochlea (Jagger and Forge, 2015), the epidermis and hair follicles of the skin (Arita et al., 2004; Di et al., 2001c), the corneal epithelium (Richard et al., 2002), placenta (Gabriel et al., 1998), neurons (Nagy et al., 2001) and epithelial tissues of the oesophagus, liver, stomach, pancreas, testis, mammary gland, sweat gland, lacrimal gland, pituitary and pineal glands (Michon et al., 2005; Uhlen et al., 2015).

GJB2 mutations, however, are not only linked to KID syndrome. To date, more than 150 *GJB2* mutations have been linked to syndromic hearing loss (SHL) or non-syndromic hearing loss (NSHL) (Kelsell et al., 1997; Xu and Nicholson, 2013). The former is associated with skin pathology and ectodermal dysfunction, whereas the latter is hearing loss only. Being classified as a SHL condition, KID syndrome has been thus far linked to 12 missense *GJB2* mutations **(Table 1.1)**, all inherited in an autosomal dominant manner. For this project, a thorough review of the literature between 2002 and 2009 was undertaken, including 40 papers published with genotypic

data. Among the 12 mutations, c.148G>A, which leads to the substitution of aspartic acid for asparagine at codon 50 (p.D50N), is the most common mutation, accounting for 47 of all 66 (71.2%) cases reviewed. This is consistent with a previous report of the largest European patient cohort (Mazereeuw-Hautier et al., 2007), which found 12/14 (86%) patients carrying this mutation. Although the rarity of KID syndrome has long limited the exploration of genotype-phenotype correlation, it is becoming clear that patients with p.G45E or p.A88V mutation usually die within several months after birth (Koppelhus et al., 2011; Sbidian et al., 2010), whereas those with p.D50N appear to have a normal life span (Mazereeuw-Hautier et al., 2007; Sakabe et al., 2012). This above information indicates that the p.D50N mutation serves as a good target for the present study aimed at developing a mutation-specific therapy for KID syndrome.

Four other SHL conditions with overlapping but distinct clinical presentation have also been linked to the *GJB2* gene, which include hystrix-like ichthyosis with deafness (HID, MIM 602540), Vohwinkel syndrome (VS, MIM 124500), Bart-Pumphrey syndrome (BPS, MIM 149200) and palmoplantar keratoderma with deafness (PPKD, MIM 148350). Similar to KID syndrome, all mutations responsible for these syndromes are dominant, single-nucleotide substitutions with only one exception, c.125delAGG (p.Δ42E) **(Table 1.1)**. These syndromes were initially recognised as independent conditions but were later grouped into two entities, KID-HID and VS-BPS-PPKD, based on the molecular aetiology (Lee and White, 2009). For example, HID, featuring spiky hyperkeratosis but lacking ocular involvement, has been linked to the p.D50N mutation that causes KID syndrome (van Geel et al., 2002). Interestingly, some KID syndrome patients with p.D50N mutation do not develop ocular abnormalities even in adulthood (Bondeson et al., 2006; Neoh et al., 2009). Likewise, VS manifests as severe honeycomb-like palmoplantar keratoderma (PPK) with constriction bands resulting in autoamputation of digits (Maestrini et al., 1999), whereas BPS displays relatively mild PPK with knuckle pads and leukonychia (Richard et al., 2004); these conditions turned out to have a common pathogenic mutation, p.G59S (Alexandrino et al., 2005). Furthermore, another VS-BPS mutation on the same residue (p.G59R), along with p.G130V, was later found to be shared by PPKD which is characterised by milder deafness and PPK with no constriction bands or knuckle pads (Iossa et al., 2009; Leonard et al., 2005). Such a phenotypic spectrum among the SHL conditions indicates that the *GJB2* function is variably affected

dependent on the nature and location of mutation. The gene function and the consequence of the mutations will be described subsequently.

Table 1.1 *GJB2* mutations linked to syndromic hearing loss

Phenotype	Mutations (cDNA)	Mutations (amino acid)	Clinical feature
Keratitis-ichthyosis -deafness syndrome (KID)	c.32G>A, c.34G>C, c.40A>T, c.42C>G, c.50C>T, c.89T>A, c.119C>T, c.134G>A, c.148G>A*, c.148G>T, c.148G>C, c.263C>T	G11E, G12R, N14K, N14Y, S17F, I30N A40V, G45E, D50N*, D50Y, D50A, A88V	Deafness, ocular impairment, hyperkeratosis (generalised), PPK (stippled), hair/nail dystrophy, cutaneous infection, malignancies (Coggshall et al., 2013)
Histrix-like ichthyosis deafness syndrome (HID)	c.148G>A*	D50N*	Deafness, hyperkeratosis (generalised, spiky, cobberstone-like), PPK (van Geel et al., 2002)
Vohwinkel syndrome (VS)	c.175G>A#, c.193T>C, c.196G>C, c.389G >T#	G59S#, Y65H, D66H, G130V#	Deafness, PPK (honeycomb-like), constriction bands (Maestrini et al., 1999)
Bart-Pumphrey syndrome (BPS)	c.160A>C, c.162C>A, c.175G>A#, c.175G>C#	N54H, N54K, G59S#, G59R#	Deafness, PPK (milder), knuckle pads, leukonychia (Richard et al., 2004)
Palmoplantar keratoderma with deafness (PPKD)	c.125delAGG, c.175G>C#, c.176G>C, c.218A>G, c.223C > T, c224G>A, c.389G>T#, c.548C>T, c.551G>A	ΔE42, G59R#, G59A, H73R, R75W, R75Q, G130V#, S183F, R184Q	Deafness, PPK (Heathcote et al., 2000)

Note: * and # indicate shared mutation by KID-HID and VS-BPS-PPKD. These two different entities are shaded in darker colour and lighter colour, respectively.

Abbreviation: PPK, palmoplantar keratoderma.

The remaining *GJB2* mutations are linked to recessive NSHL (MIM 220290) or dominant NSHL (MIM 601544), accounting for the vast majority of identified *GJB2*

mutations (Xu and Nicholson, 2013). Those NSHL mutations, including missense, nonsense, frameshift and indel mutations, contribute to approximately half of total individuals with congenital hearing loss from a diversity of ethnic groups (Chang et al., 2003; Kelsell et al., 1997; Lee and White, 2009; Petit et al., 2001; Srinivas et al., 2017). This study, however, focuses on KID syndrome and its related mutations.

1.1.3 Current treatment and hurdles

The current mainstay of treatment for KID syndrome includes a combination of emollients, and topical or oral retinoids that improve the skin barrier (Avshalumova et al., 2014; Coggshall et al., 2013). Among different oral retinoids, acitretin has been reported to improve hyperkeratotic lesions with no major adverse effects on vision or hearing (Sahoo et al., 2002). Antifungal and antibacterial agents are necessary for infection control. For keratitis, the use of topical anti-inflammatory agents such as topical corticosteroids and cyclosporine A (Serrano-Ahumada et al., 2017) and implantation of a Boston keratoprosthesis (Brown et al., 2016) have been reported. For deafness, cochlear implantation has demonstrated clinical benefit, i.e. improved hearing, speech and language skills, in at least nine cases (Arndt et al., 2010; Smyth et al., 2012). However, post-operative habilitation can be hindered by skin complications such as infection, poor wound healing, skin necrosis and extrusion of implant. Thus, regular skin assessment and management are essential post-operatively.

A major challenge in clinical practice is the development of SCC. This malignancy occurs in around 20% KID patients between the ages of 15-43 years (Natsuga et al., 2011), and metastasis of SCC and malignant proliferative trichilemmal tumours have been reported to occur even before the age of 30 years (Nyquist et al., 2007). In the latter report, the authors argued that the presence of chronic infection and/or festering inflammation (e.g. follicular occlusion triad) could contribute to malignant transformation in patients with KID syndrome, however the pathogenesis of tumour formation in this condition is not yet understood. Unfortunately, detecting the malignant lesions at an early stage is challenging. These lesions often arise underneath the base of hyperkeratotic plaques, making early biopsy and surgical removal difficult. Furthermore, the molecular basis of success in common dermatological treatment is usually not understood. For example, an early immunostaining study found that topical

application with a retinoic acid massively up-regulated Cx26, the protein product of *GJB2*, in the skin of healthy human volunteers (Masgrau-Peya et al., 1997). Although the molecular basis for good acitretin treatment response in KID syndrome patients (Patel et al., 2015; Wolfe et al., 2017) has not been specifically addressed, this routine treatment may potentially enhance expression of the functionally-detrimental mutant *GJB2* allele (see below) and could adversely affect cellular function, as originally argued by others (Levit and White, 2015). As an alternative therapeutic option, the present study aims to develop a mutation-targeted therapy for KID syndrome.

1.2 Connexin, hemichannel and gap junction

1.2.1 Connexin: nomenclature, topology and life cycle

Cx26 belongs to the connexin family, a highly-conserved transmembrane protein family consisting of 21 members in the human genome. Two alternative systems of nomenclature are in use, one based on the molecular weight of connexin peptide ('Cx' system), and the other based on the sequence homology ('GJ' system) (Kumar and Gilula, 1992; Kumar et al., 1996). According to the latter system, connexin members are classified into five subfamilies: alpha (GJA), beta (GJB), gamma (GJC), delta (GJD) and epsilon (GJE) connexins (Koval et al., 2014). At present, the GJ system is used for the names of connexin genes and the Cx system is used for their protein products (Willecke and Nielsen, 2007). For example, the *GJB2* gene encodes a beta connexin Cx26 protein with a molecular weight of 26 kDa.

The 21 connexins have a common topology with four transmembrane segments (TM1-TM4) connected by two extracellular loops (E1-E2) and a cytoplasmic loop (CL), along with an amino-terminal (NT) and a carboxyl-terminal (CT) domains that are oriented toward the cytoplasm (Maeda et al., 2009; Sanchez and Verselis, 2014) **(Figure 1.1)**. High levels of sequence homology have been reported in all transmembrane and extracellular domains among connexin homologs (Laird, 2006), with the exception of the CT domain, which has diversity in the length, amino acid sequence and size, ranging from 23 to 62 kDa (Aasen et al., 2016). This domain is thought to contribute to unique biophysical properties of different connexin subtypes (Zoidl et al., 2008). For instance, phosphorylation at residues in the CT domain of

connexin-43 (Cx43) tightly links to its protein function through regulating the channel assembly, trafficking, clustering, channel gating, and protein-protein interaction (Aasen et al., 2016), but Cx26, the smallest connexin with a very short CT domain, is considered to have a phosphorylation-independent regulatory mechanism (Traub et al., 1989). Each connexin has a unique life cycle, trafficking and channel behaviour (see below).

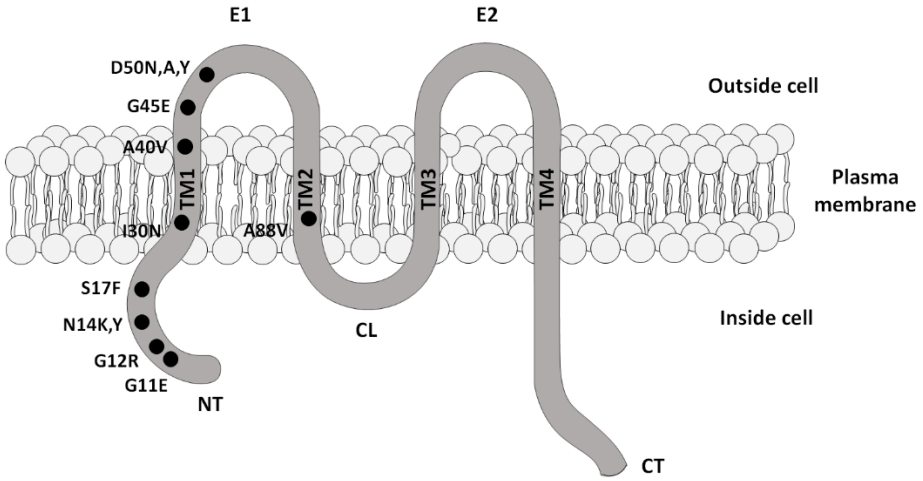

Figure 1.1 Model for the topology of connexins

Connexins share a similar topology. Taking Cx26 as an example, it is 4-transmembrane protein that has four transmembrane domains (TM1-TM4). The loops between TM1 and TM2, as well as between TM3 and TM4, are the first and second extracellular loop domains (E1 and E2), respectively. The loop between TM2 and TM3 is the cytoplasmic loop domain (CL). Amino-terminal (NT) and carboxyl-terminal (CT) domains, oriented toward the cytoplasm, are also depicted. All 12 Cx26 mutants linked to KID syndrome are shown. These mutants are concentrated in the highly-conserved NT and E1 domains, with the exception of p.I30N (TM1) and p.A88V (TM2).

Connexins are found in virtually every type of vertebrate cell (Bruzzone et al., 1996). In general, connexins are synthesised in the endoplasmic reticulum membrane and then transported to the Golgi apparatus, where six connexin subunits assemble to form a connexon before trafficking to the plasma membrane through vesicular transport along microtubules (Laird, 2006; Martin et al., 2014; Naus and Laird, 2010). On the plasma membrane, connexons can either function alone as hemichannels, or 'dock' with a compatible connexon present on the cell membrane of an adjacent cell to form a full gap junction channel **(Figure 1.2)**. Furthermore, gap junction channels can aggregate to form a gap junction plaque, a mature configuration of gap junction channels. Connexins on the cell surface are generally known to have a high turnover rate, with a

half-life of only 1.5−5 hours (Fallon and Goodenough, 1981; Laird et al., 1995; Thomas et al., 2005), followed by internalisation into one of the adjacent cells. The internalised gap junctions formed a structure known as annular gap junction or connexosome for later ubiquitination and lysosomal degradation (Leithe, 2016).

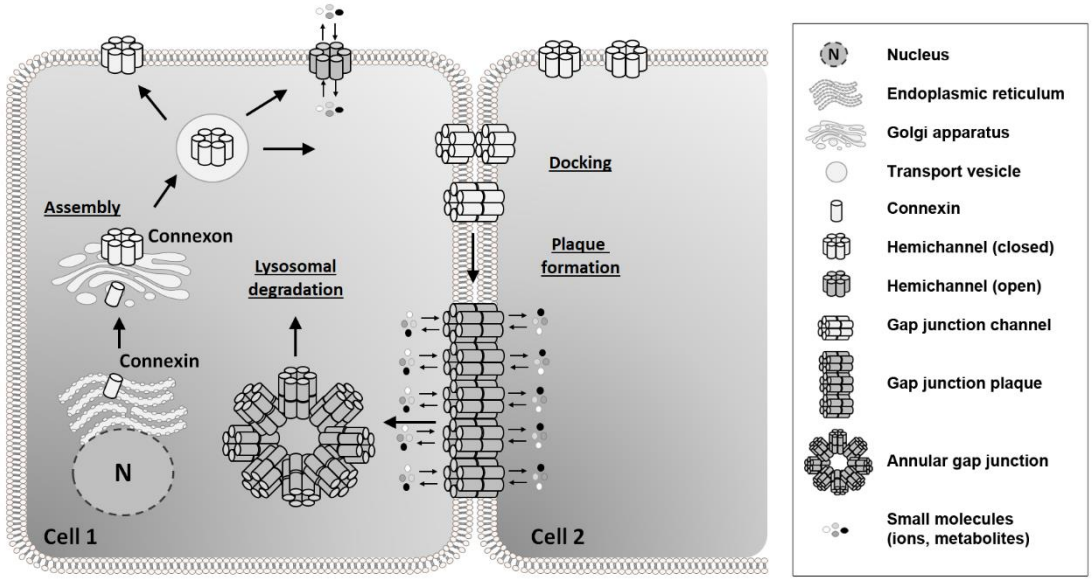

Figure 1.2 Schematic of the typical life cycle of connexins

Connexins are synthesised in the endoplasmic reticulum. After trafficking to the Golgi apparatus, correctly folded connexin subunits assemble (or oligomerise) into hexameric connexons. Connexons are then trafficked to the plasma membrane via vesicular transport along microtubules. On the plasma membrane, a connexon can function as hemichannel or dock with another hemichannel from the neighbouring cell, forming a gap junction channel. Hemichannels connect the cytoplasm and the extracellular space, while gap junction channels couple the cytoplasm from two neighbouring cells by the direct exchange of various small molecules. Gap junction channels can aggregate to form gap junction plaques, i.e. mature gap junction channels. Connexins and gap junctions are short-lived on the cell surface. After a life span of a few hours, they are internalised to form a structure known as annular gap junction, followed by lysosomal degradation.

1.2.2 Gap junction channel and hemichannel

Connexins have been studied for over five decades (Revel and Karnovsky, 1967) as the principal protein components of gap junction channels (Aasen et al., 2016). These channels form a conduit between the cytoplasm of adjacent cells, mediating the direct exchange of small molecules with a molecular weight < 1 kDa (Elfgang et al., 1995), while undocked hemichannels directly connect the cytoplasm and the extracellular space. Both forms of channels are permeable to various inorganic ions (including Na^+,

K^+, Ca^{2+}), metabolites (including glucose, lactate), signalling molecules such as adenosine triphosphate (ATP), inositol 1,4,5-triphosphate (IP_3), cyclic adenosine and guanosine monophosphate (cAMP and cGMP), along with microRNA (Bevans et al., 1998; Giaume et al., 2013; Katakowski et al., 2010; Lohman and Isakson, 2014; Niessen et al., 2000; Payton et al., 1969; Valiunas et al., 2018). With the property to provide essential electrical and biochemical coupling between adjacent cells, gap junction channels are well recognised for their role in intercellular communication and tissue coordination (Delmar et al., 2017; Lawrence et al., 1978; Saez et al., 2010; Srinivas et al., 2017). In excitable cells, e.g. cardiac and neuronal cells, the electrical coupling functions to generate rapid and synchronised responses, whereas in non-excitable cells, e.g. skin, the metabolic coupling is involved in the propagation of coordinated responses (Mese et al., 2007). These functions, collectively known as gap junction intercellular communication (GJIC), are indispensable in the regulation of cell proliferation, differentiation, apoptosis and growth (Berger et al., 2014). This notion is well supported by lethal or severe developmental phenotypes reported in mice genetically lacking Cx26 (Cohen-Salmon et al., 2002; Dicke et al., 2011; Gabriel et al., 1998), Cx43 (Reaume et al., 1995), Cx45 (Kruger et al., 2000) or Cx50 (White et al., 1998).

In contrast, hemichannels have a less clear role *in vivo*, where cells are more tightly packed and hence have fewer non-junctional plasma membranes compared to *in vitro* culture conditions (Schalper et al., 2008). These channels have been studied extensively since the earliest *in vitro* electrophysiological analyses of hemichannels in *Xenopus* oocytes expressing exogenous Cx46 (Paul et al., 1991), cultured solitary horizontal cells of the catfish (DeVries and Schwartz, 1992) and skate retinas (Malchow et al., 1993), which detected an outward membrane current with time- and voltage-dependence consistent with half of a gap junction channel (DeVries and Schwartz, 1992). Later single-channel studies on mammalian and non-mammalian cell expression systems found factors such as membrane voltage, intracellular pH, and Ca^{2+} concentration can regulate the activity of hemichannels (Bukauskas and Verselis, 2004; Delmar et al., 2017). Currently, it is accepted that, unlike gap junction channels, non-junctional hemichannels predominantly remain in the closed state under physiological conditions (Bennett et al., 1991; Contreras et al., 2003) by at least one of the following mechanisms: i) channel blockade by extracellular Ca^{2+} and Mg^{2+}, ii) post-translational

modifications, and iii) negative membrane potentials that close most hemichannels (Johnstone et al., 2012; Retamal et al., 2015). The closure of hemichannels prevents cell death induced by passive loss of ion gradients and metabolites, a consequence of persistent hemichannel opening (Garcia et al., 2016). However, hyperactivity of hemichannels has been implicated in a series of human disorders in the skin, inner ear, lens, nervous system, and heart (Retamal et al., 2015), and the relevant skin disorders will be discussed below.

Each of the 21 identified connexins is endowed with a special functional identity (Sanchez and Verselis, 2014). As an added level of complexity, hemichannels and gap junction channels can be formed by more than one type of connexin (Bevans et al., 1998; Cottrell and Burt, 2005; Koval et al., 2014). Hemichannels composed of a single type of connexin are known as homomeric hemichannels, and those formed by two or more compatible connexin types are termed heteromeric hemichannels **(Figure 1.3)**. Moreover, two identical or different types of hemichannels can dock head-to-head to form homotypic or heterotypic gap junction channels, respectively.

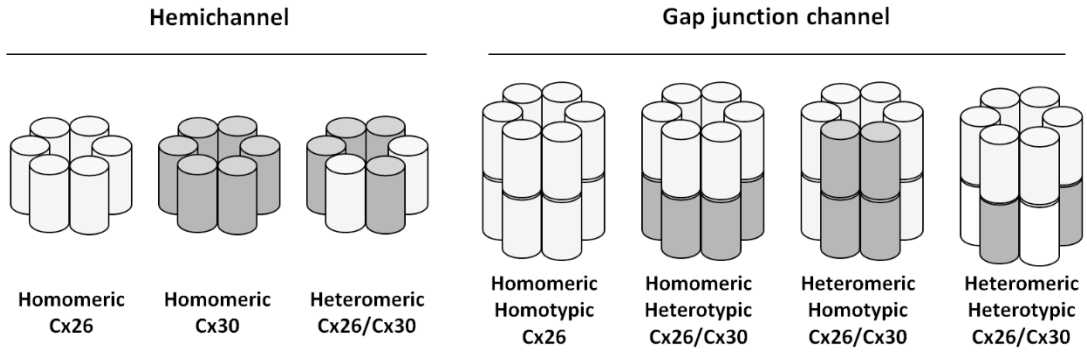

Figure 1.3 Schematic of different organisations of connexins
Connexins can assemble to form homo- and heteromeric hemichannels. These hemichannels can dock with each other to form homo- and heterotypic gap junction channels. Cx26 is represented as unfilled cylinders and Cx30 is represented as filled cylinders. Note that only compatible connexins, like Cx26 and Cx30, can form heteromeric channels.

These heterogeneously-assembled channels have biophysical behaviours which are distinct from their homogenous counterparts (Cottrell and Burt, 2005). These include half-life, ionic conductance, gating, permeability and selectivity (perm-selectivity) to specific molecules, and response to environmental stimuli or post-translational

modifications. Chronic exposure of cultured vascular smooth muscle cells, A7r5, to growth factors was found to lead to progressive loss of GJIC (Kurjiaka et al., 1998), later found to result from an elevation of Cx40-to-Cx43 expression ratio induced by the stimulus of growth factors (Cottrell et al., 2001). In support of these findings, studies by others showed that heteromeric channels formed by Cx26 and Cx32 dynamically prevented the intercellular passage of cGMP (but not cAMP); in contrast, both cGMP and cAMP passed normally via homomeric Cx32 channels (Bevans et al., 1998). The above evidence suggests that the formation of heterogeneous channels provides functional diversity in cellular communication and signalling for their respective tissue types. The process is likely to be dynamically-regulated in response to different chemical (e.g. growth factors, inflammatory signals) and physical stimuli (e.g. mechanical force).

1.2.3 Functional assays for gap junctions and hemichannels

GJIC can be measured as intercellular dye transfer, metabolic cooperation and electrical conductance (Abbaci et al., 2008). The first cell-to-cell dye transfer was reported in 1964 (Kanno and Loewenstein, 1964). A gap junction-permeant fluorescent dye was microinjected into a cell without affecting cell viability, resulting in diffusion of the dye to the adjacent cell(s). This intercellular diffusion represents the permeability and selectivity of gap junctions formed between the cells (i.e. 'coupled' cells). Later dye transfer studies employed techniques such as scrape loading (el-Fouly et al., 1987), electroporation (Raptis et al., 1994), pre-loading (also known as a parachute assay) (Goldberg et al., 1995) and fluorescence recovery after photobleaching (Wade et al., 1986), all still in use currently. On the other hand, gap junctional metabolic cooperation can be examined by incubating a population of donor cells with a radiolabelled precursor, e.g. [^{14}C]-glucose (Goldberg et al., 1998), co-culturing the cells with unlabelled recipient cells to allow intercellular transfer of the metabolite, followed by autoradiography to quantify gap junctional coupling. Finally, since gap junction permeability correlates linearly with its electrical conductance (Abbaci et al., 2008), single channel currents and gap junctional conductance in cell pairs serve as further measures for GJIC and can be quantified using electrophysiological methods (Neyton and Trautmann, 1985).

Analogous to GJIC assays, hemichannel activity can be determined by measuring transmembrane dye uptake, permeability to signalling molecules (e.g. ATP, Ca^{2+}) and transmembrane currents (Schalper et al., 2008). Solitary cells are often studied to rule out the contribution of gap junction channels. Dye uptake is a simple assay that measures permeability of a fluorescent dye through hemichannels present on the cell surface (Paul et al., 1991). Likewise, open hemichannels also lead to ATP release into the extracellular space and influx of Ca^{2+}, which can be readily detected using bioluminescence method and Ca^{2+} imaging, respectively (Cotrina et al., 1998). In addition, transmembrane currents through open hemichannels can be detected by electrophysiological methods such as patch clamp and voltage clamp (Schalper et al., 2008). Since each of the above assays has their advantages and limitations, a combination of different assays is commonly carried out to provide complementary functional information. This also helps to distinguish between connexin hemichannels and hemichannels formed by pannexins (Schalper et al., 2008), close relatives of connexins.

1.3 Connexin and skin diseases

1.3.1 The skin and epidermal barrier

The skin is the largest organ of the human body, and is composed of the hypodermis, dermis and epidermis (Nestle et al., 2009). The hypodermis is a loose connective tissue whose function is mainly fat storage. The dermis, a collagen/elastin-rich, dense connective tissue containing blood vessels and nerves, functions to nourish and supply nutrients to the epidermis and its appendages, e.g. sweat glands, sebaceous glands and hair follicles. The epidermis is the outermost layer of the skin, consisting of stratified squamous epithelial cells (keratinocytes) which form the skin barrier. This barrier protects against the body from water loss, microorganism invasion, and physical and chemical insults from the environment (Blaydon and Kelsell, 2014). Histologically, the epidermis has four layers representing four states of differentiation of keratinocytes: the basal, spinous, granular, and cornified layers. The basal layer contains epidermal stem cells which differentiate to renew the upper epidermal layers continuously. The terminal differentiation programme in epidermal keratinocytes is critical for maintaining the integrity of the epidermal barrier (Martin et al., 2014). Corneocyte is

the name given to terminally differentiated keratinocytes residing in the cornified layer, and along with cell-envelope proteins and intercellular lipids which are tightly crosslinked, these provide mechanical strength and water permeability to the barrier. Keratinocytes from lower layers in the epidermis (spinous and granular layers) express junctional proteins that strengthen the barrier (Proksch et al., 2008). The integrity of the barrier is closely linked to a Ca^{2+} gradient in the epidermis that regulates keratinocyte differentiation and lipid secretion (Bosen et al., 2015).

Also essential to the maintenance of the epidermal barrier is the epidermal junctional nexus, a complex junctional network composed of tight junctions, adherens junctions and gap junctions (Martin et al., 2014). The protein constituents of these junctions (e.g. connexins and cadherins) are differentially expressed throughout the epidermal compartments (Churko and Laird, 2013), and can interact with each other to form a structure known as a junctional nexus that regulates cellular function (Bazzoun et al., 2013). For example, Cx43 and E-cadherin (a component of adherens junctions), can associate with β-catenin (an adherens junction protein) and zonula occludens-1 (a tight junction scaffold protein), which bind to the actin cytoskeleton (Laird, 2006). These interactions are thought to modulate the dynamics of cell-cell adhesion, migration and proliferation of keratinocytes which is required for proper epidermal barrier formation (Martin and van Steensel, 2015). Furthermore, desmosomal cadherins such as desmoplakin and plakoglobin also associate with keratin filaments, the major element of keratinocytes, contributing to mechanical support (Garrod and Chidgey, 2008). Mutations disrupting the association between plakophilin-1 and keratin filaments are known to cause skin fragility (McGrath et al., 1997).

1.3.2 Connexins in the skin

1.3.2.1 Differential expression of connexins in the epidermis

Since the epidermis is an avascular tissue, the presence of connexins at cell-cell junctional sites allow communication within and between epidermal layers. This is likely to contribute to the propagation of coordinated responses to environmental stimuli, such as damage to the cornified layer (Takada et al., 2014). At least ten connexin members (beta connexins: Cx26, Cx30, Cx30.3, Cx31, Cx31.1, Cx32, and

alpha connexins: Cx37, Cx40, Cx43, Cx45) are expressed dynamically in the human epidermis (at mRNA level) (Di et al., 2001c). These connexins are differentially expressed at protein level throughout the epidermal compartments **(Figure 1.4)**, with an overlapping expression of multiple connexins detected in differentiated suprabasal epidermal layers (Cx26, Cx30, Cx30.3, Cx31, Cx40, Cx43, Cx45) and fewer connexins detected in the undifferentiated basal layer (Cx43 and, less abundantly, Cx30) (Choudhry et al., 1997; Martin et al., 2014; Salomon et al., 1994). In contrast, connexins are barely detectable in the cornified layer. These findings, mainly revealed by immunostaining, are consistent with results from ultrastructural analysis (Caputo and Peluchetti, 1977).

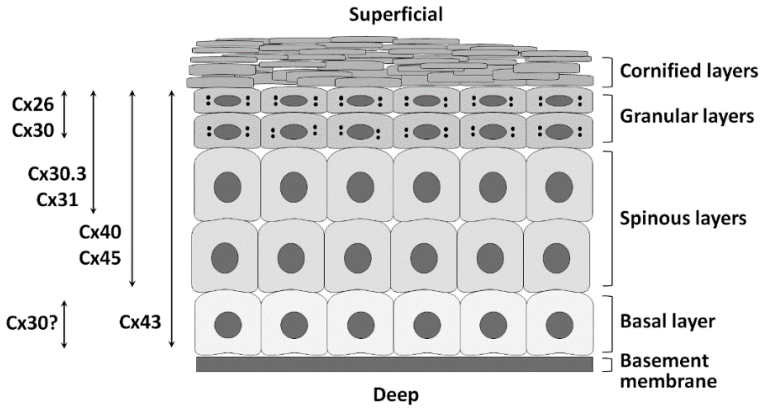

Figure 1.4 Schematic of connexin expression profile in normal human epidermis
At least ten connexins are expressed in human epidermis. Each connexin is expressed in an overlapping but distinct spatial pattern. Cx43 is expressed throughout the epidermis, while expression of Cx40 and Cx45 extensively overlaps with Cx43 but these connexins are not present in basal keratinocytes. Cx30.3 and Cx31 are expressed in the granular and upper spinous layers. In contrast, expression of Cx26 and Cx30 seems compartmentalised in granular layers, although Cx30 has been found in the basal layer in some studies (Richard et al. 2002). Certain genetic mutations in five of the connexins (Cx26, Cx30, Cx30.3, Cx31, Cx43) have been implicated in skin disorders.

Cx43 is the major epidermal connexin expressed throughout all human epidermal layers, with strongest expression found in upper differentiated keratinocyte layers and weak expression in basal keratinocytes (Di et al., 2001c). A previous flow cytometry study showed that 10% of basal keratinocytes from human foreskin did not express Cx43 and these cells had characteristics corresponding to stem cells (Matic et al., 2002).

1.3.2.2 Connexins and the epidermal barrier

Connexins are involved in keratinocyte proliferation and differentiation, which are essential for epidermal barrier formation (Choudhry et al., 1997; Djalilian et al., 2006; Lucke et al., 1999). The presence of functional gap junction channels has been confirmed in the intact human and mouse epidermis, in which keratinocytes showed epidermal compartment-dependent permeability to Lucifer Yellow, a gap junction-permeant dye (Kam et al., 1986; Salomon et al., 1988). Connexin channels are also permeable to second messengers such as IP_3 and Ca^{2+} (Saez et al., 1989), whose signalling is important in keratinocyte proliferation and differentiation (Bikle and Mauro, 2014). The Ca^{2+} signalling is involved in the establishment of the epidermal Ca^{2+} gradient, which is characterised by an increase in extracellular Ca^{2+} level as keratinocytes differentiate, with a peak in the granular layers and complete absence of extracellular Ca^{2+} in the cornified layers (Blaydon and Kelsell, 2014; Elias et al., 2002). Interestingly, in the epidermis, the distribution of Ca^{2+}, connexin expression (Figure 1.4) and GJIC (Salomon et al., 1988) seem to follow a similar pattern, with the highest levels found in the granular layers. Thus, connexins present in the epidermis may contribute to the Ca^{2+} gradient, which in turn regulates keratinocyte proliferation and differentiation. This hypothesis is supported by transgenic mice with Cx43 C-terminal mutation displayed defective epidermal barrier function with increased toluidine permeability (Maass et al., 2004).

There is also evidence of the importance of connexin in the epidermal barrier from other diseases, such as psoriasis. Psoriasis is a chronic, inflammatory skin disorder characterised by hyperproliferation and incomplete differentiation of keratinocytes, as well as disturbance of Ca^{2+} gradient across epidermal layers (Elsholz et al., 2014; Garcia et al., 2016; Menon and Elias, 1991). Up-regulation of Cx26 is a hallmark of psoriatic lesions (Labarthe et al., 1998; Lucke et al., 1999). Transcriptomic analysis of lesional psoriasis skin biopsies found massively increased *GJB2* expression (19-fold) compared to normal skin biopsies (Li et al., 2014). Significant changes in other connexin genes were also found, including up-regulation of *GJB6* (Cx30, 7-fold) and down-regulation of *GJB4* (Cx30.3, 17-fold) (Li et al., 2014; Martin and van Steensel, 2015). A later genome-wide association study linked a single-nucleotide variant in *GJB2* as a predisposing factor for psoriasis in the Chinese population (Sun et al., 2010).

In a transgenic mouse study, overexpression of *GJB2* in the suprabasal keratinocyte layers was sufficient to induce a psoriatic phenotype, that is, hyperproliferation, impaired barrier integrity and inflammatory response (Djalilian et al., 2006). The subsequent *in vitro* experiments on the mouse keratinocytes detected enhanced hemichannel-dependent ATP release that stimulates purinergic signalling pathways and influx of Ca^{2+}. These data suggest that hemichannels also regulate the integrity of epidermal barrier. Interestingly, Cx26 is normally expressed at a low, nearly undetectable level in the epidermis, but it has been found up-regulated significantly in papillomatous lesions infected by human papilloma viruses (Lucke et al., 1999) and experimentally-induced wounds (Goliger and Paul, 1995), in addition to psoriatic lesions (Labarthe et al., 1998). Altogether, these data implicate multiple connexin channels in the maintenance of the epidermal barrier, possibly via regulation of Ca^{2+} signalling.

Finally, human molecular genetic data from epidermal connexins provide further support for the role of connexins in keratinocyte proliferation and differentiation. Mutations in five connexin genes, *GJB2*, *GJB3*, *GJB4*, *GJB6*, *GJA1*, encoding Cx26, Cx31, Cx30.3, Cx30 and Cx43, respectively, are linked to a spectrum of hyperkeratotic skin disorders (Lilly et al., 2016). Other than the five *GJB2*-associated SHL conditions (KID, HID, VS, BPS, PPKD) **(Table 1.1)**, Clouston syndrome (MIM 129500, a hidrotic form of ectodermal dysplasia), characterised by PPK and hair and nail abnormalities, is linked to mutations in *GJB6* (Lamartine et al., 2000). Erythrokeratodermia variabilis et progressiva (EKV-P) (MIM 603324, 605425 and 617525), characterised by hyperkeratotic plaques and transient, figurate erythema, has been linked to *GJB3* (Richard et al., 1998), *GJB4* (Macari et al., 2000) and *GJA1* genes (Boyden et al., 2015). *GJA1* has also been linked to keratoderma- hypotrichosis-leukonychia totalis syndrome (KHLS) (MIM 104100) characterised by more severe hyperkeratosis with a hair phenotype (Wang et al., 2015). Whilst these conditions share a common feature of hyperkeratosis, there is clear heterogeneity in the clinical presentation (e.g. age of onset and distribution of lesions) and in channel function, including hemichannel and gap junction activity (Lilly et al., 2016). Each epidermal connexin therefore has unique functions, and mutations therein can lead to specific disturbances in the epidermal architecture.

1.3.2.3 Connexins in wound healing

It is becoming clear that the interplay of epidermal connexins, including Cx26, Cx30, Cx31, Cx31.1, Cx37, Cx40 and Cx43, is involved in the process of wound healing (Becker et al., 2012; Churko and Laird, 2013; Martin et al., 2014). Early data from rodent skin showed that, during initial wound healing (24−48 h post-wounding), Cx26 and Cx30 are up-regulated in all epidermal layers at the leading wound edge, whereas Cx43 and Cx31.1 are down-regulated (Coutinho et al., 2003; Goliger and Paul, 1995). In a human wound model, although Cx26 and Cx30 were only faintly detected at the wound edge during initial wound healing (Brandner et al., 2004), cells behind the edge subsequently showed a gradual recovery of Cx26 and Cx30 expression; however, Cx43 expression was barely detectable at and near the wound edge, consistent with results from rodent models. The expression of these connexins is restored after re-epithelialisation (Brandner et al., 2004; Coutinho et al., 2003; Goliger and Paul, 1995). The reduced level of GJIC-mediated dye coupling corresponded to the down-regulation of Cx43 (Goliger and Paul, 1995; Kretz et al., 2003; Wright et al., 2009). It is now clear that the marked and rapid (within < 3 h post-wounding) down-regulation of Cx43 and reduced GJIC activity at the acute healing phase can promote the migration of keratinocytes by reducing the cell-cell or cell-matrix adhesion via its binding partner, zona occuludens-1 (Martin et al., 2014; Press et al., 2017a; Tarzemany et al., 2017; Wright et al., 2012). As a result, keratinocytes migrate into the wound margin and then proliferate and differentiate, reforming the skin barrier. The recovery of Cx43 during re-epithelialisation can enhance differentiation state of keratinocytes, promoting later stages of wound healing (Churko et al., 2010).

In vivo data from transgenic mouse models have provided further support for the role of Cx43 in wound healing. In $Cx43^{Cre\text{-}ER(T)/fl}$ mice that had an 85% reduction of Cx43 expression level, Kretz and colleagues revealed shortened wound closure time compared to that in the wildtype mice (Kretz et al., 2003). In addition, keratinocytes isolated from an oculodentodigital dysplasia (ODDD, Cx43 deficiency) mouse model with Cx43 p.G60S mutation showed enhanced proliferation and differentiation (Churko et al., 2012). These findings are supported by persistent expression of Cx43 in non-healing wounds from chronic, diabetic leg ulcers (Brandner et al., 2004; Wang et al., 2007a). Those findings led to a hypothesis that inhibition of Cx43 expression

may accelerate closure of chronic diabetic wounds. With this in mind, studies over the last decade have focused on the use of Cx43-specific inhibitors. Results showed that a Cx43-specific antisense oligonucleotide significantly accelerated the wound closure and granulation tissue formation and alleviated other wound-related negative events such as inflammation (Becker et al., 2012; Mori et al., 2006; Wang et al., 2007a). Likewise, in multiple studies using different mouse or human culture models, a higher migration rate of keratinocytes was achieved by treatment with a connexin-mimetic peptide. These are molecules such as Gap26 and Gap27 that mimic Cx43 extracellular domains, and modulate its channel activity reversibly without altering overall expression level (Desplantez et al., 2012; Kandyba et al., 2008; Pollok et al., 2011; Wang et al., 2012; Wright et al., 2009). Encouraging pre-clinical data have led to the extensive development of novel Cx43-mimetic peptides (Becker et al., 2012; Evans et al., 2012; Lohman and Isakson, 2014). Recently, Grek and colleagues published effective and safe outcomes in clinical trials for αCT1, a 25-amino acid peptide mimicking the CT domain of Cx43, for the treatment of diabetic foot ulcer and cutaneous scarring (Grek et al., 2017; Grek et al., 2015). A phase 3 trial is currently under way (ClinicalTrial.gov, NCT02667327). In contrast to Cx43, the role of Cx26 in wound healing is less clear (Martin 2015) and warrants further research using human cell-based models.

1.3.2.4 Connexins in cancer

Five decades ago, loss of GJIC was first proposed to be a characteristic of cancer cells (Fentiman and Taylor-Papadimitriou, 1977; Johnson and Sheridan, 1971; Loewenstein and Kanno, 1966; McNutt and Weinstein, 1969; Nicolas et al., 1978). Successful cloning of connexin members facilitated investigation of the role of these proteins in tumours (Aasen et al., 2016; Grek et al., 2014). Early work in the 1990s found that ectopic expression of specific connexins in glioma (Naus et al., 1992; Zhu et al., 1991) or hepatoma models (Eghbali et al., 1991) was sufficient to improve GJIC and could inhibit tumour cell growth, leading to the suggestion that connexins are tumour suppressors. Consistently, multiple studies using animal models either lacking or expressing loss-of-function mutant of Cx26, Cx32 or Cx43 showed increased spontaneous or chemically-induced lung, liver and breast tumours (Aasen et al., 2016; Naus and Laird, 2010). The proposed mechanisms by which GJIC may suppress

tumour growth include the propagation of death signals and/or growth inhibition via regulating specific kinases (Huang et al., 2002; Krutovskikh et al., 2002; Tittarelli et al., 2015; Wang et al., 2007b).

However, it is currently evident that the tumour suppressive property is more complex, and is dependent on tumour stage (Chen et al., 2016; Zhang et al., 2015a), tumour type (Yang et al., 2015) and connexin subtype (Grek et al., 2014). First, a report by Ito and colleagues showed that subcutaneous injection of mouse melanoma cells expressing exogenous Cx26 led to enhanced metastasis (Ito et al., 2000), which was attributed to the exogenous GJIC between melanoma cells and endothelial cells that facilitated (rather than blocked) intravasation and extravasation. Second, in lung cancer cell lines, exogenous expression of Cx43 reversed epithelial-mesenchymal transformation (EMT) and reduced cellular resistance to cisplatin chemotherapy (Yu et al., 2014), whereas exogenous expression of Cx26 promoted EMT and rendered them gefitinib-resistant (Yang et al., 2015). Third, contrary to the findings in lung cancer cells, exogenous expression of Cx26 in breast cancer cells was shown to reverse the EMT-like property, suggesting tissue-specific tumour suppression (McLachlan et al., 2006). Finally, the contribution of GJIC-independent events may exist, such as hemichannels or the connexin interactome (McLachlan et al., 2006; Zhang et al., 2014). The context-dependent tumour suppressive effect has been reviewed exhaustively (Aasen et al., 2016).

Connexins have also been implicated in skin malignancies. Non-melanocytic, keratinocyte-derived tumours (SCC and basal cell carcinoma) exhibited increased Cx26 and Cx30 expression and variably decreased Cx43 expression (Haass et al., 2006; Tada and Hashimoto, 1997). Strikingly, in malignant melanoma tissues, the expression of Cx26 and Cx30, along with Cx43, was entirely absent within the tumour itself but drastically up-regulated in the epidermal keratinocytes adjacent to the tumour (Haass et al., 2006), and such expression pattern was not observed in benign tumour tissues (Haass et al., 2006). The absence of Cx26 and Cx30 is consistent with the reverse-transcription polymerase chain reaction (RT-PCR) results from two melanoma cell lines (Zucker et al., 2013). These findings indicate a role of Cx26 and Cx30 in the interaction between melanoma and keratinocytes in the epidermis. A subsequent study by Haass and colleagues on 40 human melanoma tissue samples identified positive

correlations between the above induced-Cx26/Cx30 expression pattern (horizontal or vertical) in the epidermis to metastasis and the proliferative index of melanoma, respectively (Haass et al., 2010). The authors argued that the level of Cx26/Cx30 expression adjacent to the tumour could be a complementary diagnostic marker for distinguishing melanoma and benign melanocytic naevi. On the other hand, Cx26 overexpression is known to render keratinocytes proliferative in the epidermis (Djalilian et al., 2006) and the resulting hyperplastic epidermis can promote proliferation and progression of melanoma, which induce angiogenesis (McCarty et al., 2003), a process linked to GJIC between melanoma and vascular endothelial cells (Hsu et al., 2000; Pollmann et al., 2005; Saito-Katsuragi et al., 2007). The above gap junction-mediated tumour-stroma interactions may facilitate diapedesis of tumour cells, leading to metastasis (Brandner and Haass, 2013).

While *in vitro* studies suggest tumour suppressive effects of Cx43 (Su et al., 2000; Tittarelli et al., 2015), accumulating data imply an unclear role of Cx43 in different tumours (Aasen et al., 2016; Brandner and Haass, 2013). Immunostaining of human melanoma tissues showed up-regulation of Cx43 with probable cytoplasmic localisation (Rezze et al., 2011; Sargen et al., 2013), in disagreement with those reported by Haass et al. (Haass et al., 2006). The cytoplasmic localisation was also reported in chemically-induced hamster tongue SCC (Saitoh et al., 1997) and in malignant cystic trichilemmal tumour tissues from a KID syndrome patient (Nyquist et al., 2007). In the latter report, the authors found markedly reduced or absent Cx26 and Cx30 expression in addition to aberrantly localised Cx31, Cx36 and Cx43. Accordingly, statistical analysis of immunostained human melanoma tissues found no correlations between Cx43 membrane staining and melanoma malignancy (Haass et al., 2010).

From the above cancer studies, several extended roles of connexins in cell survival, invasion, metastasis, chemoresistance and regulation of EMT can be inferred, in addition to proliferation, differentiation and migration which have been described in earlier sections. However, no definitive role in tumour suppression has been reported for any connexin. Therefore, it is not surprising that no connexin-targeting clinical trials for cancer have been initiated to date (Delmar et al., 2017), in contrast to the above αCT1 trials where Cx43 serves as an unequivocal target for effective wound

treatment. Future studies are warranted to classify cancer carefully based on connexin expression, which should be instrumental in establishing connexin-targeted therapy as an alternative cancer treatment programme.

1.3.3 Cx26 mutants in the skin

1.3.3.1 Cx26 mutants: loss-of-function

Typically, nonsense, frameshift and the majority of missense mutations result in loss of protein function. Nonsense and frameshift mutations produce a premature stop codon, leading to truncation of the protein product. In *GJB2*, all mutations causing NSHL are loss-of-function mutations that impair or abolish Cx26 channel function, with c.35delG being the most prevalent in Caucasians (White and Paul, 1999). In contrast, most missense mutations in *GJB2* cause both NSHL and SHL (Xu and Nicholson, 2013). For those causing NSHL, the resulting Cx26 protein can have defects in either trafficking, docking or permeability. Cx26 with c.551G >A (p.R184Q) mutation was found to have trafficking defects, showing accumulation in the Golgi apparatus (Su et al., 2010), whereas Cx26 with c.514T>A (p.W172R) has a docking defect despite being found to traffic to the plasma membrane normally (Mani et al., 2009). Finally, Cx26 with c.250G>C (p.V84L) mutation has normal membrane trafficking, forming gap junction plaques which show normal dye and electrical coupling, but has reduced permeability to IP_3, impairing the propagation of Ca^{2+} waves (Beltramello et al., 2005). Although NSHL-linked *GJB2* mutants do not cause major cutaneous pathology, some patients with these mutations were found to have thickened epidermis (D'Adamo et al., 2009; Guastalla et al., 2009; Man et al., 2007) and elevated Na+ and Cl- concentrations in sweat (Meyer et al., 2002). The authors argued that these features may be selective advantages, protecting patients against pathogen invasion, insect bites and trauma.

In contrast to NSHL, *GJB2* mutations causing SHL (including VS-BPS-PPKD and KID-HID) are single-base substitutions (with only one exception, p.Δ42E), comprising loss-of-functions and gain-of-function mutations (Martin et al., 2014). The gain-of-function mutations, causing KID-HID, will be described in the following section. To date, VS-BPS-PPKD, with a shared characteristic of PPK and deafness, is linked to 14

mutations, of which 11 are clustered in the E1 domain, with the majority affecting residues N54 (p.N54H, p.N54K), G59 (p.G59R, p.G59A, p.G59S) and R75 (p.R75W, p.R75Q) **(Table 1.1)**. Two further E1 mutations, p.Y65H and p.D66H, appear to be the molecular signature for VS and are not shared with BPS or PPKD. This notion has been confirmed by a study using transgenic mice with epidermal-specific p.D66H expression, which recapitulated VS features as observed in human patients (Bakirtzis et al., 2003), including keratoderma and constriction bands.

It is now clear that these VS-BPS-PPKD mutations are loss-of-function mutations with a relatively uniform mechanism (Lee and White, 2009; Martin et al., 2014). The most widely studied mutant is p.D66H that causes VS. By using mammalian exogenous expression systems, multiple laboratories found impaired channel function when expressing this mutant, including defective membrane trafficking with no gap junction plaque formation, reduced GJIC-mediated dye coupling and electrical coupling, and absent hemichannel-dependent ATP release (de Zwart-Storm et al., 2011a; Easton et al., 2012; Marziano et al., 2003; Rouan et al., 2001; Thomas et al., 2005). Co-expression with wildtype Cx26 or Cx30 can partially rescue the membrane trafficking and cell coupling (Marziano et al., 2003; Rouan et al., 2001), suggesting that the mutant Cx26 can interact with wildtype connexins, by forming heteromeric channels and/or sorting into the same gap junction plaque (Di et al., 2005; Marziano et al., 2003). Such interaction between mutant Cx26 and wildtype Cx26 is termed cis-dominant effect and that with the co-expressed Cx30 is termed trans-dominant effect (Lee and White, 2009). The latter effect was confirmed in a p.D66H mouse model (Bakirtzis et al., 2003). The endogenous (wildtype) Cx30 protein, which focally co-localised with mutant Cx26, exhibited cytoplasmic accumulation with reduced expression level. Similar results were reported for another VS-linked mutant, p.Y65H (de Zwart-Storm et al., 2011b). Recently, a report showed that the BPS-linked p.N54K also displayed the above defects in trafficking and GJIC (but with normal hemichannel permeability) in a cis- and trans-dominant (Cx30 and Cx43) manner (Press et al., 2017b). These dominant effects, similar to those observed in p.D66H mice, were also reported recently in two PPK-linked mutants, p.H73R and p.S183F, on Cx43 channel gating, with clear evidence of heteromeric mutant Cx26/Cx43 channel formation (Shuja et al., 2016). Finally, increased programmed cell death was reported in the epidermis of

p.D66H mice *in situ* (Bakirtzis et al., 2003), but cell death does not appear to be a major issue in mammalian cells expressing exogenous VS-BPS-PPKD mutants (Berger et al., 2014; Press et al., 2017b). Whether the mutant-associated toxicity is under-reported or subtle in the tested systems (mostly HeLa cells) remains to be confirmed.

Collectively, those data point towards a common mechanism of VS-BPS-PPKD as defective membrane trafficking. The trafficking defects might be attributed to channel docking in which the E1 domain (where most of those mutants reside) is crucial (Bai and Wang, 2014; Banks et al., 2009). As a result, there are reduced or absent gap junction channels formed on the cell surface, significantly decreasing the level of GJIC, a scenario similar to Cx26-linked NSHL where gap junctions formed by the mutant Cx26 are essentially non-functional (Martinez et al., 2009; Xu and Nicholson, 2013). Since GJIC conferred by Cx26, Cx30 and other connexin channels are required for normal hearing (Jagger and Forge, 2015; Zhang et al., 2005), the loss of Cx26-mediated GJIC can explain the hearing loss in VS-BPS-PPKD patients (Lee and White, 2009).

Apart from the above functional defects shared with NSHL, mutants linked to VS-BPS-PPKD possess an additional property, namely the trans-dominant effect on co-expressed connexins (Bakirtzis et al., 2003; Marziano et al., 2003; Press et al., 2017b; Rouan et al., 2001; Shuja et al., 2016). If such effect occurs in the epidermis where Cx26, Cx30, Cx43 and at least six other connexins are expressed, one can expect an overall impaired GJIC and a series of downstream events, such as dysregulation of Ca^{2+} gradient, affecting proliferation and differentiation of keratinocytes (Garcia et al., 2016). This may, in part, explain the presence of PPK in VS-BPS-PPKD patients. The notion is further supported by the skin involvement (PPK) reported only in a small subset of patients with ODDD, the Cx43 deficiency syndrome affecting the bone, tooth and digits but usually spares the skin (Laird, 2014). Among numerous known loss-of-function mutations for ODDD, only two C-terminal truncating mutations have been reported to have additional PPK features (van Steensel et al., 2005; Vreeburg et al., 2007). These Cx43 mutations display defective trafficking and GJIC and likely to inhibit other epidermal connexins trans-dominantly, perturbing epidermal differentiation and barrier formation, as shown by organotypic culture skin models

(Churko et al., 2010). Future work should be directed towards the mechanism of cell death in association to cytoplasmic accumulation observed in VS-BPS-PPKD mutants. Pathways related to ER stress and unfolded protein responses serve as attractive candidates (Martin et al., 2014; Tattersall et al., 2009).

1.3.3.2 Cx26 mutants: gain-of-function

In general, gain-of-function mutations, also known as activating mutations, are relatively rare in the context of inherited conditions (Rorth et al., 1998). These mutations result in acquisition of novel protein behaviour differing from its wildtype counterpart (Levit and White, 2015). For example, gain-of-function mutations in the gene coding for an innate immune sensor CARD15 cause constitutively activated nuclear factor(NF)-κB signalling, leading to an autoimmune disease (Shwin et al., 2017). In connexin genes, gain-of-function mutations can result in: i) enhanced gap junction permeability, e.g. EKV-causing Cx31 p.G12R (Diestel et al., 2002), ii) enhanced hemichannel permeability, e.g. KID syndrome-causing Cx26 p.I30N (Aypek et al., 2016), and iii) altered gating properties, e.g. Clouston syndrome-linked Cx30 p.A88V (Essenfelder et al., 2004) and KHLS- linked Cx43 p.G8V (Wang et al., 2015). In the literature, some argued that 'gain of interacting partners' should be considered as a trait of gain-of-function mutations (Lilly et al., 2016); for example, trans-dominant inhibition of VS-linked Cx26 p.D66H on Cx43 with which Cx26 does not normally assemble into heterogenous channels (Rouan et al., 2001; Thomas et al., 2004). Although the above consideration is plausible genetically, the functional nature of the mutant as well as the overall functional consequence point towards loss of channel function, as argued in (Martin et al., 2014). In this thesis, *GJB2* mutations causing VS-BPS-PPKD as well as ODDD are tentatively classified as loss-of-function mutations.

By contrast, accumulating functional evidence has shown that Cx26 mutants linked to KID-HID have enhanced hemichannel permeability in addition to altered gating (see below), and hence those pathogenic mutations are here classified as gain-of-function mutations, reviewed in (Lee and White, 2009; Martin et al., 2014). Twelve known KID syndrome mutations map to the NT domain (p.G11E, p.G12R, p.N14K, p.N14Y, p.S17F) and the E1 domain (p.A40V, p.G45E, p.D50N, p.D50Y, p.D50A), with two exceptions, p.I30N (TM1) and p.A88V (TM2) (Lee and White, 2009; Xu and

Nicholson, 2013). These two domains are thought to contain elements critical for channel gating regulation or to form the aqueous pore of the channel, whose size closely correlates to channel permeability and selectivity (Maeda et al., 2009; Sanchez and Verselis, 2014; Srinivas et al., 2017). In addition, as mentioned above, the E1 domain, residing extracellularly, is involved in docking of two connexons, a step essential for gap junction channel formation (Banks et al., 2009, Bai and Wang, 2014). Consistent with these notions, mutations linked to KID syndrome have been found to exert a series of pathological alteration on both gap junction channels and hemichannels, leading to the unique phenotype.

1.3.3.2.1 Altered gap junction communication in KID syndrome

The effects of KID syndrome mutations on gap junction channels seem inconclusive, with varying results obtained from different assay methods **(Table 1.2)** (Garcia et al., 2016). Eight mutants have been determined for GJIC. By *Xenopus* oocyte-based electrophysiological assay, the majority (p.G12R, p.N14Y, p.S17F, p.A40V, p.D50N, p.D50Y) appears to have either reduced or absent GJIC-mediated electrical coupling (Garcia et al., 2016; Garcia et al., 2015; Gerido et al., 2007; Lee et al., 2009; Mese et al., 2011; Montgomery et al., 2004; Schutz et al., 2011), except for p.N14K and p.G45E that appear to form normally functioning gap junctions (Gerido et al., 2007, Lee et al., 2009). That Cx26 p.G45E forms functional gap junction channels was confirmed by Ca^{2+} permeability assay (Stong et al., 2006). In the same year, a scrape-loading dye transfer assay (SLDT) study on p.N14Y patient-derived keratinocytes found a reduction of anionic Lucifer Yellow dye coupling (Arita et al., 2006), in disagreement with results reported elsewhere (Lee et al., 2009). Later, several contradicting results were given by the parachute assay, another dye transfer method employing a more negatively-charged dye, calcein (de Zwart-Storm et al., 2011a; Donnelly et al., 2012). These studies revealed enhanced dye coupling in HeLa Ohio cells expressing exogenous p.G12R or p.D50N mutants (Donnelly et al., 2012) and absent dye coupling in those expressing exogenous p.N14K mutant (de Zwart-Storm et al., 2011a). In keeping with studies showing impaired GJIC, many groups found absent or morphologically-abnormal gap junction plaques formed at points of cell-cell contact, by using mammalian cells expressing fluorescently-tagged Cx26 mutants (Aypek et al., 2016; de Zwart-Storm et al., 2011a; Di et al., 2005; Donnelly et al., 2012; Mese et

al., 2011; Mhaske et al., 2013; Ogawa et al., 2014; Rodriguez-Paris et al., 2016; Terrinoni et al., 2010).

The varying GJIC results indicate that gap junctions formed by KID syndrome-linked Cx26 mutants play an unclear role in the pathogenesis of KID syndrome. Given that a greater portion of these mutants show altered trafficking and/or reduced GJIC, one may speculate that the development of hearing loss as well as some skin features in KID syndrome may follow, at least in part, the mechanism proposed above in VS-BPS-PPKD. However, KID syndrome manifests as more diverse skin and eye involvement accompanied by skin infection and cancer, favouring a more complex pathomechanism. Interestingly, several lines of evidence suggest that the p.G45E mutant, causing a severe, lethal form of KID syndrome, forms normal gap junctions *in vitro* comparable to those formed by wildtype Cx26 (Stong et al., 2006, Gerido et al., 2007). This observation strongly indicates that GJIC is either not involved or plays a lesser role in the pathogenesis of KID syndrome. If this concept could be generalised to all other mutants, one may assume that hemichannels, instead of gap junction channels, may be the key player in the pathogenesis of KID syndrome.

Table 1.2 Channel functions in reported Cx26 mutants linked to KID syndrome

Cx26 mutant	Hemichannel	Gap junction channel	References
p.G11E (c.32G>A)	↑ Ca^{2+} influx	Not determined	Terrinoni et al., 2010
p.G12R (c.34G>C)	↑ Membrane currents ↑ ATP release ↑ Heteromeric Cx26/Cx43 channel (↑ Ca^{2+} influx and ATP release) Altered gating	↓ Electrical coupling ↑ Dye coupling (calcein)	Lee et al., 2009; Donnelly et al., 2012; Sanchez and Verselis, 2014; Garcia et al., 2015 Garcia 2018
p.N14Y (c.40A>T)	↑ Heteromeric Cx26/Cx43 channel (↑ Ca^{2+} influx and ATP release) Altered gating	↓ Dye coupling (Lucifer Yellow) Normal dye coupling (calcein)	Arita et al., 2006; de Zwart-Storm 2011; Garcia et al., 2015; Sanchez et al., 2016
p.N14K (c.42C>G)	↑ Membrane currents Refractory to channel closing Insensitive to pH	↓ Dye coupling (calcein) Normal electrical coupling	Lee et al., 2009; de Zwart-Storm 2011; Sanchez et al., 2016
p.S17F (c.50C>T)	↓ Membrane currents (alone) ↑ Heteromeric Cx26/Cx43 channel (↑ Ca^{2+} influx and ATP release)	↓ Electrical coupling (mutant alone)	Lee et al., 2009; Schutz et al., 2011; Garcia et al., 2015
p.I30N (c.89T>A)	↑ Dye uptake (neurobiotin) ↑ Ca^{2+} influx	Not determined	Aypek et al., 2016
p.A40V (c.119C>T)	↑ Membrane currents Dysregulation by Ca^{2+}, pH	↓ Electrical coupling	Montgomery et al., 2004; Gerido et al., 2007; Sanchez et al., 2010, 2014
p.G45E (c.134G>A)	↑ Dye uptake (neurobiotin) ↑ Ca^{2+} influx Altered voltage gating	Normal electrical coupling and Ca^{2+} coupling	Stong et al., 2006; Gerido et al., 2007; Sanchez et al., 2010; Mese et al., 2011
p.D50N (c.148G>A)	↑ Ca^{2+} influx ↑ Membrane currents Altered Ca^{2+} regulation, single-channel conductance and gating	↓ Electrical coupling ↑ Dye coupling (calcein)	Lee et al., 2009; Terrinoni et al., 2010; Donnelly et al., 2012; Lopez et al., 2013 Sanchez et al., 2013
p.D50Y (c.148G>T)	↑ Dye uptake (neurobiotin) ↑ Ca^{2+} influx Altered Ca^{2+} gating	Not determined	Lopez et al., 2013 Aypek et al., 2016
p.D50A (c.149A>C)	↑ Membrane currents	Not determined	Mhaske et al., 2013; Sanchez and Verselis, 2014
p.A88V (c.263C>T)	↑ Membrane currents Insensitive to CO_2	Not determined	Mhaske et al., 2013; Meigh et al., 2014

1.3.3.2.2 Hyperactive hemichannels in KID syndrome

Over the last decade, aberrant hemichannel activity has emerged as the leading contributor to the pathology of KID syndrome, reviewed in (Garcia et al., 2016; Lee and White, 2009; Martin et al., 2014; Sanchez and Verselis, 2014). All 12 known mutants have been studied for hemichannel activity and the data consistently indicate gain of function, resulting in formation of hyperactive (or 'leaky') hemichannels. Under physiological conditions, hemichannels are tightly regulated by Ca^{2+} and pH (Sanchez and Verselis, 2014). In the case of deregulated, hyperactive mutant hemichannels, the increased opening probability of these non-selective channels can cause: i) collapse of the cellular ionic gradient that is crucial for establishment of the resting potential and ii) escape of essential metabolites, energy sources and signalling molecules, which are detrimental to cellular function (Bennett et al., 1991; Contreras et al., 2003; Evans et al., 2012; Retamal et al., 2015; Sanchez and Verselis, 2014; Spray et al., 2006). Consistent with the above hypotheses, accumulating *in vitro* experiments have shown that mutant Cx26 channels linked to KID syndrome display impaired control by Ca^{2+} (Lopez et al., 2013; Sanchez et al., 2013), pH (Sanchez et al., 2014), and more recently CO_2 (de Wolf et al., 2016; Meigh et al., 2014). Accordingly, these mutants were found to have altered voltage gating (Garcia et al., 2018; Sanchez et al., 2016; Sanchez et al., 2013), increased ATP release into extracellular space (Donnelly et al., 2012; Garcia et al., 2015) and/or elevated intracellular Ca^{2+} level (Aypek et al., 2016; Garcia et al., 2015; Mese et al., 2011; Terrinoni et al., 2010). Further evidence is given by the significantly larger transmembrane currents detected in primary keratinocytes from a transgenic mouse model with Cx26 p.G45E mutant (Levit et al., 2015; Mese et al., 2011). The above changes in Cx26 biophysical property agree with the three-dimensional structural data obtained from crystallography (Maeda et al., 2009), which showed most residues linked to KID syndrome (G12, N14, A40, G45, D50) were spatially oriented near the pore; they may play a role in voltage-sensing and/or perm-selectivity control. In contrast, residues affected by PPKD-linked mutations, with no known role for hemichannels, are evenly located throughout the wall of Cx26 (Garcia et al., 2016; Levit et al., 2012).

Mechanistically, increased ATP release through aberrantly open hemichannels may act

as a paracrine signal, activating purinergic signalling pathways through ATP receptors (e.g. ATP-gated P2X channels) expressed in keratinocytes (Burnstock et al., 2012). The activation of those receptors, which results in Ca^{2+} flux (James and Butt, 2001), is implicated in inflammation and keratinocyte proliferation, differentiation and apoptosis (Burnstock et al., 2012; Greig et al., 2003). In addition, open hemichannels can directly mediate Ca^{2+} influx, leading to cell death (Wang et al., 2015). Consistent with the above notions, *in vitro* cell death has been reported by many laboratories in cells expressing mutants linked KID syndrome (Stong et al., 2006, Gerido et al., 2007, Lee et al., 2009, Terrinoni et al., 2010, Mhaske et al., 2013, Press et al., 2017b). Cell death can be rescued by an increase of extracellular Ca^{2+} level for a subset of mutants (Gerido et al., 2007, Lee et al., 2009). The above results suggest that the Ca^{2+} homeostasis is affected in cells expressing KID syndrome-linked mutants and, in the epidermis, this may disrupt the Ca^{2+} gradient leading to barrier defect (Garcia et al., 2016). Recently, this hypothesis has been confirmed in an elegant study using a transgenic Cx26 p.S17F mouse model (Bosen et al., 2015), which exhibited a defective water barrier featuring altered lipid processing and the presence of Ca^{2+} in the cornified layer (which is normally absent). A defective water barrier triggers compensation in the epidermis with a hyperplastic response, resulting in epidermal hyperproliferation and hyperkeratosis (Elias et al., 2012), the hallmark of KID syndrome. Furthermore, the barrier defect may also contribute to the susceptibility to bacterial and fungal superinfection, as has been reported frequently in KID syndrome (Coggshall et al., 2013). A previous work showed that peptidoglycan from *Staphylococcus aureus*, but not the skin commensal species, further enhanced the activity of p.G12R and p.D50N hemichannels and induced a pro-inflammation response (Donnelly et al., 2012). These data provide the molecular link between hemichannel-mediated inflammation signalling and bacterial susceptibility which is frequently reported in patients with KID syndrome.

1.3.3.2.3 Dominant effects on epidermal connexins

As mentioned earlier, the cis- and trans-dominant effects of mutant Cx26 play a pivotal role in the skin pathology of SHL, and this concept has been confirmed in KID syndrome (Garcia et al., 2015). In an earlier study, Lee and colleagues found an unusual hemichannel pattern only in *Xenopus* oocytes expressing homotypic Cx26

p.S17F mutant (Lee et al., 2009), which failed to form functional hemichannels, contradicting results from other KID syndrome mutants. This enigma was not resolved until 2015, when Garcia and colleagues demonstrated enhanced hemichannel activity of Cx26 p.S17F when co-expressing with wildtype Cx26 or Cx43, but not by itself (Garcia et al., 2015). Further analysis revealed that the p.S17F mutant, in addition to p.G12R and p.N14Y, exerted trans-dominant effects on Cx43 by formation of heteromeric hemichannels, resulting in increased transmembrane currents and enhanced ATP release and Ca^{2+} influx. In fact, over the last decade, the assembly of (wildtype) Cx26/Cx43 heteromeric channels has been considered absent due to incompatibility, with convincing evidence given by multiple assays (Gemel et al., 2004). Hence, the findings by Garcia et al. serve as a special case of heteromeric oligomerisation resulting from mutations in "oligomerisation compatibility checkpoint" residues in the NT domain, providing a novel mechanism for KID syndrome. Future work is warranted to determine whether mutations from the other cluster in the E1 domain can confer the same oligomerisation compatibility with Cx43. Trans-dominant effects of Cx26 p.D50N mutant have been found on Cx30, Cx30.3 and Cx31 protein trafficking in previous co-transfection studies (Di et al., 2005; Shurman et al., 2005). With a highly overlapping expression pattern in the epidermis **(Figure 1.4)**, these connexins are known to have high compatibility (Koval et al., 2014; Yum et al., 2007). Nevertheless, detailed biophysical data of these heteromeric channels, if any, are required to gain further insight into the pathogenesis of KID syndrome.

1.4 Novel and effective therapeutic intervention for KID syndrome

1.4.1 Towards developing specific therapies

Hyperactive hemichannels have emerged as the leading contributor in the pathogenesis of KID syndrome. This concept led to two recent developments of hemichannel-targeted therapy (Levit et al., 2015; Xu et al., 2017) utilising either a small molecular compound (Levit et al., 2015) or a monoclonal antibody (Xu et al., 2017). Although synthetic Cx43-mimetic peptides (mentioned earlier) have shown promise in wound treatment (Becker et al., 2012; Evans et al., 2012; Grek et al., 2014; Wong et al., 2016), the peptide mimetic technique has not yet been available for Cx26.

The first study of hemichannel-targeted therapy for KID syndrome was carried out using mefloquine, a small molecular compound previously approved for anti-malarial treatment (Levit et al., 2015). The authors provided evidence that mefloquine potently inhibited hyperactive hemichannels in *Xenopus* oocytes expressing exogenous Cx26 p.G45E and p.D50N mutants. Remarkably, this compound corrected aberrant hemichannel activity in keratinocytes isolated from a KID syndrome mouse model with Cx26 p.G45E. Very recently, abEC1.128a, a monoclonal antibody specifically binding to the E1 domain of Cx26, has been shown to target wildtype Cx26 hemichannels potently and specifically (but not gap junctions) in human keratinocytes, with no overt cytotoxicity observed *in vitro* and *in vivo* (Xu et al., 2017). Similar to mefloquine, in human keratinocytes, abEC1.128a potently inhibited normal hemichannels formed by wildtype Cx26, or hyperactive hemichannels formed by p.G45E or p.D50N mutant. Although both mefloquine and abEC1.128a hold strong therapeutic promise for KID syndrome, some safety concerns may arise with future clinical translation. For example, mefloquine has been reported to inhibit Cx36, Cx50 (Cruikshank et al., 2004) and pannexin-1 (Iglesias et al., 2009), along with multiple voltage- or volume-gated channels (Cruikshank et al., 2004; Gribble et al., 2000), and it seems toxic to the mouse cochlea and cultured human keratinocytes at 100 μM (Xu et al., 2017), despite 30 μM mefloquine already demonstrating effective inhibition of mutant hemichannels in the tested model (Levit et al., 2015). Regarding the antibody abEC1.1, it targets not only mutant Cx26 hemichannels but also wildtype Cx26 hemichannels (Xu et al., 2017). Since these molecules are in the early stages of development, whether they can improve the skin condition symptomatically and histologically with acceptable level of adverse effects remains to be carefully assessed using *in vivo* models.

Given that KID syndrome is a dominant condition in which wildtype and mutant Cx26 alleles are co-expressed, the differential pharmacological inhibition of both wildtype and mutant hemichannels needs to be considered when developing a specific therapy.

1.4.2 RNA interference for KID syndrome

Since the discovery of RNA interference (RNAi) and related pathways (Fire et al., 1998), RNA-based therapies have emerged as a powerful tool for investigation of gene

function, and potentially for treating a wide range of diseases and disorders, reviewed in (Davidson and McCray, 2011). Moreover, the high specificity of RNAi to its target mRNA sequence has led to the concept of allele-specific RNAi (Brummelkamp et al., 2002; Martinez et al., 2002). This technique theoretically allows silencing of a mutant allele without affecting its co-expressed wildtype counterpart whose sequence is highly homologous, hence holding therapeutic potential for dominant disorders. In our opinion, the allele-specific RNAi technique is likely to be a promising treatment option for KID syndrome, in which dominant, gain-of-function mutations play a major biological role in the pathogenesis. Here, an overview of RNAi techniques is presented.

1.4.2.1 RNA interference

RNAi is a conserved mechanism of post-transcriptional gene silencing found in a variety of organisms, including fungi, plants and animals (Hannon, 2002). This technique was first discovered by Fire, Mellow and colleagues, who reported potent gene silencing by exogenous double-stranded RNA in *Caenorhabditis elegans* (Fire et al., 1998). Three years later, Tuschl and colleagues found that synthetic RNA duplex, also known as small interference RNA (siRNA, 21 nucleotides), triggered sequence-specific gene silencing in mammalian cell lines (Elbashir et al., 2001a). Shortly after that, the first successful RNAi-mediated gene silencing in mouse was reported, in synthetic form (siRNA) and in plasmid form (small-hairpin RNA, or shRNA) (McCaffrey et al., 2002). These pioneering works established a versatile platform for characterisation of gene function and development of RNA-based therapies.

Mechanistically, RNAi is a two-step process. First, double-stranded RNA, typically exogenous in mammalian cells (Jackson and Linsley, 2010), is cleaved into siRNA of around 21-22 nucleotides by Dicer, a RNase III-like nuclease enzyme (Bernstein et al., 2001) **(Figure 1.5)**. The use of synthetic siRNA (usually around 21 nucleotides) can avoid the step of Dicer processing, preventing potential interferon responses which are dependent on the length of siRNA (Watts and Corey, 2012). The second step is the incorporation of siRNA into the RNA-induced silencing complex (RISC), where the siRNA is unwound by Argonaute 2 (a RNase present within RISC) into two single-stranded siRNAs (Rand et al., 2004), namely the antisense strand (or 'guide strand') and the sense strand (or 'passenger strand'). The passenger strand is cleaved (Matranga

et al., 2005), while the guide strand activates the RISC. The activated guide-RISC complex scans, recognises and binds to the target mRNA whose sequence is complementary to the guide sequence (Ameres et al., 2007). Once bound, the target mRNA is cleaved between the position 10 and 11 of the complementary antisense strand (Rand et al., 2005), allowing for post-transcriptional gene silencing. The cellular process of RNAi has been reviewed elsewhere (Jackson and Linsley, 2010; Whitehead et al., 2009).

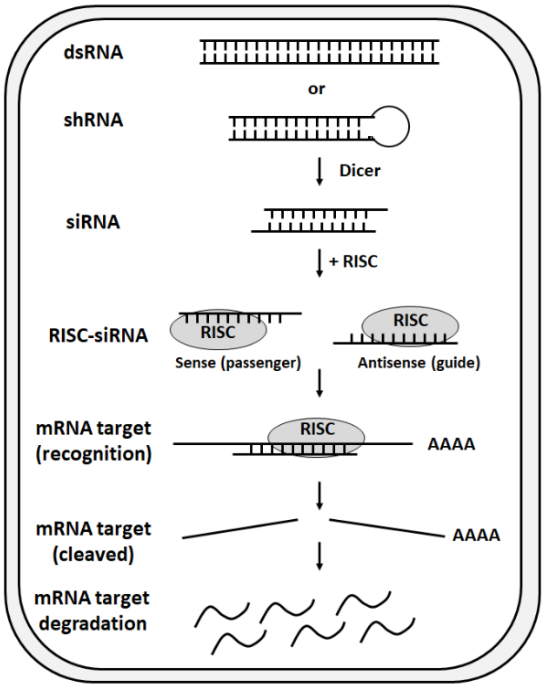

Figure 1.5 The RNA interference pathway

Long double-stranded RNA (dsRNA) or small-hairpin RNA (shRNA) in the cytosol is cleaved by the enzyme Dicer into siRNA of around 21-nt length. Alternatively, the siRNA duplex can be directly introduced into the cell. The siRNA duplex is then loaded into the RNA-induced silencing complex (RISC). The sense (passenger) strand-RISC complex is cleaved and the antisense (guide) strand activates the RISC. This allows the activated siRNA-RISC to scan for target mRNA that is complementary to the sequence of the guide strand. Once recognised and bound by the activated RISC, the target mRNA is cleaved and degraded, allowing for post-transcriptional gene silencing.

Over the last decades, promising outcomes have been given by the use of synthetic siRNA for treating viral infection (hepatitis B virus and Ebola virus) and cancer (leukaemia and neuroblastoma) (Whitehead et al., 2009). The synthetic siRNA technique has also been used for treating hearing loss in a PPKD mouse model with a c.223C>T mutation (p.R75W) in *GJB2* (Maeda et al., 2005). The author showed a

siRNA designed against the wildtype *GJB2* mRNA sequence potently inhibited the mutant *GJB2* mRNA, preventing the onset of hearing loss. This work has been patented (publication number US20070243242 A1) for its successful pre-clinical outcomes.

1.4.2.2 Allele-specific siRNA

Mismatches between a siRNA and its target mRNA sequence have been reported to weaken, or even abolish, the gene silencing effects (Amarzguioui et al., 2003; Elbashir et al., 2001b; Schwarz et al., 2006), providing the basis for designing an allele-specific siRNA that can discriminate between mRNAs differing by even at a single nucleotide. This concept is useful for developing novel treatment for conditions with dominant effects, such as KID syndrome. In those conditions, an allele-specific siRNA can silence the expression of mutant allele without affecting the expression of wildtype allele, reviewed in (Trochet et al., 2015).

Successful *in vitro* and *in vivo* outcomes of allele-specific siRNA treatment have been reported in a range of dominantly-inherited skin disorders, such as epidermal fragility disorder (Leslie Pedrioli et al., 2012), dominant dystrophic epidermolysis bullosa (Pendaries et al., 2012) and pachyonychia congenita (Hickerson et al., 2008; Smith et al., 2008). Moreover, the reversal of pathological phenotype has been reported in mouse models with hair shaft defects (Liu et al., 2016b) and centronuclear myopathy (Trochet et al., 2018). The strong therapeutic potential resulted in the first-in-human mutation-specific siRNA trial for pachyonychia congenita (Leachman et al., 2010). Intradermal injection of an allele-specific siRNA, called TD101, led to significant regression of a characteristic callus lesion in one patient with no reported adverse effects.

1.5 Hypothesis, aims and objectives

1.5.1 Hypothesis

In this project, it is hypothesised that treatment with allele-specific siRNA can improve the skin condition of KID syndrome, through specifically silencing the mutated *GJB2*

allele while leaving the wildtype allele unaffected. In this way, the remaining normally-functioning wildtype allele, instead of the mutated allele, can be expressed dominantly, leading to improvement of overall cellular functions, which can potentially reverse KID syndrome **(Figure 1.6)**.

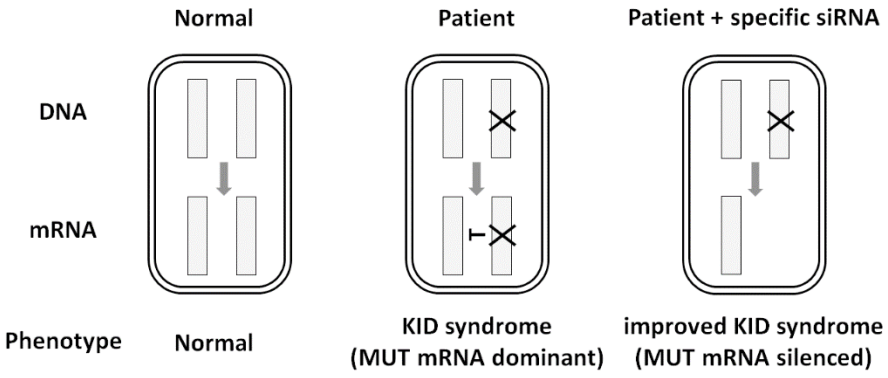

Figure 1.6 Schematic of proposed allele-specific siRNA treatment and outcome
In the context of patient skin (middle), the mutated GJB2 allele (MUT, represented by X) is known to play the dominant pathological role by producing mutant Cx26 protein, regardless of the presence of the wildtype GJB2 allele. This causes an overall aberrant Cx26 function corresponding to KID syndrome phenotype. Following treatment with the allele-specific, mutant-targeted siRNA (right), the mutant GJB2 mRNA is silenced, leaving the normally-functioning wildtype allele to be dominantly expressed. This is expected to correct the aberrant Cx26 functions, potentially reversing the pathological phenotype.

The rationale for the development of siRNA therapy in this study is as follows:

i) The molecular genetics and pathogenesis of KID syndrome is becoming clear following 16 years of studies using exogenous and endogenous *in vitro* expression systems and at least three transgenic mouse models (Mese et al., 2011; Press et al., 2017a; Schutz et al., 2011), which are supported by an increasing number of molecularly-confirmed patients.

ii) There is a hotspot mutation in *GJB2*, namely c.148G>A (p.D50N), accounting for over 70% of the reported KID syndrome cases (Mazereeuw-Hautier et al., 2007).

iii) The dominant-acting nature of KID syndrome-linked mutants (including p.D50N) has been confirmed by different experimental methods (Di et al., 2005; Meigh et al., 2014; Sanchez et al., 2016; Shurman et al., 2005), and the proposed siRNA therapy is expected to alleviate such effect on wildtype Cx26 and on other epidermal connexins.

1.5.2 Objectives

This study aims at developing allele-specific siRNA therapy for KID syndrome. To achieve the aim, there are major objectives as follows:

i) To compare the epidermal morphology and expression of Cx26, Cx30 and Cx43 between skin tissues from a normal individual and a patient heterozygous for *GJB2* c.148G>A mutation.

ii) To establish a patient-derived keratinocyte model with the c.148G>A mutation for *in vitro* experiments.

iii) To identify a *GJB2* c.148G>A-specific siRNA, which can discriminate between wildtype and mutant *GJB2* sequences differing by a single nucleotide.

iv) To investigate the effect of c.148G>A-specific siRNA on hemichannel and gap junction channel functions in patient-derived keratinocytes.

v) To further investigate the specificity and signalling pathways affected by the siRNA treatment, using RNA sequencing-based transcriptomic analysis.

This is a proof-of-concept study. If successful, this strategy could potentially be applied to a wide range of dominant skin disorders, in particular those with dominant effects, including VS, BPS, PPKD, EKV-P, ODDD and many connexin-unrelated disorders.

CHAPTER 2.
MATERIALS AND METHODS

2.1 Skin biopsies

A written informed consent was obtained from a patient with KID syndrome (KID-1 thereafter), who had been recruited in the Department of paediatric dermatology at Great Ormond Street Hospital. This study was approved by the local committee of research ethics (12/LO/1522). Punch biopsies measuring 3 mm in diameter with underlying tissue to a 5-mm depth were taken from interfollicular skin of KID-1 and two healthy donors (C32 and C38 thereafter, with ages within 5-year difference from KID-1). The skin biopsies were fixed in 4% (v/v) paraformaldehyde at 4°C overnight. On the next day, these biopsies were embedded in paraffin. All paraffin-embedded samples were sectioned at 3-µm thickness and then mounted on glass slides. For preparation of cryosections, tissues were snap-frozen in Tissue-Tek® O.C.T. (Thermo Fischer Scientific, Loughborough, UK) and then sectioned at 7 µm thickness.

2.2 Haematoxylin and eosin staining

Haematoxylin and eosin (H&E) staining was performed on paraformaldehyde-fixed paraffin-embedded tissues following a standard procedure. The sections were first deparaffinised in 100% xylene for 2 × 5 min, and then rehydrated in a series of 2 × 5 min incubations in 100% ethanol and 70% ethanol followed by incubation in water for 5 min. The samples were stained with haematoxylin (Sigma-Aldrich, UK) for 10 min and then rinsed with hot tap water. The slides were differentiated by a dip in 1% hydrochloric acid in 70% ethanol and then rinsed with tap water. The samples were stained in eosin (Sigma-Aldrich, UK) for 2 min and dehydrated in two changes of 70% ethanol, 100% ethanol, 100% xylene for 5 min each time. The air-dried slides were mounted with DPX solution (Leica Biosystems, UK).

2.3 Immunofluorescence staining of skin tissues

2.3.1 Experimental procedure

7-µm skin cryosections from KID-1 and two donors were first air-dried and then washed for 3 × 5 min in phosphate-buffered saline (PBS). The tissues were incubated in a mixture of blocking and permeabilising solution containing 3% foetal bovine serum (FBS) and 0.3% Triton X-100 in PBS for 20 min at room temperature followed

by three washes in PBS for 5 min each time. The samples were probed with a primary antibody at 4°C overnight. The catalogue number of primary antibodies used for detection of Cx26, Cx30 and Cx43 are 13-8100, 700258 and C6219 **(see Appendix II)**. On the next day, the tissues were washed for 3 × 5 min in PBS prior to probing with an Alexa-Fluor 488 or 568-conjugated secondary antibody (Life Technologies, 1:500 dilution) for 1h at room temperature. For negative controls, primary antibody was replaced by PBS prior to probing with the same secondary antibody. For detection of Cx26 and Cx30 that are less abundantly expressed in the skin, a biotinylated secondary antibody (catalogue number: BA-1000 for Cx30 and BA-2000 for Cx26, Vector Laboratories, 1:100 dilution) was incubated with the sections for 1 h at room temperature, followed by incubation with an Alexa-Fluor 488- or 568-conjugated streptavidin (Life Technologies) at 1:500 dilution for 30 min at room temperature. Nuclei were counterstained with 5 ng/ml 4,6-diamino-2-phenylindole (DAPI, Vector Laboratories) for 1-2 min and then washed three to four times for at least 10 min each time in PBS. The samples were mounted using a mounting solution containing 10% Mowiol solution (Calbiochem, Nottingham, UK) and then imaged using a Leica DMLS upright fluorescence microscope or a Zeiss LSM 510 Meta laser confocal microscope (Zeiss, Oberkochen, Germany).

For Cx26/Cx30 double immunostaining, standard staining for Cx26 was first performed until the final PBS wash after the incubation with the streptavidin, followed by standard staining for Cx30. For Cx26/Cx43 double immunostaining, Cx26 staining was first carried out and Cx43 staining followed.

2.3.2 Quantification of staining intensity

Quantification of Cx26 expression in the epidermis of immunostained skin sections was carried out using ImageJ software v1.51n (NIH, Bethesda, MD, USA). Image data recorded under the same imaging setting (laser power, digital offset and gain) from three to seven adjacent, non-overlapping fields in each slide were analysed.

First, a region of interest was drawn manually to exclude both non-specific staining in the cornified layer of epidermis as well as the dermis, which was not the focus in the study **(Figure 2.1)**. Second, a threshold of staining intensity was carefully adjusted

dependent on the type of staining, until nearly all positive signals were covered while an acceptable level of noises was included. After thresholding, the binary signals were further filtered at a medium radius of 1 pixel. To account for lower signal/noise ratio for Cx26 due to weak staining, only signals larger than 0.3 μm^2 were analysed. Finally, the remaining signals, considered as true positive signals, were redirected to the original image and the mean fluorescence intensity was measured. All above steps were recorded as an ImageJ macro, which was applied to all images recorded from the same batch of experiment. The Cx26 expression levels in C32 and C38 control skins and KID-1 skin were compared using one-way ANOVA with Tukey's multiple comparison test. Differences were considered statistically significant at $p < 0.05$.

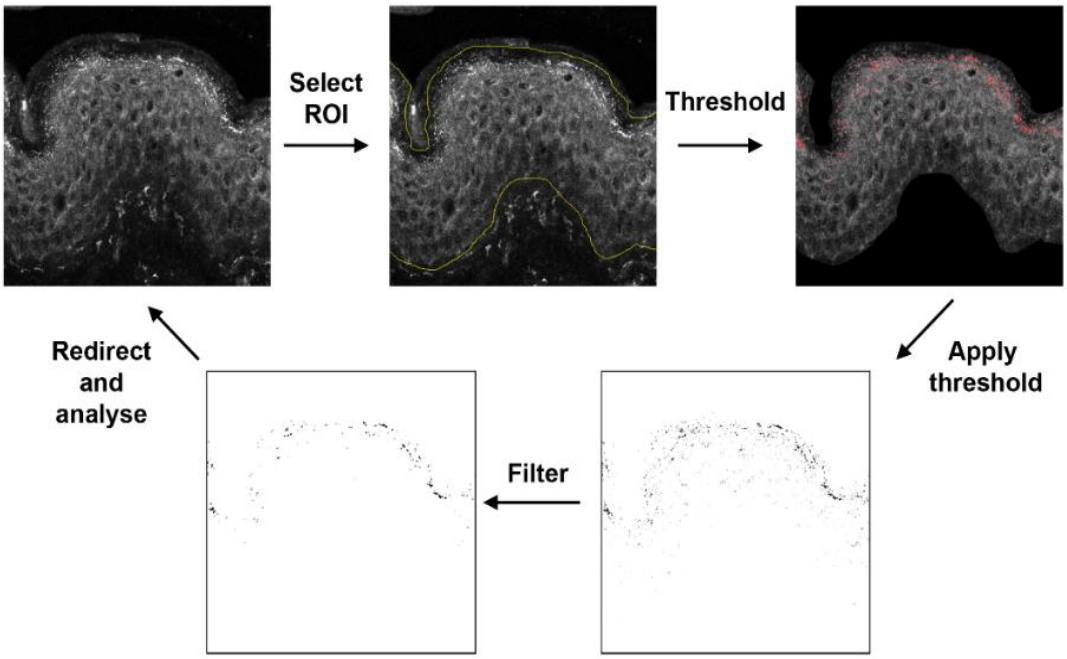

Figure 2.1. Example of quantification of connexin expression in the epidermis of immunostained skin

The image taken using a confocal microscope was processed by: 1) selecting region of interest (ROI), i.e. the epidermis with exclusion of cornified layer, which was found to have be stained non-specifically; 2) defining a threshold dependent on the background noises; 3) applying the appropriate threshold to transform the image into binary signals, facilitating further analysis; 4) filtering to exclude very small particles which are often noises; and 5) redirecting the signals to the original image for fluorescence intensity analysis.

2.4 Isolation of primary keratinocytes and fibroblasts from skin biopsies and establishment of immortalised keratinocyte cell lines

Skin punch biopsies taken from KID-1 patient or a healthy donor **(Section 2.1)** were rinsed in PBS. Excessive dermis was removed using a sterile scalpel blade. The skin tissues were treated overnight at 4°C with Dispase (50 U/mL, BD Biosciences, Plymouth, UK) that cleaved the adherent molecules at the dermo-epidermal junction, allowing for dissociation of the epidermis from the dermis.

On the next day, the epidermis was mechanically removed from the dermis using sterile forceps. The epidermis was fragmented and incubated with 0.25% trypsin in EDTA at 37°C for 40 min with agitation every 10 min. Trypsin digestion was neutralised by addition of the same volume of DMEM/10% FBS. The cell suspensions were vortexed vigorously and then filtered through a 100 µm cell strainer into a falcon tube. The filtered cell suspension was centrifuged at 850 × g for 10 min. The cell pellet was resuspended in the RM+ complete keratinocyte medium, which is DMEM/Ham's F12 medium (1:3) supplemented with 10% FBS, 0.4 µg/ml hydrocortisone, 10 ng/ml epidermal growth factor, 5 µg/ml insulin, 5 µg/ml transferrin, 100 pM choleratoxin, 20 pM liothyronine, 100 IU/ml penicillin and 100 µg/ml streptomycin. The resuspended cells were cultured in a T25 flask at 37°C in humidified 10% CO_2, with addition of lethally irradiated 3T3 cells (1×10^6 cells per 25 cm^3 growth area). Cultured primary keratinocytes were immortalised using a human papillomavirus E6/E7 method. Following enrichment for positive virally-transduced primary keratinocytes, these cells were co-cultured for an extended period with 3T3 cells in the above density. Successfully immortalised cells were subject to genotyping by Sanger sequencing using GJB2-endo-full primers **(Appendix I)** and those with correct sequences were either cryopreserved or used for further experiments. Immortalised keratinocytes derived from KID-1 or the heathy donor are designated as KID-KCs and control-KCs, respectively. These immortalised cells were cultured in the above RM+ medium without addition of 3T3 cells.

The detached dermis was also fragmented and treated with 0.45 U/ml Collagenase NB6 (SERVA Electrophoresis GmbH) at 37°C for 2 h. The suspension containing fibroblasts were centrifuged at 850 × g for 10 min. The pellet was resuspended in

DMEM supplemented with 10% FBS, 100 IU/ml penicillin and 100 µg/ml streptomycin, plated into a T25 flask, and cultured at 37°C in humidified 10% CO_2.

2.5 RNA extraction and reverse transcription-PCR

Total RNA was extracted from cultured keratinocytes and fibroblasts using TRIzol® reagent (Invitrogen, Paisley, UK), and then immediately reverse-transcribed into single-stranded complementary DNA (cDNA) using the GeneAmp® RNA PCR Core Kit (Applied Biosystems). Each reaction contained a mixture of 1 µg of RNA template, 2 µl of 10× PCR buffer II, 4 µl of 25 mM $MgCl_2$, 2 µl of dNTP Mix (each at 10 mM), 1 µl of 50 µM random hexamer, 1 µl of MuLV reverse transcriptase (50 U/µl), 1 µl RNase inhibitor (20 U/µl), making up to 20 µl final volume with DNase RNase-free water. The reaction was performed at 42°C for 45 min, followed by 99°C for 5 min to inactivate the enzyme. The cDNA product was stored at -20°C until downstream experiments.

For semi-quantitative reverse transcription PCR (RT-PCR), cDNA templates were PCR-amplified using the primers given in **Appendix I**. The glyceraldehyde-3-phosphate dehydrogenase (GAPDH) primers were used as loading control. The reaction conditions were: initial denaturation at 94°C for 10 min, followed by 30 thermocycles of 94°C for 30s, 60°C for 30s and 72°C for 30s, and then a final extension at 72°C for 10 min. The amplicons were analysed by 1.5% agarose gel electrophoresis.

For real-time quantitative RT-PCR (qPCR), cDNA templates were amplified using the iQ ™ SYBR® Green Supermix (Bio-Rad). The primers used are listed in **Appendix I**. The reactions were performed in triplicate in a Rotor-Gene 6000 thermocycler (Corbett Research, Cambridge, UK) with conditions as follows: initial denaturation at 94°C for 5 min, followed by 40 thermocycles of 95°C for 30s, 60°C for 30s and 72°C for 30s, and then a final extension at 72°C for 10 min. A melt curve analysis from 72°C to 95°C was performed at the end of reaction to ensure only a single product was obtained. The data were normalised using the GAPDH gene and relative expression of *GJB2* was calculated using the $2^{-\Delta\Delta Ct}$ method.

2.6 Immunoprecipitation and immunoblotting

The method of immunoprecipitation was modified from a previous study (Di et al., 2005). Cells were cultured in a 100-mm dish to confluence. On the day of experiment, cells were washed twice with ice-cold PBS and then lysed in 0.5 ml ice-cold immunoprecipitation lysis buffer containing 10 mM Tris-HCl (pH 7.4), 150 mM NaCl, 1% Triton X-100, 0.5% NP-40, 1 mM EDTA, 1 mM EGTA, 1 mM PMSF supplemented with cOmplete ™ protease inhibitor cocktail (Roche). Samples were incubated on ice for 15 min with occasional vortexing, followed by centrifugation at 12,000 × g at 4°C for 10 min. The supernatant containing soluble proteins was measured for protein concentration by Bradford assay (Bio-Rad, Hertfordshire, UK). 1−1.5 mg protein was transferred into a fresh Eppendorf tube. The information of antibodies used for precipitation is shown in **Appendix II**. To precipitate Cx26, either the in-house (IP^1 condition; 4.5 µl per sample) or the commercial (IP^2 condition; catalogue number 71-0500; 3 µl per sample) rabbit anti-Cx26 polyclonal antibody was added to the lysate, followed by incubation at 4°C for 2.5 h using an end-over-end tube rotator. After incubation, 60 µl protein G-Sepharose beads (50% slurry, Amersham) was added to the sample and mixed overnight at 4°C. On the next day, the beads, associated with antigen-antibody complex, were collected by centrifugation at 12,000 × g for 1 min. Pellets were washed three times with 1 ml immunoprecipitation lysis buffer without detergents. After washes, excessive buffer was removed carefully. The final pellet was resuspended with 40 µl of a sample buffer containing 125 mM Tris-HCl (pH 6.8), 5% β-mercaptoethanol, 4% sodium dodecyl sulfate (SDS), 10% glycerol and 0.0004% bromophenol blue, and boiled at 95°C for 10 min with occasional vortexing to dissociate the antigen-antibody complex from the beads. The sample was centrifuged briefly at 12,000 × g for 1 min and the supernatant containing the antigen-antibody complex was either analysed immediately with immunoblotting or transferred to a fresh tube and stored at -80°C for later analysis. For preparation of non-immunoprecipitated samples from cells or tissues (e.g. mouse liver), the lysis buffer containing 50 mM Tris-HCl (pH 8.0), 150 mM NaCl, 5 mM EDTA and 1 mM PMSF supplemented with the protease inhibitor cocktail was used. 10−80 µg of protein samples were mixed with the SDS-containing sample buffer, boiled at 95°C for 10 min, and then analysed by immunoblotting.

For immunoblotting, protein samples of equal amount were separated by SDS-polyacrylamide gel electrophoresis (SDS-PAGE) using a 12% NuPAGE ™ Bis-Tris Mini Gels (Novex, Thermo Fisher Scientific). The gel was run at 150V in the NuPAGE ™ MES SDS running buffer (catalogue number NP0002, Thermo Fisher Scientific) until the samples had run to the bottom of the gel. Following SDS-PAGE, protein samples were transferred to a PVDF membrane at 100V for 1 h in a pre-chilled transfer buffer containing 25 mM Tris, 192 mM glysine, 20% methanol. Blots were blocked with 5% skimmed milk (Sigma) and then probed with primary antibodies listed in **Appendix II**. For detection of endogenous Cx26 in keratinocytes, the mouse anti-Cx26 antibody from Life Technologies (IB^1 condition; catalogue number 13-8100) or the one from Merck (IB^2 condition; catalogue number MABT198) was used. For detection of exogenous fusion Cx26-GFP protein in transduced HeLa cells, the rabbit anti-Cx26 antibody from Life Technologies (catalogue number 71-0500) was used. All above antibodies were diluted 1:1000 in 5% skimmed milk and probing was performed overnight at 4°C. On the next day, blots were washed three times on a shaker using a wash buffer containing 0.05% Tween-20 in PBS. Blots were then incubated at room temperature for 1 h with either an anti-mouse (GE Healthcare, Buckinghamshire, UK; 1:4000 dilution) or an anti-rabbit (Sigma, Gillingham, UK; 1:7000 dilution, in 3% skimmed milk) horseradish peroxidase-conjugated secondary antibodies, followed by three washes. After a prolonged final wash for around 15 min, signals were detected using the ECL ™ Prime Western Blotting Detection system (Amersham, UK) according to the manufacturer's manual. Densitometric analysis was performed on scanned images of blots.

2.7 Immunofluorescence staining for cultured cells

Keratinocytes were plated on 11-mm glass coverslips and cultured to reach confluence. The cells were fixed in 4% paraformaldehyde (v/v) for 20 min at room temperature, and then incubated in the mixture of blocking and permeabilising solutions containing 3% FBS and 0.3% Triton X-100 in PBS at room temperature for 20 min followed by three washes in PBS for 5 min each time. The cells were then incubated with a primary antibody at 4°C overnight. The information of primary antibodies used is shown in **Appendix II**. For detection of endogenous Cx26 in cultured immortalised keratinocytes (KID- and control-KCs), the mouse anti-Cx26 antibody from Life

Technologies (catalogue number 13-8100) was used. For detection of exogenous Cx26-GFP fusion protein in lentivirally-transduced HeLa cells, the in-house rabbit anti-Cx26 antibody (Di et al., 2001a) was used. In some experiments, E-cadherin was also stained to indicate the plasma membrane using the rabbit antibody from Abcam (catalogue number ab40772). On the next day, cells were washed three times in PBS for 5 min each time and then incubated with a secondary antibody conjugated with Alexa-Fluor 488 or 568 (Life Technologies, 1:500 dilution) for 1h at room temperature. DAPI was used to counterstain the nuclei at a concentration of 5 ng/ml. The samples were mounted using 10% Mowiol and then imaged using a Leica DMLS upright fluorescence microscope or a Zeiss LSM 510 Meta laser confocal microscope (Zeiss, Oberkochen, Germany).

2.8 CRISPR/Cas9 genome editing

2.8.1 sgRNA design and cloning

CRISPR/Cas9 genome editing was performed according to a protocol published elsewhere (Ran et al., 2013). Three single guide RNAs (sgRNAs), g1, g2, and g4 were designed using the CRISPR Design Tool (http://crispr.mit.edu). Each sgRNA is complementary to a certain GJB2 locus near the nucleotide position 148 of the coding region. Designed sgRNAs were synthesised by Invitrogen. The sgRNA sequences are:

g1_sense: 5’-ACCGCATCTCCCACATCCGGCTAT-3';
g1_antisense: 5'-AACATAGCCGGATGTGGGAGATGC-3';

g2_sense: 5’-ACCGTCGCATTATGATCCTCGTTG-3';
g2_antisense: 5'-AACCAACGAGGATCATAATGCGAC-3';

g4_sense: 5'-ACCGCCATCTCCCACATCCGGCTA-3’;
g4_antisense: 5'-AACTAGCCGGATGTGGGAGATGGC-3'.

Each pair of sense and antisense DNA oligos was annealed to form a double-stranded structure and then cloned into the p.LeGO-167-Cas9-iC-mCherry lentiviral vector (a gift from Dr. Ulrike Mock) using the SapI site. The ACCG overhang, underlined in each sense sgRNA sequence, functions to permit directional SapI cloning. On completion of plasmid construction, the recombinant plasmids were sequenced using the universal U6 primer.

2.8.2 SURVEYOR® assay and T-A cloning for assessing *GJB2*-editing efficiency of designed sgRNAs

HEK-293T cells were used for evaluation of gene-editing efficiency by the designed sgRNA. HEK-293T cells were cultured in the same condition as dermal fibroblasts **(Section 2.4)** in the DMEM/10% FBS medium. These cells were transfected with each of the sgRNA-Cas9 constructs using FuGene® 6 (Promega) at a FuGene®-to-plasmid ratio of 2:1. Genomic DNA was isolated from transfected cells 72h post-transfection. PCR amplicons of sgRNA target sites were generated using the GJB2-SURVEYOR-F/R primers **(Appendix I)**, and then analysed for the presence of sgRNA-Cas9-induced mutations on the target *GJB2* loci using the SURVEYOR® Mutation Detection Kit (Transgenomic, Omaha, NE, USA), according to the manufacturer's instructions. In brief, the amplicon was denatured at 95°C for 10 min and then annealed to form DNA heteroduplex by cooling from 95°C to 85°C at -2°C/s and then from 85% to 25°C at -0.3°C/s, followed by digestion with the SURVEYOR® nuclease at 42°C for 1h. The digested products were separated by 1.5% agarose gel electrophoresis. The size of the intact, uncleaved amplicon is 539 bp and cleaved products are estimated to be about (280, 260 bp) for g1- and g4-Cas9 and about (380, 160 bp) for g2-Cas9.

The presence of sgRNA-Cas9-induced mutations was also analysed by T-A cloning followed by sequencing. Briefly, the above PCR amplicons were subcloned into the pGEM®-T vector (Promega, Hampshire, UK) overnight at 4°C. On the next day, JM109 competent cells were transformed with the ligated products, and then selected by white-blue screening using X-Gal (50 mg/ml, Sigma-Aldrich, Poole, UK) and isopropyl β-D-1-thiogalactopyranoside (IPTG, 100 mM). Plasmids were extracted from positive colonies and then double-digested with NdeI and SacII (NEB) to confirm the insert. Plasmids containing the insert were verified by Sanger sequencing using the SP6 primer **(Appendix I)**. Sequence data were analysed and aligned using Sequencher software v5.2 (Gene Codes Corporation, USA).

2.8.3 Generation of N/TERT cells with mono-allelic *GJB2* deletion

A normal diploid keratinocyte cell line, N/TERT (Dickson et al., 2000), was used for generating the *GJB2*$^{+/-}$ cell lines. N/TERT cells were cultured in the RM+ complete keratinocyte medium **(Section 2.4)**. These cells were transfected with the g4-Cas9

construct which displayed higher cleaving efficiency in 293T cells. Transfection was performed using the FuGene® 6 reagent at a FuGene®-to-plasmid ratio of 2.5:1. To enrich positive cells, fluorescence-activated cell sorting (FACS) for mCherry-positive cells was performed 48h post-transfection using a FACS Aria II Cell Sorter (BD Biosciences, UK). Sorted single cells were cultured in 96-well plates and were checked regularly for clonal appearance after two weeks post-sorting. Upon confluence, cells were harvested for genomic DNA extraction using a ZR-96 Quick-gDNA ™ kit (Zymo Research), followed by PCR and Sanger sequencing using the GJB2-CRISPR-seq-F/R primers **(Appendix I)**. Clones with heterozygous mutations were subject to T-A cloning followed by sequencing **(Section 2.8.2)** to identify the desired clones with a mono-allelic *GJB2* deletion.

Immunofluorescence staining for Cx26 was carried out in N/TERT clones with desired *GJB2* mutations. The experimental procedure followed the methods described in **Section 2.7**. Cells were counterstained with rhodamine-conjugated phalloidin (Thermo Fisher Scientific) at room temperature for 40 min to visualise actin filaments. The morphology of the desired clones was also examined and imaged using an inverted microscope (Olympus IX71).

2.9 Scrape-loading dye transfer assay for GJIC assessment

2.9.1 Experimental procedure

This assay was modified from a previous study (Yum et al., 2007). Two different plasma membrane-impermeant but gap junction-permeant tracers were used in this study, including Cascade Blue (fluorescent, molecular weight 548 Da, charge -3, catalogue number C3239, Invitrogen) and neurobiotin (non-fluorescent, molecular weight 323 Da, charge +1, catalogue number SP-1120, Vector Laboratories). Stock solutions were prepared at concentrations of 80 mg/ml and 20 mg/ml, respectively. Dextran-rhodamine B (fluorescent, molecular weight 10 kDa, catalogue number D1824, Invitrogen) was used as a negative control.

Keratinocytes (N/TERT cells, control-KCs or KID-KCs) were plated at a high density onto a 6-well plate or a 60-mm dish, allowing formation of cell-cell contact and the

resulting gap junction channels. Cells were gently washed twice with Ca^{2+}, Mg^{2+}-containing Hank's balanced salt solution (HBSS, catalogue number 14025092). The medium was then switched to divalent-free HBSS (catalogue number 14175095) containing Cascade Blue or neurobiotin at 1:300 dilution or 1:200 dilution, respectively. The latter solution with addition of 100 μM carbenoxolone (CBX, gap junction blocker, Sigma, UK) was used as negative control. Multiple parallel scrape lines were made with a sharp scalpel blade to promote uptake of tracers by the wounded cells, followed by incubation at 37°C for 20 min for Cascade Blue or 10 min for neurobiotin to allow dye transfer. Cells were washed twice with HBSS containing divalent ions and then fixed with 4% (v/v) paraformaldehyde at 4°C for 20 min. For cells scrape-loaded with the non-fluorescent tracer neurobiotin, samples were permeabilised with 0.3% Triton X-100 for 10 min and then stained with Alexa Flour 568-streptavidin conjugate (Invitrogen, 1:400 dilution) at room temperature for 30 min. After three washes with PBS, samples were imaged with an Olympus IX71inverted microscope for both fluorescent and phase contrast channels. The same imaging condition was applied to all samples for each channel and at least six scrape-wounded images and three background (non-scrape-wounded) images were taken from each group.

2.9.2 Quantification of dye transfer

The above images were analysed using the ImageJ software v1.51n. Dye transfer, as a measure of GJIC activity, was quantified by measuring the total area between the scrape line and the point at which the fluorescence level reduced to 1.5 × the background fluorescence level. As shown in **Figure 2.2**, images were processed by filtering out small-sized non-specific signals and applying a threshold, i.e. 1.5 × the average background level **(Figure 2.2b-c)**. Following these steps, the total area of dye transfer was recorded and calculated using Microsoft Excel. Comparison was made by one-way ANOVA (N/TERT clones) or Student's *t*-test (control- and KID-KCs) using GraphPad Prism 6 software.

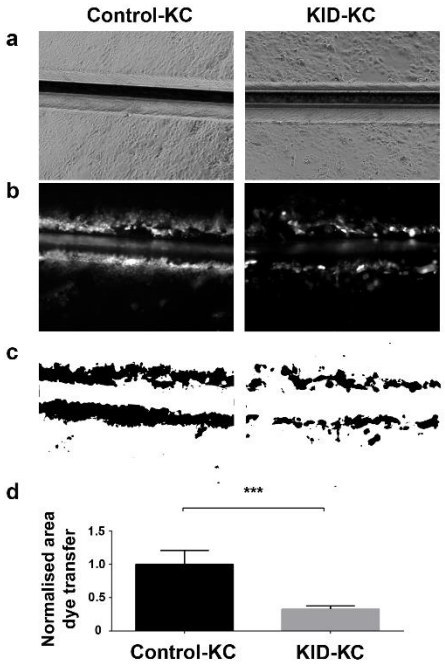

Figure 2.2 Image analysis for scrape-loading dye transfer assay
(a) Example phase contrast scrape loading images of Control-KCs (left) and KID-KCs (right). *The images show a linear scrape made on the monolayer cultures using a scalpel blade. (b) Example raw digital image data of Cascade Blue dye transfer from the linear scrape wound. (c) Example image processing. Small-sized, non-specific signals were filtered out and a threshold at 1.5× respective background fluorescence intensity level was applied. (d) Example analysis of total area of dye transfer following image processing. Comparison was made between total dye transfer areas in these cell lines using Student's t-test.*

2.10 ATP release assay for assessing hemichannel activity

Hemichannel-mediated ATP release, representing hemichannel activity, was measured using an ATP Bioluminescent Assay Kit (catalogue number FL-AA, Sigma-Aldrich, Gillingham, UK), which is based on measurement of photons (bioluminescence) produced during the reaction between luciferase/luciferin and ATP. A mixture of luciferase and luciferin (i.e. 'ATP Assay Mix', referred to as the assay mix thereafter) and a ATP standard were provided in the kit. Prior to ATP measurement from cultured cells, this method was optimised as follows.

Firstly, five different dilutions (1:10, 1:100, 1:200, 1:300 and 1:400) of the assay mix were reacted with either 0 or 10 μM ATP standard, followed by luminescence measurement using a FLUOstar Optima luminometer (BMG Labtech, Aylesbury, UK). This step allowed to determine the optimal dilution of the assay mix for subsequent

experiments. Secondly, a range of low concentrations of ATP standard (2.5−30 nM, diluted in PBS or DMEM) were each reacted with the assay mix at the optimised dilution from the previous step, followed by the same luminescence measurement. This allowed to determine the analytical sensitivity of the assay, which is defined as the minimum concentration (minus two standard deviations) that does not overlap with the background level (plus two standard deviations) (Li and Cassone, 2015). Thirdly, using the above parameters, a suitable range of ATP concentrations were investigated by reacting serially-diluted ATP standards (0−10 μM) with the assay mix at the optimised dilution. The ATP concentrations that had yielded luminescence with a linear correlation were used to construct a standard curve in further experiments.

The present ATP release assay was modified from previous studies (Donnelly et al., 2012; Easton et al., 2012). Connexin-null HeLa cells and connexin-rich N/TERT cells were used to set up the assay. 1.2×10^5 HeLa cells and 2.4×10^5 N/TERT cells were plated in duplicate onto a 24-well plate and the assay was performed on the next day. Cells were gently washed three times with PBS and then incubated in serum-free DMEM at room temperature for 30 min. For pharmacological blockade, cells were incubated in the above DMEM with additional 100 μM CBX. After incubation, cells were acutely challenged with PBS containing zero Ca^{2+} for 2.5 min, a common approach to open connexin hemichannels (de Wolf et al., 2016; Donnelly et al., 2012; Verselis and Srinivas, 2008), allowing release of ATP to the medium. 50 μl of each medium was harvested and snap-frozen on dry ice. For baseline measurement, PBS was replaced by DMEM containing 1.8 mM Ca^{2+}. To determine ATP concentration in these samples, 50 μl of samples was reacted with 50 μl of the assay mix at the optimised dilution and the reaction mixture was measured immediately for luminescence at room temperature. Three independent experiments were performed, each with two technical replicates. Data were normalised to the baseline level and hemichannel activity was expressed as fold change in ATP concentration between the baseline and zero-Ca^{2+}-challenged samples.

2.11 Determination of candidate cell lines for siRNA screening

Cell lines suitable for siRNA screening were selected from six candidate cell lines **(Table 2.1)**. Endogenous expression of *GJB2* gene in six candidate cell lines was

examined by RT-PCR using the GJB2-endogenous-F/R primers **(Appendix II, Section 2.5)**.

Table 2.1 Candidate cell lines for siRNA screening

Cell ID	Cell type	Immortalisation	Culture medium
HeLa	Human cervical cancer	Spontaneously transformed	DMEM/ 10% FBS
HT1080	Human fibroblastoma	Spontaneously transformed	DMEM/ 10% FBS
P6KC	Human keratinocyte	Human papillomavirus E6/E7	RM+/ 10% FBS
P8KC	Human keratinocyte	Human papillomavirus E6/E7	RM+/ 10% FBS
HaCaT	Human keratinocyte	Spontaneously transformed	RM+/ 10% FBS
N/TERT	Human keratinocyte	Human telomerase reverse transcriptase	RM+/ 10% FBS

2.12 Generation of HeLa and N/TERT cells stably expressing *GJB2-GFP*

2.12.1 Lentiviral vector construction and packaging

Lentiviral vectors were designed, constructed and packaged by Dr. Wei-Li Di. This study employed an HIV-1 derived, self-inactivating lentiviral vector pLNT-SFFV-MCS **(Figure 2.3)**. The SFFV promoter was removed using EcoRI and XhoI sites, and the CMV promoter and the *GJB2-GFP* transgene were cloned into the vector using AseI and NotI sites. In the transgene, the *GFP* cDNA was fused to the 3' terminus of wildtype *GJB2* cDNA or *GJB2* cDNA containing c.148G>A (p.D50N) mutation. On completion of vector construction, the wildtype and mutant transgene sequences were verified by Sanger sequencing.

Lentiviruses were packaged by co-transfecting HEK-293T cells with wildtype or mutant lentiviral plasmids, together with an envelope plasmid coding for an envelope protein pseudotyped with a vesicular stomatitis virus (VSV-G) envelope, and a packaging plasmid pCMV8.74 coding for lentiviral gag, pol and accessory proteins, tat and rev **(Figure 2.3)**. Infectious lentiviruses were harvested 72 hours post-transfection, filtered with a 0.45-μm pore cellulose acetate filter, and then ultra-

centrifuged at 50,000 × g for 2h. Concentrated viral pellets were resuspended in DMEM medium for 30 min on ice. The lentivirus stocks were kept at -80°C until use. The packaged lentiviruses were harvested and titred by flow cytometry for GFP expression. The viral titres were 8.8×10^7 IU/ml for wildtype viruses and 4.9×10^6 IU/ml for mutant viruses.

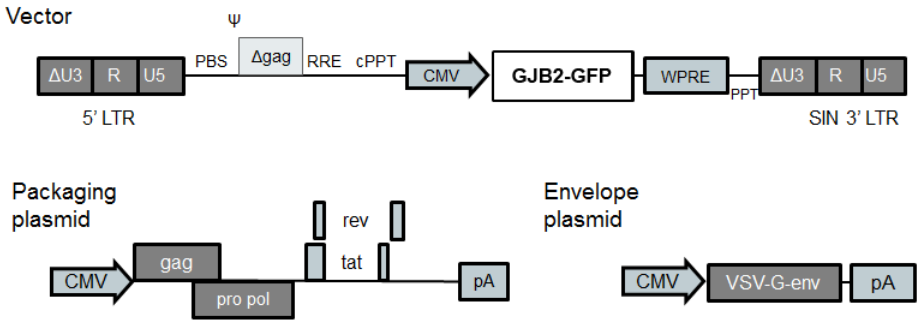

Figure 2.3 Schematic of the LNT-CMV-GJB2-GFP lentiviral vectors

Top panel shows a self-inactivating, HIV-1-based vector with the transgene cloned in, which encodes the wildtype or c.148G>A mutant GJB2 fused to GFP reporter at 3' terminus driven by the cytomegalovirus (CMV) promoter. Bottom panel shows two accessory plasmids, including the packaging plasmid (left) encoding lentiviral gag, pol and accessory proteins and the envelope plasmid (right) pseudotyped with envelope proteins from vesicular stomatitis virus (VSV). LTR, long terminal repeat. PBS, tRNA primer binding site. RRE, rev response elements. CMV, cytomegalovirus promotor. VSV-G env, envelope pseudotyped with the G glycoprotein of vesicular stomatitis virus. cPPT, central polypurine tract. WPRE, woodchuck hepatitis virus post-transcriptional regulatory element.

2.12.2 Generation of HeLa and N/TERT cells expressing *GJB2-GFP*

Two selected cell lines, HeLa and N/TERT, were transduced with either wildtype or mutant lentiviruses. 72 h later, the transduction efficiency was determined by flow cytometry analysis (BD FACSCalibur ™) for the percentage of GFP^+ populations. These GFP^+ populations were enriched from total lentivirally transduced cells by fluorescence-activated cell sorting (FACS) using a Beckman Coulter MoFlo XDP cell sorter. From each sample, 10^6–10^7 GFP^+ cells were sorted and immediately cultured in the standard condition. To verify cell enrichment, semi-quantitative RT-PCR was performed using transgene-specific primers, GJB2-GFP-RT1-F/R **(Appendix I, Section 2.5)**, and GAPDH primers were used as internal control. Transgene expression at protein level was verified by immunostaining for Cx26 using the in-house antibody

(Appendix II, Section 2.7), and images were recorded using a Leica DMLS upright fluorescence microscope.

For enrichment of HeLa clones expressing the full-length *GJB2* transgene, single-cell cloning was carried out from bulk populations of lentivirally-transduced, FACS-enriched GFP^+ cells. Single cells were cultured and checked regularly for clonal expansion. Expanded clones were subject to RT-PCR for full-length *GJB2* expression using the GJB2-endo-full-F/R primers **(Appendix I, Section 2.5)** and fluorescence microscopy for Cx26-GFP expression.

2.13 Design of allele-specific siRNAs

Nineteen candidate siRNAs with a targeting sequence complementary to c.148G>A in *GJB2* were designed using a sequence-walk approach (Hickerson et al., 2008) and synthesised by Sigma (Dorset, UK). The reference sequence for *GJB2* (GenBank accession number NM_004004), mutated *GJB2* sequence and the designed siRNA sequences were aligned in **Section 3.3.2.1 (Figure 3.22)**. An siRNA against GFP (AM4626, Applied Biosystems) was used as a positive control. An irrelevant control siRNA against *hHAS2* (designated "control siRNA" hereafter) was synthesised from Sigma. The sequence of the control siRNA is:

Sense 5'-AUAUCGUCAUGGUCUUCAU[dT][dT]-3';
Antisense 5'-AUGAAGACCAUGACGAUAU[dT][dT]-3'.

2.14 Transfection of siRNA and evaluation of gene silencing

On the day before transfection, cells were plated at 1×10^4, 1×10^5, 5×10^5 per well onto 96-, 24- or 6-well plates, respectively, for N/TERT cells, KID- and control-KCs, or 0.7×10^4, 0.7×10^5, 3.5×10^5 per well, respectively, for HeLa cells. These seeding numbers allowed cells to reach a density between 50% and 70% on the next day, suitable for transfection using Lipofectamine® RNAiMAX and Lipofectamine® 2000 reagents (Thermo Fisher Scientific). Growth medium was first removed from the well. Unless otherwise stated, for 96-, 24- and 6-well plates, 5, 10, 40 pmol of siRNA was mixed gently with 0.25, 0.5, 2 µl of either of the transfection reagents in total volumes of 100 µl, 200 µl and 800 µl (in OptiMEM®, Thermo Fisher Scientific), followed by

incubation at room temperature for 20 min. The above transfection complexes, each containing 50 nM siRNA, were then added to the cells. The cells were incubated at 37°C for 6 h, and the medium was then replaced with growth medium, followed by incubation at 37°C until analysis of gene silencing 24 h or 48 h post-transfection.

siRNA-mediated silencing of exogenous *GJB2-GFP* and endogenous *GJB2* at mRNA level was assessed by qPCR using the GJB2-GFP-qPCR primers (HeLa and N/TERT) and the GJB2-endo-full primers (control- and KID-KCs) **(Appendix I, Section 2.5)**, respectively. At protein level, silencing of exogenous transgene was assessed by immunoblotting using the rabbit anti-Cx26 antibody 71-0500 **(Appendix II, Section 2.6)**, and flow cytometry using FACSCalibur™ (BD Biosciences, Oxon, UK).

For flow cytometry analysis, briefly, a non-fixed cell suspension was prepared in PBS containing 2% FBS. 10,000 cells from each sample were acquired using the FL1 channel with a 530-nm emission filter. Data were analysed using the FlowJo software v10 (Tree Star Inc., Ashland, Oregon, USA) and the silencing efficiency was indicated by the decrease of mean GFP intensity (I) in siRNA-transfected cells. Data were normalised against the control level. The Cx26-GFP silencing efficiency was calculated as: $[1- (I_{\text{allele-specific siRNA}} / I_{\text{control siRNA}})] \times 100\%$.

2.15 Patch clamp technique for hemichannel assessment

Whole-cell patch clamp was carried out in KID- or control-KCs at room temperature. Cells were seeded at a low density onto 12-mm glass coverslips in a 35-mm culture dish to prevent cell-cell contact and the resulting formation of intercellular channels that may confound hemichannel analysis. On the next day, coverslips were transferred to an experimental chamber filled with a Tyrode's bath solution containing (in mM): NaCl 137.7, KCl 5.4, NaOH 2.3, $MgCl_2$ 1, glucose 10, and HEPES 5 (pH 7.4). Patch pipettes were pulled from glass capillaries to a resistance of 3-6 MΩ with a horizontal puller (P-87, Sutter Instruments, Novato, CA). The pipettes were filled with a pipette solution containing (in mM): K-aspartate 120, HEPES 5, ethylene glycol tetraacetic acid 10, and NaATP 3 (pH 7.2). Solitary KID-KCs and control-KCs were chosen for measurement of membrane capacitance (C_m), along with membrane currents (I_m) invoked while the membrane potential was stepped from -110 mV to +110 mV in 20

mV increments. Membrane currents recorded at the beginning of each pulse, i.e. instantaneous currents, were used for quantification. Voltage and current signals were recorded using an Axopatch-1D patch clamp amplifier coupled to a Digidata 1322A interface (Axon Instruments). Data were acquired and analysed using Clampex 9.2 and Clampfit 10.2 software (Axon instruments), respectively. To control for variability in size of the cells being recorded, membrane current density, calculated as I_m/C_m, was used as a direct measure of hemichannel activity. Comparison was made between current density at individual membrane voltages using two-tailed Student's *t*-test.

2.16 Neurobiotin uptake assay for hemichannel assessment

2.16.1 Experimental procedure

This assay was modified from a previous study (Mese et al., 2011). A positively-charged, non-fluorescent tracer, neurobiotin (catalogue number SP-1120, Vector Laboratories) was used. KID- or control-KCs were plated at a low density onto 22-mm coverslips in a 6-well plate to prevent formation of intercellular channels. On the next day, cells were gently washed twice with Ca^{2+}, Mg^{2+}-containing Hank's balanced salt solution (HBSS, catalogue number 14025092), and then incubated with divalent-free HBSS (catalogue number 14175095) containing neurobiotin at 1:200 dilution at 37°C for 10 min to allow uptake of neurobiotin through open hemichannels under the divalent-free condition. Following two washes with Ca^{2+}, Mg^{2+}-containing HBSS, cells were fixed with 4% (v/v) paraformaldehyde at 4°C for 20 min. The fixed samples were permeabilised with 0.3% Triton X-100 for 10 min and then stained with Alexa Fluor 568-streptavidin conjugate (Invitrogen, 1:400 dilution) at room temperature for 30 min to visualise neurobiotin. Samples were counterstained with DAPI to demonstrate the seeding density. Following three washes with PBS, samples were imaged using an inverted microscope (Olympus IX71). For each channel, the same exposure time was applied to all samples.

2.16.2 Data analysis for neurobiotin uptake assay

Five to ten neurobiotin uptake images taken from each group were analysed using ImageJ software v1.51n. The hemichannel activity was indicated by the level of neurobiotin uptake, which was determined by the fluorescence intensity within the cell.

As shown in **Figure 2.4**, images were processed by filtering out small-sized non-specific signals and applying a suitable threshold **(Figure 2.4b)**. Following these steps, the average fluorescent intensity within individual cells in each image was calculated with Microsoft Excel. Data were normalised to the level of fluorescent intensity in untreated control-KCs or control-KCs treated with control siRNA. Comparison was made by Student's *t*-test using GraphPad Prism 6 software.

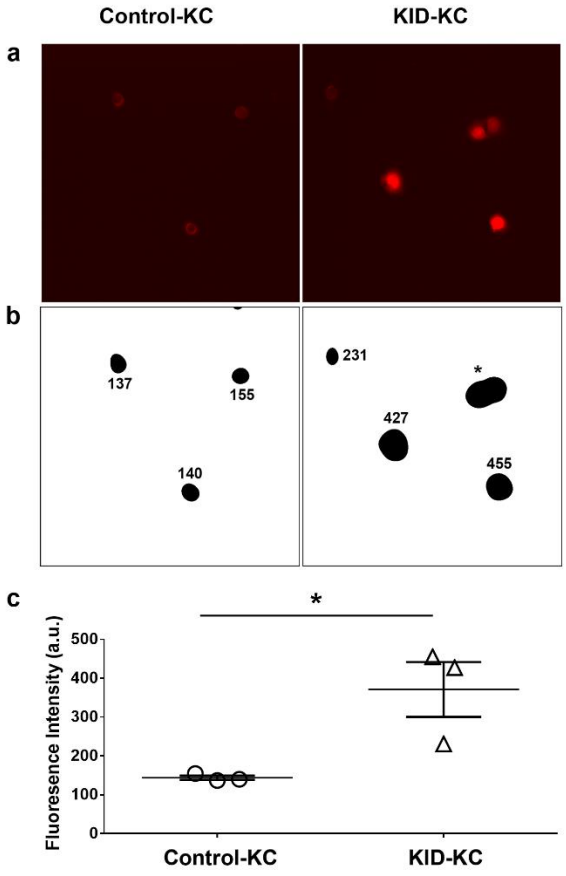

Figure 2.4 Image analysis for neurobiotin uptake assay
*Example images of neurobiotin uptake (red) by control-KCs (left) and KID-KCs (right) are shown (a). These images were processed by ImageJ. Small-sized signals were filtered out and an appropriate threshold was determined and applied to the images. Fluorescence intensity within single cells was measured, and the reads are shown as numbers in (b). Note that cell clumps or doublets (asterisk) were excluded. Comparison was made between average fluorescence intensity of the two images using Student's t-test (c). *p < 0.05.*

2.17 RNA-Seq based transcriptomic study

KID-KCs were transiently transfected, or not transfected, with S7 in triplicate at a confluency of around 70%. After 24 h, total RNA was extracted **(see Section 2.5)** and

the concentrations and purities of the samples were measured on a Nanodrop spectrophotometer. The concentrations were between 350−400 ng/µl and the A260/280 ratios between 2.0−2.5. For further quality control specific to RNA-Seq experiments, RNA concentration was calculated by Qubit™ (Thermo Fisher Scientific) and RNA integrity examined by the Bioanalyser (Agilent), which automatically generated a RNA integrity number (RIN) to indicate the integrity of analysed RNA.

500 ng of total RNA was used for RNA-Seq experiments. RNA samples were processed using a KAPA mRNA HyperPrep Kit (Roche) according to the manufacturer's instructions. In brief, mRNA was isolated from total RNA using Oligo dT beads to precipitate poly-adenylated transcripts. The purified mRNA was fragmented using chemical hydrolysis (heat and divalent metal cation) and primed with random hexamers. Strand-specific first strand cDNA was generated by reverse transcription in the presence of Actinomycin D, which allows for RNA-dependent DNA synthesis while preventing DNA-dependent DNA synthesis that affects the results. The second cDNA strand was synthesised using dUTP in place of dTTP, to mark the second strand. The resulting cDNA was then tailed with adenosine at the 3' end to prevent self-ligation and adapter dimerisation. Truncated adaptors, containing a T overhang, are ligated to the A-tailed cDNA. Successfully ligated cDNA was then enriched by limited cycle PCR (10 cycles). The high-fidelity polymerase used in the PCR was unable to extend through uracil, and therefore only the first strand was amplified for sequencing, making the library strand specific. The primers extended adaptors to full length and contained a sample-specific 6-bp index sequence which allow the libraries to be uniquely identified. The libraries were sequenced with a 43-bp paired-end run using a NextSeq 500 instrument (Illumina, San Diego, US).

Run data were first demultiplexed and converted to fastq files using the bcl2fastq Conversion Software (Illumina, v2.19). Fastq files were pre-processed to remove adapter contamination and poor-quality base calls using a 5' to 3' sliding window approach, by which reads were trimmed when the quality drops below Q20. Reads shorter than 20-bp after trimming were discarded (Trimmomatic v0.36). Next, trimmed reads were mapped to the hg38 reference genome using the gapped aligner, RNA-STAR (v2.5b). To reduce bias arising from the PCR performed during library preparation, mapped data were deduplicated using the Picard Tools (v2.7.1). The

remaining reads were counted per transcript by FeatureCounts software (v1.4.6p5). Normalisation, modelling and differential expression analysis were then carried out using SARTools (BioConductor, v1.3.2), an integrated QC and DESeq2 wrapper. All reference genomes and annotation were obtained from the Illumina iGenomes repository.

A list of genes was generated with fold change, *p*-values and adjusted *p*-values (*p*-adj, using Benjamini-Hochberg method) (Benjamini et al., 2001; Love et al., 2015). For each comparison, genes with statistically significant difference in expression level between treated and untreated KID-KC samples were determined at *p*-adj < 0.05 and $|\log_2$ fold change$| \geq 1$, and these differentially expressed genes are abbreviated as DEGs hereafter. These DEGs were further analysed by bioinformatics tools, including the Genome-wide Enrichment of Seed Sequence matches (GESS, www.flyrnai.org/gess) for analysing off-targets of S7 resulting from seed sequence matches, the Search Tool for the Retrieval of Interacting Genes/Proteins (STRING, string-db.org) for analysing protein-protein interaction, and Ingenuity® Pathway Analysis software v.01-12 (IPA®, Ingenuity Systems, Redwood City, CA) for analysing pathways/networks related to siRNA S7. Genes given by GESS analysis (i.e. genes with seed sequence match with siRNA S7) are listed in **Appendix III** and those genes were compared against the list of DEGs to identify off-targets of S7. For IPA®, the canonical pathways analysis was carried out, in which DEGs were analysed for enriched IPA® pathways against a background of all human genes by Fisher exact tests calculating the likelihood that this is due to random chance. This helped to identify signalling pathways significantly relevant to S7 treatment in KID-KCs.

2.18 Statistical analysis

All data were expressed as the mean ± standard error of the mean (SEM). Statistical tests used in this study were described in each section. The Student's *t*-test and the one-way analysis of variance (ANOVA) with post-hoc Tukey's multiple comparison test were performed using GraphPad Prism 6 software. Differences with a *p*-value less than 0.05 were considered statistically significant. **p* < 0.05; ***p* < 0.01; and ****p* < 0.001.

CHAPTER 3. RESULTS

3.1 The *GJB2* c.148G>A mutation causes abnormal Cx26 expression and hyperkeratotic skin architecture

The missense mutation c.148G>A in *GJB2* is the most common causative mutation linked to KID syndrome. A patient (KID-1) clinically diagnosed as KID syndrome was recruited in this study at Great Ormond Street Hospital. Genetic testing identified a heterozygous c.148G>A mutation in *GJB2*, which results in a substitution of aspartic acid with asparagine at the position 50 of Cx26 protein (p.D50N). The patient had bilateral sensorineural hearing loss, vascularising keratitis with photophobia, and generalised ichthyotic skin lesions with nail dystrophy. A biopsy was taken from interfollicular skin of KID-1 and the biopsy was paraffin-embedded and sectioned **(see Section 2.1)**. Biopsies taken from interfollicular skin of two unaffected healthy donors, C32 and C38, were used as controls **(see Section 2.1 for details of donors)**. The skin phenotype was examined by Haematoxylin and Eosin (H&E) staining **(see Section 2.2)**, and the expression and distribution of Cx26 were examined by immunostaining **(see Section 2.3)**.

3.1.1 Hyperkeratosis with prominent rete ridges in the skin of KID-1

The epidermis of KID-1 showed basket-weave hyperkeratosis, focal parakeratosis, mild acanthosis with prominent rete ridges compared to the normal skin **(Figure 3.1.1)**. There was also mild spongiosis in upper layers of keratinocytes and follicular plugging. In the papillary dermis, a mild perivascular lymphocytic infiltrate was observed. The reticular dermis and subcutis were unremarkable. These histological findings were consistent with two previous reports of patients harbouring the *GJB2* c.148G>A mutation (Liu et al., 2016a; Watanabe et al., 2007).

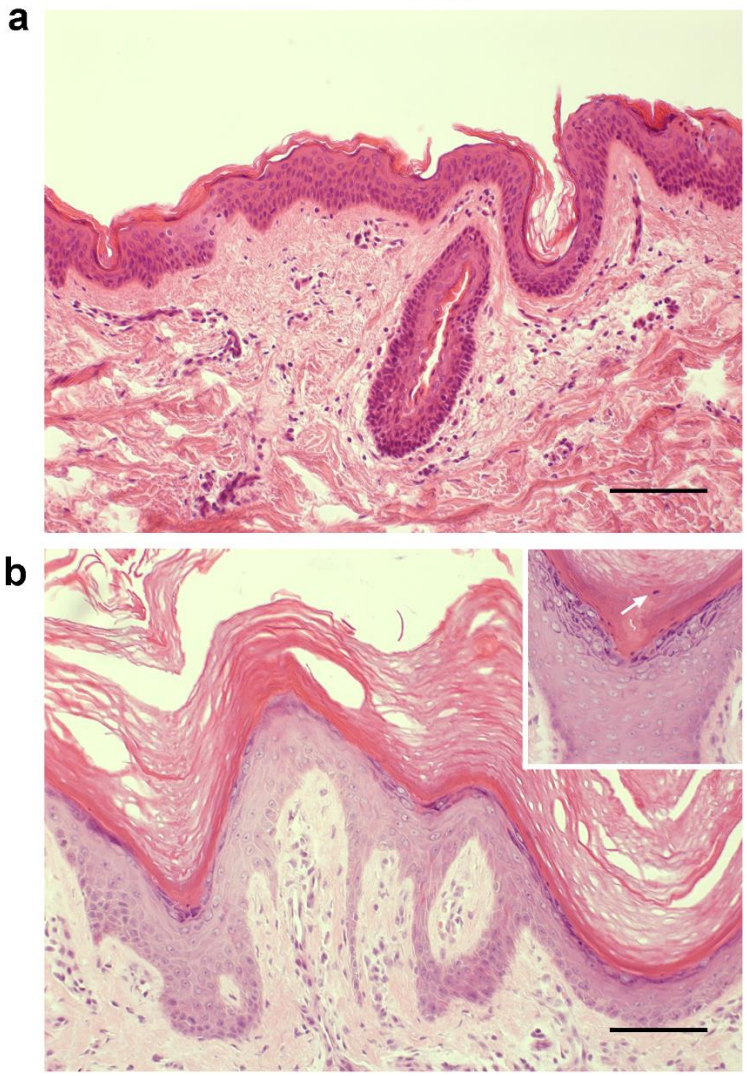

Figure 3.1.1 Morphology of the skin from KID-1

H&E staining was performed on the skin from a normal control donor (a) and patient KID-1 (b). The KID-1 skin showed basket-weave hyperkeratosis, focal parakeratosis (inset, arrow), mild spongiosis (inset) and mild acanthosis with elongated rete ridges in the epidermis, compared to the normal control skin. Bar = 100 µm.

3.1.2 Increased Cx26 expression in the epidermis of KID-1

The expression of Cx26 was examined by immunofluorescence staining using the anti-Cx26 mouse antibody 13-8100 **(see Appendix II)**. In the epidermis of control skin, weak Cx26 expression was found in the granular cell layers, with a punctate staining pattern **(Figure 3.1.2a-b, e-f)**. The positive staining in the cornified layer was non-specific, as it was also present in the negative control where staining was performed without primary antibody **(Figure 3.1.2d, h)**. In contrast, KID-1 epidermis displayed stronger Cx26 expression in the suprabasal layers with a punctate pattern **(Figure**

3.1.2c, g). The Cx26 expression slightly extended to both cornified layer and, occasionally, lower epidermal layers, indicative of ectopic distribution **(Figure 3.1.2g)**. In dermis, strong Cx26 expression was found in hair follicles and sweat glands and ducts in both KID and control skin **(Figure 3.1.2i-j)**, consistent with previous results (Di et al., 2005). Quantification of staining intensity **(see Section 2.3.2**) found a significant increase in Cx26 expression level in KID-1 epidermis, by 12% and 17%, compared to that in C32 and C38 epidermis, respectively (1 ± 0.07, n = 8 for C32; 0.97 ± 0.10, n = 3 for C38; 1.14 ± 0.02, n = 8 for KID-1; $p < 0.01$ when KID-1 vs C32; $p < 0.05$ when KID-1 vs C38, one-way ANOVA with Tukey's multiple comparison test, **Figure 3.1.2k**). Cx26 is known to be absent (Salomon 1994) or expressed at very low level (Martin et al., 2014) in normal skin, but up-regulated in hyperkeratotic skin lesions such as lichenified plaque of eczema (Di et al., 2001a), viral wart (Rouan et al., 2001) and psoriatic plaques (Labarthe et al., 1998; Lucke et al., 1999), along with KID syndrome (Arita et al., 2006; Choung et al., 2008; Nyquist et al., 2007; Richard et al., 2002). These findings were in line with the current results.

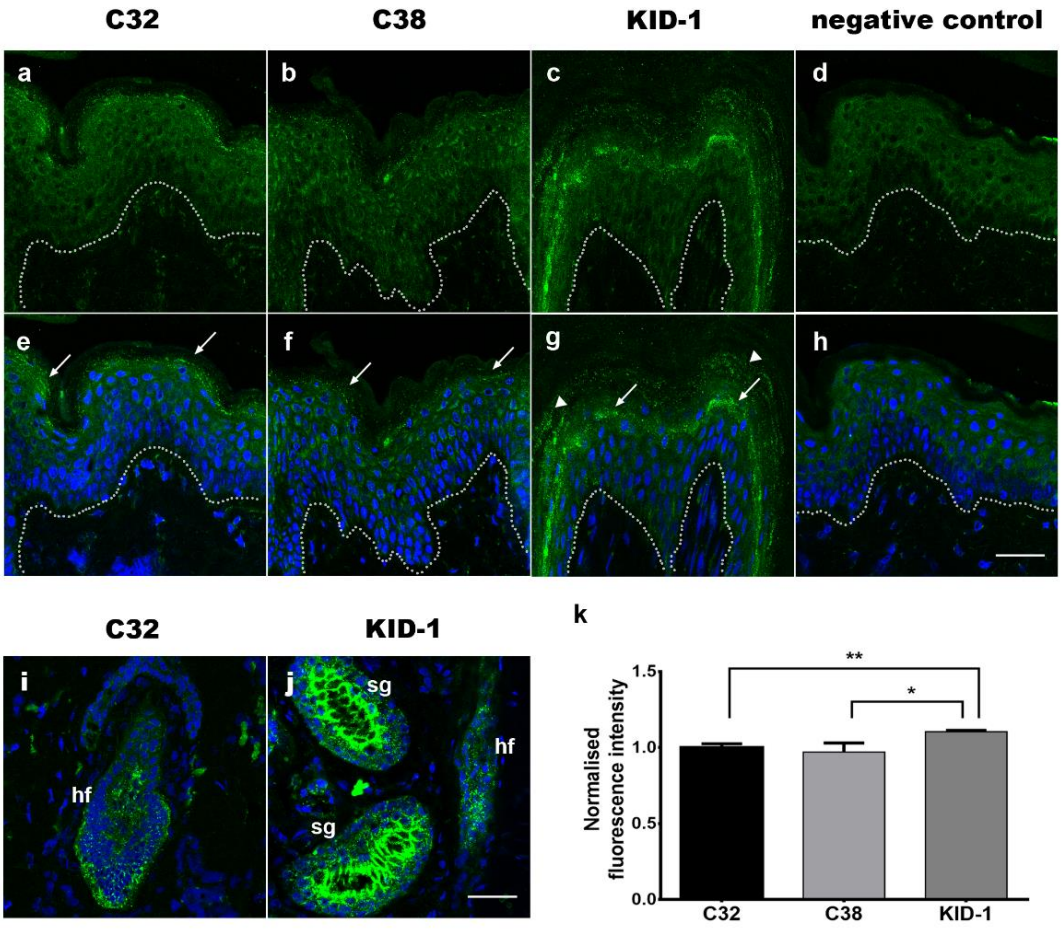

Figure 3.1.2 Increased Cx26 expression in KID-1 epidermis

*The expression of Cx26 (green) in normal skin C32 (a, e, i) and C38 (b, f) and KID-1 skin (c, g, j) was examined by immunostaining. Characteristic punctate staining with formation of gap junction plaques (e-g, arrows) was found in suprabasal epidermal layers, hair follicles (hf) and sweat glands (sg) of all skin tissues. Extended Cx26 expression was seen in the cornified layer of KID-1 skin (c, g arrowheads). Negative staining (d, h) without use of primary antibody indicates the background level. Note that positive signals were found in the cornified layer of both normal skin and negative control, indicating non-specific staining. Nuclei were counterstained with DAPI (blue). The dotted lines show the dermal-epidermal junction. (k) Quantification of Cx26 expression level in the epidermis. There was increased Cx26 expression in KID-1 skin, compared to that in C32 skin (**p < 0.01) and in C38 skin (*p < 0.05). n = 3−8. Bar = 40 μm.*

3.1.3 Cx26 co-localised with Cx30 in KID-1 epidermis

In vitro studies have shown interaction of Cx26 with Cx30 (Di et al., 2005; Yum et al., 2007) and, very recently, with Cx43 (Garcia et al., 2015; Shuja et al., 2016). To examine whether the distribution of Cx26 overlapped with Cx30 and Cx43, immunostaining for these connexins was performed alone or in conjunction with Cx26 in the patient skin **(see Section 2.3)**.

The expression of Cx30 in normal epidermis was found in a punctate pattern in the suprabasal layers, predominantly in the granular cell layers (**Figure 3.1.3a-b, e-f)**, with weak staining observed in the basal layer **(Figure 3.1.3b)**, which is consistent with previous observation (Richard et al., 2002). Similar expression pattern was found in KID-1 epidermis **(Figure 3.1.3c, g)**. Double-immunostaining for Cx30 and Cx26 showed that both connexins were compartmentalised in the granular layers, co-localising extensively and forming gap junction plaques at multiple foci in both normal and KID-1 epidermis (**Figure 3.1.3e-g)**. These results were in agreement with previous *in vitro* studies showing heteromeric assembly of Cx26/Cx30 channels (Yum et al., 2007).

Cx43 expression was observed throughout all epidermal layers with clear formation of gap junction plaques at the cell membranes in both normal and KID-1 epidermis **(Figure 3.1.3i-k, m-o)**. Cx43 was more abundantly expressed in the granular layers and upper spinous layers and less in the basal layer.

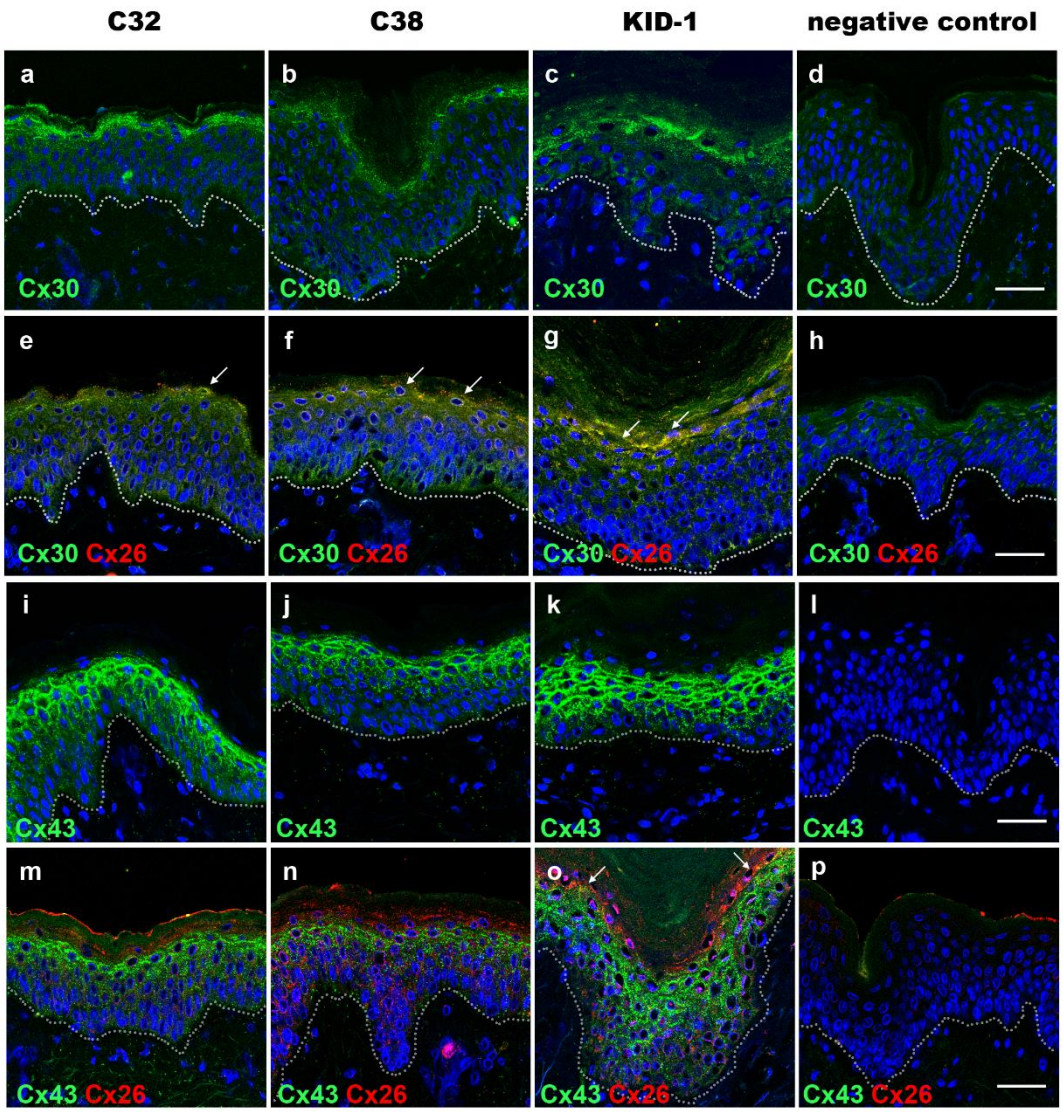

Figure 3.1.3 Expression of Cx30 and Cx43 in KID-1 and control epidermis

The expression of Cx30 (a-c, green) and Cx43 (i-k, green) in normal skin C32 (a, i) and C38 (b, j) and KID-1 skin (c, k) was examined by immunostaining. Cx30 was expressed in a punctate pattern in upper suprabasal layers in all skin tissues (a-c). Note the weak Cx30 staining in the basal layer of C38 epidermis (b). Cx43 was expressed throughout the epidermis, with strong membranous staining observed in the suprabasal layers (i-k). Double-staining of Cx26 (red) with Cx30 (e-g, green) and with Cx43 (m-o, green) was also performed, with areas of co-localisation appearing yellow. Co-localisation was found between Cx26 and Cx30 in the granular layers (e-g, arrows). In contrast, expression of Cx26 and Cx43 barely overlapped in normal epidermis (m-n), but they appeared to overlap focally in the granular layers of KID-1 epidermis (o, arrows). Nuclei were counterstained with DAPI (blue). The dotted lines show the dermal-epidermal junction. Bar = 40 μm.

Double-immunostaining for Cx43 and Cx26 showed that, while staining of both connexins was observed in the granular layers of normal epidermis, there was little

evidence of expression overlap **(Figure 3.1.3m-n)**. This finding was consistent with previous staining results on skin tissues (Kamibayashi et al., 1993). In KID-1 epidermis, by contrast, focal overlaps of Cx43 and Cx26 were observed in the granular layers **(Figure 3.1.3o)**. Although a number of Cx26 mutants have been found to interact with Cx43 *in vitro* in exogenous expression systems (Garcia et al., 2015; Shuja et al., 2016), the interaction between Cx26 p.D50N and Cx43 *in vivo* remains to be confirmed in future work.

3.1.4 Abnormal Cx26 expression in KID-1 keratinocytes

Despite altered Cx26 expression and distribution found in the epidermis of KID-1, the multi-layered structure of epidermis hindered detailed analysis for subcellular localisation of Cx26 in KID-1 keratinocytes. To overcome this hurdle, as well as to facilitate further expression and functional studies, a KID-1 patient-derived keratinocyte cell line (KID-KC) was generated by immortalising primary keratinocytes isolated from KID-1 skin **(see Section 2.4)**. An immortalised control keratinocyte cell line (control-KC) was also generated from keratinocytes isolated from a healthy control donor using the same procedure. Primary dermal fibroblasts were also isolated from the same biopsies of KID-1 (KID-FB) and the healthy donor (control-FB) **(see Section 2.4)**. These cell lines were genotyped by Sanger Sequencing using the GJB2-genomic-start primer **(Appendix I)**. The expression of *GJB2* mRNA was examined by RT-PCR and qPCR using the GJB2-endo-full-F/R primers spanning nearly the entire *GJB2* coding sequence, and the GAPDH primers were used as internal control **(Appendix I, Section 2.5**) The expression of Cx26 protein was also examined by immunoblotting and immunostaining **(see Section 2.6 and 2.7)**.

3.1.4.1 KID-KC: a good model to represent primary KID-1 keratinocytes

The immortalised KID-KCs at passage 5 and control-KCs at passage 1 were found to have a mixture of polygonal or flattened appearance **(Figure 3.1.4a-b)**, with little morphological difference observed between these cell lines. Similarly, there was little morphological difference between KID-FBs and control-FBs **(Figure 3.1.4c-d)**. Sequence analysis identified the heterozygous missense *GJB2* c.148G>A mutation in both KID-KCs and KID-FBs (**Figure 3.1.4b, d**). Control-KCs and -FBs showed

wildtype *GJB2* sequence **(Figure 3.1.4a, c)**.

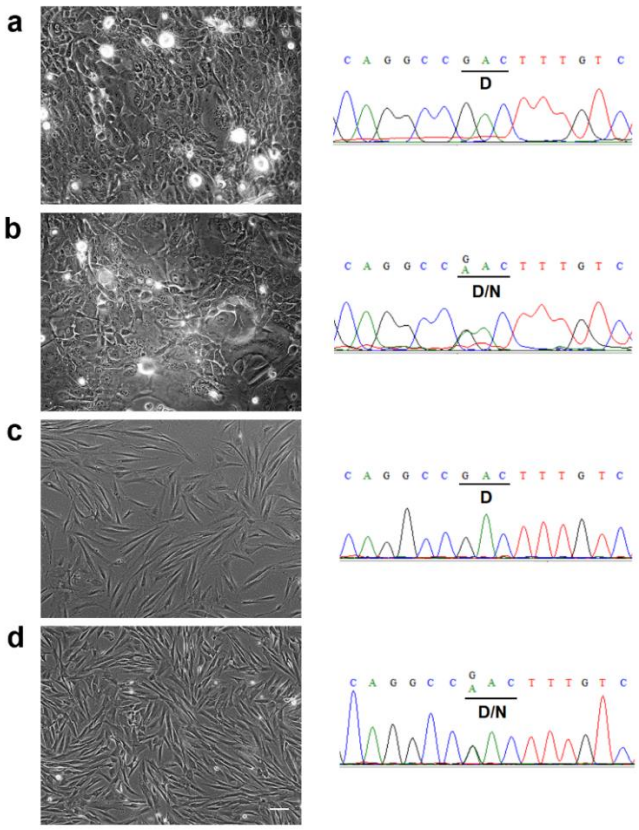

Figure 3.1.4 Morphology and genomic sequences of immortalised keratinocytes and primary fibroblasts from KID-1 and a healthy donor

Epidermal keratinocytes (KCs) and dermal fibroblasts (FBs) were cultured and phase contrast images (left panels) were recorded using a light microscope. Genomic DNA was extracted from cultured cells for sequence analysis (right panels). The sequence results of KID-KCs (b) and -FBs (d) confirmed the presence of the heterozygous c.148G>A mutation in GJB2, resulting in the p.D50N change at protein level. Control-KCs (a) and -FBs (c) showed wildtype GJB2 sequence. Bar = 100 µm

The morphology and genotypes of immortalised keratinocytes were monitored over a prolonged culture period of up to 40 passages. Both KID- and control-KCs showed a consistently high proliferation rate, and KID-KCs maintained the c.148G>A mutation stably *in vitro*. Therefore, these immortalised cells were used in further expression and functional studies. For quality control, cells with a passage number between 5−20 were used and regular mycoplasma testing was performed to ensure the use of mycoplasma-free cells in all experiments.

3.1.4.2 Decreased *GJB2* mRNA expression in KID-1 keratinocytes

RT-PCR analysis for full-length *GJB2* mRNA expression showed a 771-bp band in both KID-KCs and control-KCs **(Figure 3.1.5a)**. In contrast, no amplicons were detected in KID- or control-FBs, although the *GAPDH* gene was expressed in all fibroblast samples. These findings suggested that *GJB2* was expressed in keratinocytes, but not in fibroblasts, regardless of these cells being derived from the patient or the healthy donor. To further quantify *GJB2* expression, qPCR was subsequently carried out using SYBR® Green and the same primers. The results showed a 75% reduction of *GJB2* mRNA expression in KID-KCs, compared to that in control-KCs (0.25 ± 0.06 vs 1.02 ± 0.1, n = 4 per group, $p < 0.001$, Student's t-test) **(Figure 3.1.5b**). The results were consistent across four independent experiments.

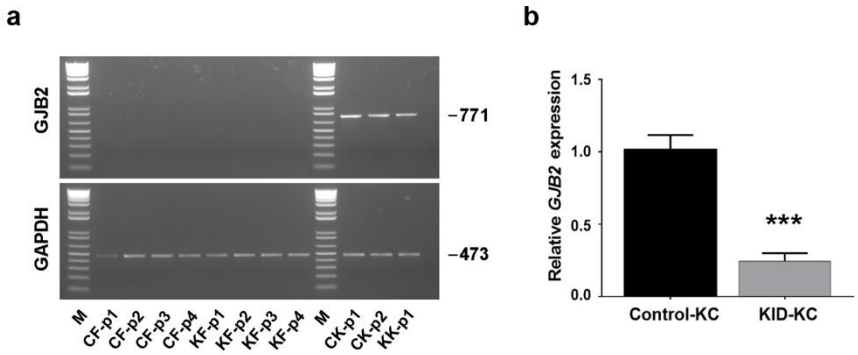

Figure 3.1.5 Reduced GJB2 mRNA expression in KID-1 keratinocytes

*RT-PCR with specific full-length GJB2 primers (771 bp) or GAPDH primers (473 bp, as internal control) was performed in cDNA samples extracted from cultured keratinocytes and fibroblasts. The PCR amplicons were analysed by 1.5% agarose gel electrophoresis (a). M: molecular-weight markers; CF: control fibroblast; KF: KID patient fibroblast; CK: control keratinocyte; KK: KID patient keratinocyte. The passage number of the cell culture was shown as p1−p4. Full-length GJB2 band was detected in keratinocytes but not in fibroblasts. SYBR Green qPCR was run in cDNA samples from control keratinocytes (Control-KC) and KID patient keratinocytes (KID-KC) using the same setting as RT-PCR. There was a significant reduction in GJB2 expression in KID-KCs compared to that in control-KCs. The bar chart (b) shows the data from three independent experiments. Each bar represents the mean ± SEM. ***p <0.001*

3.1.4.3 Reduced Cx26 protein expression in KID-1 keratinocytes

The expression level of Cx26 protein was also examined in the KID- and control-KCs. Studies by others have shown successful immunoblot detection of Cx26 orthologs using commercial antibodies in crude protein extracts from rodent cells or tissues

(Churko et al., 2010; Press et al., 2017a; Saitoh et al., 1997; Walcott et al., 2002), or from human cells ectopically expressing Cx26 (Elfgang et al., 1995; Yum et al., 2007; Zhang et al., 2011). However, preliminary testing in our lab found that published methods could not detect endogenous Cx26 protein in human keratinocytes, possibly due to low expression level of Cx26 in these cells or low specificity of the antibodies used. Therefore, a total of six antibodies against Cx26 **(Appendix II)** were tested and optimised to detect endogenous human Cx26.

Crude protein extracts from mouse heart and liver (positive control), HeLa cells (negative control) and control-KCs were run on 12% SDS-PAGE **(see Section 2.6)**. The results showed multiple bands, with 5 out of 6 antibodies **(Figure 3.1.6a-d, f)** detecting the target band at approximately 26 kDa in mouse liver lysate. Among the 5 antibodies, 3 also detected the 26 kDa band in HeLa cell lysate **(Figure 3.1.6c, d, f)**.

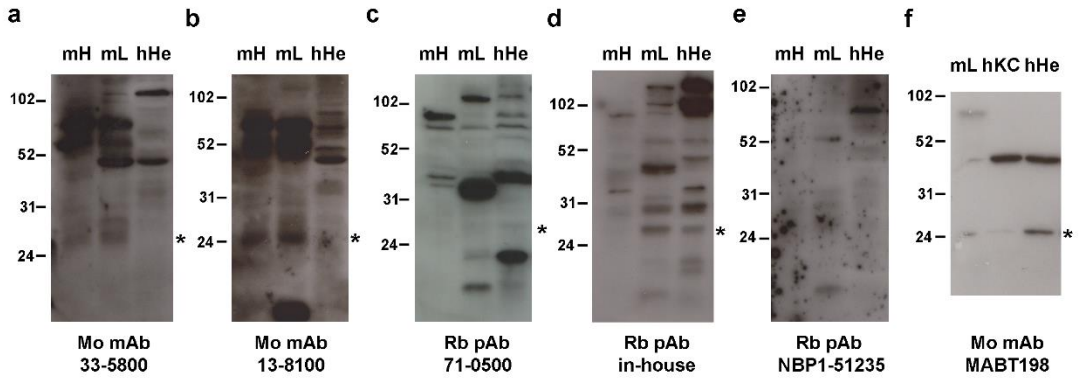

Figure 3.1.6 Immunoblotting for Cx26 using six different antibodies

40-80 µg crude protein lysates were harvested from mouse heart (mH) and mouse liver (mL), human HeLa cells (hHe) and immortalised normal human keratinocytes (hKC). Endogenous Cx26 expression was examined by immunoblotting using six different antibodies. Asterisks indicate the expected ~26 kDa band. Although the band was detected by all but one (e) antibodies in the mouse liver sample, multiple bands were observed in all blots.

The presence of extra bands in immunoblot experiments was reported elsewhere when the antibody 33-5800 or 71-0500 was used (Nagy et al., 2001; Shuja et al., 2016). These bands may result from either non-specific detection, oligomer formation (Gassmann et al., 2009), or low abundancy of Cx26 in the samples. A feasible approach to test these possibilities is immunoprecipitation, in which the target Cx26 is immunoprecipitated (or pulled down) from crude cell lysates using a first anti-Cx26 antibody conjugated to Protein-G Sepharose beads **(see Section 2.6)**. The resulting

bead-antibody-antigen immunocomplexes are then detected for Cx26 expression by the same immunoblot approach using a second anti-Cx26 antibody. The above approach allows for concentration of the target protein, which is expected to significantly increase the signal-noise ratio of the assay.

The in-house rabbit polyclonal antibody (Rb_pAb_in-house) was chosen for pull-down of Cx26 and one of the mouse monoclonal antibodies (13-8100) chosen for immunoblot detection **(Appendix II)**. This condition is referred to IP^1/IB^1. By this approach, a 26 kDa band was detected in the mouse liver sample **(Figure 3.1.7a)**, which was absent in the HeLa sample; however, this band was also absent in control-KC sample that was supposed to express Cx26.

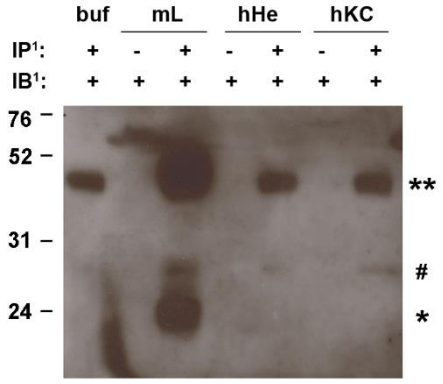

Figure 3.1.7 Failure to detect Cx26 in human keratinocytes using immunoprecipitation with the IP^1/IB^1 condition

Crude lysates of mouse liver (mL), human HeLa cells (hHe) and human keratinocytes (hKC) were immunoprecipitated (IP) using the Rb_pAb_in-house antibody (referred to as IP^1 condition). Lysis buffer (buf) was used as negative control. Immunoblotting (IB) was performed using the Mo_mAb_13-8100 antibody (referred to as IB^1 condition). Molecular weight markers are indicated at left (in kD). This approach detected the 26 kDa target band (asterisk) in mouse liver lysate, which was absent in HeLa lysate; however, the band was also absent in human keratinocyte lysate. Note the heavy chain of immunoglobin (double asterisk) detected at 53 kDa and a non-specific band (hash) at 28 kDa in samples undergone the IP^1 process.

A possible cause of the failure in detecting Cx26 in control-KCs by the initial condition (IP^1/IB^1) might be due to a lack of ability to recognise Cx26 of human origin by the antibody 13-8100. To test the hypothesis, this antibody was replaced with another monoclonal mouse antibody (Mo_mAb_MABT198). This approach is referred to as

IP^1/IB^2, and it resulted in successful detection of target band at approximately 26 kDa in the control-KC sample, in addition to the mouse liver sample **(Figure 3.1.8**). The band was not detected in the HeLa sample.

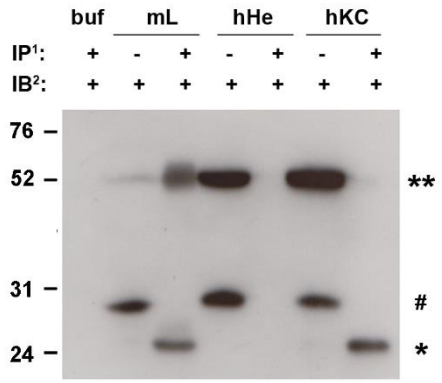

Figure 3.1.8 Detection of Cx26 in human keratinocytes using an optimised immunoprecipitation condition, IP^1/IB^2

Crude lysates of mouse liver (mL), human HeLa cells (hHe) and human keratinocytes (hKC) were immunoprecipitated (IP) using the Rb_pAb_in-house antibody (referred to as IP^1). Lysis buffer (buf) was used as negative control. Immunoblotting (IB) was performed using the Mo_mAb_ MABT198 antibody (referred to as IB^2). Molecular weight markers are indicated at left (in kDa). This approach detected the target band at 26 kDa (asterisk) in both mouse liver and human keratinocyte lysates. Note the non-specific bands detected at 52 kDa (double asterisk) and at 28 kDa (hash) in samples not undergone IP^1 process.

The IP^1/IB^2 approach was used on KID-KC samples. Surprisingly, this approach only detected the target band in control-KCs, but not in KID-KCs (**Figure 3.1.9**, left 3 lanes). The negative result from the KID-KC sample led to two hypotheses with regard to the p.D50N mutation either affecting the Cx26 epitope for antibody recognition leading to inefficient pull-down, or causing a significant reduction of overall Cx26 protein expression level in KID-KCs. The latter seemed unlikely because there was detectable Cx26 expression in KID-1 epidermis. To test these hypotheses, the Rb_pAb_71-0500 antibody, instead of the in-house antibody, was used for pull-down, followed by the same immunoblotting procedure for Cx26 detection. This condition is referred to IP^2/IB^2, and it led to successful detection of Cx26 in both control- and KID-KCs at approximately 26 kDa (**Figure 3.1.9**, right 3 lanes). The results favoured the hypothesis that the p.D50N mutant, located at the first extracellular loop domain (E1), affected the binding of the in-house antibody which recognises an epitope within the cytoplasmic loop domain (CL) (Di et al., 2001a). In the immunoblot result, there was

diminished Cx26 expression in KID-KCs compared to the control cells **(Figure 3.1.9)**, in keeping with the qPCR results. The final condition (IP^2/IB^2) was used in further studies involved in immunoblotting for endogenous Cx26.

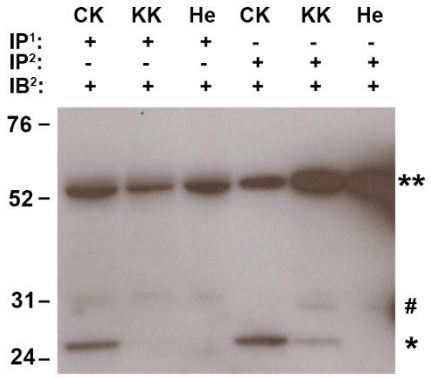

Figure 3.1.9 Further optimised condition, IP^2/IB^2, found reduced Cx26 expression level in KID-KCs

Crude lysates of control-KCs (CK), KID-KCs (KK) and HeLa cells (He, negative control) were immunoprecipitated (IP) using either the Rb_pAb_in-house antibody (referred to as IP^1) or the Rb_pAb_71-0500 antibody (referred to IP^2). Immunoblotting (IB) was performed using the Mo_mAb_ MABT198 antibody (referred to as IB^2). Molecular weight markers are indicated at left (in kD). The IP^1/IB^2 approach (left 3 lanes) failed to detect the target band at ~26 kDa (asterisk) in KID-KC sample. When the IP^2/IB^2 condition (right 3 lanes) was used, Cx26 was successfully detected in both control- and KID-KCs, but not in HeLa sample. In KID-KCs, a reduction in Cx26 expression level was found compared to control-KCs. Note the non-specific bands at 52 kDa (double asterisk) and at 31 kDa (hash).

3.1.4.4 Altered subcellular localisation and gap junction plaque formation in KID-1 keratinocytes

In earlier immunostaining sections, the observation of Cx26 subcellular localisation was hampered by the multi-layered structure of skin tissues. To explore whether the heterozygous p.D50N mutation altered Cx26 localisation in KID-KCs, immunostaining was carried out using the same antibody, 13-8100 **(Section 2.7, Appendix II)**. E-cadherin, an epithelial marker, was also stained to visualise the cell membrane.

In control-KCs, punctate or small linear Cx26 staining was observed at cell-cell contact sites, a sign of gap junction plaque formation **(Figure 3.1.10a-c)**. Overlaps between Cx26 and E-cadherin expression were frequently observed, suggesting that

wildtype Cx26 could traffic to the plasma membrane. By contrast, Cx26 in KID-KCs failed to accumulate at membrane regions and showed a primarily discrete punctate staining pattern in the cytoplasm and plasma membrane **(Figure 3.1.10d-f)**. On rare occasions, Cx26 proteins aggregated to form small gap junction plaques at points of cell-cell contacts **(Figure 3.1.10d, f)**. Although a portion of those plaques overlaid with E-cadherin, their size and pattern were rather dissimilar to those observed in the control-KCs. Observationally, Cx26 expression was reduced in KID-KCs compared to control-KCs, in agreement with the qPCR and immunoblot results.

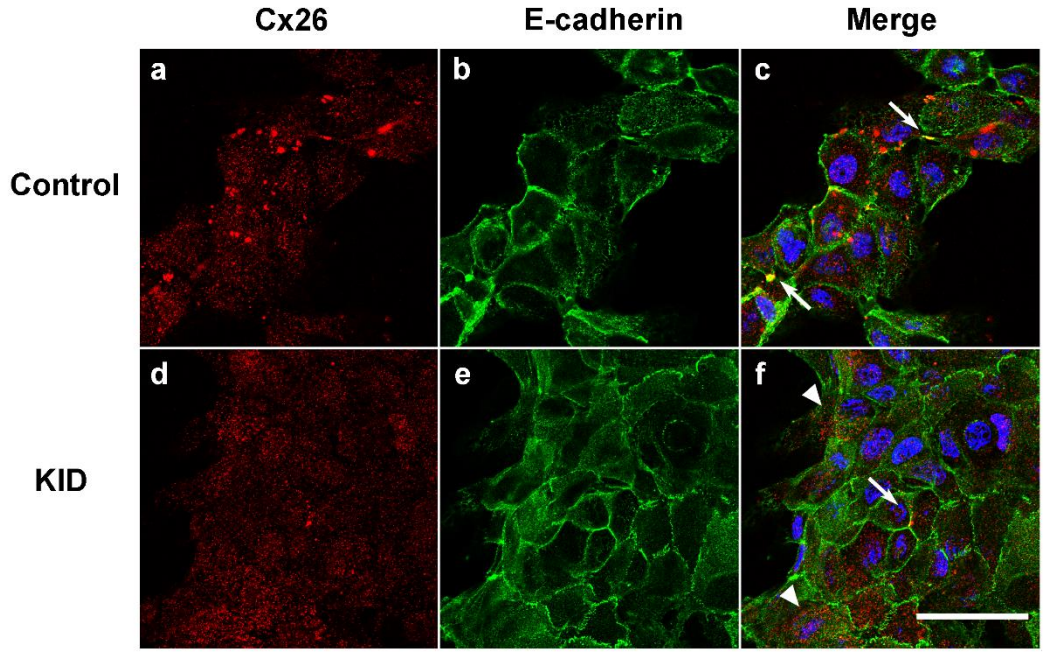

Figure 3.1.10 Images of localisation of Cx26 protein in control- and KID-KCs
Control- (a-c) and KID-KCs (d-f) were double-immunostained for Cx26 (red) and E-cadherin (green). DAPI (blue) was counterstained to indicate the nuclei. Both control- and KID-KCs displayed punctate Cx26 staining, but with different subcellular localisation. Cx26 in control-KCs trafficked to plasma membranes efficiently, forming large gap junction plaques which overlaid with E-cadherin extensively (c, arrows). In contrast, Cx26 in KID-KCs were localised discretely to cytoplasm and plasma membranes (f, arrowheads). On very rare occasions, gap junction plaques were found at cell-cell junctions (f, arrow). Bar = 40 μm.

3.1.5 Section summary

Previous studies of Cx26 mutants linked to KID syndrome largely relied on the use of exogenous expression systems, such as transfected HeLa cells which express the mutant of interest homozygously. These systems have limited ability to model the

heterozygous nature of Cx26 mutants in KID syndrome. In this study, KID-KC, the keratinocyte cell line derived from patient KID-1 heterozygous for the commonest mutation c.148G>A (p.D50N), was successfully established. *In vitro*, this cell line maintained the keratinocyte morphology and proliferation rate while displaying characteristic aberrant membrane trafficking and gap junction plaque formation associated with the p.D50N mutant. Furthermore, an immunoprecipitation approach was successfully optimised, which clearly demonstrated low-level endogenous Cx26 expression in KID-KCs. This patient-derived cell line can act as a good cell model for future studies of the pathomechanism underlying KID syndrome.

3.2 Normal gap junction channel activity in keratinocytes with one functional *GJB2* allele

We proposed to develop the therapeutic strategy using siRNA to silence the expression of the mutant *GJB2* allele with c.148G>A variant, thus allowing the wildtype *GJB2* allele to play a dominant functional role. However, whether keratinocytes with a single wildtype *GJB2* allele are able to maintain normal channel function is currently unclear. To address this question, a keratinocyte cell line with mono-allelic *GJB2* deletion (*GJB2*$^{+/-}$) was generated from a diploid normal human keratinocyte cell line using CRISPR/Cas9 genome editing via the non-homologous end joining (NHEJ) pathway. The Cx26 channel function was subsequently examined in this cell line.

3.2.1 Designed single guide sgRNAs generated mutations at target *GJB2* loci

Three candidate sgRNAs, g1, g2 and g4, each complementary to a certain 20-nucleotide *GJB2* sequence upstream of the protospacer adjacent motif (PAM), were designed using the Optimized CRISPR Design online tool **(Section 2.8.1, Figure 3.2.1)**.

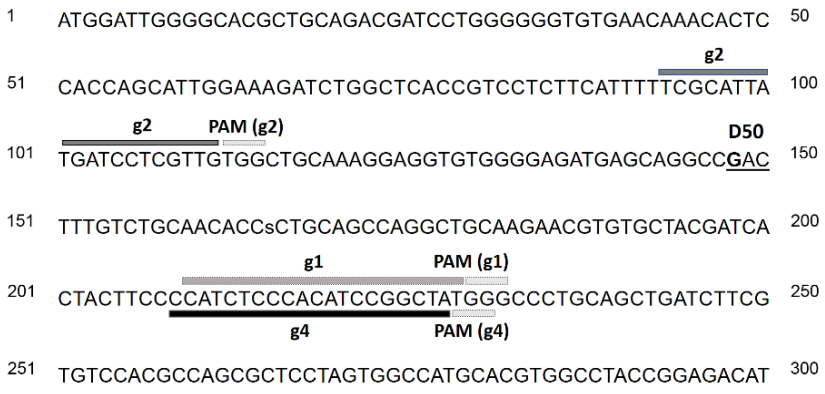

Figure 3.2.1 Design of candidate GJB2-specific single guide RNAs
*Single guide RNAs (g1, g2, g4), each complementary to a specific, 20-bp sequence (dark grey or black line) immediately upstream of protospacer adjacent motif (PAM, with NGG sequence, light grey lines), were designed within human GJB2 coding sequence. Upon target sequence recognition by sgRNA, a Cas9-induced DNA double-strand break is predicted to occur around 3-bp upstream the PAM, initiating gene editing. The codon D50 (GAC) is underlined with the nucleotide c.148G bolded (**GAC**). The nucleotide position is numbered and 50 bases are shown in each line.*

The sgRNAs were individually cloned into the lentiviral vector, p.LeGO-167-Cas9-iC-mCherry **(see Section 2.8.1 for details)**, which encodes the Cas9 nuclease gene and the mCherry reporter gene separated by an internal ribosome entry site (IRES). Positive colonies were picked up and sequences of the insert were confirmed by Sanger sequencing using the U6 primer **(Appendix I)**. These recombinant plasmids with g1, g2 or g4 inserted are hereafter referred to as g1-, g2- and g4-Cas9, respectively.

These sgRNA-encoding plasmids were first validated for *GJB2* gene editing in HEK-293T cells. Cells were transfected with any of the three plasmids **(see Section 2.8.2)** and the transfection efficiency was examined 72h post-transfection by flow cytometry for mCherry-positive cells. The transfection efficiency was similar across the three plasmids, ranging from 57.6% to 62.8% **(Figure 3.2.2)**.

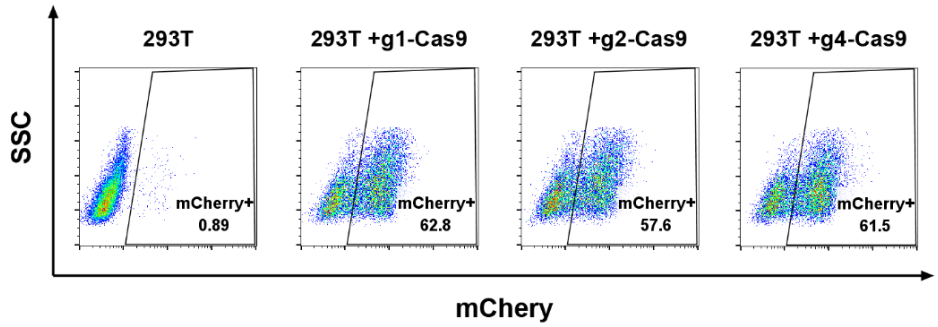

Figure 3.2.2 High transfection efficiency with sgRNA-Cas9 plasmids in HEK-293T cells
HEK-293T cells (293T) were transiently transfected with any of three sgRNA-Cas9 plasmids (g1-, g2-, g4-Cas9) using FuGene® 6, followed by flow cytometry analysis for transfection efficiency 72h post-transfection. Untransfected cells (293T) cultured alongside were used as a negative control. Transfection efficiency is represented as the percentage of mCherry-positive cells, as shown by the flow cytograph. The transfection efficiency was around 60% across all three transfected cell samples.

The *GJB2*-editing activity of the sgRNA-Cas9 plasmids, usually presented as insertions or deletions in the *GJB2* target sequence created by NHEJ, were measured by SURVEYOR® nuclease assay and T-A cloning followed by sequencing **(see Section 2.8.2)**.

A *GJB2* region flanking estimated sgRNA-Cas9 target sites was PCR-amplified from genomic DNA of g1-, g2- or g4-Cas9 plasmid-transfected HEK-293T cells using the SURVEYOR-GJB2-F/R primers **(Appendix I)**. The 539-bp amplicons were digested

with the SURVEYOR® nuclease and then analysed by agarose gel electrophoresis. No cleaved bands were detected at estimated sizes of around 260 and 280 bp for g1- and g4-Cas9, and around 160 and 380 bp for g2-Cas9 **(Figure 3.2.3)**.

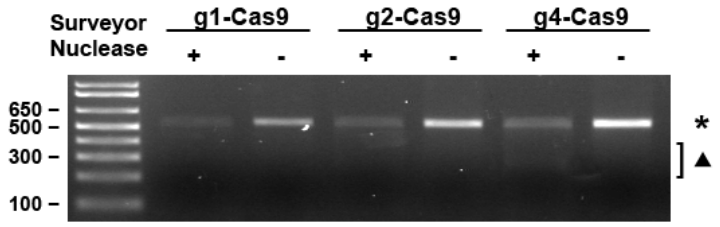

Figure 3.2.3 SURVEYOR® assay failed to detect sgRNA-Cas9-induced mutations in transfected HEK-293T cells

HEK-293T cells transfected with either of g1-, g2-, or g4-Cas9 plasmids were analysed for GJB2-editing efficiency by SURVEYOR® assay. A GJB2 region flanking estimated sgRNA-Cas9 target sites was PCR-amplified from genomic DNA of the transfected cells. PCR products were reannealed to form heteroduplex and then treated (+) or not treated (-) with the SURVEYOR® nuclease. The intact PCR product was detected at 539 bp in all samples (asterisk). No cleaved bands were detected at the estimated sizes (260-280 bp for g1 and g4; 160 bp and 380 bp for g2; the range is indicated by filled triangle).

The absence of cleaved bands could be due to low gene editing efficiency or relatively low sensitivity of the agarose gel electrophoresis-based SURVEYOR® assay. Therefore, the PCR amplicons were subcloned into the T-A cloning vector, pGEM®-T (see Section 2.8.2). Positive colonies were analysed by restriction enzyme digestion using NdeI and SacII, and those with positive insert were further confirmed by Sanger sequencing. The results clearly showed that cells transfected with sgRNA-Cas9 plasmids had mutations in GJB2, including missense mutations, insertions and deletions, adjacent to the sgRNA target sites (Figure 3.2.4). The GJB2-editing efficiencies were 33.3% (3/9) for g1-Cas9, 10% (1/10) for g2-Cas9, and 30% (3/10) for g4-Cas9.

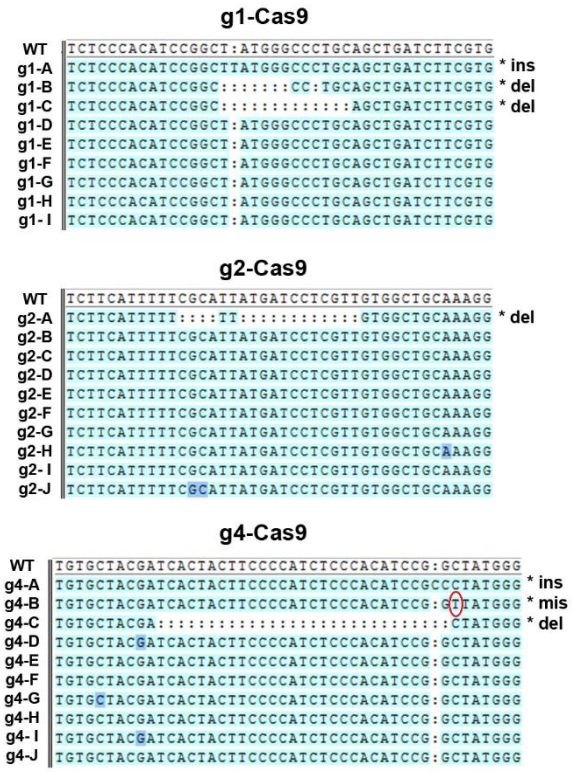

Figure 3.2.4 T-A cloning/sequencing confirmed GJB2 gene editing by all designed sgRNAs *HEK-293T cells transfected with either g1-, g2-, or g4-Cas9 plasmids were analysed for GJB2-editing efficiency by T-A cloning and subsequent Sanger sequencing. PCR amplicons of a genomic GJB2 DNA region spanning the estimated sgRNA-Cas9 target sites were subcloned into the pGEM®-T vector for sequence analysis. Sequencing of the resulting recombinant plasmids (g1-A to I, g2-A to J, g4-A to J) showed that all three designed sgRNAs edited GJB2 gene at their predicted target sites. Sequences of T-A cloning recombinant plasmids were aligned with the reference wildtype GJB2 sequence (WT), which revealed different types of mutations (asterisks), including missense mutation (mis, red circle), insertions (ins) and deletions (del).*

These findings confirmed that all three sgRNAs could cleave their respective target genomic DNA regions, generating various types of mutations via the NHEJ pathway. The sgRNAs g1 and g4, which displayed higher gene editing efficiency, were thus favourable choices for editing *GJB2* gene in keratinocytes. As these two sgRNAs had target sites close to each other, only g4 was selected for further experiments.

3.2.2 Keratinocyte cell line with *GJB2*$^{-/-}$ generated by CRISPR/Cas9

Following validation of sgRNA-mediated *GJB2* targeting in HEK-293T cells, a normal diploid keratinocyte cell line, N/TERT (Dickson et al., 2000), was used for generating

the *GJB2*$^{+/-}$ cell line **(see Section 2.8.3)**. N/TERT cells were transfected with g4-Cas9 and the transfection efficiency was examined 48 h later by flow cytometry for mCherry-positive cells. Approximately 8% transfection efficiency was observed. The mCherry-positive cells were sorted as single cells using FACS and then cultured for clonal expansion. The *GJB2* sequence of every expanded clone was examined by Sanger sequencing to identify desired clones with *GJB2*$^{-/-}$.

A total of 76 transfected N/TERT clones were grown (designated g4-B03−B23 and g4-C01−C55). Sequence analysis found 17/76 clones (22.37%) contained insertions or deletions near the PAM site of g4 **(Figure 3.2.5)**, confirming editing of *GJB2* in the N/TERT genome. Of the 17 positive clones, 15 (88.24%) had heterozygous mutations and two (11.76%) had homozygous mutations. The two clones with homozygous mutations are g4-C23 and g4-C36 **(Figure 3.2.5)**.

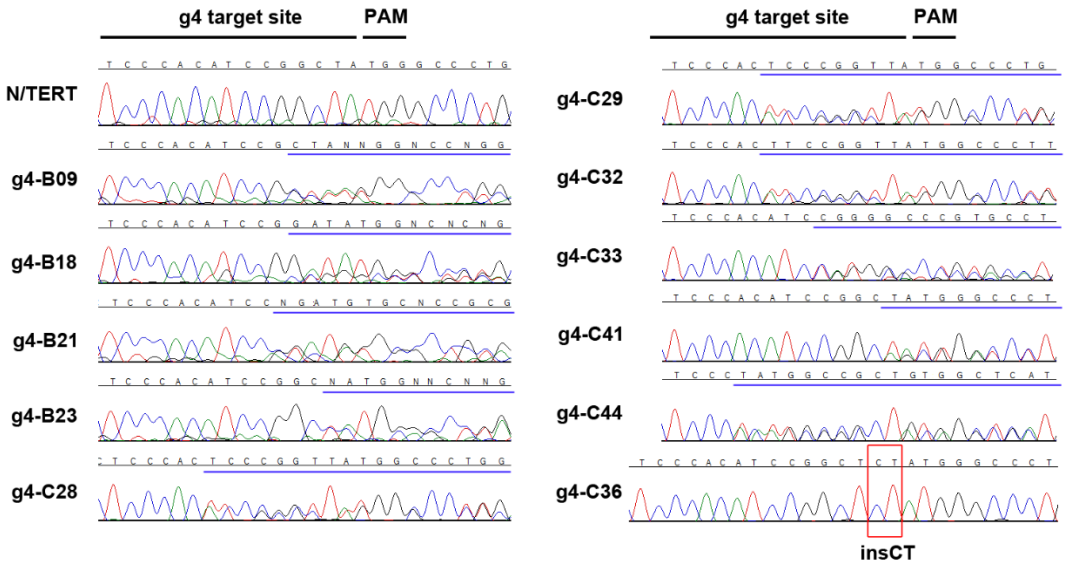

Figure 3.2.5 N/TERT clones with positive GJB2 gene editing
N/TERT cells were transiently transfected with g4-Cas9 and then subject to single-cell FACS sorting for positive cells. Expanded clones (designated g4-B/C followed by clone number) were analysed by sequencing of a GJB2 region spanning g4 target site. Sequence chromatograms of 11 grown clonal cell lines and untransfected cells (N/TERT, as reference sequence) are aligned. Different deletions (blue lines) were identified, which in most cases were heterozygous. A homozygous 2-bp insertion (insCT, red box) was found in the g4-C36 clone. Note that 6 of total 17 identified gene-edited clones are not shown due to either noisy sequence traces or gene editing occurring slightly outside the range of display.

To further confirm the genotype of clones with heterozygous mutation, a *GJB2* fragment containing the g4 target site was PCR-amplified from genomic DNA of five selected clones (g4-B09, -B21, -B23, -C41, -C44) and then subcloned into the pGEM®-T vector **(Section 2.8.3)**. Plasmids from positive colonies were subject to bidirectional sequencing using the GJB2-CRISPR-seq-F/R primers **(Appendix I)**. The results showed five different deletions in these clones, including two in-frame deletions c.227_238del12 for g4-C41 and c.218_226del9 for g4-C44; and three frameshift deletions c.224delG for g4-B09, c.224_225del2 for g4-B21 and c.227_233del7 for g4-B23 **(Table 3.2.1)**. The frameshift mutations were predicted to result in a premature termination codon, leading to truncation of Cx26 protein **(Table 3.2.1)**. Clones g4-B09 and g4-B21, both heterozygous for *GJB2* deletion, were chosen for further studies. The clone g4-C36 with homozygous *GJB2* deletion (*GJB2*$^{-/-}$), which served as a *GJB2*-null model, was also selected.

Table 3.2.1. Sequences of N/TERT clones with *GJB2* gene editing

Clone	Genomic DNA sequence (g4 target site – PAM)	cDNA change	aa change
N/TERT	CCCCATCTCCCACATCCGGCTATGG	Wildtype GJB2	Wildtype Cx26
g4-B09	CCCCATCTCCCACATCCGGCTATGG (het)	**c.224del1**	**L76Yfs*6**
g4-B21	CCCCATCTCCCACATCCGGCTATGG (het)	**c.224_225del2**	**R75Pfs*26**
g4-B23	CCCCATCTCCCACATCCGGCTATGG (het)	**c.227_233del7**	**L76Pfs*4**
g4-C41	CCCCATCTCCCACATCCGGCTATGG… (het)	c.227_238del12	L76-L79del4
g4-C44	CCCCATCTCCCACATCCGGCTATGG (het)	c.218_226del9	H73-R75del3
g4-C23	CCCCATCTCCCACATCCGGCTATGG… (homo)	c.222_278del57	I74-A92del19
g4-C36	CCCCATCTCCCACATCCGGCTCTATGG (homo)	**c.227_228ins2**	**W77Yfs*6**

- Deleted (del) sequences are shown in red alphabets and inserted (ins) sequences in blue alphabets.
- Frameshift (fs) mutation (bolded) is indicated in the format of fs*N. For instance, L76Yfs*6, where frameshift occurs from residue L76 that is substituted for tyrosine (Y) and a stop codon is predicted to appear 6 amino acids downstream of L76Y.
- Het, heterozygous. Homo, homozygous. PAM: protospacer adjacent motif (e.g. TGG for g4).

3.2.3 Normal morphology of keratinocytes with *GJB2*$^{+/-}$

The morphology of clones g4-B09, -B21 and -C36 was examined using inverted light microscopy. All clonal cell lines showed cobblestone-like appearance without obvious morphological difference from the parental N/TERT cells **(Figure 3.2.6a-d)**. The Cx26

expression was also examined by immunostaining using the 13-8100 antibody **(see Section 2.7)** and fluorescent images were recorded using a confocal microscope. The results showed punctate Cx26 staining in both *GJB2*$^{+/-}$ clones, g4-B09 and g4-B21, with gap junction plaques formed at cell-cell junctions **(Figure 3.2.6f-g)**. The pattern of Cx26 staining in these *GJB2*$^{+/-}$ clones was comparable to that in parental N/TERT cells, albeit weaker in intensity. In contrast, no Cx26 expression was detected in the *GJB2*$^{-/-}$ clone, g4-C36 **(Figure 3.2.6h)**. These findings suggest that keratinocytes with a single wildtype *GJB2* allele had normal morphology, membrane trafficking and gap junction plaque formation of Cx26 *in vitro*.

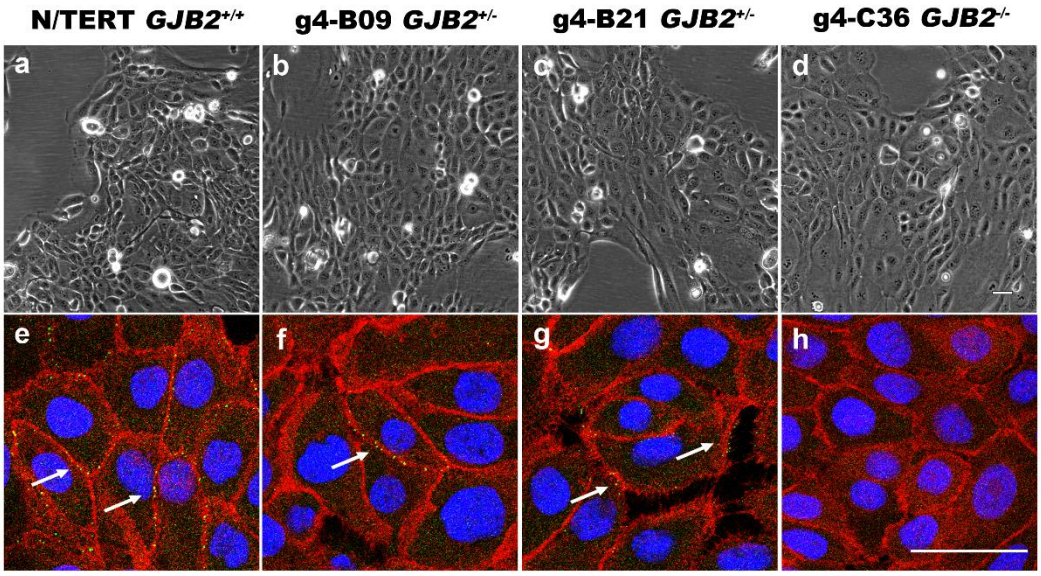

Figure 3.2.6 Morphology and Cx26 expression in N/TERT clones lacking GJB2
N/TERT clones with GJB2$^{+/-}$ *(g4-B09 and g4-B21) and GJB2*$^{-/-}$ *(g4-C36), along with their parental GJB2*$^{+/+}$ *cells (N/TERT) were examined for morphology (a-d) and Cx26 expression (e-h). On light microscopy, no obvious morphological difference was seen among these cells. Immunostaining for Cx26 (green) showed punctate staining with formation of gap junction plaques at cell-cell junctions (f-g, arrows) in both GJB2*$^{+/-}$ *clones, similar to that observed in GJB2*$^{+/+}$ *cells (e, arrows), despite a reduction in Cx26 fluorescence intensity in GJB2*$^{+/-}$ *clones. No Cx26 expression was detected in g4-C36 clone (h). Phalloidin (red) and DAPI (blue) were used to visualise actin filaments and nuclei, respectively. Bar = 40 µm.*

3.2.4 Normal gap junction channel activity in keratinocytes with *GJB2*$^{+/-}$

The function of gap junction channels, termed gap junction intercellular communication (GJIC), mediates the exchange of ions and small molecules (< 1 kDa) between the cytoplasm of adjacent cells. In general, studies of GJIC activity rely on

measuring the intercellular dye transfer (dye coupling), electrical conductance (electrical coupling) or metabolic cooperation (metabolic coupling) (Abbaci et al., 2008). Among various methods, dye transfer approaches are widely employed because these approaches, in general, do not require specialised equipment. By introducing a gap junction-permeant dye (e.g. Lucifer Yellow, Cascade Blue, neurobiotin) into a cell, the subsequent transfer of the dye to its neighbouring cell(s) through functional gap junction intercellular channels can be traced and measured. The dye is usually introduced by microinjection (Di et al., 2001b; Di et al., 2002), electroporation (De Vuyst et al., 2008) or scrape-loading (Yum et al., 2007). The latter, also known as the scrape-loading dye transfer assay (SLDT), is a rapid and less technically demanding approach, allowing simultaneous measurement of GJIC among a relatively large number of cells (el-Fouly et al., 1987). The SLDT assay was chosen in this study **(see Section 2.9.1)**, and was performed on N/TERT clones with *GJB2*$^{+/-}$ (g4-B09, g4-B21). The parental N/TERT cells, along with the g4-C36 clone with *GJB2*$^{-/-}$, were also assayed as controls.

Cascade Blue, an anionic, 548-Da fluorescent tracer known to pass Cx26 channels (Marziano et al., 2003), was scrape-loaded into the cells using a pipette tip. This was followed by incubation for 20 min to allow dye transfer between adjacent, gap junction-coupled cells. Images of dye transfer were recorded and the area under positive dye transfer regions, indicating the level of dye coupling, was quantified **(see Section 2.9.2)**. Dextran-Rhodamine B, another fluorescent tracer with a molecular weight of 10 kD (beyond the size limit of gap junction), was used as a control.

The results showed that all tested clones transferred Cascade Blue to 3-5 cell layers away from the scrape line **(Figure 3.2.7a-d)**. Quantification of dye transfer area found no statistical difference between *GJB2*$^{+/-}$ clones (g4-B09 or g4-B21) and parental N/TERT cells (220277 ± 48296 μm^2 vs 213901 ± 49620 μm^2 vs 237137 ± 36929 μm^2, numbers of images = 31, 32, 35, $p > 0.05$, one-way ANOVA with Tukey's multiple comparison test) (**Figure 3.2.7l**). However, the g4-C36 cells with *GJB2*$^{-/-}$ showed a reduced dye transfer area compared to the parental N/TERT cells (196874 ± 84635 μm^2 vs 237137 ± 36929 μm^2, numbers of images = 40 and 35, $p < 0.05$). Pharmacological blockade with carbenoxolone (CBX), a non-selective blocker of gap junction channels and hemichannels (Djalilian et al., 2006; Verselis and Srinivas,

2013), significantly decreased the dye coupling in parental N/TERT cells **(Figure 3.2.7e)**. There was no transfer of Dextran-Rhodamine B in all tested cell lines, where the dye was confined to the primarily loaded cells along the scrape line **(Figure 3.2.7f-j)**, suggesting that Cascade Blue was transferred through functional gap junction channels. This experiment was repeated three times and the results were consistent.

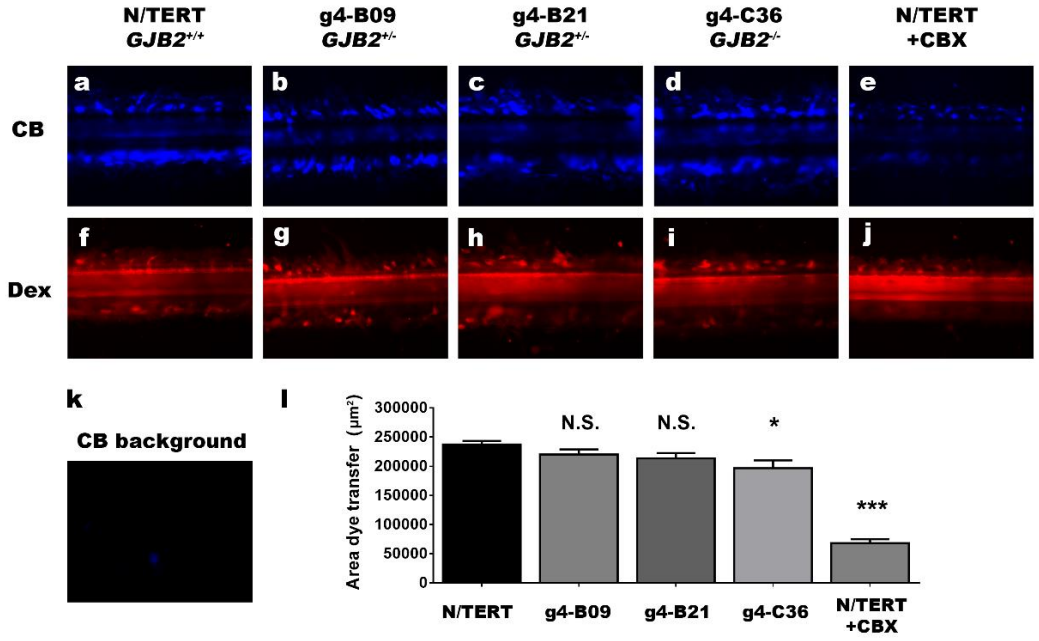

Figure 3.2.7 Normal dye coupling in GJB2$^{+/-}$ keratinocytes

*The Cascade Blue-based scrape-loading dye transfer assay was performed to assess dye coupling through gap junction channels formed by N/TERT clones with GJB2$^{+/-}$ (g4-B09 and g4-B21), GJB2$^{-/-}$ (g4-C36), or parental GJB2$^{+/+}$ N/TERT cells (N/TERT). Dextran-Rhodamine B (Dex) with a size beyond the permeability of gap junction was used as control. Carbenoxolone (CBX) was used to block gap junction channels. Representative images of transfer of CB (a-e, k) and Dex (f-j) from the primarily-loaded cells along the scrape line are shown. Note the absence of CB signals in unwounded N/TERT cells (k). Quantification of the images showed no significant difference in dye coupling between GJB2$^{+/-}$ cells and parental cells (l), although slightly reduced dye coupling was seen in GJB2$^{-/-}$ cells. Data are mean ± SEM. *p < 0.05; ***p < 0.001; N.S. not significant.*

These results indicate that keratinocytes with a single wildtype allele of *GJB2* had normally functioning gap junction channels. In contrast, keratinocytes lacking both *GJB2* alleles had a statistically significant reduction in dye coupling. Whether this reduction is biologically significant remains to be confirmed by other GJIC assays, e.g. double patch clamp electrophysiology for assessment of electrical coupling.

3.2.5 The optimised ATP release assay did not specifically reflect hemichannel activity in N/TERT cells

Cx26 also forms hemichannels that serve as a direct conduit between the cytoplasm and the extracellular space by passing ions and signalling molecules across the membrane (Retamal et al., 2015). Hemichannel activity can be determined by measuring transmembrane electrical conductance (e.g. Na^+, K^+) or permeability to hemichannel-permeant signalling molecules (e.g. ATP, Ca^{2+}) (Schalper et al., 2008). Unlike GJIC assays, hemichannel assays are conducted on unopposed, solitary cells which rule out the contribution of gap junction channels. Common methods include patch clamp technique (Lee et al., 2009), dye uptake assay (Mese et al., 2011) and measurement of intracellular Ca^{2+} and ATP release (Donnelly et al., 2012; Garcia et al., 2015). The latter ATP release measurement, a sensitive, luciferin/luciferase-based bioluminescent assay, was selected for measuring hemichannel activity in this study.

This approach, modified from previously published methods (Lohman and Isakson, 2014; Stout et al., 2002), was based on the conversion of luciferin into oxyluciferin by the enzyme luciferase in the presence of ATP in culture medium, which results in the emission of a photon (Ford et al., 1996). Photons can be detected using a luminometer. The ATP release through open connexin hemichannels can be triggered by mechanical stimuli (Zhao et al., 2005), certain peptidoglycans (Donnelly et al., 2012) and zero extracellular Ca^{2+} challenge (Easton et al., 2012; Zhao et al., 2005). Prior to measurement of ATP release from cultured cells, three parameters specific to the assay were determined. These are: i) the appropriate dilution for the luciferin/luciferase solution, ii) the analytical sensitivity for the assay, and iii) the linear range of ATP concentrations for optimal ATP measurement **(see Section 2.10).**

Firstly, the optimal dilution for the provided luciferin/luciferase solution (ATP Assay Mix, referred to as 'the assay mix' thereafter) was determined as described previously (Fukuda et al., 2015). Five dilutions of the assay mix, ranging from 1:400 to 1:10, were reacted with 0 or 10 μM ATP standards, and the luminescence was measured using a luminometer **(see Section 2.10)**. The luminescence was plotted against the dilutions of the assay mix **(Figure 3.2.8)**. The results showed that the maximal displacement for 10 μM ATP occurred when the assay mix was diluted 1:10. Hence, this dilution was

applied to further ATP experiments.

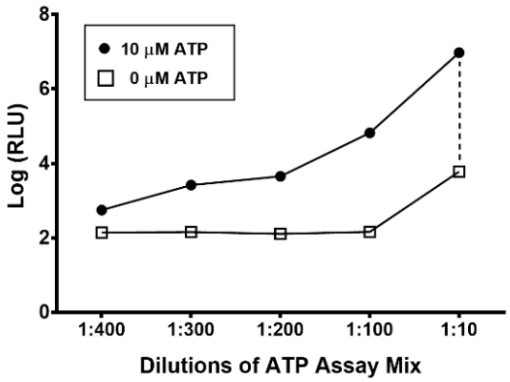

Figure 3.2.8 Determination of the optimal dilution for the ATP Assay Mix
Different dilutions of ATP Assay Mix, ranging from 1:400 to 1:10, were reacted with 0 μM (□) or 10 μM (●) ATP standards. Luminescence was measured and expressed in relative light unit (RLU). The maximal displacement (dashed line) was found at 1:10 dilution of the ATP Assay Mix.

Secondly, the analytical sensitivity (also known as lower limit of detection), which can be calculated as the minimum concentration of standard sample (minus 2SD) that does not overlap with the zero level plus 2SD (Li and Cassone, 2015), was determined for two buffer systems DMEM and PBS. ATP standards at a range of low concentrations (diluted in DMEM or PBS), along with zero concentration, were reacted with the assay mix at 1:10 dilution, followed by luminescence measurement **(see Section 2.10)**. The analytic sensitivity was found to be 5 nM for DMEM and 2.5 nM for PBS **(Figure 3.2.9)**. These concentrations of ATP standard can be used as the lowest point when constructing a standard curve in further experiments.

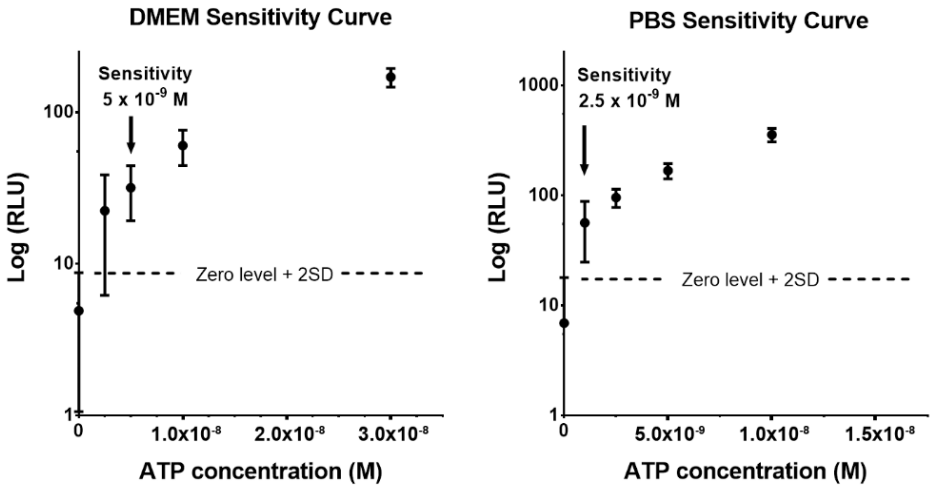

Figure 3.2.9 Determination of analytical sensitivity for ATP assay

Different low concentrations of ATP standards (n = 10 each concentration), diluted in either PBS or DMEM, were reacted with the assay mix at 1:10 dilution. Samples were measured for luminescence, which is expressed in relative light unit (RLU). The analytical sensitivity was determined as 5.0×10^{-9} M (5 nM) for samples diluted in DMEM and 2.5×10^{-9} M (2.5 nM) for samples diluted in PBS, where the concentrations minus 2SD did not overlap with the zero concentration (zero level) plus 2SD (n = 10).

Thirdly, a standard curve was generated from an appropriate concentration range of ATP standard within which a linear correlation was present. To determine this range, serially-diluted ATP standards (0−10 μM, in PBS or DMEM) were reacted with the assay mix. A linear correlation was seen when the ATP concentration was between 2.5 nM to 3 μM for the PBS system (R^2= 0.9955) and between 10 nM and 10 μM for the DMEM system (R^2= 0.996) **(Figure 3.2.10)**. Saturation of luminescence signals was seen when a sample contained ATP at a concentration beyond the upper limit, 10 μM.

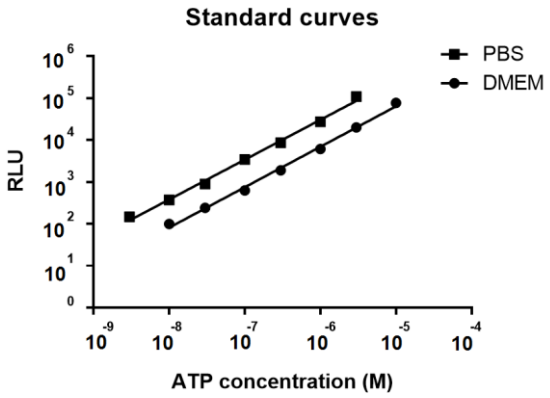

Figure 3.2.10 Standard curves of ATP assay

ATP standard was diluted in PBS (■) or DMEM (●) to a range of concentrations from 0 to 1×10^{-5} M. Serially-diluted ATP standard was reacted with the assay mix at 1:10 dilution. A linear correlation between ATP concentration and luminescence was seen when ATP concentration was 2.5 nM and 3 μM (PBS system) and between 10 nM and 10 μM (DMEM system).

The optimised method was tested in parental, *GJB2*$^{+/+}$ N/TERT cells cultured in a 24-well plate, with connexin-null HeLa cells measured in parallel as a negative control. The ATP concentration in the culture media was measured to be between 20 and 200 nM, which fell in the linear range of this assay. This testing was repeated three times and similar data were obtained, suggesting that the optimised luminescence measurement approach was reliable in measuring extracellular ATP in cultured cell

samples. Thus, the hemichannel-dependent ATP release was carried out in these cells **(see Section 2.10)**. Cells were initially incubated in DMEM medium containing 1.8 mM Ca^{2+} that inhibited hemichannels (Sanchez et al., 2014) and the extracellular ATP was measured as baseline level. Cells were subsequently challenged with zero-Ca^{2+} PBS to open hemichannels (de Wolf et al., 2016; Donnelly et al., 2012; Easton et al., 2012; Verselis and Srinivas, 2008) and the ATP release via open hemichannels were measured.

The results showed elevated ATP release in N/TERT cells upon zero-Ca^{2+} challenge, by an average of 63%, compared to the baseline level **(Figure 3.2.11)**. This response was blocked by CBX, indicating that the elevated ATP level was dependent on connexin channels. This finding is consistent with previous results from mammalian cells ectopically expressing Cx26 (Easton et al., 2012; Xu et al., 2017). However, a similar ATP release response to zero-Ca^{2+} challenge was seen in connexin-null HeLa cells. Specifically, HeLa cells showed a 70% increase in ATP release when exposed to zero-Ca^{2+}, compared to baseline level. Likewise, this response was potently inhibited by CBX. The results from HeLa cells were consistent across three independent experiments **(Figure 3.2.11a)**.

The reason for the similar response between the above two cell types with highly distinct connexin expression profiles is unknown. However, it is conceivable that this assay can be confounded by the presence of gap junction intercellular channels, pannexin channels (Lohman et al., 2012), or residual ATP in the medium. Furthermore, this assay is highly sensitive that the results were affected easily by individual sample preparation, as shown by variable data from N/TERT samples **(Figure 3.2.11a)**. For these reasons, the ATP release assay was not used in the study, but instead, two alternative hemichannel assays were considered, i.e. patch clamp and dye uptake assay. These assays are described in **Section 3.4**.

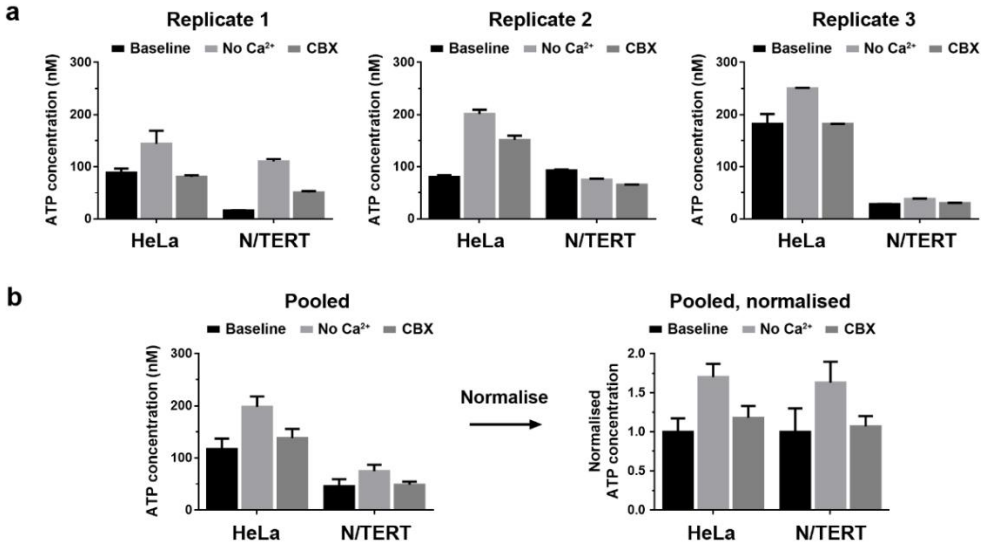

Figure 3.2.11 Optimised ATP assay failed to distinguish hemichannel activity between HeLa and N/TERT cells

HeLa (connexin-null) and N/TERT cells (connexin-rich) were assayed for ATP release upon zero-Ca^{2+} challenge. Cultured cells were challenged with zero calcium (No Ca^{2+}) followed by ATP measurement. For baseline measurement (baseline), DMEM containing 1.8 mM Ca^{2+} was used. For hemichannel blockade, 100 μM carbenoxolone (CBX) was used. This assay was performed in three biological replicates (a), each with two technical replicates. For further comparison, data from three independent experiments were pooled and shown in original scale (b, left) and normalised scale to respective baseline levels (b, right). There was indistinguishable zero-Ca^{2+}-evoked ATP release between HeLa and N/TERT cells. Data are mean ± SEM.

3.2.6 Section summary

Two *GJB2*$^{+/-}$ and one *GJB2*$^{-/-}$ keratinocyte cell lines were generated using CRISPR/Cas9. To my knowledge, this is the first attempt to delete *GJB2* gene using genome editing. These cell lines not only facilitate the evaluation of the outcome for the proposed allele-specific siRNA therapy, but also act as excellent cell models for studies of a variety of Cx26-involved biological processes, such as wound healing and tumorigenesis. *In vitro*, both *GJB2*$^{+/-}$ keratinocyte cell lines had morphology, membrane trafficking, gap junction plaque formation and GJIC comparable to their parental diploid cells. These findings strongly support that the proposed siRNA therapy may serve as a feasible therapeutic strategy for KID syndrome without causing major gap junction defects in keratinocytes, although future work is required to confirm the hemichannel activity in these cell lines.

3.3 S7 inhibited *GJB2* c.148G>A mutant expression potently and specifically

In this section, a set of 19 candidate allele-specific siRNAs were designed. Prior to testing these siRNAs in the patient-derived KID-KCs, two cellular models stably expressing exogenous wildtype or mutant *GJB2* gene were generated. These models allowed for screening of the siRNAs to discover a potent and specific siRNA against the mutant *GJB2*. The functional effect of the mutation-specific siRNA was subsequently assessed using qPCR, immunoblotting and flow cytometry.

3.3.1 Stable expression of wildtype and mutant *GJB2-GFP* in HeLa and N/TERT cell lines

3.3.1.1 HeLa and N/TERT as suitable cell models for siRNA screening

A *GJB2-GFP* fusion reporter system was employed to achieve highly-efficient siRNA screening due to its ability to monitor target gene expression in real-time. HeLa cells without endogenous connexin expression (Elfgang et al., 1995) were used to express the fusion transgene. Since these cervical epithelial cancer cells were of limited relevance to KID syndrome theoretically, epidermal keratinocytes were also used. To determine a suitable keratinocyte model for siRNA studies, RT-PCR for an endogenous *GJB2* region were carried out in four immortalised human keratinocyte cell lines **(see Section 2.11)**, including P6- and P8KC (keratinocyte lines generated in-house), HaCaT and N/TERT (commercial keratinocyte lines) **(Table 2.1)**. The *GJB2* expression in HeLa and HT1080 (a human fibroblastoma cell line) cells was also examined in parallel**.**

No *GJB2* transcript was detected in HeLa cells **(Figure 3.3.1)**, consistent with the immunoblot results in an earlier section **(see Section 3.1.4.3, Figure 3.1.9)**. *GJB2* expression was detectable in P6-, P8KC and N/TERT keratinocytes, but weakly in HT1080 and absent in HaCaT cells. Endogenous *GJB2* expression in HaCaT cells has been controversial. One study detected *GJB2* mRNA in HaCaT cells (Donnelly et al., 2012), but others failed to detect Cx26 protein in these cells by immunoblotting (Aypek, 2015). Thus, N/TERT cells, instead of HaCaT cells, were selected to express the transgene in subsequent siRNA studies. Connexin-null HeLa cells were also selected.

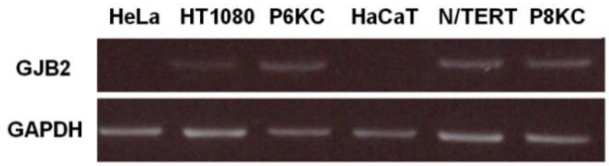

Figure 3.3.l Endogenous expression of GJB2 mRNA in cell lines
Total RNA extracted from six different cell lines was analysed by semi-quantitative RT-PCR for endogenous GJB2 expression using primers specific to a fragment of GJB2 cDNA. GAPDH-specific primers were used as internal control. HeLa cells that did not express GJB2 endogenously and N/TERT cells that expressed GJB2 abundantly were selected for subsequent siRNA screening.

3.3.1.2 Ectopic expression of *GJB2-GFP* transgene in HeLa and N/TERT cells

A HIV-1 derived, self-inactivating lentiviral vector was used to allow stable expression of *GJB2-GFP* transgene in the selected cell lines **(see Section 2.12)**. The vector was constructed to encode either wildtype *GJB2-GFP* or mutant *GJB2-GFP* containing the c.148G>A mutation, whose expression was driven by the cytomegalovirus promoter **(Figure 2.3)**. Their protein products are hereafter referred to as wildtype and mutant Cx26-GFP, respectively. Lentivirally-transduced HeLa and N/TERT cells were enriched for GFP^+ populations using FACS. The transgene expression in sorted cells was determined by RT-PCR using the GJB2-GFP-RT1 primers spanning *GJB2* and *GFP* cDNA **(Appendix I, Section 2.5)** and immunostaining using the in-house antibody against Cx26 **(Appendix II, Section 2.7)**.

The RT-PCR results showed a marked increase in the transcript of *GJB2-GFP* in FACS-enriched HeLa cells compared to non-enriched cells **(Figure 3.3.2)**. The FACS-enriched HeLa and N/TERT cells also showed expression of Cx26 protein **(Figure 3.3.3b, e, h, k)** with the Cx26 staining co-localising with GFP signals **(Figure 3.3.3c, f, i, l)**. For those transduced with wildtype lentiviruses, the Cx26-GFP fusion protein expression was found predominantly in a punctate or linear pattern at cell-cell interfaces with formation of gap junction plaques **(Figure 3.3.3c, i)**. By contrast, the mutant fusion protein showed a primarily perinuclear expression pattern, consistent with previous reports (de Zwart-Storm et al., 2011a; Di et al., 2005; Donnelly et al., 2012; Terrinoni et al., 2010). Gap junction plaques were observed at sites of cell-cell contact in a small subset of mutant-expressing N/TERT cells, but these were not seen

in mutant-expressing HeLa cells, indicating that endogenous wildtype connexins expressed in N/TERT cells, but absent in HeLa cells, could partially rescue trafficking of the mutant protein. Similar *in vitro* rescue has previously been reported in HeLa cells co-transfected with wildtype and mutant *GJB2* (de Zwart-Storm et al., 2011a; Marziano et al., 2003). There was otherwise no difference in fusion protein expression between HeLa and N/TERT cells. These results indicate that both HeLa and N/TERT cells can synthesise, fold and transport the exogenous wildtype and mutant Cx26-GFP fusion proteins.

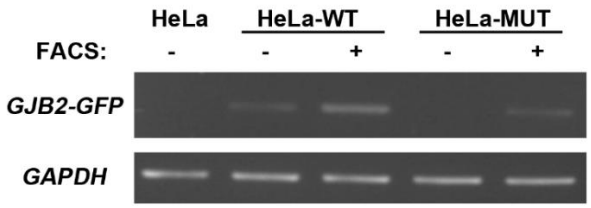

Figure 3.3.2 FACS enriched expression of GJB2-GFP transgene in HeLa cells
HeLa cells expressing wildtype (HeLa-WT) or mutant (HeLa-MUT) GJB2-GFP transgene were enriched by FACS for GFP^+ cells. The enriched (+) or non-enriched (-) HeLa cells were subject to RT-PCR analysis for GJB2-GFP expression. GAPDH was used as loading control. There was increased GJB2-GFP transcript detected in both FACS-sorted WT and MUT cells, compared to that in non-FACS-sorted cells. No GJB2 mRNA expression was detected in the parental HeLa cells (HeLa).

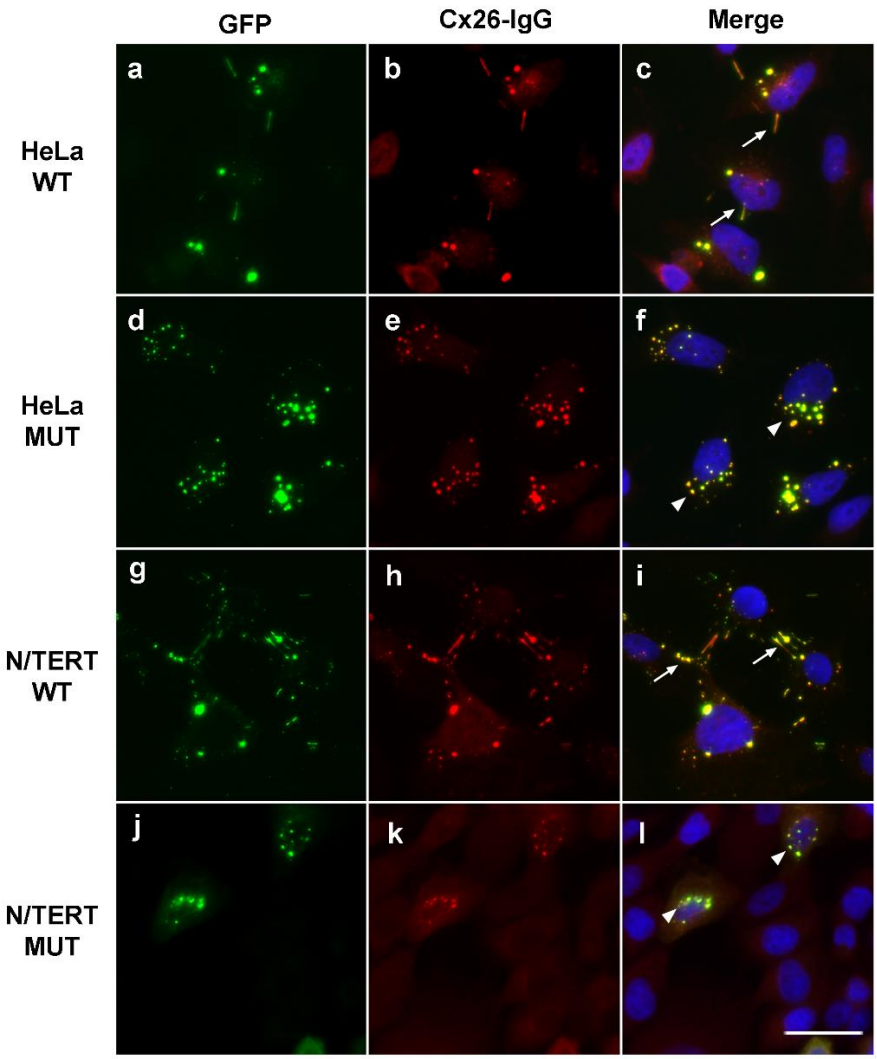

Figure 3.3.3 Expression of Cx26-GFP fusion protein in lentivirally-transduced, FACS-enriched HeLa and N/TERT cells

Lentivirally-transduced, FACS-sorted Hela and N/TERT cells (bulk GFP$^+$ populations) were examined for fusion protein expression by immunostaining using the in-house antibody against Cx26 (b, e, h, k, red) or by GFP signals (a, d, g, j, green). There was extensive co-localisation of both signals (c, f, i, l, yellow). In cells expressing wildtype GJB2-GFP (WT), punctate staining and gap junction plaques were primarily found at cell-cell junctions (c, i, arrows). In cells expressing mutant transgene (MUT), by contrast, a perinuclear staining pattern was observed (f, l, arrowheads) with markedly reduced gap junction plaques formation at cell-cell junctions. Bar = 60µm.

3.3.1.3 Successful isolation and expansion of single HeLa clones expressing full-length *GJB2*

In the FACS-enriched GFP$^+$ N/TERT and HeLa cells, a subsequent RT-PCR analysis using GJB2-GFP-RT2-F/R primers for a region spanning nearly full-length *GJB2*

cDNA, the *GJB2-GFP* fusion region and the first 86 bp of *GFP* cDNA **(Appendix I, Figure 3.3.4b)** surprisingly revealed two shorter forms of the *GJB2-GFP* transgene (571 bp and approximately 700 bp), in addition to the full-length target band (766 bp) **(Figure 3.3.4a)**. Sequencing analysis of the 571-bp band revealed a 195-bp in-frame deletion between positions 453−647 of the *GJB2* cDNA, but the deletion did not affect the *GJB2-GFP* fusion region **(Figure 3.3.4b)**. The other shorter band (approximately 700 bp) was also isolated and purified for sequencing, but the sequence trace had high background noises, perturbing base reading. The unsuccessful sequencing was possibly due to low abundance of the 700-bp transcript.

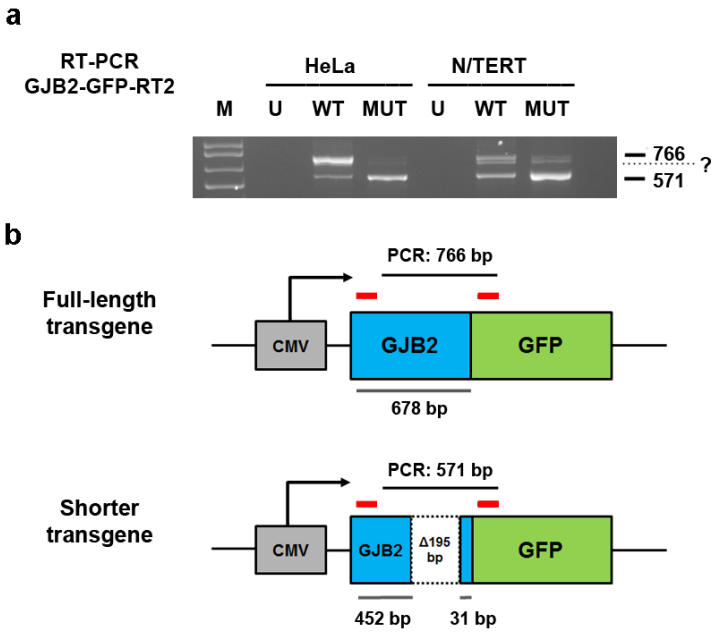

Figure 3.3.4 Identification of two shorter forms of GJB2-GFP transgene in bulk FACS-enriched GFP⁺ HeLa and N/TERT cells

RT-PCR analysis for a 766-bp, transgene-specific region found two additional, shorter forms of amplicons (around 500 and 700 bp in length) in bulk FACS-enriched GFP⁺ HeLa and N/TERT cells expressing wildtype (WT) or mutant (MUT) transgene (a). Sanger sequencing of the band sized around 500 bp identified an in-frame 195-bp deletion within GJB2 cDNA (b). The GFP sequence was intact. Sequencing of the other shorter band (around 700 bp) was unsuccessful. Red boxes in (b) denote binding sites for the PCR primers. M, DNA marker.

This 195-bp deletion within *GJB2* has not been reported elsewhere, nor detected earlier in the native *GJB2* cDNA sequence in control-KCs or KID-KCs **(Section 3.1.4.2, Figure 3.1.5)**. A possible cause of the deletion in the transgene was alternative splicing, which may be attributed to certain lentiviral elements that had potentially affected mRNA processing in the host cells (Cavazzana-Calvo et al., 2010; Heckl et al., 2012).

To test whether a cryptic splice site was present within the exogenous *GJB2-GFP* transgene sequence, the transgene sequence was submitted to the Berkeley Drosophila Genome Project splice site predictor (www.fruitfly.org) (Reese et al., 1997). The start site of the 195-bp deletion, i.e. GT dinucleotide at cDNA positions 453 and 454, was predicted to be a cryptic donor splice site (with a score of 0.95; score range: 0−1), favouring the above hypothesis. Although the alternative splicing issue may be resolved by using codon optimised *GJB2* sequence (Mauro and Chappell, 2014) instead of using native *GJB2* sequence, an alternative step to tackle the issue is isolation of the full-length *GJB2*-expressing HeLa populations from the bulk populations. To achieve that, single cell cloning was carried out from bulk FACS-enriched, GFP^+ wildtype-expressing and mutant-expressing HeLa cells **(see Section 2.12)**. Grown clones were analysed for transgene expression by RT-PCR using the same primers followed by sequencing. The transgene expression at protein level was examined using fluorescence microscopy **(see Section 2.5 and 2.12)**.

A total of 5 wildtype-expressing and 79 mutant-expressing HeLa clones were grown to confluence. RT-PCR analysis detected the full-length 766-bp band in all 5 (100%) wildtype-expressing clones (referred to as W1-W5), of which W4 and W5 also showed the 571-bp band **(Figure 3.3.5a)**. Sequencing of these clones found full-length *GJB2* sequence. In contrast, only 1 of the 79 (1.27%, referred to as M1 clone) mutant-expressing clones showed the 766-bp band, while the others showed only the shorter 571-bp band (**Figure 3.3.5a)**. Sequence analysis of the M1 clone confirmed expression of full-length *GJB2* sequence containing the c.148G>A mutation. There was no remarkable morphological difference between these clonal cells and their parental HeLa cells. Fluorescence microscopic examination of two wildtype (W1 and W3) and two mutant clones (M1 and M2) showed expression of Cx26-GFP fusion protein **(Figure 3.3.5b)**; however, there were distinct expression patterns between those mutant clones. The fusion protein in the M2 clone (expressing shorter transgene) showed cytoplasmic localisation, while the M1 clone (expressing full-length transgene) showed a punctate Cx26-GFP expression pattern, although the above cytoplasmic localisation was observed in a small subset of M1 cells.

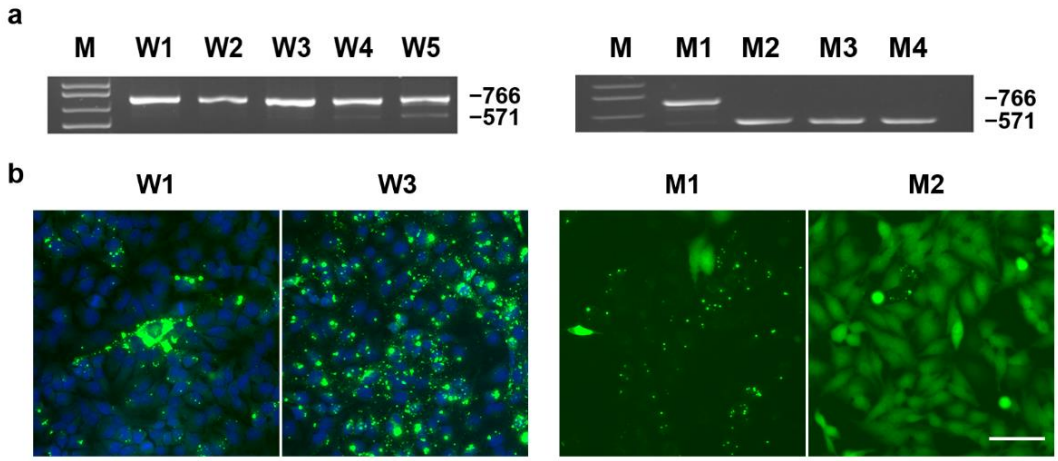

Figure 3.3.5 Expression of Cx26-GFP transgene in clonal HeLa cell lines

Single cell cloning of bulk lentivirally-transduced, FACS-sorted HeLa cells resulted in expansion of 5 wildtype and 79 mutant GJB2-GFP expressing clones. All 5 wildtype clones (W1-W5) and 4 representative mutant clones (M1-M4) were first analysed by RT-PCR for GJB2-GFP expression (a) with 2 clones from each group also examined using fluorescence microscopy for Cx26-GFP expression (b). All 5 wildtype clones (W1-W5) expressed full-length transgene (766-bp), with W4 and W5 clones also expressing weakly the shorter transgene (571-bp) (a, left). Among mutant clones, only the M1 clone expressed full-length transgene, whereas M2, M3, M4 clones expressed the shorter form (a, right). Both W1 and W3 clones showed strong, punctate Cx26-GFP expression (b, left panels). Mutant Cx26-GFP protein in the M2 clone (expressing shorter transgene) showed cytoplasmic localisation, while the majority of M1 clonal cells (expressing full-length transgene) showed a punctate Cx26-GFP expression pattern. Bar = 80μm.

The W1 clone that expressed the full-length wildtype transgene at a moderate level and proliferated at a comparable rate to the parental HeLa cells was selected for subsequent siRNA screening. The M1 clone expressing full-length mutant transgene was also selected. On the other hand, although bulk FACS-enriched GFP^+ N/TERT keratinocytes expressed the wildtype or mutant transgene with the 195-bp deletion, the deletion did not affect the c.148G>A mutation at which the siRNAs were designed to target (see below), and hence these cells were also used for siRNA screening to rule out cell-type specific artefacts. The selected cells are hereafter referred to as HeLa-W1, HeLa-M1, N/TERT-WT and N/TERT-MUT.

3.3.2 Discovery of siRNA S7 that selectively targeted the *GJB2* c.148G>A mutant over wildtype *GJB2*

3.3.2.1 Sequence walk for design of allele-specific siRNAs

The sequence walk method has proven effective in identifying siRNAs capable of discriminating between mutant and wildtype alleles, leading to differential inhibition (Hickerson et al., 2008; Trochet et al., 2015). By using this approach, 19 candidate allele-specific siRNAs, S1-S19, were designed, with each spanning and including the c.148G>A mutation in *GJB2* **(Figure 3.3.6)**. These siRNAs were designed in the standard 19 + 2 format, i.e. a 19-nucleotide (-nt) targeting sequence followed by a deoxythymidine dinucleotide overhang at the 3' end. The latter overhang has been shown to increase nuclease resistance of siRNAs within cells and in culture media (Elbashir et al., 2001a) and included in routine siRNA design. In this study, an irrelevant, non-targeting control siRNA (si-cont, against *hHAS2*), was used as a negative control, and the Silencer® siRNA targeted to *GFP* (si-GFP) was used as a positive control.

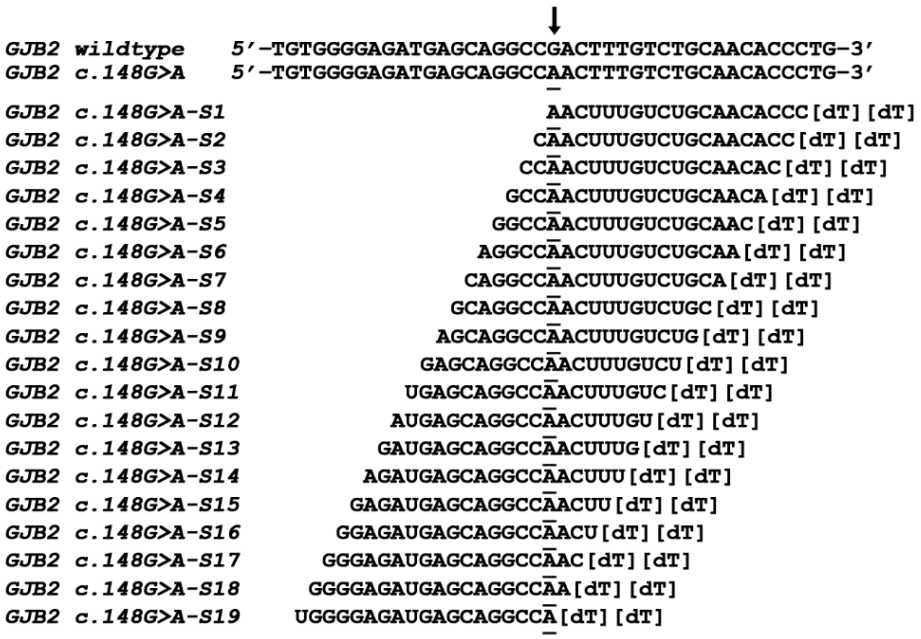

Figure 3.3.6 Sequence walk for design of candidate specific siRNAs

19 siRNAs in 19 + 2 format (19-nt targeting sequence plus a deoxythymidine dinucleotide, or dTdT) were designed using the sequence walk method. This method allowed screening of 19 possible siRNAs that specifically target the single-nucleotide substitution at cDNA position 148 (c.148G>A, arrow) of GJB2. These siRNA are referred to as GJB2 c.148G>A_S1-S19 (or S1-S19 in short form). Wildtype and mutant GJB2 cDNA sequences are shown and aligned with the 19 siRNAs, with the c.148G>A mutation underlined.

3.2.2.2 Optimisation of siRNA transfection

Optimisation of transient siRNA transfection was carried out prior to siRNA screening using si-GFP. Three parameters were optimised to enhance the transfection efficiency, including transfection reagent, concentration of siRNA, and time point for knockdown analysis. Various concentrations of si-GFP, ranging from 0.05, 0.5, 5 to 50 nM, were tested in bulk FACS-enriched GFP^+ HeLa or N/TERT cells expressing wildtype *GJB2-GFP* (HeLa-WT and N/TERT-WT, respectively). siRNA was delivered using either Lipofectamine® 2000 (L2K) or Lipofectamine® RNAiMAX (RNAiMAX) **(see Section 2.14)**. The inhibition of GFP expression by si-GFP was analysed by flow cytometry at 24h and 48h.

si-GFP was shown to inhibit the GFP expression in both HeLa- and N/TERT-WT cells in a dose-dependent manner **(Figure 3.3.7)**. Only mild Cx26-GFP inhibition (about 10%) was observed when cells were treated with 0.05 nM si-GFP. Stronger inhibition was observed as si-GFP concentration was increased. At the highest si-GFP concentration tested, 50 nM, transfection by RNAiMAX exhibited stronger GFP inhibition than that by L2K in both HeLa-WT cells (86% vs 63%) and N/TERT-WT cells (54% vs 42%) at 24h **(Figure 3.3.7a, c)**. Similar inhibitory effects were observed at a further time point of 48h **(Figure 3.3.7b, d)**, suggesting that efficient Cx26-GFP knockdown was achieved as early as 24h post-transfection. Since a lower concentration of siRNA (≤ 50 nM) is generally recommended to avoid potential cytotoxicity or off-target events (Fedorov et al., 2006), si-GFP concentrations higher than 50 nM were not tested. No appreciable cytotoxicity was observed under a light microscope in transfected cells over the period of 48h.

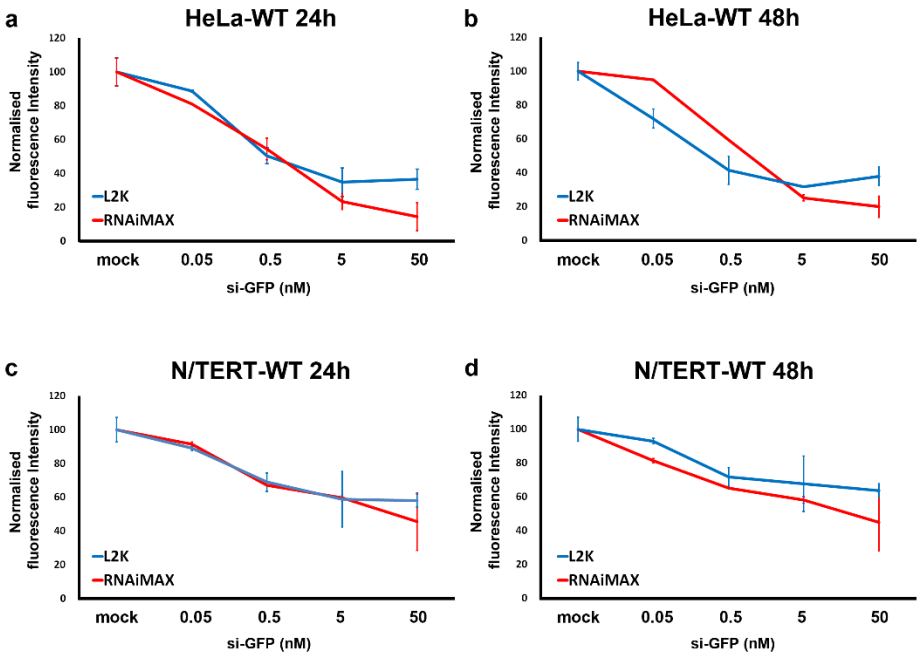

Figure 3.3.7 Optimisation of siRNA transfection using si-GFP

siRNA transfection was optimised on HeLa-WT and N/TERT-WT cells. These cells were transiently transfected in duplicate with different concentrations of a siRNA against GFP (si-GFP) using Lipofectamine® 2000 (L2K, blue) or Lipofectamine® RNAiMAX (RNAiMAX, red). 24h (a, c) or 48h (b, d) post-transfection, cells were analysed by flow cytometry for GFP expression, whose decrease directly correlates to the siRNA knockdown efficiency. Data were normalised to mock control (transfection reagent without siRNA) levels. GFP was inhibited by si-GFP in a dose-dependent manner. At the highest concentration (50 nM), transfection with RNAiMAX induced stronger GFP inhibition than transfection with L2K in both cell lines at 24h and 48h. Data are mean ± SD.

Since the si-GFP concentration of 50 nM delivered with RNAiMAX displayed the most potent inhibition on Cx26-GFP without causing overt cell death, these transfection conditions were used in subsequent siRNA studies. Similarly, the 24h time point was used thereafter, unless otherwise stated.

3.3.2.3 Identification of S7 as a potent and mutation-specific siRNA

Transient transfection of siRNA S1-S19 into HeLa-W1 and HeLa-M1 cells, as well as N/TERT-WT and N/TERT-MUT cells, was performed with the optimised conditions and siRNA-mediated gene knockdown was determined by flow cytometry for Cx26-GFP fusion protein expression 24h post-transfection **(see Section 2.14)**.

Differential inhibition was observed between mutant and wildtype Cx26-GFP in tested cell lines **(Figure 3.3.8)**. Although varying results were observed in several siRNAs between HeLa and N/TERT cells, ten siRNAs demonstrated reproducible inhibitory activity between the two cellular models. The siRNAs can be categorised into three groups based on their targeting specificity: group 1: no effect on wildtype or mutant Cx26, such as S1; group 2: inhibition of both wildtype and mutant Cx26 with poor specificity, such as S3, S6, S12, S13, S15, S16, S19; and group 3: specific inhibition of mutant Cx26 with little effects on wildtype Cx26, such as S7 and S10. The inhibition efficiency of S7 and S10 was approximately 50% for both HeLa-M1 and N/TERT-MUT cells, while these siRNAs did not inhibit the expression of the wildtype protein. These results indicated that S7 and S10 discriminated between the wildtype and mutant *GJB2* sequences. Since S7 showed high reproducibility in terms of specific inhibition of mutant *GJB2* across three independent screenings, this siRNA was selected for further study.

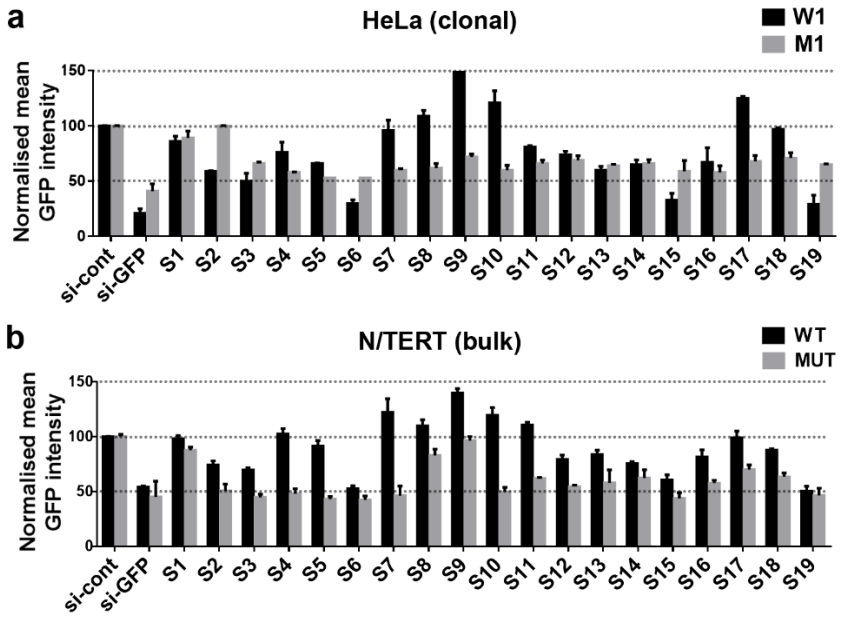

Figure 3.3.8 S7 − the most potent and specific inhibitor for mutant GJB2

Clonal HeLa (a) and bulk N/TERT cells (b) expressing wildtype (W1 and WT) or mutant (M1 and MUT) GJB2-GFP transgene were transiently transfected with each of 19 candidate siRNAs (S1-S19), siRNA against GFP (si-GFP, positive control), or the irrelevant control siRNA (si-cont, negative control). Transfected cells were analysed by flow cytometry for GFP expression. The decrease in GFP intensity represents the inhibition of GJB2 by siRNA. Data were normalised to the si-cont levels. The bar charts show representative results from three independent experiments. S7, the lead siRNA, potently and specifically inhibited the c.148G>A mutant, but did not inhibit the wildtype GJB2. Data are mean ± SEM.

3.3.3 Robust mutation-specificity of S7 confirmed by mRNA and protein expression

The specificity of S7 for mutant *GJB2* was further confirmed by examining the *GJB2* gene expression at mRNA and protein levels in HeLa-W1 and -M1 cells transfected with either S7 or the non-targeting control siRNA. The inhibition of the transgene was assessed by qPCR using the GJB2-GFP-qPCR primers. The GAPDH primers were used as internal calibrator **(Appendix I, Section 2.5)**. At protein level, the efficacy of S7 was examined using flow cytometry for GFP intensity **(see Section 2.14)** and immunoblotting using the antibody 71-0500 against Cx26 **(Appendix II, Section 2.6)**.

The qPCR results showed a reduction in *GJB2-GFP* transcript of 82% in HeLa-M1 cells treated with S7, compared to those treated with control siRNA (0.18 ± 0.03 vs 1.00 ± 0.14, n = 2 independent experiments each group, $p < 0.05$, Student's t-test) **(Figure 3.3.9)**. There was no significant difference in *GJB2-GFP* mRNA between the HeLa-W1 cells treated with either S7 or control siRNA (0.98 ± 0.10 vs 1.00 ± 0.16, n = 2 independent experiments each group, $p > 0.05$, Student's t-test).

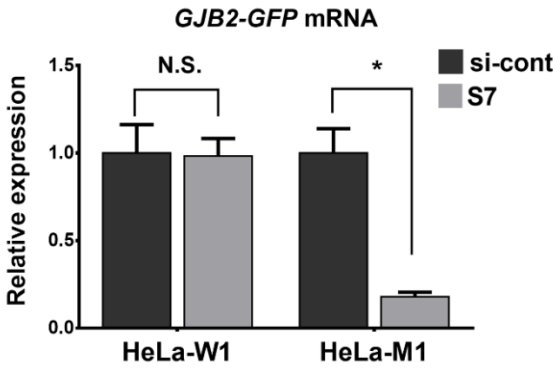

Figure 3.3.9 Potent and specific mutation-targeting of S7 confirmed at mRNA level
*HeLa-W1 and -M1 clones transiently transfected with either control siRNA (si-cont) or S7 was analysed by qPCR 24h post-transection. Transgene-specific primers spanning the GJB2-GFP border were used. GAPDH was used as an internal calibrator. The bar chart shows pooled data from 2 independent experiments with each in triplicate. S7 inhibited the transgene mRNA potently and specifically in HeLa-M1 cells, while leaving the wildtype unaffected. Data are mean ± SEM. *p < 0.05. N.S, not significant.*

Flow cytometry analysis was also performed in siRNA-treated HeLa-W1 and -M1 cells, where the knockdown efficiency in *GJB2* was represented by the decrease of

GFP intensity. The results showed that S7 caused a marked shift in the distribution of GFP^+ HeLa-M1 populations towards the negative GFP gate **(Figure 3.3.10a),** implying robust inhibition of Cx26-GFP expression. This shift was absent in HeLa-M1 cells treated with the control siRNA or HeLa-W1 cells treated with S7 or the control siRNA. Quantification of fluorescence intensity found a significant reduction in Cx26-GFP expression of 51% in HeLa-M1 cells treated with S7 compared to those treated with the control siRNA (0.49 ± 0.06 vs 1.00 ± 0.02, $n = 4$ each group, $p < 0.001$, Student's t-test), consistent with the initial screening results. There was no significant difference in Cx26-GFP expression between HeLa-W1 cells treated with either S7 or control siRNA (0.97 ± 0.06 vs 0.93 ± 0.07, $n = 4$ each, $p > 0.05$, Student's t-test).

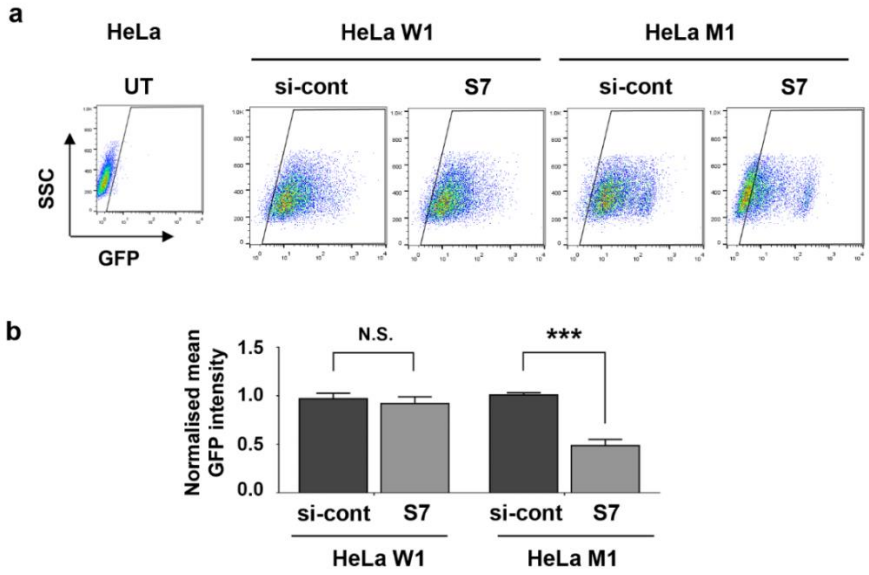

Figure 3.3.10 Potent and specific mutation-targeting of S7 confirmed by flow cytometry
*Clonal HeLa cells expressing wildtype (HeLa-W1) or mutant GJB2-GFP (HeLa-M1) transfected with either S7 or the control siRNA (si-cont) were analysed by flow cytometry for GFP expression. Non-transduced (UT) HeLa cells were used as a gating control. Prior to siRNA transfection, approximately 90% untreated W1 and untreated M1 cells were GFP^+. Treatment with S7 caused a left shift of GFP^+ HeLa-M1 cells towards negative GFP gate (a) and this shift was not seen in HeLa-W1 cells. Quantification of GFP intensity (b) showed 51% reduced GFP expression in the M1 cells treated with S7, compared to that in those treated with si-cont. The bar chart is pooled data from four independent experiments. Data are mean ± SEM. ***p <0.001. N.S, not significant.*

The results of Cx26 immunoblotting showed that, in both HeLa-W1 and -M1 cells, the target band was detected at approximately 53 kDa, a size corresponding to the fusion of Cx26 (26 kDa) and GFP (27 kDa), consistent with a previous report (Di et al., 2005).

The 53-kDa band was not seen in parental HeLa cells. There was a clear reduction in the target band intensity in HeLa-M1 cells treated with S7 compared to those transfected with the control siRNA **(Figure 3.3.11a)**. Densitometric analysis confirmed that the reduction was 81.33% (n = 3 independent experiments) **(Figure 3.3.11b**). A minor reduction of 12.33% in Cx26 expression level was also found in HeLa-W1 treated with S7 compared to those treated with control siRNA (n = 3 independent experiments); however, the reduction may have resulted from experimental artefact as such reduction in the wildtype expression was not detected by other assays. Future work will be required to verify this observation.

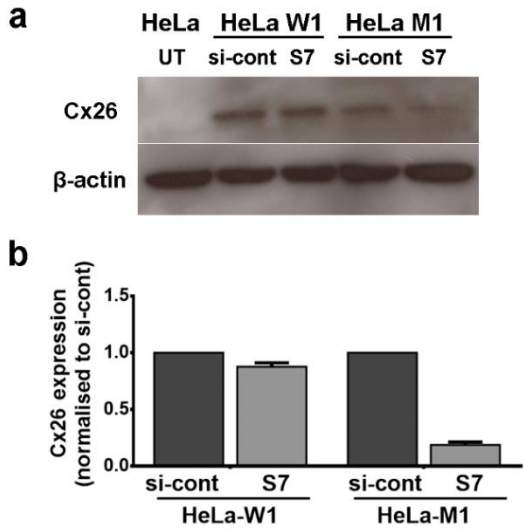

Figure 3.3.11 Potent and specific mutation-targeting of S7 confirmed by immunoblotting *HeLa-W1 or -M1 transfected with S7 or the control siRNA (si-cont) were analysed by immunoblotting for Cx26 expression. β-actin was used as a loading control. The target band was found in all samples except for non-transduced HeLa cells (HeLa UT). Data were normalised to the respective si-cont levels. A marked decrease in the band intensity was found in S7-treated HeLa-M1 cells relative to that in si-cont-treated HeLa-M1 cells (a), which by densitometric analysis was found to be 81%. There was mild difference in band intensity between HeLa-W1 cells treated with either of siRNAs. The bar chart is pooled data from three independent experiments. Data are mean ± SEM.*

The duration of silencing effect of S7 was further evaluated in S7-treated N/TERT-MUT keratinocytes at 24 h, 48 h and 72 h post-transfection using qPCR analysis for transgene expression. The GJB2-GFP-qPCR primers were used for detection of the transgene while avoiding detection of the endogenous *GJB2* expression in N/TERT keratinocytes. GAPDH primers were used as internal calibrator **(Appendix I, Section 2.5)**.

The levels of mutant transgene inhibition by S7 were 59.80 ± 2.68% ($p < 0.001$, n = 3) at 24h, 53.76 ± 3.82% at 48h ($p < 0.01$, n = 3) and 43.14 ± 4.08% at 72h post-transfection ($p < 0.01$, n = 3), compared to untreated cells harvested at the respective time points **(Figure 3.3.12)**. These findings suggested that the S7-mediated inhibition of mutant *GJB2* could last at least 72 h from the time of initial treatment in keratinocytes *in vitro*.

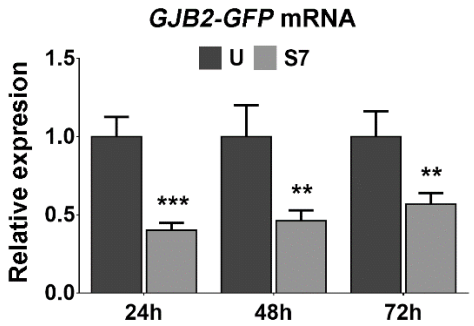

Figure 3.3.12 Duration of gene silencing action of S7 in keratinocytes
*N/TERT-MUT cells were transiently transfected, or not transfected (U), with S7 and the expression of GJB2-GFP transgene at different time points up to 72h was measured by qPCR. The bar chart shows pooled transgene expression data from three independent experiments. The results showed that the gene silencing efficiency of S7 at 24 h, 48 h and 72 h were 60%, 54% and 43%, respectively. Data are mean ± SEM. **p <0.01 or ***p <0.001.*

3.3.4 Section summary

In this section, two exogenous expression systems, HeLa and N/TERT, stably expressing the wildtype or mutant *GJB2-GFP* fusion transgene were established. By using these systems, S7, the potent siRNA against the commonest mutation linked to KID syndrome, was identified and its robust inhibitory effect on the mutant was confirmed at mRNA and protein levels, with a duration of at least 72 h. Strikingly, S7 did not inhibit the wildtype sequence which differed from the mutant sequence by a single base, nor cause appreciable loss of cell viability in the tested skin and non-skin models. This provides a sound context for further functional testing in cells treated with this siRNA.

3.4 S7 reversed aberrant Cx26 channel function in KID-KCs

S7 has been shown to specifically inhibit *GJB2 mRNA with c.148G>A* mutation, leading to efficient knockdown of the mutant Cx26 protein. The Cx26 subunit forms gap junction channels and hemichannels which mediate the communication between neighbouring cells, or between the cytoplasm and extracellular space, by the passage of ions and small molecules. Previous studies showed that the c.148G>A mutation in *GJB2* affected both hemichannel and gap junctional channel functions. Specifically, the mutation causes enhanced hemichannel activity and impaired GJIC, as shown by measurement of the electrical conductance (Lee et al., 2009; Lopez et al., 2013; Sanchez et al., 2013; Xu et al., 2017), Ca^{2+} influx (Terrinoni et al., 2010) and ATP release (Donnelly et al., 2012; Garcia et al., 2015). However, those functional studies used exogenous expression systems, such as transfected HeLa cells, which had limited ability to model the heterozygous state of *GJB2* mutations in KID syndrome. Thus, KID-KCs, which expressed heterozygous c.148G>A endogenously, were used for evaluating Cx26 channel function. This was followed by treatment with the mutation-specific S7, and subsequent measurement of the change in channel function.

3.4.1 S7 selectively inhibited mutant *GJB2* allele in KID-KCs

KID-KCs and control-KCs were treated with S7 or the non-targeting control siRNA at 50 nM. Twenty-four hours post-treatment, the endogenous *GJB2* mRNA and Cx26 protein expression was examined by qPCR using the GJB2-endo-full primers spanning full-length endogenous *GJB2* cDNA **(Appendix I, Section 2.5)** and immunoprecipitation using the IP^2/IB^2 approach **(Section 2.6 and Section 3.1.4.3)**.

No significant loss of viability in the treated cells was observed by light microscopy, suggesting that the siRNAs had no cytotoxicity *in vitro*. The qPCR results showed a significant reduction in total *GJB2* mRNA of 41% in KID-KCs treated with S7, compared to those treated with the control siRNA (0.59 ± 0.04 vs 1.00 ± 0.06, $n = 3$, $p < 0.01$, Student's t-test) **(Figure 3.4.1)**. In the control-KCs treated with S7, there was slightly increased mRNA expression compared to cells treated with the control siRNA, but the increase was not statistically significant (1.18 ± 0.10 vs 1.00 ± 0.10, $n = 3$, $p = 0.26$, Student's t-test). As the specificity of S7 for mutant *GJB2* mRNA (instead of

wildtype *GJB2* mRNA) has been confirmed in **Section 3.3**, the observation of 41% inhibition here indicated that the mutant allele in KID-KCs was potently suppressed by S7.

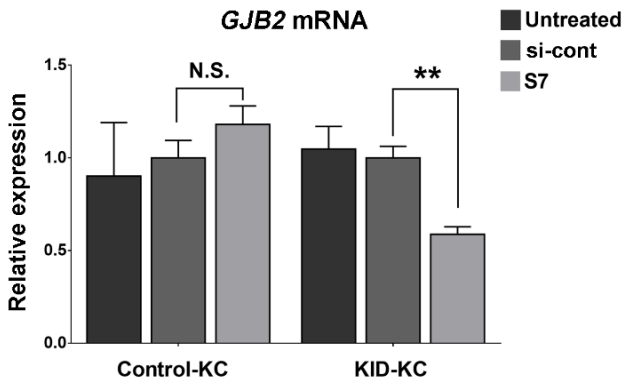

Figure 3.4.1 S7 selectively inhibited mutant GJB2 allele in KID-KCs
*The expression of GJB2 mRNA in KID- or control-KCs treated, or not treated, with S7 or the control siRNA (si-cont) were measured by qPCR using primers spanning full-length GJB2 cDNA. There was a significant reduction in total GJB2 mRNA expression in KID-KCs treated with S7 compared to those treated with si-cont, whereas no reduction was detected in control-KCs. The bar chat shows pooled data from three independent experiments. Data are mean ± SEM. **p < 0.01; N.S, not significant.*

The expression of Cx26 protein in KID-KCs and control-KCs was further examined by immunoprecipitation and immunoblotting. The results revealed an average decrease of 56% (range 52−64%, n = 3) in endogenous Cx26 protein expression in KID-KCs treated with S7, compared to those treated with the control siRNA **(Figure 3.4.2)**. In contrast, there was a mild increase of 11% (range 5−16%, n = 3) in Cx26 expression in control-KCs treated with S7, compared to those treated with control siRNA. This experiment was repeated three times and the results were consistent. These results indicated that S7 had strong selectivity for the mutant *GJB2* c.148G>A allele over the wildtype *GJB2* allele of the KID-KCs, which was confirmed at mRNA and protein levels.

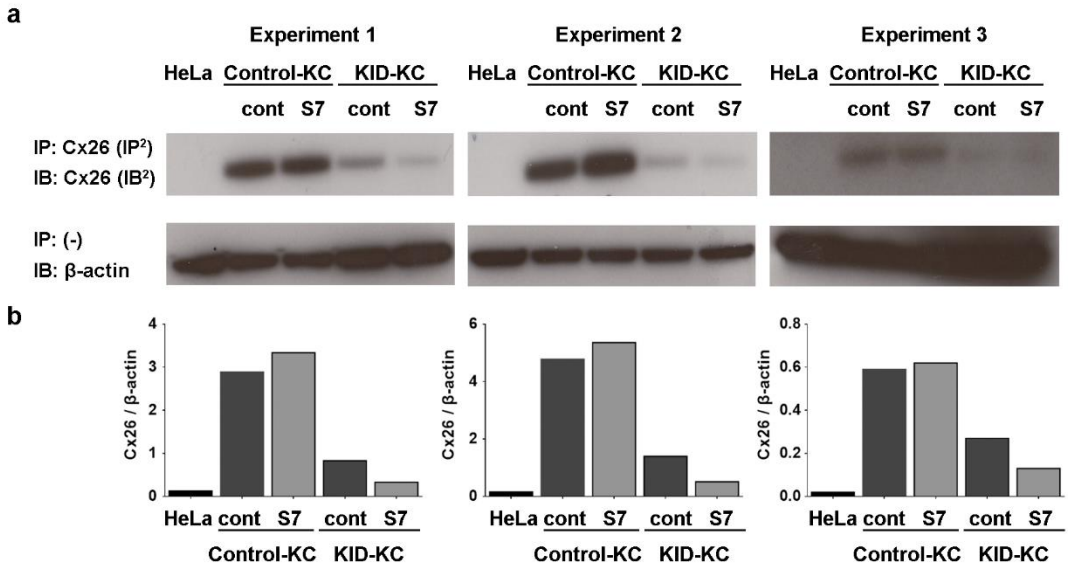

Figure 3.4.2 Selective inhibition of mutant GJB2 allele by S7 confirmed at protein level
The total proteins in KID-KCs or control-KCs treated with S7 or the control siRNA (cont) were immunoprecipitated for Cx26 and then measured for Cx26 expression using the IP^2/IB^2 approach ***(see Section 2.6)****. β-actin was used as loading control. Non-transduced HeLa cells (HeLa) were used as negative control. Results from three independent experiments are shown (a). The bar charts show expression level of Cx26, calculated as the Cx26/β-actin ratio, from individual blots (b). There was a 56% reduction in Cx26 expression in KID-KCs treated with S7, compared to those treated with control siRNA. There was only a mild difference in Cx26 expression in control-KCs treated with either of the siRNAs.*

3.4.2 Aberrant hemichannel and gap junction functions in KID-KCs were corrected following S7 treatment

The function of Cx26 in KID-KCs was further assessed by patch clamp **(Section 2.15)** and dye uptake for hemichannel activity **(Section 2.16)**, and the SLDT assay for GJIC **(Section 2.9)**.

3.4.2.1 Patch clamp revealed hyperactive hemichannels in KID-KCs, which were corrected by S7 treatment

Patch clamp is the most sensitive and quantitative electrophysiological technique to detect functional gap junction channels that conduct electrical signals (Abbaci et al., 2008). This technique permits recording of whole-cell or single-channel currents passing across the plasma membranes through the channels. The former recording

configuration enables studies of electrical behaviour of the entire cell in response to experimental conditions, e.g. membrane voltage and Ca^{2+} concentration which are known to regulate activity of hemichannels formed by Cx26 (Bargiello et al., 2012). Therefore, the whole-cell recording was chosen as the starting functional assay for Cx26. In general, this method requires an electrolyte-filled glass pipette, which is placed in contact with a small patch of plasma membrane of a chosen cell. This is followed by the application of gentle suction to establish a high-resistant (gigaohm, GΩ) seal between the pipette and the patch of membrane, a critical step that significantly reduces the experimental noises. The patch of membrane is then ruptured by application of further suction, allowing the detection of whole-cell membrane currents. The zero-Ca^{2+} recording condition for Cx26 hemichannels in keratinocytes have been published previously (Levit et al., 2015) and the recorded membrane currents under this condition represent the hemichannel activity. Solitary KID- and control-KCs, with no contribution of gap junction intercellular channels, were analysed for hemichannel activity by the above condition **(Section 2.15)**.

KID-KCs and control-KCs were clamped at 0 mV and then stepped from -110 mV to +110 mV in 20 mV increments and the membrane currents were measured **(Figure 3.4.3a)**. Moderate membrane currents were recorded from control-KCs at both depolarising and hyperpolarising membrane voltages **(Figure 3.4.3b)**. In contrast, markedly larger currents were elicited from KID-KCs, more prominently at depolarising voltages **(Figure 3.4.3b)**. The current density-voltage plot showed larger current densities in KID-KCs at all tested voltages ranging from -110 mV to +110 mV in comparison to those in control-KCs, with a statistical significance found between +30 mV and +110 mV **(Figure 3.4.3c)**. The maximum current density recorded from KID-KCs was 80% greater than that in control-KCs (9.0 ± 1.3 pA/pF, n = 21 cells vs 5.0 ± 0.6 pA/pF, n = 14 cells, measured at +110 mV, $p < 0.05$, Student's t-test). The increase of whole-cell currents suggested that the heterozygous c.148G>A mutation conferred an aberrant electrical property to the KID-KCs.

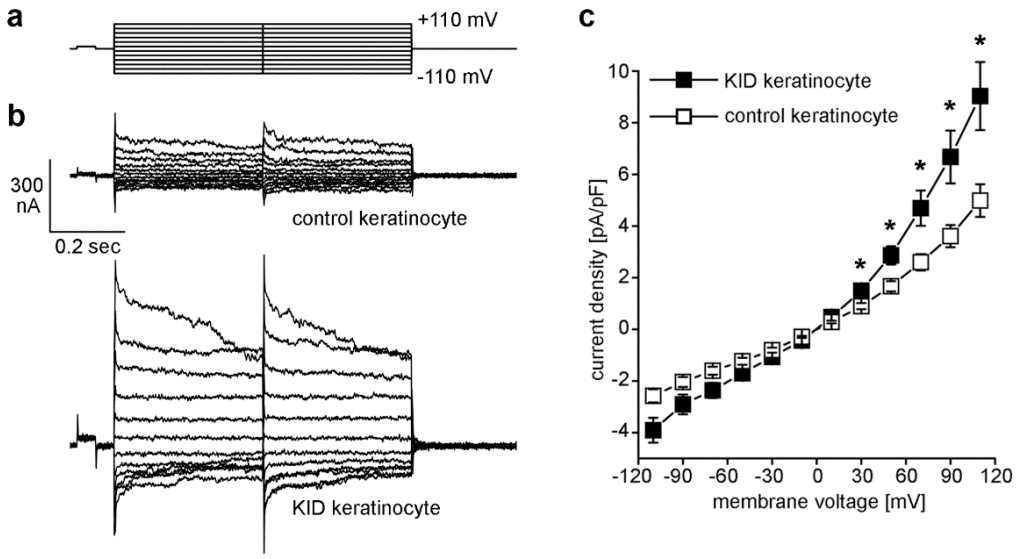

Figure 3.4.3 Increased whole-cell membrane currents in KID-KCs

Whole-cell membrane currents were recorded from solitary KID- or control-KCs using whole-cell patch clamp analysis with a voltage step protocol from -110 mV to +110 mV in 20 mV increments (a). Modest currents were recorded from control-KCs (b, top) and large currents were recorded from KID-KCs (b, bottom). Current density plotted against membrane voltage showed greater whole-cell current density elicited from the KID-KCs (n = 21 cells) compared to the control-KCs (n = 14 cells) (c). Comparison was made at individual membrane voltages. Asterisks represent $p < 0.05$ in current density between two cell lines at the same membrane voltage.

KID-KCs and Control-KCs were then treated with S7 or the control siRNA, and the membrane currents were measured using the same patch clamp parameters described above. When treated with the control siRNA, KID-KCs showed approximately 50% larger whole-cell membrane current density compared to the control-KCs at all depolarising membrane voltages tested (n = 20 cells and 10 cells, respectively) **(Figure 3.4.4b-d)**. This is in line with the records from their untreated counterparts, suggesting little effects of the control siRNA on the whole-cell currents. In contrast to control siRNA, the allele-specific siRNA, S7, demonstrated robust suppression in membrane currents recorded from KID-KCs across all voltages tested, but it had negligible effects on membrane currents from control cells **(Figure 3.4.4b-d)**, confirming the allele-specific action of S7. Statistical analysis of current density at the maximum tested voltage revealed a significant reduction of 35% in KID-KCs treated with S7 in comparison to those treated with control siRNA (9.02 ± 1.16 pA/pF, n = 20 cells vs 5.86 ± 0.43 pA/pF, n = 22 cells, measured at +110 mV, $p < 0.05$, Student's t-test)

(Figure 3.4.4d). No difference was found in the membrane current density between control-KCs treated with S7 or control siRNA at any tested voltage (n =10 cells each group, $p > 0.05$, Student's t-test). Notably, the membrane current densities recorded from S7-treated KID-KCs were comparable to those recorded from the control-KCs **(Figure 3.4.4d)**, indicating that potent suppression of the c.148G>A mutation by S7 corrected the aberrant electrical behaviour of KID-KCs.

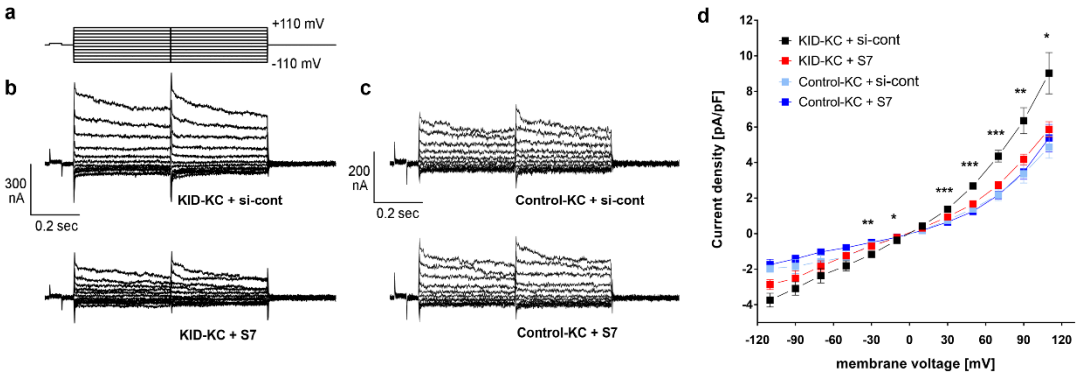

Figure 3.4.4 S7 suppressed aberrantly enhanced whole-cell currents in KID-KCs

*KID- or control-KCs were treated with S7 or control siRNA (si-cont) and whole-cell patch clamp was performed using a voltage step protocol from -110 to +110 mV in 20 mV increments (a). Representative membrane currents records from KID-KCs (b) and control-KCs (c), along with the plot of current density against membrane voltage, are shown (d). Comparison was made at individual membrane voltages. Larger current densities were found in KID-KCs treated with si-cont at all tested voltages (black, n = 20), which were suppressed by S7 (red, n = 22) with statistical significances found between -30 mV and +110 mV. In contrast, no difference in current density was detected between control-KCs treated with S7 (dark blue) or control siRNA (light blue, n = 10 each). Data are mean ± SEM. *p <0.05, **p < 0.01, ***p < 0.001.*

3.4.2.2 Dye uptake assay confirmed the reversal of aberrant hemichannel activity by S7

Dye uptake is a simple and widely-used permeability assay for hemichannel assessment, in which the cellular uptake of small molecular tracers under the ~1-kDa size limit through open hemichannels is measured. These tracers do not enter cells with intact plasma membranes but enter through open hemichannels. Commonly used tracers are Lucifer Yellow (Polusani et al., 2016; Xu et al., 2017), propidium iodide (Press et al., 2017b; Stong et al., 2006), and non-fluorescent tracer, neurobiotin (Aypek et al., 2016; Mese et al., 2011). As neurobiotin with a positive charge appeared to be

more permeant through homotypic Cx26 channels than anionic tracers such as Lucifer Yellow (Kanaporis et al., 2011; Yum et al., 2007), this tracer was chosen to evaluate its uptake by the keratinocytes.

KID-KCs and control-KCs were incubated for 10 min with neurobiotin diluted in a Ca^{2+}-free buffer **(see Section 2.16)**, and then fixed and stained with Alexa Fluor 568-streptavidin to visualise neurobiotin signals using a fluorescence microscope.

The results showed a lower level of neurobiotin uptake by the control-KCs, whereas there was a much higher level of neurobiotin uptake in the cytoplasm of KID-KCs **(Figure 3.4.5)**. Quantification of images revealed a 40% increase of neurobiotin uptake by KID-KCs compared to that by the control-KCs (1.40 ± 0.10, n = 29 cells vs 1.00 ± 0.04, n = 34 cells, $p < 0.001$, Student's t-test). These findings suggest that hemichannels formed in KID-KCs had elevated permeability, indicating hyperactive hemichannels.

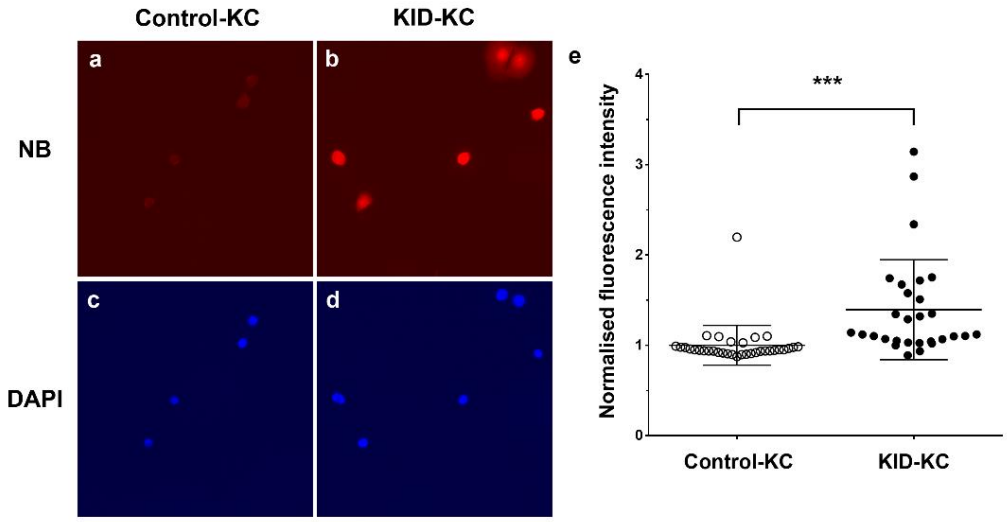

Figure 3.4.5 Increased neurobiotin uptake by KID-KCs

*Solitary KID- (b) and control-KCs (a) were analysed for hemichannel permeability by neurobiotin (NB) uptake assay. NB was diluted in zero-Ca^{2+} buffer to open hemichannels and signals of NB were visualised with Alexa Fluor 568-streptavidin (red, a, b). DAPI was used to show the seeding density (blue, c, d). Representative NB uptake images (a, b) and the result of quantification of the images (e) are shown. There was a marked enhanced dye uptake by KID-KCs (n = 29 cells) compared to that by control-KCs (n = 34 cells). Data are the mean ± SEM. Each dot represents the NB uptake level of a single cell. ***p < 0.001.*

KID-KCs and control-KCs were then treated with the control siRNA and S7. Treatment with the control siRNA did not alter neurobiotin uptake in these keratinocytes, but treatment with S7 selectively inhibited neurobiotin uptake in KID-KCs **(Figure 3.4.6a-d)**. Quantification of the images showed significantly decreased neurobiotin uptake in S7-treated KID-KCs compared to those treated with control siRNA (1.01 ± 0.15, n = 21 images vs 1.31 ± 0.30, n = 27 images, $p < 0.001$, Student's t-test) **(Figure 3.4.6c, d, i)**. No difference was seen between neurobiotin uptake by control-KCs treated with either of the siRNAs (n = 18 images each, $p > 0.05$). Three independent experiments were performed and the results were consistent.

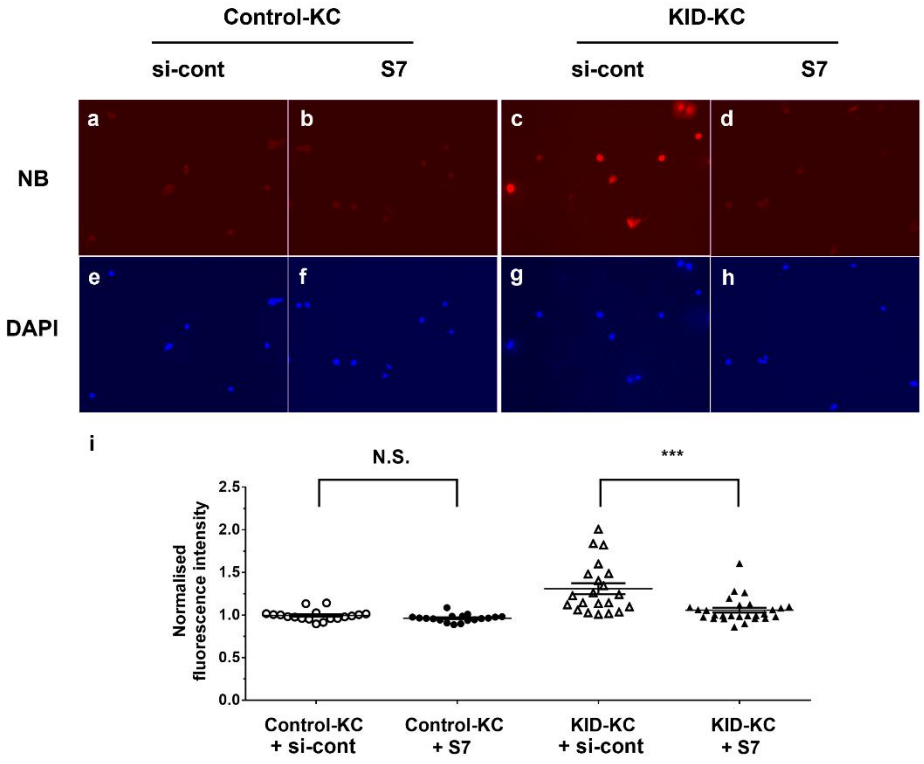

Figure 3.4.6 S7 inhibited the abnormally enhanced neurobiotin uptake by KID-KCs
*Solitary KID- and control-KCs treated with S7 or control siRNA (si-cont) were analysed for hemichannel permeability by neurobiotin (NB) uptake assay. NB was diluted in a zero-Ca^{2+} buffer to open hemichannels and signals of NB uptake were visualised with Alexa Fluor 568-streptavidin (red, a-d). DAPI was used to show the seeding density (blue, e-h). Representative dye uptake images (a-d) and the result of quantification of the images (i) are shown. There was a significantly reduced NB uptake by KID-KCs treated with S7 (n = 21 images) compared to those treated with si-cont (n = 27 images), while the reduction was not observed in control-KCs (n = 18 images). Data are mean ± SEM. Each dot represents the average NB uptake level from a single image taken from each of three independent experiments. ***p < 0.001. N.S. not significant.*

These findings indicate that, in addition to inhibiting the conductance of electrical signals, S7 also corrected the aberrantly enhanced permeability in KID-KCs. These results were consistent with the patch clamp results.

3.4.2.3 S7 treatment restored gap junction intercellular communication in KID-KCs

GJIC in KID- and control-KCs was measured using the SLDT assay. In addition to using the negatively-charged Cascade Blue as a tracer (Marziano et al., 2003), the positively-charged neurobiotin was also used. Confluent cultures of KID-KCs and control-KCs were scrape-loaded with either Cascade Blue or neurobiotin, and then incubated to allow dye transfer **(see Section 2.9.1)**. Cells were fixed and images were recorded using a fluorescence microscope.

In control-KCs, both Cascade Blue and neurobiotin tracers diffused from the initially scrape-loaded cells to the neighbouring cells, with neurobiotin diffusing more extensively **(Figure 3.4.7a, f)**, indicating the presence of functional gap junction channels. In contrast, the diffusion of both tracers decreased markedly in KID-KCs **(Figure 3.4.7b, g)**, particularly that for Cascade Blue, which was almost confined to the first line of the scrape-wounded cells. Negative control cells without scrape-wounding (unwounded) showed little or no dye uptake **(Figure 3.4.7c-d, h-i)**, although slightly enhanced uptake of neurobiotin by KID-KCs was seen compared to that by control-KCs. Quantification of the images after thresholding out unwounded background signals **(see Section 2.9.2)** revealed a reduction of 75% for Cascade Blue transfer and of 58% for neurobiotin transfer in KID-KCs, compared to the levels in control-KCs (for Cascade Blue: 0.25 ± 0.01, vs 1.00 ± 0.25, n = 2, p = 0.09; for neurobiotin: 0.42 ± 0.03, n = 3 vs 1.00 ± 0.10, n = 2, $p < 0.01$, Student's t-test) **(Figure 3.4.7e, j)**.

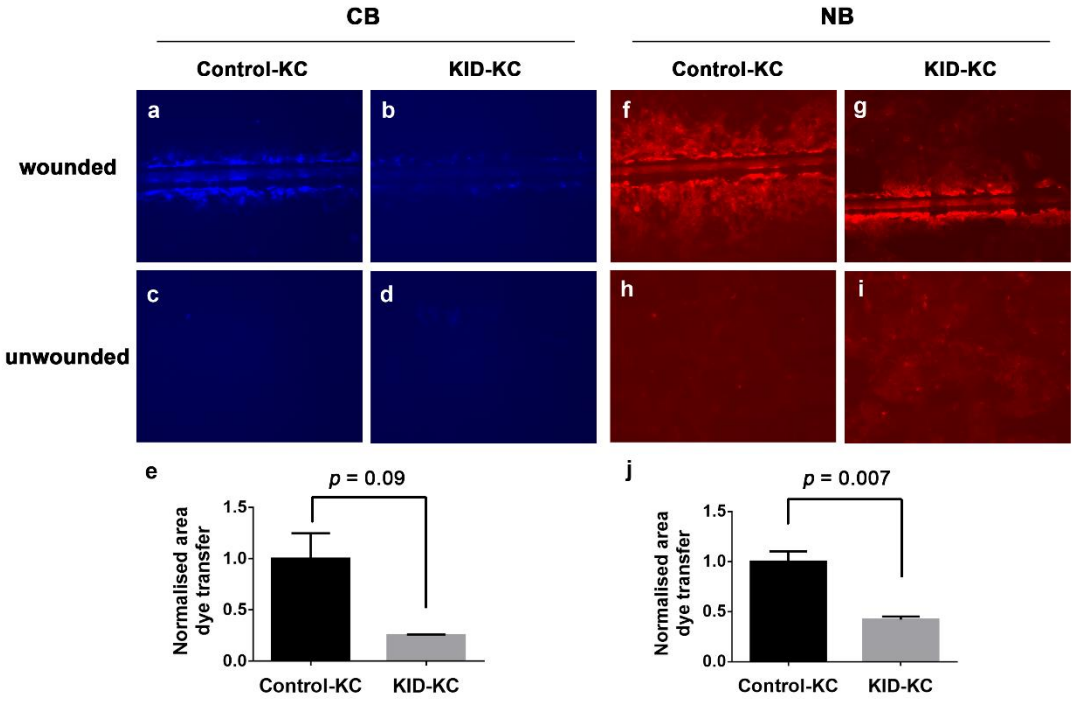

Figure 3.4.7 Impaired gap junction intercellular communication in KID-KCs

The scrape-loading dye transfer assay was performed to assess dye coupling through gap junction channels formed by KID- or control-KCs. Both anionic tracer, Cascade Blue (CB, blue), and cationic tracer, neurobiotin (NB, red), were used. Representative images of transfer of CB (a-b) and NB (f-g) from the primarily-loaded cells along the scrape are shown. The uptake of the tracers by unwounded cells is also shown to indicate background level (c-d, h-i). The total area under the regions of positive transfer of CB (e) or NB (j) was quantified by ImageJ. The results showed markedly reduced transfer of both dyes with statistical significance found in NB. Data were normalised to the level of control-KCs from 2-3 images in a single experiment. Each bar represents the mean ± SEM.

KID-KCs and control-KCs were subsequently treated with control siRNA or S7, and intercellular transfer of neurobiotin was measured using the same SLDT settings. When treated with control siRNA, KID-KCs displayed markedly reduced neurobiotin transfer compared to control-KCs **(Figure 3.4.8a, c)**, resembling that observed in untreated cells. In contrast, treatment with S7 enhanced neurobiotin transfer in KID-KCs **(Figure 3.4.8d)**. Quantification of the images showed significant improvement in neurobiotin transfer of 24% in KID-KCs treated with S7, compared to those treated with the control siRNA (1.24 ± 0.03, n = 34 images vs 1.00 ± 0.02, n = 37 images, $p <$ 0.01, Student's t-test) **(Figure 3.4.8f)**. There was no statistical difference in neurobiotin transfer between control-KCs treated with either S7 or control siRNA (1.00 ± 0.03, n = 30 images vs 1.00 ± 0.03, n = 35 images, $p >$ 0.05, Student's t-test)

(Figure 3.4.8e). These results suggest that S7 restored the function of gap junction channels formed by KID-KCs.

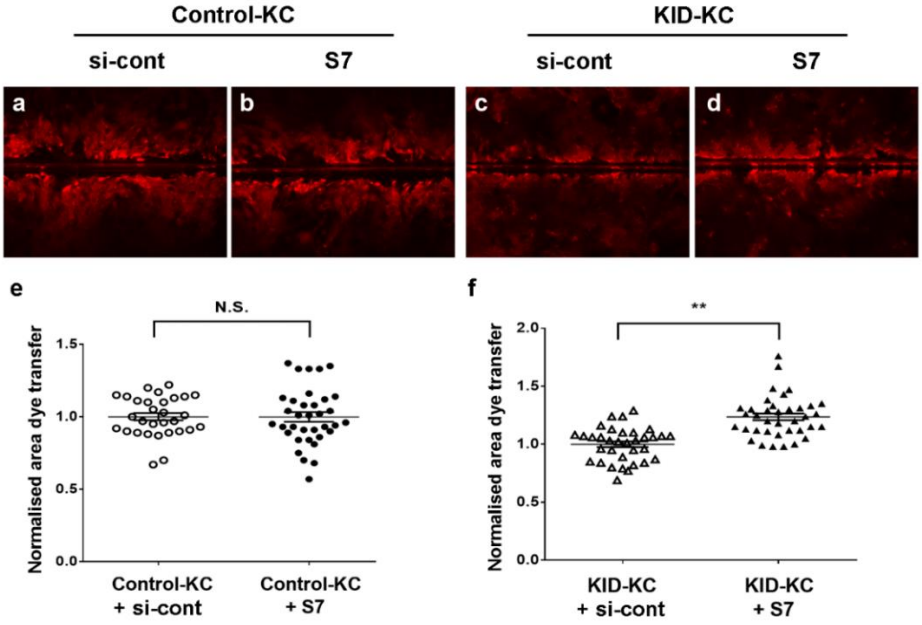

Figure 3.4.8 S7 restored gap junction coupling between KID-KCs

*The scrape-loading dye transfer assay was performed to assess diffusion of neurobiotin (red) via gap junction intercellular channels between KID-KCs or control-KCs following treatment with S7 or control siRNA (si-cont). Representative images of neurobiotin transfer (a-d) from the primarily-loaded cells along the scrape are shown. Quantification of the images showed that S7 restored dye coupling in KID-KCs, but it had negligible effects on control-KCs. The dot plots represent pooled data from three independent experiments and each symbol represents average dye transfer from a single image. Data are mean ± SEM. **p < 0.01. N.S, not significant.*

3.4.3 Section summary

This is the first functional characterisation of keratinocytes derived from a KID syndrome patient. The data show that the presence of the heterozygous mutation c.148G>A in *GJB2* was sufficient to induce an aberrant functional channel behaviour in patient keratinocytes, including enhanced hemichannel activity and defective GJIC. Subsequent treatment with S7, the potent and specific inhibitor of the *GJB2* c.148G>A mutation, successfully corrected the aberrant channel function in patient keratinocytes without altering the channel function in normal keratinocytes. These findings provide an important proof-of-concept that the allele-specific siRNA approach can be a potentially effective treatment for KID syndrome.

3.5 RNA-Seq confirmed allele-specific targeting of S7 with few off-target effects in KID-KCs

While S7 has shown therapeutic potential by inhibiting the mutant *GJB2* allele expression and reversing the aberrant Cx26 channel function in KID-KCs, two key issues needed to be addressed are i) whether the effectiveness and specificity of S7 could be confirmed at mRNA level by a second method (allele-specific on-target effects), and ii) whether there were off-target effects in other regions of the transcriptome. In the last decade, RNA-sequencing (RNA-Seq) has become a key technology to study the transcriptome of cells. This technique harnesses high-throughput sequencing to obtain genome-wide expression profiles from samples, followed by bioinformatics analysis to identify unprecedented gene expression details in relation to the experimental condition (Wang et al., 2009).

In addition, the possibility of gathering preliminary data on the downstream changes (e.g. signalling pathways or molecular interactions) of the on-target and off-target effects was considered a useful by-product of using this technique, although the experiment was not designed specifically for this purpose. These data would therefore be gathered as a basis for future work.

KID-KCs were treated in triplicate with 50 nM S7 **(see Section 2.14)**. Untreated KID-KCs, also in triplicate, were run in parallel as control. Twenty-four hours post-treatment, total RNA was extracted from the cells and subject to RNA-Seq experiments **(see Section 2.17)**.

3.5.1 Generation of RNA-Seq data with high reliability

The integrity of total RNA samples extracted from the cells was examined using the Agilent Bioanalyser. The results showed that RNA integrity numbers (RINs), the index for RNA integrity, were between 9.8 and 9.9 across all six samples, indicating highly-intact RNA samples with little signs of degradation **(Figure 3.5.1a)**. Each of the total RNA samples was enriched for mRNA using poly-T beads, which were then used for cDNA library preparation. All six libraries were subject to high-throughput sequencing, which yielded an average of 73.5 ± 7.6 million of 43-bp reads, totalling approximately

three Giga-bases of cDNA sequence per library. Sequence reads from each library were evaluated for quality using FastQC software, which showed high read quality across all bases at each sequenced position in all libraries **(Figure 3.5.1b)**. There was no contamination of adapter sequences.

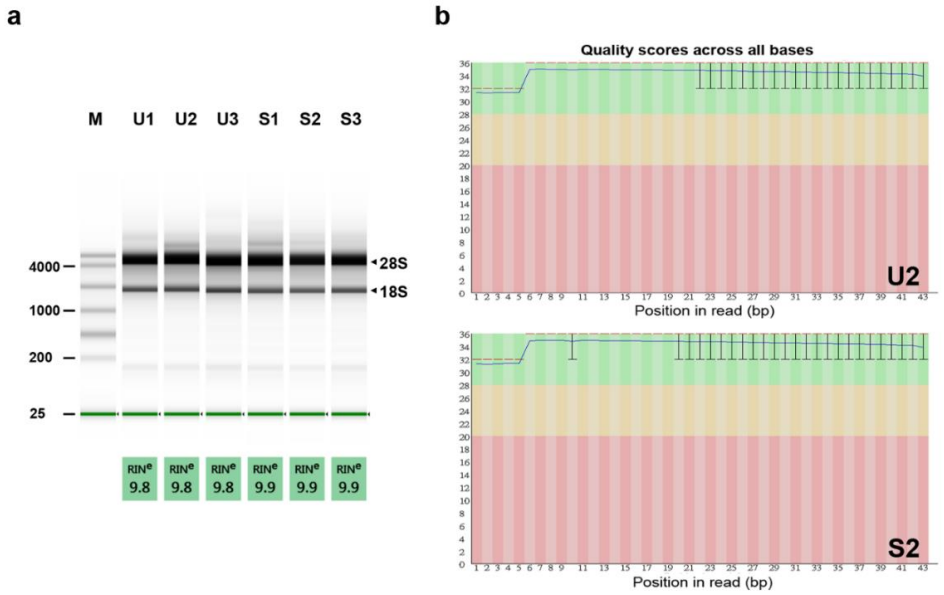

Figure 3.5.1 Quality control for intact RNA samples and sequence data generated from high-throughput sequencing

Prior to sequencing, the RNA integrity was first analysed by an Agilent Bioanalyser (a). The first lane shows RNA ladder, followed by six total RNA samples extracted from KID-KCs untreated (U1-U3) or treated with S7 (S1-S3). The RNA integrity number (RIN, range: 1-10, with 10 being the most intact and 1 being the most degraded) was determined by the presence or absence of degraded products from the entire electrophoretic trace of RNA samples. After sequencing, FastQC analysis was performed on the sequence data at each base along the 43-bp length of reads. A representative result from each group is shown (U2 and S2). The x axis shows the position in read (in bp) and the y axis shows the quality score. Quality scores over 28 (green zone) are considered good quality calls. The blue lines represent the mean score and the whiskers represent 10% and 90% points.

Raw sequence reads were mapped to the latest human reference genome (UCSC Genome Browser assembly ID: hg38). Approximately 15 million reads out of total 75 million reads per library were mapped to 26485 genes, among which 6818 genes (25.74%) had null read counts and were excluded from further analysis, leaving 19667 remainders to be further analysed. The sequence reads mapped to the *GJB2* c.148 locus were first examined to confirm the on-target effect of S7. Subsequently, the 19667 genes were normalised using the DESeq2 package on R software to take into account the sample variations introduced by the experimental steps, and then subject to

differential expression analysis to identify genes whose expression level differed in S7-treated cells from untreated cells (referred to as differentially expressed genes, or DEGs). As this analysis employed multiple statistical testing, a process known to result in increased false positive rates (Love et al., 2015), two steps were taken to control for this issue. First, genes with negligible expression levels (counts < 10) were removed to reduce sampling errors, leaving 10683 genes on the dataset. Second, each *p*-value given by multiple testing was corrected using the Benjamini-Hochberg method (Benjamini et al., 2001; Love et al., 2015), which generated an adjusted *p*-value (p-adj). The dataset was filtered with a widely used threshold, i.e. p-adj < 0.05 and fold change ≥ 2 (Huang et al., 2017b; Rath et al., 2017; Speranza et al., 2017; Zhang et al., 2015b). Genes that had passed the filter were considered as DEGs, which were further analysed by bioinformatics tools to identify potential off-target effects and associated pathways/networks.

For off-target effects, the Genome-wide Enrichment of Seed Sequence matches (GESS) analysis (Yilmazel et al., 2014) was carried out to confirm whether the differential expression of the DEGs resulted from sequence matches between siRNA seed region (positions 2−8 from 5' end) and mRNA sequences of the DEGs (Jackson et al., 2006; Seok et al., 2017; Shang et al., 2015). For pathway/network analysis, the Search Tool for the Retrieval of Interacting Genes/Proteins (STRING) and Ingenuity® Pathway Analysis (IPA®) were used. By these analyses, DEGs and/or any genes of interest were connected into an interactive network and associated with biological pathways documented in curated databases such as the Gene Ontology (GO) database (Chowdhury and Sarkar, 2015; Jin et al., 2014). It should be noted that those programmes leverage gene co-expression network analysis or enrichment analysis (Kramer et al., 2014), in which a very small number of analysed DEGs (as detected in this study, see below) is not recommended (Huang et al., 2017a). As per the official guidance of IPA® that recommends using a set of 100−3,000 genes for analysis, a lower threshold (p-adj < 0.05, fold change ≥ 1.3) was applied to the raw RNA-Seq dataset, which generated a new DEG set, known as DEG-2.

By using the above combined workflow for RNA-Seq data acquisition, processing and analysis, the on-target and off-target effects of S7 as well as pathways/networks in relation to S7 treatment were comprehensively studied.

3.5.2 S7 inhibited the mutant allele in KID-KCs

The allele-specificity of S7 in KID-KCs was confirmed indirectly using qPCR and immunoblotting, in which the primers or antibodies detected overall *GJB2* expression without the ability to discriminate between different alleles **(Section 3.4.1)**. As the RNA-Seq technique is able to detect gene expression directly in an allele-specific manner, this allows for direct assessment of the effectiveness and specificity of S7 on the mutant allele containing the G-to-A substitution on c.148 locus in *GJB2*.

At the c.148 locus, the heterozygous A/G allele was seen in KID-KCs, where both G (wildtype) and A (mutant) alleles were co-expressed as transcripts. Of note, the ratio of G to A in untreated KID-KCs at baseline was not 50:50, but 60:40 in percentage **(Figure 3.5.2a)**. Following S7 treatment, there was a 30% decrease in frequency of the mutant A allele in treated cells compared with untreated cells **(Figure 3.5.2a-b)**. An increase of 20% in the wildtype G allele frequency was also detected in S7-treated cells, compared to untreated cells **(Figure 3.5.2a-b)**. Quantification of the above data showed statistical significance ($p < 0.05$, n = 3 for both the decrease in mutant allele frequency and increase in wildtype allele frequency, Student's t-test) **(Figure 3.5.2b)**. This confirmed the effectiveness of the mutant allele knockdown.

a

	Allele count (allele frequency)		
	G	A	total
U	78.3 ± 7.3 (60.3% ± 1.2%)	52.3 ± 7.6 (39.7% ± 1.2%)	130.6 (100%)
S7	94.0 ± 4.2 (72.0% ± 1.8%)	37.0 ± 4.2 (28.0% ± 1.8%)	131.0 (100%)

b

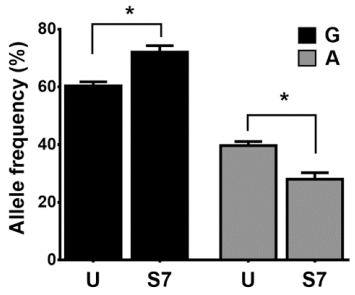

Figure 3.5.2 RNA-Seq confirmed specificity of S7 for GJB2 c.148G>A mutant allele
*RNA-Seq sequence reads mapped to the GJB2 c.148 locus in untreated (U) or S7-treated (S7) KID-KCs were analysed. The wildtype allele (c.148G) and mutant allele (c.148G>A) are displayed as G and A, respectively. The count and frequency for each allele are shown and expressed as mean ± SEM (a). Quantification of the allele frequency data showed that S7 treatment resulted in a decrease in the mutant allele frequency and an increase in the wildtype allele frequency (b). *p < 0.05.*

3.5.3 Low-level off-target effects of S7 treatment on KID-KCs

A major issue for RNA interference-based studies are unintended alterations in unrelated gene expression, resulting from off-target events. To understand the potential off-target effects of S7 in KID-KCs, the differential expression profiles between S7-treated and untreated KID-KCs were analysed. The statistically significant DEGs were further subject to the GESS analysis for off-target prediction **(see Section 2.17)**.

First, the distribution of transcript read counts (i.e. expression level) for the 19667 non-zero genes before and after normalisation was plotted **(Figure 3.5.3).** It can be seen that, after normalisation, there was very little variation in distribution of read count among three biological replicates of each group, suggesting high data reproducibility. On the other hand, no remarkable differences in count distribution were found across all six libraries regardless of S7 treatment, suggesting that this therapeutic siRNA induced only very mild global effects, if any, on the transcriptome of KID-KCs.

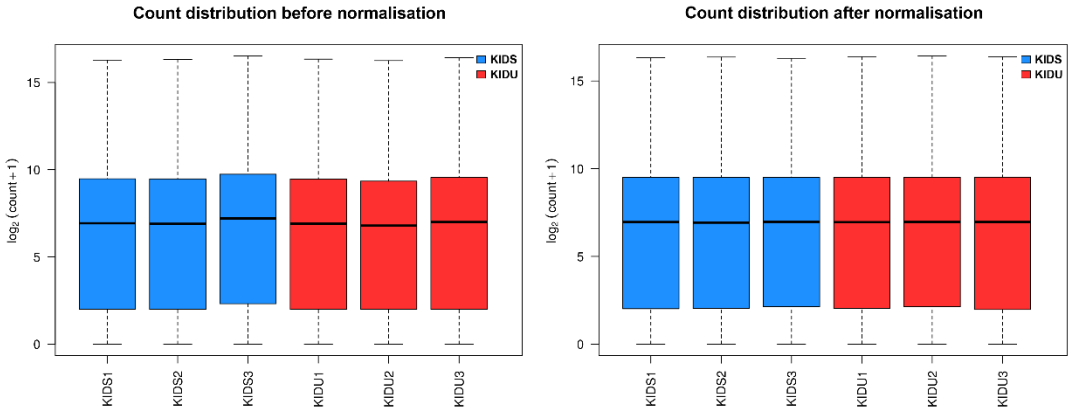

Figure 3.5.3 Mild global effects of S7 on the KID-KC transcriptome
Distribution of sequence read count (expression level) of non-zero genes in libraries obtained from KID-KCs treated with S7 (KIDS, shown as replicates KIDS1−KIDS3, blue boxes) or those untreated (KIDU, shown as replicates KIDU1−KIDU3, red boxes) before normalisation (left panel) and after normalisation (right panel). For visibility reason, log_2 (count +1) instead of log_2 (count) was used. All 6 libraries had similar distribution of gene expression globally.

Second, when the widely-used threshold (fold change ≥ 2, p-adj < 0.05%) was applied to the RNA-Seq dataset, only six significant DEGs were identified **(Table 3.5.1)**. The range of fold change for these DEGs was 2.01−2.32, with the maximum fold changes seen in genes *MMP1* and *GLB1L2*.

Table 3.5.1 Differentially expressed genes (fold-change ≥ 2 and adjusted p-value < 5%)

Gene	*Protein*	*Fold change*	*p-value*	*adj p-value*
MMP10	*Matrix metalloproteinase-10*	*2.05, up*	*2.12E-32*	*4.19E-30*
MMP1	*Matrix metalloproteinase-1*	*2.24, up*	*8.45E-24*	*9.50E-22*
NSA2	*Ribosome biogenesis homolog*	*2.16, down*	*2.05E-71*	*1.99E-68*
AFAP1L1	*Actin filament-associated protein 1-like 1*	*2.01, down*	*1.21E-29*	*1.99E-27*
GLB1L2	*Galactosidase beta 1 like 2*	*2.32, down*	*3.12E-16*	*2.17E-14*
GPR137	*G protein-coupled receptor 137*	*2.01, down*	*1.06E-10*	*3.96E-09*

Third, the GESS analysis of the six DEGs predicted only *GPR137* as an off-target of S7, among a total of 180 genes that were predicted to have sequence matches between their coding sequences and S7 seed sequence genome-wide **(Appendix III)**. Further sequence comparison found that both 3'-untranslated region and coding sequence of the *GPR137* gene were complementary to the seed region of either the passenger or guide strand of S7. These sequence matches implied that the 2.01-fold down-regulation of *GPR137* was likely to result from seed region-dependent off-target effects. The other five DEGs were not predicted by GESS analysis, and were therefore more likely to be on-target downstream alterations.

Taking these results together, S7 had low-level off-target effects on the patient keratinocytes. The change in expression level of the DEGs, with the exception of *GPR137*, was likely to result from on-target effects, in other words, *GJB2*-related biological processes. To investigate the possible functional connection between *GJB2* and the DEGs, the RNA-Seq data were subject to further bioinformatics analyses.

3.5.4 S7 activated matrix metalloprotease signalling in KID-KCs

Two powerful bioinformatics tools, STRING and IPA®, were subsequently used for pathway/network analysis. STRING analyses protein-protein interaction based on factors such as previous experimental findings, text-mining and co-expression data (Franceschini et al., 2013; Szklarczyk et al., 2015), whereas IPA® analyses the input genes by associating them with documented pathways and molecular functions. The DEG-2 dataset composed of 344 DEGs **(see Appendix IV)** was analysed by these programmes.

The 344 DEGs consisted of 249 down-regulated genes and 95 up-regulated genes. By STRING analysis, an interactive network containing 112 genes was identified **(Figure 3.5.4)**, with 2 major clusters of genes connected to each other. These include a MMP network (*MMP1*, *MMP9*, *MMP10*, *TIMP2*, *PLAU*, *TFPI2*, *COL4A1*, *HBEGF*, *CXCL5*) and an immune network (*TLR2*, *IL1R1*, *IL1RAP*, *MYD88* and *IKBKG*). Among six most differentially expressed genes from the earlier analysis **(Table 3.5.1)**, four (*MMP1*, *MMP10*, *NSA2* and *AFAP1L1*) were found in this network. The *GJB2* gene was only connected to *SPRR2A* (encoding small proline rich protein 2A) based on previous indirect interaction data (Djalilian et al., 2006), but not connected to any other genes. This may be due to an unknown limitation of the STRING algorithm, and/or the fact that Cx26 protein is not known to be directly located on any signalling pathways (although it regulates other pathways via the exchange of second messengers).

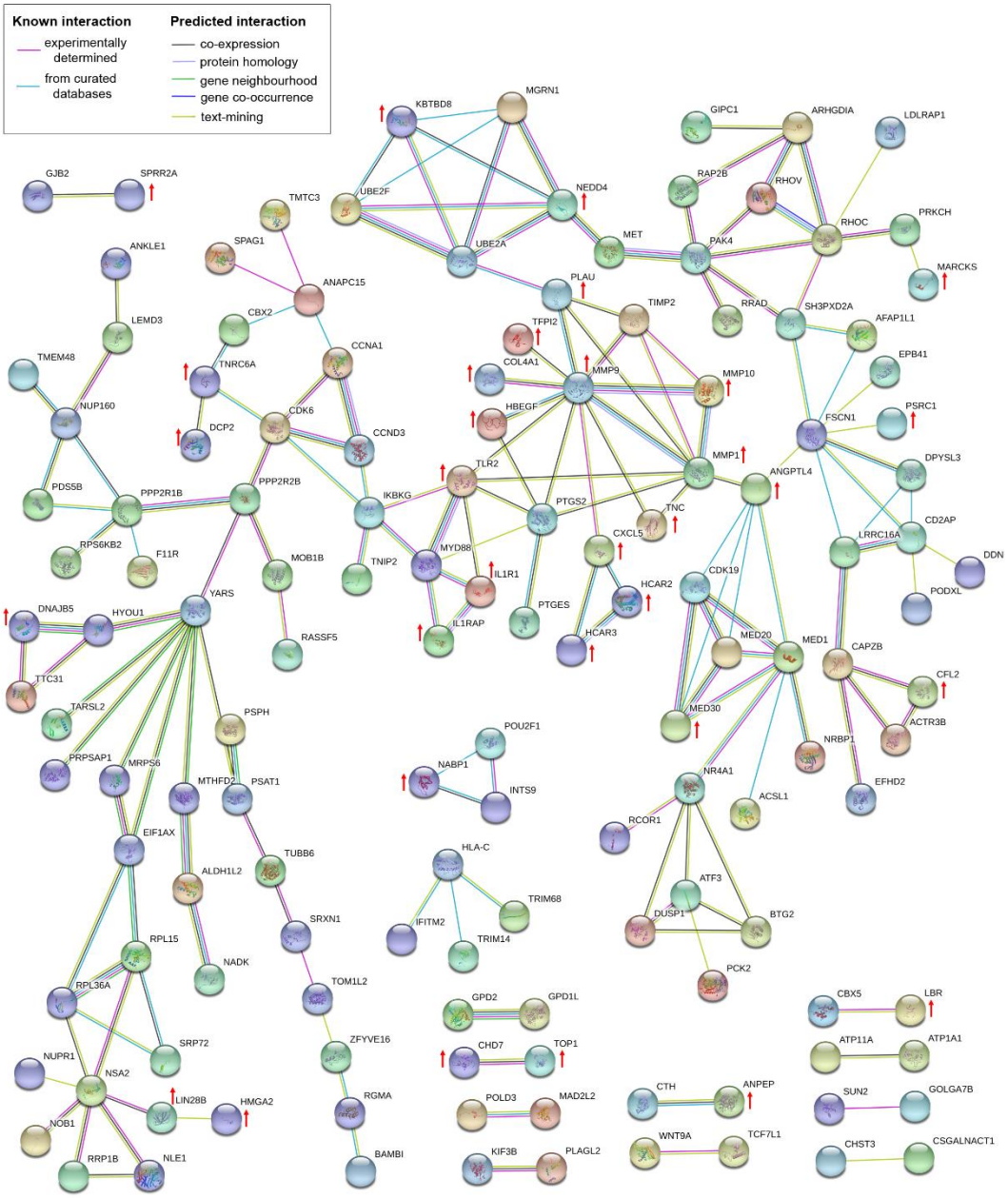

Figure 3.5.4 Interactive network of DEGs generated in the DEG-2 dataset

Functional network of the DEG-2 set of 344 genes ***(see Appendix IV)****. The nodes represent genes (filled, crystal structure known; unfilled, crystal structure unknown). Among 344 genes, 112 genes were connected to form a big network consisting of several clusters. Lines with different colours represent 7 different types of evidence for interaction (see legend on the top left). Gene with red arrows are up-regulated and otherwise down-regulated.*

When known interactors of *GJB2,* namely *GJB6* (Cx30, up-regulated by 14.5%) and *GJA1* (Cx43, down-regulated by 8%), as well as their known interactors, including *TJP1* (tight junction protein-1, or zonula occludens-1, up-regulated by 14.2%) and *CDH1* (E-cadherin, up-regulated by 14.5%), were included in the STRING analysis

with the above MMP and immune clusters, a new network more relevant to the epidermis was constructed, with *GJB2* connected to the MMP cluster through *GJA1*, *TJP1* and *CDH1* **(Figure 3.5.5)**. Three GO terms from the molecular function category were significantly enriched, including "metalloendopeptidase activity (GO:0004222)", "interleukin (IL)-1 receptor activity (GO:0004908)" and "endopeptidase activity (GO:0004175)" (p = 0.012, 0.012 and 0.046, respectively, corrected by false discover rate).

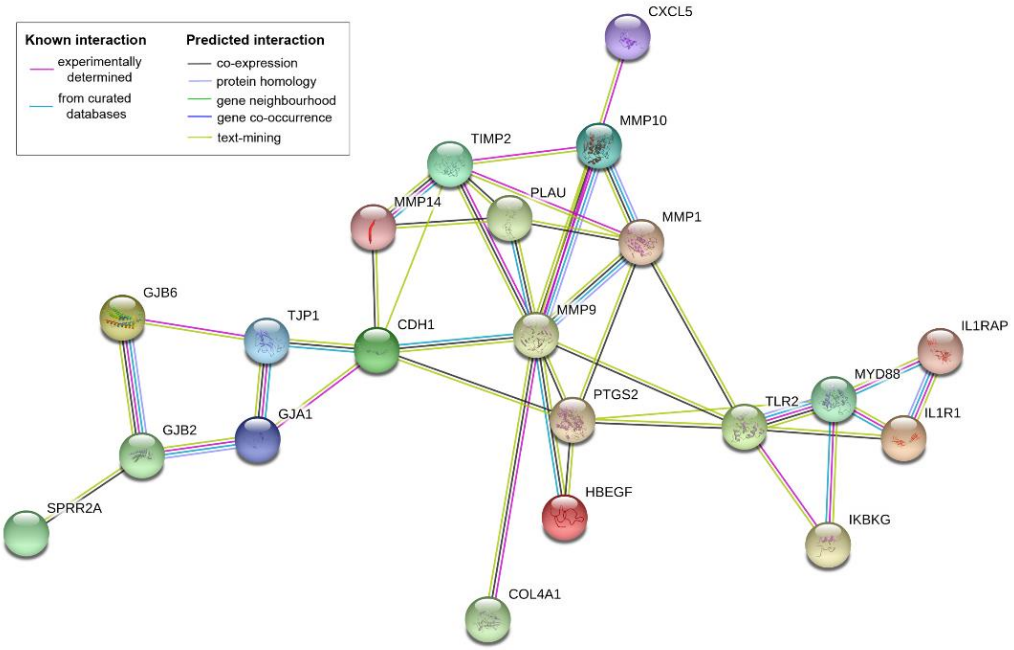

Figure 3.5.5 Interactive network between selected DEG-2 genes and interactors of GJB2
GJB2 and its known interactors (GJB6, GJA1, TJP1, CDH1), along with genes from two selected epidermis-relevant clusters from DEG-2 set were subject to STRING analysis. The nodes represent genes (filled, crystal structure known; unfilled, crystal structure unknown). Lines with different colours represent 7 different types of evidence for interaction (see legend on the top left).

The 344 DEGs were also analysed by IPA®. A summary with top five enriched canonical pathways and cellular functions is shown in **Table 3.5.2**. The MMP signalling pathway was significantly enriched (p = 0.000207) by these DEGs and this pathway was predicted to be activated, consistent with the STRING results. For the other four enriched pathways, no clear directional data (activation or inhibition) were given by the analysis.

Table 3.5.2 Top five enriched pathways given by IPA® Canonical Pathway Analysis

Name	***p-value***	***Overlap****	***Activation / Inhibition***
Semaphorin Signalling in Neurons (CFL2↑, DPYSL3↓, MET↓, PAK4↓, RHOC↓, HOV↓)	*1.33×10^{-4}*	*11.3% (6/53)*	*Not available*
Inhibition of Matrix Metalloproteases (MMP1↑, MMP9↑, MMP10↑, TFPI2↑, TIMP2↓)	*2.07×10^{-4}*	*12.8% (5/39)*	*Inhibition*
Glycerol-3-phophate Shuttle (GPD1L↓, GPD2↓)	*1.30×10^{-3}*	*50% (2/4)*	*Not available*
Oncostatin M Signalling (MMP1↑, PLAU↑, ELK1↓, OSMR↓)	*1.58×10^{-3}*	*11.8% (4/34)*	*Neither*
Serine Biosynthesis (PSAT1↓, PSPH↓)	*2.15×10^{-3}*	*40.0% (2/5)*	*Not available*

** Pathway overlap: the ratio of DEGs on the pathway to total genes documented on the pathway*

3.5.5 Section summary

The RNA-Seq analysis provided the first direct evidence of allele-specific targeting of S7 at transcriptional level. A surprising finding in this experiment was that S7 treatment not only significantly inhibited the mutant *GJB2* allele, but also resulted in up-regulation of the wildtype *GJB2* allele. The exact mechanism is not clear, but it can be suspected that these dual effects could be responsible for the substantial phenotypic reversal in KID-KCs, as presented in the last section. On the other hand, key to assessing the potential usefulness of any siRNA therapy is an RNA-Seq analysis for potential off-target effects. Importantly, the expression of only six other genes genome-wide was found to be significantly altered by S7, with only one of these predicted as an off-target by GESS. This is an important result as it implies a comparatively low rate of off-target whole genome effects of S7 in KID-KCs.

CHAPTER 4: DISCUSSION

4.1 Establishment of a patient-derived keratinocyte cell line that displayed aberrant channel phenotype

The most important cell model generated in this study was KID-KC, a keratinocyte cell line derived from KID syndrome patient keratinocytes harbouring a heterozygous mutation at c.148G>A (p.D50N) in *GJB2*. Functional studies in this cell model have shown abnormal channel function, suggesting its usefulness to investigate the efficacy and specificity of the siRNA therapy.

Previous studies largely relied on the exogenous expression of *GJB2* with c.148G>A mutation in different cell types, including *Xenopus* oocytes, HeLa, SAOS2 cells, HaCaT and primary corneal epithelial cells (Di et al., 2005; Donnelly et al., 2012; Gudmundsson et al., 2017; Lopez et al., 2013; Press et al., 2017b; Sanchez et al., 2013; Shurman et al., 2005; Terrinoni et al., 2010; Xu et al., 2017). Despite providing valuable functional insights of the mutant protein, those systems have several limitations when used for preclinical evaluation of new treatment. First, some of those cells are irrelevant to KID syndrome, such as Xenopus oocytes and HeLa cells. Second, vectors can only deliver *GJB2* gene with a homozygous mutation which does not represent the genetic state in KID patients who are heterozygous for a *GJB2* mutation. Third, those systems lack physiological control of gene expression due to the use of non-human promoters, such as viral promoters. There has been a report of *in vitro* functional assessment using primary patient keratinocytes heterozygous for mutation c.42C>G (p.N14Y) in *GJB2*, which showed impaired GJIC (Arita et al., 2006). However, since primary keratinocytes have short lifespan in *in vitro* culture (Kaur and McDougall, 1988) and patient cells are in general of low accessibility due to the rarity of the condition, it would be unrealistic to use primary keratinocytes for research or preclinical studies. Therefore, generation of a disease-relevant, immortalised cell model that maintains features of their normal counterparts is necessary.

In this study, primary keratinocytes from a patient with KID syndrome were successfully immortalised using human papilloma viruses. The immortalised cells, KID-KCs, maintained keratinocyte morphology and other features such as differentiation. These cells can be cultured and propagated *in vitro* for at least four to five months (at least 40 passage) without losing the morphology of keratinocytes or

the expression of c.148G>A mutation. Phenotypically, KID-KCs displayed altered subcellular localisation, gap junction plaque formation and aberrant function of Cx26. These results suggest that immortalised KID-KCs are a useful disease model that can represent primary patient keratinocytes.

The defective gap junctional coupling in KID-KCs observed in the SLDT assay may have resulted from altered inter-connexon interaction and connexon docking conferred by the p.D50N substitution (Sanchez et al., 2013). Consistent with this notion, immunostaining of KID-KCs revealed reduction of gap junction plaque formation at sites of cell-cell contact. Since Cx26 gap junctions allow the exchange of small molecules including Ca^{2+}, impaired gap junctional coupling in keratinocytes may influence the intracellular Ca^{2+} concentration, which is essential for keratinocyte differentiation (Blaydon and Kelsell, 2014; Tu and Bikle, 2013). Disruption of the Ca^{2+} concentration in the epidermis may significantly impact the epidermal barrier function, causing the skin phenotype (Bosen et al., 2015; Garcia et al., 2015; Srinivas et al., 2017).

KID-KCs were also found to have aberrant hemichannel behaviour, including enhanced conductance of electrical signals (patch clamp) and increased permeability to small cationic molecules (neurobiotin uptake). The crystallography-based three-dimensional structural data of Cx26 showed that D50 is a pore-lining residue (Maeda et al., 2009). The substitution of the negatively-charged aspartic acid for uncharged asparagine at this residue is likely to impact the biophysical property of Cx26 hemichannels, such as permeability/selectivity (Maeda et al., 2009) and gating regulation by extracellular Ca^{2+} (Lopez et al., 2013; Sanchez et al., 2013). As a consequence, 'leaky' mutant Cx26 hemichannels, with a large aqueous pore allowing permeation of various ions and metabolites, may adversely impact the cellular homeostasis by releasing ATP to extracellular space, activating purinergic signalling (Martin et al., 2014), and/or by altering the entry of electrolytes (Levit and White, 2015).

Consistent with the above theory, profound cell death in cells transiently transfected with the p.D50N mutant *in vitro* has also been reported (Common et al., 2004; Lee et al., 2009; Press et al., 2017b; Terrinoni et al., 2010). However, no overt cell death was

observed in cultured KID-KCs throughout this study. This can be explained by the possibility of rescuing effects of the co-expressed endogenous wildtype Cx26 or other connexins in the keratinocytes. The RNA-Seq data appear to support the hypothesis, in which the KID-KCs had a wildtype-to-mutant *GJB2* transcript ratio of 60:40 (not 50:50) at baseline, indicating possible self-rescuing down-regulation of the mutant allele. Future studies are required to determine a 'threshold' wildtype-to-mutant ratio above which cell death/mutant phenotype can be reversed.

4.2 Differential Cx26 expression between the epidermis and cultured keratinocytes of patient KID-1

Immunostaining of patient KID-1 skin sections revealed normally-appearing gap junction plaques, along with enhanced overall Cx26 expression, which was in stark contrast to *in vitro* cultured KID-KCs where significantly reduced Cx26 expression was detected. In KID-1 epidermis, Cx26 was predominantly detected in upper suprabasal keratinocyte layers and was barely detectable in proliferating basal keratinocytes. Thus, it is conceivable that our culture conditions, which render keratinocytes more proliferative than differentiating, may contribute to lower Cx26 expression in KID-KCs. Such low Cx26 expression may have impeded detection of gap junction plaques in cultured KID-KCs. On the other hand, co-expressing wildtype connexins have been shown to rescue defective trafficking in certain Cx26 mutants (Marziano et al., 2003). While such rescuing effects by other wildtype connexins are likely to have occurred in keratinocytes in culture and in the epidermis, the latter *in vivo* condition might have provided additional rescue to mutant Cx26, possibly through more complex interaction with connexins and/or non-connexin molecules. Similar observation has been reported previously on Cx30.3, which displayed membrane trafficking in the epidermis, but had clearly altered subcellular localisation in culture (Di et al., 2005).

In KID-1 epidermis, Cx26 was found to extensively co-localise with Cx30, consistent with previous double-immunostaining results in patient skin with the p.G12R mutation (Richard et al., 2002). These data provide further evidence of interaction between these compatible connexins in the epidermis (Di et al., 2005; Di et al., 2001c; Yum et al., 2007). Simultaneous detection of Cx26 and Cx43 in KID-1 epidermis also found focal

expression overlaps; however, preliminary data of stacked Cx26 and Cx43 confocal microscopic images taken from cultured KID-KCs did not show clear superimposition (unpublished data), reminiscent of confocal imaging data reported elsewhere (Gemel et al., 2004). As trans-dominant effects of mutant Cx26 on Cx43 have been linked to the pathogenesis of hyperkeratotic skin disorders (Churko et al., 2010; Garcia et al., 2015; Shuja et al., 2016), whether the residue D50 acts as an oligomerisation compatibility checkpoint, as do other Cx26 residues including G12, N14, S17, H73 and S183 (Garcia et al., 2015; Shuja et al., 2016), requires future *in vitro* functional studies to confirm.

4.3 S7 has strong selectivity for the mutant *GJB2* mRNA with few off-targets, effectively reversing aberrant phenotype in KID-KCs

The action of previously reported strategies to inhibit connexins, including synthetic peptide mimetics and monoclonal antibodies, is mediated by either modulating the interaction between target connexins and their binding partners or altering the biophysical property of target connexin channels (Becker et al., 2012; Grek et al., 2015; Xu et al., 2017). In contrast, the therapeutic siRNA in this study silences target gene expression at transcriptional level by degrading mRNA with a matched sequence, thereby blocking the translation of target protein (Jackson and Linsley, 2010). This naturally-occurring mechanism is endowed with high sequence specificity (Trochet et al., 2015), and its advantage in treating dominant disorders is the ability to discriminate mutant and wildtype mRNA sequences differing by even a single base, leading to differential gene silencing, as seen in this work centred on S7. This siRNA exhibited strong specificity towards the *GJB2* allele with c.148G>A mutation, rather than the wildtype allele in HeLa, N/TERT and KID-KC models, confirmed by qPCR, immunoblotting, flow cytometry. As a result, multiple functional assays showed clear reversal of hemichannel and gap junction functionality in KID-KCs, while the channel function in normal keratinocytes was not altered.

The allele-specificity of S7 with few off-targets in KID-KCs was directly confirmed by RNA-Seq, the transcriptomic analysis with high sensitivity and single-base resolution (Tang et al., 2010). Only six genes (*GLB1L2*, *NSA2*, *GPR137*, *AFAP1L1*, *MMP1*, *MMP10*) in the KID-KC transcriptome were significantly altered, of which

only *GPR137* was predicted as an off-target by GESS, whereas the other five genes may have resulted from transfection-related events (e.g. immune response) or events secondary to allele-specific *GJB2* inhibition. *NSA2* and *GPR137* are involved in cell proliferation (Zhang et al., 2010; Zong et al., 2014), with *GPR137* also associated with migration of prostate cancer cells (Ren et al., 2016), a role shared with *AFAP1L1* and the MMP genes (Takahashi et al., 2014). *GLB1L2* encodes a member of galactosidase with currently unclear physiological function (Bansho et al., 2017). Future work is required to validate the altered expression of these genes as well as to understand the biology related to the alteration in keratinocytes.

siRNA technology has been previously attempted in one study to treat hearing loss in a PPKD mouse model, which was generated by *in vivo* transfection with a plasmid vector encoding a dominant *GJB2* mutant p.R75W (human sequence) (Maeda et al., 2005). The authors used a siRNA designed against wildtype human *GJB2*, rather than wildtype mouse *Gjb2* or mutant human *GJB2*. The results showed efficient inhibition of the exogenous, mutant human *GJB2* mRNA *in vivo*, successfully preventing the onset of hearing loss in treated mice. Although the siRNA did not inhibit endogenous *Gjb2* in the mice (due to two mismatches between human and mouse sequences), in the context of human PPKD treatment, the siRNA would be likely to inhibit the wildtype *GJB2*. Such non-specific targeting may limit its clinical application. In contrast, we harnessed the sequence walk method, whereby 19 designed siRNAs have perfect base-paring with the c.148G>A mutant mRNA sequence but have a single-base mismatch with the wildtype sequence, minimising non-specific effects on the wildtype mRNA. Consistent with the concept, 12 out of 19 siRNAs displayed preferential silencing of the mutant allele over the wildtype allele, with S7 showing the most robust selectivity for the mutant.

A possible concern regarding allele-specific therapy is haploinsufficiency, in which the expression of the remaining wildtype allele is not sufficient to maintain gene function. This scenario can be ruled out by results from CRISPR-Cas9-edited, *GJB2*$^{+/-}$ N/TERT clones, g4-B09 and g4-B21, which had normal morphology, proliferation, as well as normally-functioning gap junction channels. The toleration to the lack of Cx26 favours the presence of functional redundancy and compensation among connexin members in keratinocytes (Bedner et al., 2012; Blaydon and Kelsell, 2014). A similar example is

given by ODDD patients heterozygous or homozygous for loss-of-function mutation in *GJA1* (Cx43) gene, who develop abnormalities in multiple organs but rarely in the skin (Laird, 2014; Richardson et al., 2006). These findings provide a sound basis for future clinical translation of the siRNA S7. On the other hand, the N/TERT clones *GJB2* deletion will be useful in future mechanistic studies involving *GJB2*, including epidermal barrier formation (Djalilian et al., 2006), wound healing (Polusani et al., 2016), carcinogenesis (Natsuga et al., 2011; Nyquist et al., 2007), along with cancer stem cell maintenance, a process recently linked to Cx26 (Thiagarajan et al., 2018).

4.4 Activation of MMP signalling in S7-treated KID-KCs

The central finding in the network analysis is up-regulation of multiple MMP genes (*MMP1*, *MMP9*, *MMP10* and *MMP14*) in KID-KCs by S7. The protein products of MMP genes function to proteolytically degrade different types of extracellular matrix proteins and basement membrane components such as collagen, gelatin, laminin and E-cadherin (Caley et al., 2015). MMP proteins are reported to be activated during inflammation (Gan et al., 2001; Nissinen and Kahari, 2014) and wound healing (Krampert et al., 2004). A number of MMP-regulating genes, including those coding for tissue inhibitors of metalloproteinases-2 (*TIMP2*), heparin-binding EGF-like growth factor (*HB-EGF*), urokinase-type plasminogen activator (*PLAU*), type IV collagen (*COL4A1*, as MMP substrate) and cyclooxygenase 2 (COX-2, encoded by *PTGS2*), were significantly altered, with an overall effect favouring activation of MMP signalling. The molecular mechanism by which the activation was initiated remains unknown. Due to the cost of RNA-Seq, normal control keratinocytes were not included in this experiment; however, qPCR analysis is currently under way to examine the above alteration of gene expression in both normal and patient cells.

Although MMP signalling has not been linked to KID syndrome pathogenesis, the association between Cx26 and MMP proteins has been reported (Kalra et al., 2006; Yano and Yamasaki, 2001). Using HepG2 cells (human hepatoma cell line) stably expressing Cx26, Yano and Yamasaki found that antisense oligonucleotide-mediated Cx26 knockdown led to decreased expression of E-Cadherin, causing enhanced cell invasion and migration capacity and MMP-9 activity *in vitro* (Yano and Yamasaki, 2001). Similarly, Kalra et al. reported that MDA-MB-435 cells (breast cancer cell line)

overexpressing either of three forms of Cx26 (wildtype, GFP-Cx26 fusion and p.D66H mutant) migrated slower with different invasion capacities, and all three strains had reduced MMP-9 activity and increased TIMP-1 activity (Kalra et al., 2006). Both studies suggested that Cx26 may function to reverse tumour phenotype through reducing MMP-9 expression and/or activity. Since KID syndrome is a skin tumour-predisposing disorder (Mazereeuw-Hautier et al., 2007), investigation of the interplay among Cx26, E-cadherin and MMPs in KID-KCs will provide clues for future tumour treatment in clinical settings.

On the other hand, the activation of MMPs has been associated with higher motility in keratinocytes (Krampert et al., 2004). In fact, using time-lapse microscopy, KID-KCs were observed to have markedly reduced motility, compared to control-KCs (unpublished data). In support of this, keratinocytes isolated from transgenic KID syndrome mice with the p.S17F mutation showed reduced migration *in vitro* in response to scratch wounding (Press et al., 2017a). Paradoxically, delayed wound healing does not appear to be a major issue in clinical management of KID syndrome patients, with only few studies reporting poor wound closure post-operatively (Smyth et al., 2012). It is noteworthy that GJIC, which was found impaired in KID-KCs, may have also contributed to their reduced motility (Polusani et al., 2016). Thus, future work is warranted to assess whether S7 can improve motility of patient keratinocytes. Also, whether wound healing defects in KID syndrome patients have been under-reported or are just subclinical is to be confirmed by careful dermatological assessment.

4.5 Prospect of allele-specific siRNA therapy for KID syndrome

The present study has shown that, in KID syndrome patient keratinocytes, aberrant Cx26 channel activity resulting from the hotspot mutation c.148G>A can be effectively and specifically targeted by siRNA S7, leading to marked reversal of channel function in patient cells with low-level off-target effects. These data provide proof-of-concept for the use of S7 in targeted therapy for KID syndrome. In the context of patient skin, the S7-mediated reversal of connexin channel function could potentially reverse the disturbed epidermal Ca^{2+} gradient (Bosen et al., 2015), leading to improved hyperkeratotic phenotype. Moreover, since enhanced hemichannel activity has been linked to release of inflammatory cytokines when exposing c.148G>A-expressing

keratinocytes to peptidoglycans from an opportunistic pathogen, *Staphylococcus aureus* (Donnelly et al., 2012), S7 is also likely to contribute towards control of skin infection and inflammation. Furthermore, the c.148G>A mutation has been found in a substantial percentage (71−86%) of patients with KID syndrome. Thus, the siRNA S7 targeting the mutation would serve as an important step towards personalised therapy for KID syndrome, which currently has no effective specific treatment options.

The main challenge for translational development of the siRNA therapy is *in vivo* delivery into keratinocytes. Two common delivery routes, i.e. systemic and topical delivery, are feasible options for KID syndrome and the choice depends on distribution of skin lesions in individual cases. For those with generalised skin lesions, systemic delivery may be considered; however, this route of administration requires careful bio-distribution and safety assessment. In contrast, topical delivery may presumably avoid significant systemic effects. Nonetheless, the water-impermeable epidermal barrier is often a hurdle against this transdermal delivery route (Kikuchi et al., 2008). In a pioneering phase 1b clinical trial, intradermal injection of a siRNA, called TD101, into pachyonychia congenita patient foot lesions has shown therapeutic potential (Leachman et al., 2010), but repetitive intradermal injection, which causes intense pain, could preclude this method as a long-term, viable treatment option. Also, 'naked' siRNA is unstable *in vivo* due to the presence of serum nucleases or phagocytes, and its size (approximately 13 kDa) and negative charge may also affect cell uptake (Bumcrot et al., 2006; Miele et al., 2012; Whitehead et al., 2009). To overcome the obstacles and to achieve non-invasive, pain-free topical delivery, several groups have developed nanoparticle-based methods using spherical siRNA-gold nanoparticle conjugates (Zheng et al., 2012) or cationic liposome-siRNA nanocomplexes (Hattori et al., 2013; Jose et al., 2017). Those nanocarriers not only confer protection to their siRNA cargo against nuclease degradation, but also can be flexibly engineered to allow targeted delivery, controlled release and enhanced cellular uptake of siRNA (Miele et al., 2012). Other strategies, including the use of "self-delivery" modified siRNA (Hegde et al., 2014) and cell-penetrating peptides (Aufenvenne et al., 2013; Desai et al., 2010; Desai et al., 2013; Ruan et al., 2016), have also been attempted to enhance transdermal delivery efficiency. More effective siRNA delivery options are on the horizon.

4.6 Future studies

Future work will be directed to optimising nanoparticle delivery methods to facilitate efficient transdermal delivery of siRNA. A human-murine chimeric KID syndrome mouse model has been generated in our laboratory (unpublished data). This model was constructed by grafting the organotypic-cultured KID-1 skin (composed of KID-1 keratinocytes and fibroblasts) onto an immunodeficient mouse, and the engrafted region displayed hyperkeratotic lesions on histological examination, resembling the skin lesions in human patients. Due to the transient silencing effect of siRNA which lasts for approximately seven days *in vivo* (Tagalakis et al., 2018), repeated siRNA dosing would be necessary in future application. On the other hand, since siRNA-related off-target effects (Caffrey et al., 2011; Fedorov et al., 2006; Jackson et al., 2003) and immune response (Judge et al., 2005) have been reported to be dose-dependent, future work will also determine the lowest concentration of S7 that produces maximal on-target silencing effects. A chemically-modified (e.g. 2'-O-methyl-modified) siRNA may be used to reduce potential immune response (Judge et al., 2006) and/or increase the potency and duration of silencing *in vivo* (Kenski et al., 2012; Wu et al., 2014).

Finally, as an alternative strategy to siRNA-based therapy, CRISPR/Cas genome editing may be a feasible option for KID syndrome treatment. Other than the NHEJ pathway that often causes disruption of a target gene, the homology-directed repair (HDR) strategy of CRISPR/Cas allows for site-specific correction of the c.148G>A mutation into a wildtype *GJB2* sequence in the target genome, theoretically leading to 'normalisation' of the gene function (Hsu et al., 2014). The efficiency of HDR has been significantly improved over the recent years (Chu et al., 2015; Maruyama et al., 2015; Paquet et al., 2016), and the identification of g4, the *GJB2*-specific sgRNA, in this study serves as important preliminary data for the additional CRISPR/Cas9 work. The work will be carried out in the near future.

4.7 Conclusion

This study employs the allele-specific siRNA technology to silence the mutant *GJB2* allele without affecting the wildtype *GJB2* allele. The siRNA screening identified S7 as the most potent and specific siRNA against the mutant allele with c.148G>A

mutation. The potent inhibition of the mutant allele resulted in significant reversal of both aberrant hemichannel and gap junction channel activity in patient keratinocytes, indicating functional correction of Cx26 following the siRNA treatment. Moreover, RNA-Seq analysis demonstrated that S7 treatment did not significantly affect the global gene expression profile in the patient keratinocytes, suggesting very mild off-target effects of S7.

Collectively, this proof-of-concept study suggests that allele-specific siRNA serves as potentially effective and safe therapeutic intervention for KID syndrome − a debilitating condition without specific treatment option available at present. Development of topical delivery platform for chemically-modified siRNA is under way. If successful, the allele-specific siRNA technique can be adapted to other skin conditions with dominant mutations.

APPENDIX

Appendix I: Primers

Primers	Sequence	Temp °C	Product size
GJB2-endogenous-F	5’-AGAGACCCCAACGCCGAG-3’	60	472 bp
GJB2-endogenous-R	5’-GGAGCCTTCGATGCGGAC-3’		
GJB2-endo-full-F	5’-CTCCCGACGCAGAGCAAA-3’	60	771 bp
GJB2-endo-full-R	5’-GGTTGCCTCATCCCTCTCAT-3’		
GJB2-GFP-RT1-F	5’-CTGTGGACTGCTTTGTGTCC-3	60	339 bp
GJB2-GFP-RT1-R	5’-CGGTGGTGCAGATGAACTTC-3’		
GAPDH-F	5’-CCCATCACCATCTTCCAGGA-3’	60	473 bp
GAPDH-R	5’-CCAGTGAGCTTCCCGTTCAGC-3’		
GJB2-GFP-RT2-F	5’-GTGTGAACAAACACTCCACC-3’	60	766 bp
GJB2-GFP-RT2-R	5’-CTGAACTTGTGGCCGTTTAC-3’		
GJB2-CRISPR-seq-F	5’-CACGTTCAAGAGGGTTTGG-3’	60	648 bp
GJB2-CRISPR-seq-R	5’- AGATGCTGCTTGTGTAGG-3’		
Primers for qPCR			
GJB2-GFP-qPCR-F	5’-AAGCCAGTTGTCGACGGTA-3’	60	131 bp
GJB2-GFP-qPCR-F	5’-CTGAACTTGTGGCCGTTTAC-3’		
Primers for SURVEYOR® nuclease essay			
GJB2-SURVEYOR-F	5’-CCTGTGTTGTGTGCATTCG-3’	60	539 bp
GJB2-SURVEYOR-R	5’-ATGGAGAAGCCGTCGTAC-3’		
Primers for sequencing			
GJB2-genomic-start	5’-ATGGATTGGGGCACGCTG-3’	N/A	N/A
SP6 (for T-A cloning)	5'-ATTTAGGTGACACTATAG-3'	N/A	N/A

Appendix II: Antibodies

Antibody	Species clonality	Cat #	Epitope	IF (tissue)	IF (cells)	WB
Cx26 In-house[#] **(IP[1] condition)** (Rb-pAb-in-house)	Rabbit pAb	In-house (Di et al., 2001a)	CL	N/A	1:100 (Cx26-GFP fusion)	N/A
Cx26 Life Tech[#] **(IP[2] condition)** (Rb-pAb-71-0500)	Rabbit pAb	71-0500	CL	N/A	N/A	1:1,000 (Cx26-GFP fusion)
Cx26 Life Tech (Mo-mAb-13-8100)	Mouse mAb	13-8100	CL	1:50*	1:50	1:1000 (KC; **IB[1] condition**)
Cx26 Merck (Mo-mAb-MABT198)	Mouse mAb	MABT198	Proprietary, details not available	N/A	N/A	1:1000 (KC; **IB[2] condition**)
Cx26 Life Tech (Mo-mAb-33-5800)	Mouse mAb	33-5800	CT	N/A	N/A	1:1000, MB
Cx26 Novus (Rab-pAb-NBP151235)	Rabbit pAb	NBP1-51235	TM2	N/A	N/A	1:1000, MB
Cx30 Life Tech	Mouse mAb	700258	CT	1:50*	N/A	N/A
Cx43 Sigma	Rabbit pAb	C6219	CT	1:500	N/A	N/A
E-cadherin Abcam	Rabbit mAb	ab40772	5th domain	N/A	1:100	N/A
β-actin Sigma	Mouse mAb	A5441	N-terminal	N/A	N/A	1:20,000

* represents an additional step of probing with biotinylated secondary antibody required.

[#] represents antibodies used for immunoprecipitation pull-down of Cx26.

- Abbreviations: Life Tech, Life Technologies; TM2: transmembrane domain-2; CL, cytoplasmic loop; CT, carboxyl-terminal domain; KC, keratinocyte; MB, multiple bands

Appendix III: List of 180 genes predicted to have seed sequence match with S7

ABCA1	*CRB2*	*IFT88*	*MED13L*	*PLXNB1*	*SLC6A8*
ABCC3	*CREBBP*	*IGF2R*	*MED17*	*PPP4R1*	*SMCR7*
ADAMTS7	*CSPG4*	*IGSF9B*	*MEGF8*	*PPRC1*	*SON*
ADCK4	*CTNNA1*	*INTS10*	*MST1R*	*PRKCQ*	*SPEN*
ADCY1	*CUL9*	*IQGAP3*	*MTF2*	*PRR14L*	*STRBP*
ADCY10	*CYP2S1*	*KANSL2*	*MYO16*	*PRSS21*	*SVIL*
ADH4	*DAGLA*	*KANSL3*	*NAT10*	*PRX*	*SYNE2*
AFP	*DMBT1*	*KAT5*	*NAV3*	*PSD3*	*SZT2*
AGBL1	*DSG2*	*KCNH4*	*NBEAL2*	*PTPRB*	*TAF1*
ANKRD28	*DTNA*	*KCNH5*	*NCOA1*	*RAB11FIP5*	*TAF5L*
APOB	*DZANK1*	*KCNK16*	*NEURL4*	*REG1A*	*TBCD*
ARHGAP44	*EDC4*	*KDR*	*NLRC5*	*RINT1*	*TEK*
ASH1L	*ERN1*	*KIAA0556*	*NLRP8*	*RNF17*	*TENM1*
ATP13A1	*ESPL1*	*KIAA1671*	*NOD1*	*RREB1*	*TENM4*
BCAN	*FBXW2*	*KIAA1755*	*NOS2*	*RTTN*	*TEP1*
BIRC6	*FCGBP*	*KIDINS220*	*OCA2*	*RYR3*	*TLE2*
BPIFB4	*FLT1*	*KNTC1*	*OR51E1*	*SCN2A*	*TLR8*
C12orf55	*FOCAD*	*LAMA1*	*PCDH19*	*SCN3A*	*TMPRSS4*
C12orf63	*FRAS1*	*LAP3*	*PCDHB13*	*SEC23A*	*TRAK2*
C16orf62	*GALNT8*	*LIM2*	*PCDHB16*	*SEC31B*	*TRIM60*
C5	*GJA10*	*LLGL2*	*PCDHGA6*	*SEMA4A*	*TTC3*
C6orf132	*GNRHR*	*LOC101929274*	*PCNXL3*	*SLC12A1*	*TUBGCP6*
CACNA1B	*GPR112*	*LOC400499*	*PI4KA*	*SLC26A6*	*UNC13A*
CAND2	***GPR137***	*LRP1B*	*PIGV*	*SLC30A5*	*URB1*
CDS2	*GRM3*	*LTBP4*	*PIWIL2*	*SLC35B1*	*UTRN*
CNOT1	*GRM8*	*LTN1*	*PKD1*	*SLC37A2*	*VPS13D*
COL15A1	*GSG2*	*LY75*	*PKHD1*	*SLC44A3*	*VWF*
COL20A1	*GTPBP2*	*LY75-CD302*	*PLCB3*	*SLC45A3*	*WNK2*
COL4A2	*HLCS*	*MAGEL2*	*PLEKHG2*	*SLC4A4*	*WRN*
COPA	*HLTF*	*MAP7*	*PLEKHM2*	*SLC5A9*	*ZSWIM8*

* Only the expression of GPR137 (underlined, bolded) is significantly altered by S7 in KID-KCs

Appendix IV: List of the DEG-2 set of 344 genes analysed by IPA®

Gene ID	Fold change	Adjusted *p*-value
DSG3	0.639	1.43E-135
ARHGDIA	0.519	2.75E-135
LINC00707	0.548	8.21E-124
ATP1A1	0.597	3.91E-122
F11R	0.572	2.93E-119
TUBB6	0.642	1.84E-99
MET	0.647	2.87E-85
PXDN	0.596	1.46E-82
RHOC	0.592	1.03E-75
HMGA2	1.535	3.31E-69
NSA2	0.463	1.99E-68
RPL15	0.709	5.78E-66
HYOU1	0.581	1.24E-65
MMP9	1.951	4.90E-65
NPLOC4	0.579	7.75E-65
PLAU	1.404	2.30E-61
PEA15	0.678	9.41E-56
CBX5	0.670	1.52E-54
SH3PXD2A	0.740	1.02E-51
TMEM109	0.516	3.92E-47
GLTP	0.575	7.44E-46
SERPINB7	0.739	8.06E-46
CAPNS1	0.682	1.30E-45
CXCL5	1.742	6.26E-45
HMCES	0.529	2.37E-44
LRP11	0.683	1.77E-42
CD2AP	0.621	2.09E-42
NRBP1	0.573	4.77E-42
ANXA11	0.710	6.27E-41
GIPC1	0.712	2.31E-39
EFHD2	0.624	3.64E-39
ENDOD1	0.688	1.02E-36
HDHD1	0.525	6.38E-36
OSBPL10	0.626	1.12E-34
MYD88	0.604	8.37E-34
YARS	0.678	1.76E-33
ALCAM	0.717	2.26E-33
SLC5A3	0.659	7.48E-33
PTGS2	0.564	1.07E-32
NUP160	0.659	3.74E-32
G3BP2	0.724	1.14E-31
KHDRBS1	0.733	5.26E-31
TNRC6A	1.436	6.48E-31
EIF1AX	0.689	1.86E-30
TINAGL1	1.352	1.86E-30
NCEH1	1.539	2.07E-30
CCDC6	0.700	3.07E-30
RCOR1	0.719	3.08E-30
MMP10	2.054	4.19E-30
TMEM64	0.564	2.12E-29
TOM1L2	0.695	3.63E-29
SRP72	0.762	4.10E-29
SPAG1	0.524	6.44E-29
ACSL1	0.752	2.39E-28
CCND3	0.565	2.96E-28
ANGPTL4	1.927	3.57E-28
HEG1	1.354	4.23E-28
TMEM2	1.414	1.23E-27
AFAP1L1	0.499	1.99E-27
IL1RAP	1.508	2.24E-27
TNC	1.330	3.04E-27
RFWD3	0.691	9.42E-27
OSMR	0.699	3.52E-26
UBE2A	0.674	9.42E-26
TOP1	1.317	2.11E-25
TPP1	0.634	2.42E-25
PSAT1	0.687	2.74E-25
CAPZB	0.755	3.38E-25
SLC31A1	0.633	5.18E-25
ELK3	0.751	1.57E-24
UQCRQ	0.566	5.66E-24
GPD2	0.698	9.53E-24
CHST3	0.636	1.20E-23
TTPAL	0.725	1.34E-23
HAS2	1.530	2.89E-23
LRRC58	0.711	1.51E-22
LBR	1.372	2.32E-22
RAP2B	0.715	6.39E-22
RRP1B	0.715	6.48E-22
PLCD1	0.670	6.97E-22
MMP1	2.243	9.50E-22
ARHGEF37	0.632	2.33E-21
SLC25A23	0.616	2.56E-21
GHITM	0.757	4.68E-21
LRRC16A	0.681	1.04E-20
CDK6	0.755	3.15E-20
PRPSAP1	0.611	9.15E-20
GRB7	0.547	2.61E-19
ANPEP	1.501	9.24E-19
MED1	0.748	1.28E-18
PMEPA1	0.742	3.80E-18
MUM1L1	0.522	3.83E-18

Gene ID	Fold change	Adjusted *p*-value
CARNMT1	0.556	4.06E-18
PLAGL2	0.645	4.23E-18
NDC1	0.754	4.38E-18
OSTM1	1.561	3.47E-17
FYCO1	0.706	4.88E-17
RRAD	0.708	6.52E-17
TFPI2	1.334	1.29E-16
RALGAPA1	0.596	1.45E-16
TRIM14	0.643	1.63E-16
CFL2	1.393	2.59E-16
ADRBK2	0.618	3.06E-16
NBEAL2	0.752	7.75E-16
STC2	0.615	7.94E-16
MTHFD2	0.765	1.11E-15
KCTD20	1.316	1.23E-15
JOSD1	0.741	3.61E-15
GOLT1B	0.702	4.98E-15
TMEM181	0.740	5.91E-15
USP40	0.645	1.22E-14
COL4A1	1.307	1.42E-14
HBEGF	1.367	1.69E-14
WIPF2	0.689	1.75E-14
GLB1L2	0.431	2.17E-14
FAM110C	1.358	3.22E-14
ABHD17C	0.698	5.52E-14
CDR2L	0.592	5.54E-14
GXYLT1	1.534	5.97E-14
CHD7	1.360	7.66E-14
LDLRAP1	0.648	1.12E-13
NEDD4	1.309	1.61E-13
SRXN1	0.726	3.27E-13
ALDH1L2	0.697	6.19E-13
ZZZ3	0.723	7.10E-13
DCP2	1.462	9.78E-13
INTS9	0.529	1.12E-12
SUN2	0.715	1.20E-12
FAM3C	1.429	1.99E-12
RP2	1.429	3.05E-12
PPP2R1B	0.767	3.61E-12
SMIM13	0.679	5.35E-12
PPRC1	0.752	6.85E-12
NABP1	1.360	6.86E-12
ATP11A	0.753	7.21E-12
LEMD3	0.760	7.76E-12
CCNYL1	1.322	1.44E-11
QTRTD1	0.711	1.75E-11
INHBA	1.453	1.76E-11
TMTC3	0.766	1.77E-11
DAB2IP	0.759	1.95E-11
DAP	0.732	2.05E-11
CXADR	0.744	2.13E-11
SLC35A2	0.636	2.44E-11
GYS1	0.749	2.74E-11
PAK4	0.669	3.30E-11
CDK19	0.633	3.80E-11
FSCN1	0.709	5.90E-11
THBD	0.712	6.15E-11
PRKCH	0.707	9.03E-11
C5ORF24	0.714	1.01E-10
WBP1L	0.690	1.12E-10
KIF3B	0.763	1.36E-10
PDS5B	0.750	1.47E-10
SKAP2	0.735	1.67E-10
PCK2	0.686	2.07E-10
RPS6KB2	0.715	2.30E-10
AP1M1	0.693	3.62E-10
SAMD8	1.349	3.70E-10
PLEKHM2	0.766	3.75E-10
PTGES	0.767	4.39E-10
MOB1B	0.748	5.25E-10
RRM2B	0.698	5.46E-10
TNIP2	0.645	9.03E-10
DDAH1	1.475	9.44E-10
NADK	0.729	1.32E-09
ZFYVE16	0.764	1.49E-09
ANAPC15	0.607	1.70E-09
PRSS22	1.535	1.77E-09
C6ORF120	1.507	2.04E-09
MGRN1	0.652	2.32E-09
TIMP2	0.752	3.53E-09
B4GALT4	0.753	3.88E-09
GPR137	0.498	3.96E-09
ENTPD7	1.449	4.48E-09
DGCR2	0.722	5.02E-09
GAS5	0.761	7.90E-09
GPD1L	0.688	8.19E-09
NOB1	0.738	8.19E-09
POLD3	0.737	9.06E-09
ERAL1	0.738	1.49E-08
EPB41	0.751	1.59E-08
MAD2L2	0.573	1.67E-08
TCF7L1	0.611	2.42E-08
VPS18	0.711	2.85E-08
GNPDA1	0.668	2.94E-08
PCTP	0.644	3.38E-08
RASSF5	0.706	3.50E-08

Gene ID	Fold change	Adjusted *p*-value
IL1R1	1.458	3.57E-08
FOXRED2	0.584	4.15E-08
FAM160B1	1.318	4.97E-08
DUSP1	0.767	8.45E-08
LINC00294	0.643	1.01E-07
MDK	0.688	1.13E-07
PLEKHA8	1.367	1.24E-07
VSNL1	0.711	1.47E-07
SREK1IP1	0.760	1.54E-07
TMEM167B	0.687	2.90E-07
TBC1D13	0.654	3.71E-07
TRAPPC1	0.759	3.86E-07
SMIM14	0.538	3.88E-07
BTG2	0.657	3.96E-07
SERPINB9	1.353	4.18E-07
TARSL2	0.709	5.93E-07
CA12	0.749	7.91E-07
DOCK4	1.308	9.37E-07
EFS	0.741	9.98E-07
DENND4B	0.715	1.09E-06
AKAP12	1.334	1.20E-06
DMWD	0.683	1.20E-06
POU2F1	0.760	1.27E-06
SNHG3	0.753	1.34E-06
FTO	0.768	1.49E-06
UBE2F	0.728	1.84E-06
SLC30A7	1.304	2.19E-06
ZNF367	1.300	2.20E-06
CDH16	0.667	2.41E-06
INAFM2	1.401	2.42E-06
MAML1	0.769	2.61E-06
IFITM2	0.708	2.65E-06
SLC6A9	0.746	2.77E-06
LRRC20	0.596	2.95E-06
SNX4	1.305	4.10E-06
DPYSL3	0.644	5.00E-06
ELK1	0.736	6.52E-06
C12ORF43	0.673	7.74E-06
NHLRC3	1.575	9.22E-06
RHOV	0.683	9.61E-06
LINC00958	0.746	1.02E-05
FAIM	0.636	1.02E-05
TPPP	0.701	1.06E-05
MRPS6	0.769	1.44E-05
HCAR2	1.426	1.58E-05
ZBTB34	1.392	1.63E-05
SEP3	0.564	2.06E-05
CRNN	1.561	2.15E-05
ANKRD46	1.553	2.19E-05
PSPH	0.713	2.22E-05
SPRR2A	1.300	2.61E-05
IGFL2	0.702	4.58E-05
RGP1	0.745	5.21E-05
SLC35B4	1.300	5.63E-05
RNF146	0.692	8.77E-05
SIDT2	0.671	1.01E-04
ZSWIM4	1.374	1.04E-04
CSGALNACT1	0.609	1.24E-04
ARL15	0.717	1.31E-04
STRADB	1.405	1.39E-04
TMEM255A	0.617	1.45E-04
NLE1	0.710	1.45E-04
SLC46A3	1.311	1.46E-04
EPS8	0.693	1.57E-04
HLA-C	0.694	1.59E-04
CCNA1	0.710	1.59E-04
MB21D1	0.737	2.54E-04
GLCE	0.766	2.88E-04
CA9	0.542	3.10E-04
NUPR1	0.639	3.19E-04
RN7SL1	0.634	4.09E-04
TIFA	0.733	4.37E-04
TTC31	0.745	4.43E-04
LBH	0.762	4.77E-04
RPS6KA6	0.663	9.13E-04
IGSF9	0.755	9.85E-04
BAMBI	0.665	1.08E-03
ATG2A	0.760	1.09E-03
BEND3	0.754	1.14E-03
VPS28	0.755	1.20E-03
PPP2R2B	0.650	1.20E-03
AKNA	0.678	1.31E-03
NLRX1	0.762	1.33E-03
LCORL	1.392	1.34E-03
MED20	0.763	1.41E-03
KBTBD8	1.382	1.44E-03
LOC284454	0.682	1.48E-03
CHAC1	0.644	1.52E-03
PODXL	0.620	1.65E-03
HDHD2	1.311	1.84E-03
TSPYL5	0.758	2.19E-03
LSM11	1.314	2.20E-03
ADAMTS15	0.762	2.45E-03
CNEP1R1	1.346	2.89E-03
WNT9A	0.721	2.97E-03
SNHG12	0.705	3.27E-03

Gene ID	Fold change	Adjusted *p*-value
PRTFDC1	0.738	3.41E-03
PSRC1	1.383	3.52E-03
HCAR3	1.597	3.87E-03
MAMDC2	1.505	4.15E-03
LETMD1	0.768	4.16E-03
TRIM68	0.696	4.17E-03
C17ORF51	0.714	4.25E-03
CDC42EP2	1.303	4.35E-03
NRCAM	1.377	4.39E-03
ZC3HAV1L	0.685	4.78E-03
LIN28B	1.462	5.30E-03
ARMCX1	1.322	6.68E-03
TLR2	1.330	6.83E-03
CBX2	0.712	7.19E-03
DNAJB5	1.367	7.21E-03
C9ORF91	0.722	7.34E-03
HSPB8	0.751	7.34E-03
GOLGA7B	0.746	7.40E-03
NCKAP5	1.363	7.89E-03
ATF3	0.721	8.04E-03
FUCA1	1.341	8.29E-03
ANKLE1	0.711	8.98E-03
CTH	0.694	9.32E-03
SNHG5	0.767	1.01E-02
MAL	1.511	1.02E-02
PRSS27	1.479	1.09E-02
WTIP	0.737	1.14E-02
EPB41L4A	1.314	1.16E-02
POLL	0.765	1.37E-02
RN7SL2	0.533	1.55E-02
PAQR5	0.766	1.56E-02
TMPPE	1.547	1.61E-02
CYSRT1	1.362	1.64E-02
SNHG15	0.760	1.79E-02
TRAF5	0.712	1.94E-02
CD99L2	0.697	1.98E-02
PNMAL1	0.740	2.02E-02
MIR100HG	1.335	2.02E-02
RGMA	0.663	2.12E-02
TMC7	1.322	2.14E-02
USP30	0.715	2.14E-02
FLVCR2	0.733	2.21E-02
KIAA1467	1.346	2.21E-02
ZNF738	1.385	2.25E-02
ZNF138	1.364	2.42E-02
RPL36A	0.711	2.49E-02
ACTR3B	0.656	2.84E-02
LINC00472	1.370	2.99E-02
CRNDE	0.751	3.21E-02
MBD5	1.301	3.35E-02
IKBKG	0.676	3.70E-02
NR4A1	0.677	3.80E-02
STYK1	1.444	3.88E-02
WFDC5	1.451	3.97E-02
PKIA	1.525	4.17E-02
MED30	1.345	4.48E-02
NEFM	1.306	4.65E-02
DDN	0.697	4.68E-02
NANOS1	1.384	4.88E-02
ZNF624	1.456	4.91E-02

REFERENCES

Aasen, T., Mesnil, M., Naus, C.C., Lampe, P.D., and Laird, D.W. (2016). Gap junctions and cancer: communicating for 50 years. Nature reviews Cancer *16*, 775-788.

Abbaci, M., Barberi-Heyob, M., Blondel, W., Guillemin, F., and Didelon, J. (2008). Advantages and limitations of commonly used methods to assay the molecular permeability of gap junctional intercellular communication. Biotechniques *45*, 33-52, 56-62.

Al Fahaad, H. (2014). Keratitis-ichthyosis-deafness syndrome: first affected family reported in the Middle East. International medical case reports journal *7*, 63-66.

Alexandrino, F., Sartorato, E.L., Marques-de-Faria, A.P., and Steiner, C.E. (2005). G59S mutation in the GJB2 (connexin 26) gene in a patient with Bart-Pumphrey syndrome. American journal of medical genetics Part A *136*, 282-284.

Alvarez, A., del Castillo, I., Pera, A., Villamar, M., Moreno-Pelayo, M.A., Moreno, F., Moreno, R., and Tapia, M.C. (2003). De novo mutation in the gene encoding connexin-26 (GJB2) in a sporadic case of keratitis-ichthyosis-deafness (KID) syndrome. American journal of medical genetics Part A *117A*, 89-91.

Amarzguioui, M., Holen, T., Babaie, E., and Prydz, H. (2003). Tolerance for mutations and chemical modifications in a siRNA. Nucleic acids research *31*, 589-595.

Ameres, S.L., Martinez, J., and Schroeder, R. (2007). Molecular basis for target RNA recognition and cleavage by human RISC. Cell *130*, 101-112.

Arita, K., Akiyama, M., Aizawa, T., Umetsu, Y., Segawa, I., Goto, M., Sawamura, D., Demura, M., Kawano, K., and Shimizu, H. (2006). A novel N14Y mutation in Connexin26 in keratitis-ichthyosis-deafness syndrome: analyses of altered gap junctional communication and molecular structure of N terminus of mutated Connexin26. The American journal of pathology *169*, 416-423.

Arita, K., Akiyama, M., Tsuji, Y., McMillan, J.R., Eady, R.A., and Shimizu, H. (2004). Gap junction development in the human fetal hair follicle and bulge region. The British journal of dermatology *150*, 429-434.

Arndt, S., Aschendorff, A., Schild, C., Beck, R., Maier, W., Laszig, R., and Birkenhager, R. (2010). A novel dominant and a de novo mutation in the GJB2 gene (connexin-26) cause keratitis-ichthyosis-deafness syndrome: implication for cochlear implantation. Otology & neurotology : official publication of the American Otological Society, American Neurotology Society [and] European Academy of Otology and Neurotology *31*, 210-215.

Aufenvenne, K., Larcher, F., Hausser, I., Duarte, B., Oji, V., Nikolenko, H., Del Rio, M., Dathe, M., and Traupe, H. (2013). Topical enzyme-replacement therapy restores transglutaminase 1 activity and corrects architecture of transglutaminase-1-deficient skin grafts. American journal of human genetics *93*, 620-630.

Avshalumova, L., Fabrikant, J., and Koriakos, A. (2014). Overview of skin diseases linked to connexin gene mutations. International journal of dermatology *53*, 192-205.

Aypek, H. (2015). Deciphering functions of aberrant hemichannels formed by

connexin 26-I30N and D50Y mutations. Master dissertation *İzmir Institute of Technology*, Turkey.

Aypek, H., Bay, V., and Mese, G. (2016). Altered cellular localization and hemichannel activities of KID syndrome associated connexin26 I30N and D50Y mutations. BMC Cell Biol *17*, 5.

Bai, D., and Wang, A.H. (2014). Extracellular domains play different roles in gap junction formation and docking compatibility. Biochem J *458*, 1-10.

Bakirtzis, G., Choudhry, R., Aasen, T., Shore, L., Brown, K., Bryson, S., Forrow, S., Tetley, L., Finbow, M., Greenhalgh, D., *et al.* (2003). Targeted epidermal expression of mutant Connexin 26(D66H) mimics true Vohwinkel syndrome and provides a model for the pathogenesis of dominant connexin disorders. Hum Mol Genet *12*, 1737-1744.

Banks, E.A., Toloue, M.M., Shi, Q., Zhou, Z.J., Liu, J., Nicholson, B.J., and Jiang, J.X. (2009). Connexin mutation that causes dominant congenital cataracts inhibits gap junctions, but not hemichannels, in a dominant negative manner. J Cell Sci *122*, 378-388.

Bansho, Y., Lee, J., Nishida, E., and Nakajima-Koyama, M. (2017). Identification and characterization of secreted factors that are upregulated during somatic cell reprogramming. FEBS Lett *591*, 1584-1600.

Bargiello, T.A., Tang, Q., Oh, S., and Kwon, T. (2012). Voltage-dependent conformational changes in connexin channels. Biochim Biophys Acta *1818*, 1807-1822.

Bazzoun, D., Lelievre, S., and Talhouk, R. (2013). Polarity proteins as regulators of cell junction complexes: implications for breast cancer. Pharmacol Ther *138*, 418-427.

Becker, D.L., Thrasivoulou, C., and Phillips, A.R. (2012). Connexins in wound healing; perspectives in diabetic patients. Biochim Biophys Acta *1818*, 2068-2075.

Bedner, P., Steinhauser, C., and Theis, M. (2012). Functional redundancy and compensation among members of gap junction protein families? Biochim Biophys Acta *1818*, 1971-1984.

Beltramello, M., Piazza, V., Bukauskas, F.F., Pozzan, T., and Mammano, F. (2005). Impaired permeability to Ins(1,4,5)P3 in a mutant connexin underlies recessive hereditary deafness. Nat Cell Biol *7*, 63-69.

Benjamini, Y., Drai, D., Elmer, G., Kafkafi, N., and Golani, I. (2001). Controlling the false discovery rate in behavior genetics research. Behav Brain Res *125*, 279-284.

Bennett, M.V., Barrio, L.C., Bargiello, T.A., Spray, D.C., Hertzberg, E., and Saez, J.C. (1991). Gap junctions: new tools, new answers, new questions. Neuron *6*, 305-320.

Berger, A.C., Kelly, J.J., Lajoie, P., Shao, Q., and Laird, D.W. (2014). Mutations in Cx30 that are linked to skin disease and non-syndromic hearing loss exhibit several distinct cellular pathologies. J Cell Sci *127*, 1751-1764.

Bergman, R., Mercer, A., Indelman, M., Sprecher, E., Haim, N., Zoller, L., Ben-Izhak, O., and Hershkovitz, D. (2012). KID syndrome: histopathological, immunohistochemical and molecular analysis of precancerous and cancerous skin lesions. The British journal of dermatology *166*, 455-457.

Bernstein, E., Caudy, A.A., Hammond, S.M., and Hannon, G.J. (2001). Role for a

bidentate ribonuclease in the initiation step of RNA interference. Nature *409*, 363-366.

Bevans, C.G., Kordel, M., Rhee, S.K., and Harris, A.L. (1998). Isoform composition of connexin channels determines selectivity among second messengers and uncharged molecules. J Biol Chem *273*, 2808-2816.

Bikle, D.D., and Mauro, T.M. (2014). Calcium, Orai1, and epidermal proliferation. J Invest Dermatol *134*, 1506-1508.

Binder, B., Hennies, H.C., Kraschl, R., and Smolle, J. (2005). [Connexin 26 mutation and keratitis-ichthyosis-deafness (KID) syndrome]. Journal der Deutschen Dermatologischen Gesellschaft = Journal of the German Society of Dermatology : JDDG *3*, 105-108.

Blaydon, D.C., and Kelsell, D.P. (2014). Defective channels lead to an impaired skin barrier. J Cell Sci *127*, 4343-4350.

Bondeson, M.L., Nystrom, A.M., Gunnarsson, U., and Vahlquist, A. (2006). Connexin 26 (GJB2) mutations in two Swedish patients with atypical Vohwinkel (mutilating keratoderma plus deafness) and KID syndrome both extensively treated with acitretin. Acta dermato-venereologica *86*, 503-508.

Bosen, F., Celli, A., Crumrine, D., vom Dorp, K., Ebel, P., Jastrow, H., Dormann, P., Winterhager, E., Mauro, T., and Willecke, K. (2015). Altered epidermal lipid processing and calcium distribution in the KID syndrome mouse model Cx26S17F. FEBS Lett *589*, 1904-1910.

Boyden, L.M., Craiglow, B.G., Zhou, J., Hu, R., Loring, E.C., Morel, K.D., Lauren, C.T., Lifton, R.P., Bilguvar, K., Yale Center for Mendelian, G., *et al.* (2015). Dominant De Novo Mutations in GJA1 Cause Erythrokeratodermia Variabilis et Progressiva, without Features of Oculodentodigital Dysplasia. J Invest Dermatol *135*, 1540-1547.

Brandner, J.M., and Haass, N.K. (2013). Melanoma's connections to the tumour microenvironment. Pathology *45*, 443-452.

Brandner, J.M., Houdek, P., Husing, B., Kaiser, C., and Moll, I. (2004). Connexins 26, 30, and 43: differences among spontaneous, chronic, and accelerated human wound healing. J Invest Dermatol *122*, 1310-1320.

Brown, C., Rowlands, M., Lee, D., Geffin, J.A., and Huang, J. (2016). Keratoprosthesis in pediatric keratitis-icthyosiform-deafness syndrome. Journal of AAPOS : the official publication of the American Association for Pediatric Ophthalmology and Strabismus *20*, 73-75.

Brummelkamp, T.R., Bernards, R., and Agami, R. (2002). Stable suppression of tumorigenicity by virus-mediated RNA interference. Cancer cell *2*, 243-247.

Bruzzone, R., White, T.W., and Goodenough, D.A. (1996). The cellular Internet: on-line with connexins. Bioessays *18*, 709-718.

Bukauskas, F.F., and Verselis, V.K. (2004). Gap junction channel gating. Biochim Biophys Acta *1662*, 42-60.

Bumcrot, D., Manoharan, M., Koteliansky, V., and Sah, D.W. (2006). RNAi therapeutics: a potential new class of pharmaceutical drugs. Nat Chem Biol *2*, 711-719.

Burns, F.S. (1915). A case of generalized congenital keratoderma with unusual

involvement of eyes, ears and nasal and buccal mucous membranes. J Cutan Dis *33*, 255-260.

Burnstock, G., Knight, G.E., and Greig, A.V. (2012). Purinergic signaling in healthy and diseased skin. J Invest Dermatol *132*, 526-546.

Bygum, A., Betz, R.C., Kragballe, K., Steiniche, T., Peeters, N., Wuyts, W., and Nothen, M.M. (2005). KID Syndrome: report of a Scandinavian patient with connexin-26 gene mutation. Acta dermato-venereologica *85*, 152-155.

Caceres-Rios, H., Tamayo-Sanchez, L., Duran-Mckinster, C., de la Luz Orozco, M., and Ruiz-Maldonado, R. (1996). Keratitis, ichthyosis, and deafness (KID syndrome): review of the literature and proposal of a new terminology. Pediatric dermatology *13*, 105-113.

Caffrey, D.R., Zhao, J., Song, Z., Schaffer, M.E., Haney, S.A., Subramanian, R.R., Seymour, A.B., and Hughes, J.D. (2011). siRNA off-target effects can be reduced at concentrations that match their individual potency. PLoS One *6*, e21503.

Caley, M.P., Martins, V.L., and O'Toole, E.A. (2015). Metalloproteinases and Wound Healing. Adv Wound Care (New Rochelle) *4*, 225-234.

Caputo, R., and Peluchetti, D. (1977). The junctions of normal human epidermis. A freeze-fracture study. J Ultrastruct Res *61*, 44-61.

Cavazzana-Calvo, M., Payen, E., Negre, O., Wang, G., Hehir, K., Fusil, F., Down, J., Denaro, M., Brady, T., Westerman, K., *et al.* (2010). Transfusion independence and HMGA2 activation after gene therapy of human beta-thalassaemia. Nature *467*, 318-322.

Chang, E.H., Van Camp, G., and Smith, R.J. (2003). The role of connexins in human disease. Ear Hear *24*, 314-323.

Chen, Q., Boire, A., Jin, X., Valiente, M., Er, E.E., Lopez-Soto, A., Jacob, L., Patwa, R., Shah, H., Xu, K., *et al.* (2016). Carcinoma-astrocyte gap junctions promote brain metastasis by cGAMP transfer. Nature *533*, 493-498.

Choudhry, R., Pitts, J.D., and Hodgins, M.B. (1997). Changing patterns of gap junctional intercellular communication and connexin distribution in mouse epidermis and hair follicles during embryonic development. Dev Dyn *210*, 417-430.

Choung, Y.H., Shin, Y.R., Kim, H.J., Kim, Y.C., Ahn, J.H., Choi, S.J., Jeong, S.Y., and Park, K. (2008). Cochlear implantation and connexin expression in the child with keratitis-ichthyosis-deafness syndrome. Int J Pediatr Otorhinolaryngol *72*, 911-915.

Chowdhury, S., and Sarkar, R.R. (2015). Comparison of human cell signaling pathway databases--evolution, drawbacks and challenges. Database (Oxford) *2015*.

Chu, V.T., Weber, T., Wefers, B., Wurst, W., Sander, S., Rajewsky, K., and Kuhn, R. (2015). Increasing the efficiency of homology-directed repair for CRISPR-Cas9-induced precise gene editing in mammalian cells. Nat Biotechnol *33*, 543-548.

Churko, J.M., Kelly, J.J., Macdonald, A., Lee, J., Sampson, J., Bai, D., and Laird, D.W. (2012). The G60S Cx43 mutant enhances keratinocyte proliferation and differentiation. Exp Dermatol *21*, 612-618.

Churko, J.M., and Laird, D.W. (2013). Gap Junction Remodeling in Skin Repair Following Wounding and Disease. Physiology *28*, 190-198.

Churko, J.M., Langlois, S., Pan, X., Shao, Q., and Laird, D.W. (2010). The potency of the fs260 connexin43 mutant to impair keratinocyte differentiation is distinct from other disease-linked connexin43 mutants. Biochem J *429*, 473-483.

Coggshall, K., Farsani, T., Ruben, B., McCalmont, T.H., Berger, T.G., Fox, L.P., and Shinkai, K. (2013). Keratitis, ichthyosis, and deafness syndrome: a review of infectious and neoplastic complications. Journal of the American Academy of Dermatology *69*, 127-134.

Cohen-Salmon, M., Ott, T., Michel, V., Hardelin, J.P., Perfettini, I., Eybalin, M., Wu, T., Marcus, D.C., Wangemann, P., Willecke, K., *et al.* (2002). Targeted ablation of connexin26 in the inner ear epithelial gap junction network causes hearing impairment and cell death. Curr Biol *12*, 1106-1111.

Common, J.E., Di, W.L., Davies, D., and Kelsell, D.P. (2004). Further evidence for heterozygote advantage of GJB2 deafness mutations: a link with cell survival. J Med Genet *41*, 573-575.

Conrado, L.A., Marques, S.A., Lastoria, J.C., Cuce, L.C., Marques, M.E., and Dillon, N.L. (2007). Keratitis-ichthyosis-deafness (KID) syndrome with squamous cell carcinoma. International journal of dermatology *46*, 403-406.

Contreras, J.E., Saez, J.C., Bukauskas, F.F., and Bennett, M.V. (2003). Gating and regulation of connexin 43 (Cx43) hemichannels. Proc Natl Acad Sci U S A *100*, 11388-11393.

Cotrina, M.L., Lin, J.H., Alves-Rodrigues, A., Liu, S., Li, J., Azmi-Ghadimi, H., Kang, J., Naus, C.C., and Nedergaard, M. (1998). Connexins regulate calcium signaling by controlling ATP release. Proc Natl Acad Sci U S A *95*, 15735-15740.

Cottrell, G.T., and Burt, J.M. (2005). Functional consequences of heterogeneous gap junction channel formation and its influence in health and disease. Biochim Biophys Acta *1711*, 126-141.

Cottrell, G.T., Wu, Y., and Burt, J.M. (2001). Functional characteristics of heteromeric Cx40-Cx43 gap junction channel formation. Cell communication & adhesion *8*, 193-197.

Coutinho, P., Qiu, C., Frank, S., Tamber, K., and Becker, D. (2003). Dynamic changes in connexin expression correlate with key events in the wound healing process. Cell biology international *27*, 525-541.

Criscione, V., Lachiewicz, A., Robinson-Bostom, L., Grenier, N., and Dill, S.W. (2010). Porokeratotic eccrine duct and hair follicle nevus (PEHFN) associated with keratitis-ichthyosis-deafness (KID) syndrome. Pediatric dermatology *27*, 514-517.

Cruikshank, S.J., Hopperstad, M., Younger, M., Connors, B.W., Spray, D.C., and Srinivas, M. (2004). Potent block of Cx36 and Cx50 gap junction channels by mefloquine. Proc Natl Acad Sci U S A *101*, 12364-12369.

D'Adamo, P., Guerci, V.I., Fabretto, A., Faletra, F., Grasso, D.L., Ronfani, L., Montico, M., Morgutti, M., Guastalla, P., and Gasparini, P. (2009). Does epidermal thickening explain GJB2 high carrier frequency and heterozygote advantage? Eur J Hum Genet *17*, 284-286.

Davidson, B.L., and McCray, P.B., Jr. (2011). Current prospects for RNA interference-based therapies. Nat Rev Genet *12*, 329-340.

de Berker, D., Branford, W.A., Soucek, S., and Michaels, L. (1993). Fatal keratitis ichthyosis and deafness syndrome (KIDS). Aural, ocular, and cutaneous histopathology. Am J Dermatopathol *15*, 64-69.

De Vuyst, E., De Bock, M., Decrock, E., Van Moorhem, M., Naus, C., Mabilde, C., and Leybaert, L. (2008). In situ bipolar electroporation for localized cell loading with reporter dyes and investigating gap junctional coupling. Biophys J *94*, 469-479.

de Wolf, E., van de Wiel, J., Cook, J., and Dale, N. (2016). Altered CO2 sensitivity of connexin26 mutant hemichannels in vitro. Physiol Rep *4*.

de Zwart-Storm, E.A., Rosa, R.F., Martin, P.E., Foelster-Holst, R., Frank, J., Bau, A.E., Zen, P.R., Graziadio, C., Paskulin, G.A., Kamps, M.A., *et al.* (2011a). Molecular analysis of connexin26 asparagine14 mutations associated with syndromic skin phenotypes. Exp Dermatol *20*, 408-412.

de Zwart-Storm, E.A., van Geel, M., Veysey, E., Burge, S., Cooper, S., Steijlen, P.M., Martin, P.E., and van Steensel, M.A. (2011b). A novel missense mutation in GJB2, p.Tyr65His, causes severe Vohwinkel syndrome. The British journal of dermatology *164*, 197-199.

Delmar, M., Laird, D.W., Naus, C.C., Nielsen, M.S., Verselis, V.K., and White, T.W. (2017). Connexins and Disease. Cold Spring Harbor Perspectives in Biology, a029348.

Desai, P., Patlolla, R.R., and Singh, M. (2010). Interaction of nanoparticles and cell-penetrating peptides with skin for transdermal drug delivery. Mol Membr Biol *27*, 247-259.

Desai, P.R., Marepally, S., Patel, A.R., Voshavar, C., Chaudhuri, A., and Singh, M. (2013). Topical delivery of anti-TNFalpha siRNA and capsaicin via novel lipid-polymer hybrid nanoparticles efficiently inhibits skin inflammation in vivo. J Control Release *170*, 51-63.

Desplantez, T., Verma, V., Leybaert, L., Evans, W.H., and Weingart, R. (2012). Gap26, a connexin mimetic peptide, inhibits currents carried by connexin43 hemichannels and gap junction channels. Pharmacological research : the official journal of the Italian Pharmacological Society *65*, 546-552.

DeVries, S.H., and Schwartz, E.A. (1992). Hemi-gap-junction channels in solitary horizontal cells of the catfish retina. J Physiol *445*, 201-230.

Di, W.L., Common, J.E., and Kelsell, D.P. (2001a). Connexin 26 expression and mutation analysis in epidermal disease. Cell communication & adhesion *8*, 415-418.

Di, W.L., Gu, Y., Common, J.E., Aasen, T., O'Toole, E.A., Kelsell, D.P., and Zicha, D. (2005). Connexin interaction patterns in keratinocytes revealed morphologically and by FRET analysis. J Cell Sci *118*, 1505-1514.

Di, W.L., Lachelin, G.C., McGarrigle, H.H., Thomas, N.S., and Becker, D.L. (2001b). Oestriol and oestradiol increase cell to cell communication and connexin43 protein expression in human myometrium. Mol Hum Reprod *7*, 671-679.

Di, W.L., Monypenny, J., Common, J.E., Kennedy, C.T., Holland, K.A., Leigh, I.M., Rugg, E.L., Zicha, D., and Kelsell, D.P. (2002). Defective trafficking and cell death is characteristic of skin disease-associated connexin 31 mutations. Hum Mol Genet *11*, 2005-2014.

Di, W.L., Rugg, E.L., Leigh, I.M., and Kelsell, D.P. (2001c). Multiple epidermal

connexins are expressed in different keratinocyte subpopulations including connexin 31. J Invest Dermatol *117*, 958-964.

Dicke, N., Pielensticker, N., Degen, J., Hecker, J., Tress, O., Bald, T., Gellhaus, A., Winterhager, E., and Willecke, K. (2011). Peripheral lymphangiogenesis in mice depends on ectodermal connexin-26 (Gjb2). J Cell Sci *124*, 2806-2815.

Dickson, M.A., Hahn, W.C., Ino, Y., Ronfard, V., Wu, J.Y., Weinberg, R.A., Louis, D.N., Li, F.P., and Rheinwald, J.G. (2000). Human keratinocytes that express hTERT and also bypass a p16(INK4a)-enforced mechanism that limits life span become immortal yet retain normal growth and differentiation characteristics. Mol Cell Biol *20*, 1436-1447.

Diestel, S., Richard, G., Doring, B., and Traub, O. (2002). Expression of a connexin31 mutation causing erythrokeratodermia variabilis is lethal for HeLa cells. Biochem Biophys Res Commun *296*, 721-728.

Djalilian, A.R., Kim, J.Y., Saeed, H.N., Holland, E.J., and Chan, C.C. (2010). Histopathology and treatment of corneal disease in keratitis, ichthyosis, and deafness (KID) syndrome. Eye *24*, 738-740.

Djalilian, A.R., McGaughey, D., Patel, S., Seo, E.Y., Yang, C., Cheng, J., Tomic, M., Sinha, S., Ishida-Yamamoto, A., and Segre, J.A. (2006). Connexin 26 regulates epidermal barrier and wound remodeling and promotes psoriasiform response. J Clin Invest *116*, 1243-1253.

Donnelly, S., English, G., de Zwart-Storm, E.A., Lang, S., van Steensel, M.A., and Martin, P.E. (2012). Differential susceptibility of Cx26 mutations associated with epidermal dysplasias to peptidoglycan derived from Staphylococcus aureus and Staphylococcus epidermidis. Exp Dermatol *21*, 592-598.

Easton, J.A., Donnelly, S., Kamps, M.A., Steijlen, P.M., Martin, P.E., Tadini, G., Janssens, R., Happle, R., van Geel, M., and van Steensel, M.A. (2012). Porokeratotic eccrine nevus may be caused by somatic connexin26 mutations. J Invest Dermatol *132*, 2184-2191.

Eghbali, B., Kessler, J.A., Reid, L.M., Roy, C., and Spray, D.C. (1991). Involvement of gap junctions in tumorigenesis: transfection of tumor cells with connexin 32 cDNA retards growth in vivo. Proc Natl Acad Sci U S A *88*, 10701-10705.

el-Fouly, M.H., Trosko, J.E., and Chang, C.C. (1987). Scrape-loading and dye transfer. A rapid and simple technique to study gap junctional intercellular communication. Exp Cell Res *168*, 422-430.

Elbashir, S.M., Harborth, J., Lendeckel, W., Yalcin, A., Weber, K., and Tuschl, T. (2001a). Duplexes of 21-nucleotide RNAs mediate RNA interference in cultured mammalian cells. Nature *411*, 494-498.

Elbashir, S.M., Martinez, J., Patkaniowska, A., Lendeckel, W., and Tuschl, T. (2001b). Functional anatomy of siRNAs for mediating efficient RNAi in Drosophila melanogaster embryo lysate. The EMBO journal *20*, 6877-6888.

Elfgang, C., Eckert, R., Lichtenberg-Frate, H., Butterweck, A., Traub, O., Klein, R.A., Hulser, D.F., and Willecke, K. (1995). Specific permeability and selective formation of gap junction channels in connexin-transfected HeLa cells. The Journal of cell biology *129*, 805-817.

Elias, P., Ahn, S., Brown, B., Crumrine, D., and Feingold, K.R. (2002). Origin of the

epidermal calcium gradient: regulation by barrier status and role of active vs passive mechanisms. J Invest Dermatol *119*, 1269-1274.

Elias, P.M., Williams, M.L., and Feingold, K.R. (2012). Abnormal barrier function in the pathogenesis of ichthyosis: therapeutic implications for lipid metabolic disorders. Clinics in dermatology *30*, 311-322.

Elsholz, F., Harteneck, C., Muller, W., and Friedland, K. (2014). Calcium--a central regulator of keratinocyte differentiation in health and disease. European journal of dermatology : EJD *24*, 650-661.

Essenfelder, G.M., Bruzzone, R., Lamartine, J., Charollais, A., Blanchet-Bardon, C., Barbe, M.T., Meda, P., and Waksman, G. (2004). Connexin30 mutations responsible for hidrotic ectodermal dysplasia cause abnormal hemichannel activity. Hum Mol Genet *13*, 1703-1714.

Evans, W.H., Bultynck, G., and Leybaert, L. (2012). Manipulating Connexin Communication Channels: Use of Peptidomimetics and the Translational Outputs. The Journal of Membrane Biology *245*, 437-449.

Fallon, R.F., and Goodenough, D.A. (1981). Five-hour half-life of mouse liver gap-junction protein. The Journal of cell biology *90*, 521-526.

Fedorov, Y., Anderson, E.M., Birmingham, A., Reynolds, A., Karpilow, J., Robinson, K., Leake, D., Marshall, W.S., and Khvorova, A. (2006). Off-target effects by siRNA can induce toxic phenotype. RNA *12*, 1188-1196.

Fentiman, I.S., and Taylor-Papadimitriou, J. (1977). Cultured human breast cancer cells lose selectivity in direct intercellular communication. Nature *269*, 156-158.

Fire, A., Xu, S., Montgomery, M.K., Kostas, S.A., Driver, S.E., and Mello, C.C. (1998). Potent and specific genetic interference by double-stranded RNA in Caenorhabditis elegans. Nature *391*, 806-811.

Ford, S.R., Chenault, K.H., Bunton, L.S., Hampton, G.J., McCarthy, J., Hall, M.S., Pangburn, S.J., Buck, L.M., and Leach, F.R. (1996). Use of firefly luciferase for ATP measurement: other nucleotides enhance turnover. J Biolumin Chemilumin *11*, 149-167.

Franceschini, A., Szklarczyk, D., Frankild, S., Kuhn, M., Simonovic, M., Roth, A., Lin, J., Minguez, P., Bork, P., von Mering, C., *et al.* (2013). STRING v9.1: protein-protein interaction networks, with increased coverage and integration. Nucleic acids research *41*, D808-815.

Fukuda, M., Kaneko, N., Kawaguchi, K., Hevroy, E.M., Hara, A., and Shimizu, M. (2015). Development of a time-resolved fluoroimmunoassay for salmon insulin-like growth factor binding protein-1b. Comp Biochem Physiol A Mol Integr Physiol *187*, 66-73.

Gabriel, H.D., Jung, D., Butzler, C., Temme, A., Traub, O., Winterhager, E., and Willecke, K. (1998). Transplacental uptake of glucose is decreased in embryonic lethal connexin26-deficient mice. The Journal of cell biology *140*, 1453-1461.

Gan, X., Wong, B., Wright, S.D., and Cai, T.Q. (2001). Production of matrix metalloproteinase-9 in CaCO-2 cells in response to inflammatory stimuli. J Interferon Cytokine Res *21*, 93-98.

Garcia, I.E., Bosen, F., Mujica, P., Pupo, A., Flores-Munoz, C., Jara, O., Gonzalez, C.,

Willecke, K., and Martinez, A.D. (2016). From Hyperactive Connexin26 Hemichannels to Impairments in Epidermal Calcium Gradient and Permeability Barrier in the Keratitis-Ichthyosis-Deafness Syndrome. J Invest Dermatol *136*, 574-583.

Garcia, I.E., Maripillan, J., Jara, O., Ceriani, R., Palacios-Munoz, A., Ramachandran, J., Olivero, P., Perez-Acle, T., Gonzalez, C., Saez, J.C., *et al.* (2015). Keratitis-ichthyosis-deafness syndrome-associated Cx26 mutants produce nonfunctional gap junctions but hyperactive hemichannels when co-expressed with wild type Cx43. J Invest Dermatol *135*, 1338-1347.

Garcia, I.E., Villanelo, F., Contreras, G.F., Pupo, A., Pinto, B.I., Contreras, J.E., Perez-Acle, T., Alvarez, O., Latorre, R., Martinez, A.D., *et al.* (2018). The syndromic deafness mutation G12R impairs fast and slow gating in Cx26 hemichannels. J Gen Physiol.

Garrod, D., and Chidgey, M. (2008). Desmosome structure, composition and function. Biochim Biophys Acta *1778*, 572-587.

Gassmann, O., Kreir, M., Ambrosi, C., Pranskevich, J., Oshima, A., Roling, C., Sosinsky, G., Fertig, N., and Steinem, C. (2009). The M34A mutant of Connexin26 reveals active conductance states in pore-suspending membranes. J Struct Biol *168*, 168-176.

Gemel, J., Valiunas, V., Brink, P.R., and Beyer, E.C. (2004). Connexin43 and connexin26 form gap junctions, but not heteromeric channels in co-expressing cells. J Cell Sci *117*, 2469-2480.

Gerido, D.A., DeRosa, A.M., Richard, G., and White, T.W. (2007). Aberrant hemichannel properties of Cx26 mutations causing skin disease and deafness. Am J Physiol Cell Physiol *293*, C337-345.

Giaume, C., Leybaert, L., Naus, C.C., and Saez, J.C. (2013). Connexin and pannexin hemichannels in brain glial cells: properties, pharmacology, and roles. Front Pharmacol *4*, 88.

Gilliam, A., and Williams, M.L. (2002). Fatal septicemia in an infant with keratitis, ichthyosis, and deafness (KID) syndrome. Pediatric dermatology *19*, 232-236.

Goldberg, G.S., Bechberger, J.F., and Naus, C.C. (1995). A pre-loading method of evaluating gap junctional communication by fluorescent dye transfer. Biotechniques *18*, 490-497.

Goldberg, G.S., Lampe, P.D., Sheedy, D., Stewart, C.C., Nicholson, B.J., and Naus, C.C. (1998). Direct isolation and analysis of endogenous transjunctional ADP from Cx43 transfected C6 glioma cells. Exp Cell Res *239*, 82-92.

Goliger, J.A., and Paul, D.L. (1995). Wounding alters epidermal connexin expression and gap junction-mediated intercellular communication. Mol Biol Cell *6*, 1491-1501.

Greig, A.V., Linge, C., Cambrey, A., and Burnstock, G. (2003). Purinergic receptors are part of a signaling system for keratinocyte proliferation, differentiation, and apoptosis in human fetal epidermis. J Invest Dermatol *121*, 1145-1149.

Grek, C.L., Montgomery, J., Sharma, M., Ravi, A., Rajkumar, J.S., Moyer, K.E., Gourdie, R.G., and Ghatnekar, G.S. (2017). A Multicenter Randomized Controlled Trial Evaluating a Cx43-Mimetic Peptide in Cutaneous Scarring. J Invest Dermatol *137*, 620-630.

Grek, C.L., Prasad, G.M., Viswanathan, V., Armstrong, D.G., Gourdie, R.G., and Ghatnekar, G.S. (2015). Topical administration of a connexin43-based peptide augments healing of chronic neuropathic diabetic foot ulcers: A multicenter, randomized trial. Wound repair and regeneration : official publication of the Wound Healing Society [and] the European Tissue Repair Society *23*, 203-212.

Grek, C.L., Rhett, J.M., and Ghatnekar, G.S. (2014). Cardiac to cancer: connecting connexins to clinical opportunity. FEBS Lett *588*, 1349-1364.

Gribble, F.M., Davis, T.M., Higham, C.E., Clark, A., and Ashcroft, F.M. (2000). The antimalarial agent mefloquine inhibits ATP-sensitive K-channels. British journal of pharmacology *131*, 756-760.

Griffith, A.J., Yang, Y., Pryor, S.P., Park, H.J., Jabs, E.W., Nadol, J.B., Jr., Russell, L.J., Wasserman, D.I., Richard, G., Adams, J.C., *et al.* (2006). Cochleosaccular dysplasia associated with a connexin 26 mutation in keratitis-ichthyosis-deafness syndrome. The Laryngoscope *116*, 1404-1408.

Guastalla, P., Guerci, V.I., Fabretto, A., Faletra, F., Grasso, D.L., Zocconi, E., Stefanidou, D., D'Adamo, P., Ronfani, L., Montico, M., *et al.* (2009). Detection of epidermal thickening in GJB2 carriers with epidermal US. Radiology *251*, 280-286.

Gudmundsson, S., Wilbe, M., Ekvall, S., Ameur, A., Cahill, N., Alexandrov, L.B., Virtanen, M., Hellstrom Pigg, M., Vahlquist, A., Torma, H., *et al.* (2017). Revertant mosaicism repairs skin lesions in a patient with keratitis-ichthyosis-deafness syndrome by second-site mutations in connexin 26. Hum Mol Genet *26*, 1070-1077.

Haass, N.K., Ripperger, D., Wladykowski, E., Dawson, P., Gimotty, P.A., Blome, C., Fischer, F., Schmage, P., Moll, I., and Brandner, J.M. (2010). Melanoma progression exhibits a significant impact on connexin expression patterns in the epidermal tumor microenvironment. Histochem Cell Biol *133*, 113-124.

Haass, N.K., Wladykowski, E., Kief, S., Moll, I., and Brandner, J.M. (2006). Differential induction of connexins 26 and 30 in skin tumors and their adjacent epidermis. The journal of histochemistry and cytochemistry : official journal of the Histochemistry Society *54*, 171-182.

Hannon, G.J. (2002). RNA interference. Nature *418*, 244-251.

Haruna, K., Suga, Y., Oizumi, A., Mizuno, Y., Endo, H., Shimizu, T., Hasegawa, T., and Ikeda, S. (2010). Severe form of keratitis-ichthyosis-deafness (KID) syndrome associated with septic complications. The Journal of dermatology *37*, 680-682.

Hattori, Y., Date, M., Arai, S., Kawano, K., Yonemochi, E., and Maitani, Y. (2013). Transdermal Delivery of Small Interfering RNA with Elastic Cationic Liposomes in Mice. J Pharm (Cairo) *2013*, 149695.

Heckl, D., Schwarzer, A., Haemmerle, R., Steinemann, D., Rudolph, C., Skawran, B., Knoess, S., Krause, J., Li, Z., Schlegelberger, B., *et al.* (2012). Lentiviral vector induced insertional haploinsufficiency of Ebf1 causes murine leukemia. Mol Ther *20*, 1187-1195.

Hegde, V., Hickerson, R.P., Nainamalai, S., Campbell, P.A., Smith, F.J., McLean, W.H., and Pedrioli, D.M. (2014). In vivo gene silencing following non-invasive siRNA delivery into the skin using a novel topical formulation. J Control Release *196*, 355-362.

Hickerson, R.P., Smith, F.J., Reeves, R.E., Contag, C.H., Leake, D., Leachman, S.A.,

Milstone, L.M., McLean, W.H., and Kaspar, R.L. (2008). Single-nucleotide-specific siRNA targeting in a dominant-negative skin model. J Invest Dermatol *128*, 594-605.

Hsu, M., Andl, T., Li, G., Meinkoth, J.L., and Herlyn, M. (2000). Cadherin repertoire determines partner-specific gap junctional communication during melanoma progression. J Cell Sci *113 (Pt 9)*, 1535-1542.

Hsu, P.D., Lander, E.S., and Zhang, F. (2014). Development and applications of CRISPR-Cas9 for genome engineering. Cell *157*, 1262-1278.

Huang, J., Vendramin, S., Shi, L., and McGinnis, K.M. (2017a). Construction and Optimization of a Large Gene Coexpression Network in Maize Using RNA-Seq Data. Plant Physiol *175*, 568-583.

Huang, R., Lin, Y., Wang, C.C., Gano, J., Lin, B., Shi, Q., Boynton, A., Burke, J., and Huang, R.P. (2002). Connexin 43 suppresses human glioblastoma cell growth by down-regulation of monocyte chemotactic protein 1, as discovered using protein array technology. Cancer Res *62*, 2806-2812.

Huang, Y., Pan, J., Chen, D., Zheng, J., Qiu, F., Li, F., Wu, Y., Wu, W., Huang, X., and Qian, J. (2017b). Identification and functional analysis of differentially expressed genes in poorly differentiated hepatocellular carcinoma using RNA-seq. Oncotarget *8*, 35973-35983.

Iglesias, R., Spray, D.C., and Scemes, E. (2009). Mefloquine blockade of Pannexin1 currents: resolution of a conflict. Cell communication & adhesion *16*, 131-137.

Iossa, S., Chinetti, V., Auletta, G., Laria, C., De Luca, M., Rienzo, M., Giannini, P., Delfino, M., Ciccodicola, A., Marciano, E., *et al.* (2009). New evidence for the correlation of the p.G130V mutation in the GJB2 gene and syndromic hearing loss with palmoplantar keratoderma. American journal of medical genetics Part A *149A*, 685-688.

Ito, A., Katoh, F., Kataoka, T.R., Okada, M., Tsubota, N., Asada, H., Yoshikawa, K., Maeda, S., Kitamura, Y., Yamasaki, H., *et al.* (2000). A role for heterologous gap junctions between melanoma and endothelial cells in metastasis. J Clin Invest *105*, 1189-1197.

Jackson, A.L., Bartz, S.R., Schelter, J., Kobayashi, S.V., Burchard, J., Mao, M., Li, B., Cavet, G., and Linsley, P.S. (2003). Expression profiling reveals off-target gene regulation by RNAi. Nat Biotechnol *21*, 635-637.

Jackson, A.L., Burchard, J., Schelter, J., Chau, B.N., Cleary, M., Lim, L., and Linsley, P.S. (2006). Widespread siRNA "off-target" transcript silencing mediated by seed region sequence complementarity. RNA *12*, 1179-1187.

Jackson, A.L., and Linsley, P.S. (2010). Recognizing and avoiding siRNA off-target effects for target identification and therapeutic application. Nat Rev Drug Discov *9*, 57-67.

Jagger, D.J., and Forge, A. (2015). Connexins and gap junctions in the inner ear--it's not just about K(+) recycling. Cell Tissue Res *360*, 633-644.

James, G., and Butt, A.M. (2001). P2X and P2Y purinoreceptors mediate ATP-evoked calcium signalling in optic nerve glia in situ. Cell Calcium *30*, 251-259.

Jan, A.Y., Amin, S., Ratajczak, P., Richard, G., and Sybert, V.P. (2004). Genetic heterogeneity of KID syndrome: identification of a Cx30 gene (GJB6) mutation in a

patient with KID syndrome and congenital atrichia. J Invest Dermatol *122*, 1108-1113.

Janecke, A.R., Hennies, H.C., Gunther, B., Gansl, G., Smolle, J., Messmer, E.M., Utermann, G., and Rittinger, O. (2005). GJB2 mutations in keratitis-ichthyosis-deafness syndrome including its fatal form. American journal of medical genetics Part A *133A*, 128-131.

Jin, L., Zuo, X.Y., Su, W.Y., Zhao, X.L., Yuan, M.Q., Han, L.Z., Zhao, X., Chen, Y.D., and Rao, S.Q. (2014). Pathway-based analysis tools for complex diseases: a review. Genomics Proteomics Bioinformatics *12*, 210-220.

Johnson, R.G., and Sheridan, J.D. (1971). Junctions between cancer cells in culture: ultrastructure and permeability. Science *174*, 717-719.

Johnstone, S.R., Billaud, M., Lohman, A.W., Taddeo, E.P., and Isakson, B.E. (2012). Posttranslational modifications in connexins and pannexins. J Membr Biol *245*, 319-332.

Jonard, L., Feldmann, D., Parsy, C., Freitag, S., Sinico, M., Koval, C., Grati, M., Couderc, R., Denoyelle, F., Bodemer, C., *et al.* (2008). A familial case of Keratitis-Ichthyosis-Deafness (KID) syndrome with the GJB2 mutation G45E. European journal of medical genetics *51*, 35-43.

Jose, A., Labala, S., and Venuganti, V.V. (2017). Co-delivery of curcumin and STAT3 siRNA using deformable cationic liposomes to treat skin cancer. J Drug Target *25*, 330-341.

Judge, A.D., Bola, G., Lee, A.C., and MacLachlan, I. (2006). Design of noninflammatory synthetic siRNA mediating potent gene silencing in vivo. Mol Ther *13*, 494-505.

Judge, A.D., Sood, V., Shaw, J.R., Fang, D., McClintock, K., and MacLachlan, I. (2005). Sequence-dependent stimulation of the mammalian innate immune response by synthetic siRNA. Nat Biotechnol *23*, 457-462.

Kalra, J., Shao, Q., Qin, H., Thomas, T., Alaoui-Jamali, M.A., and Laird, D.W. (2006). Cx26 inhibits breast MDA-MB-435 cell tumorigenic properties by a gap junctional intercellular communication-independent mechanism. Carcinogenesis *27*, 2528-2537.

Kam, E., Melville, L., and Pitts, J.D. (1986). Patterns of junctional communication in skin. J Invest Dermatol *87*, 748-753.

Kamibayashi, Y., Oyamada, M., Oyamada, Y., and Mori, M. (1993). Expression of gap junction proteins connexin 26 and 43 is modulated during differentiation of keratinocytes in newborn mouse epidermis. J Invest Dermatol *101*, 773-778.

Kanaporis, G., Brink, P.R., and Valiunas, V. (2011). Gap junction permeability: selectivity for anionic and cationic probes. Am J Physiol Cell Physiol *300*, C600-609.

Kandyba, E.E., Hodgins, M.B., and Martin, P.E. (2008). A murine living skin equivalent amenable to live-cell imaging: analysis of the roles of connexins in the epidermis. J Invest Dermatol *128*, 1039-1049.

Kanno, Y., and Loewenstein, W.R. (1964). Intercellular Diffusion. Science *143*, 959-960.

Katakowski, M., Buller, B., Wang, X., Rogers, T., and Chopp, M. (2010). Functional microRNA is transferred between glioma cells. Cancer Res *70*, 8259-8263.

Kaur, P., and McDougall, J.K. (1988). Characterization of primary human keratinocytes transformed by human papillomavirus type 18. J Virol *62*, 1917-1924.

Kelsell, D.P., Dunlop, J., Stevens, H.P., Lench, N.J., Liang, J.N., Parry, G., Mueller, R.F., and Leigh, I.M. (1997). Connexin 26 mutations in hereditary non-syndromic sensorineural deafness. Nature *387*, 80-83.

Kenski, D.M., Butora, G., Willingham, A.T., Cooper, A.J., Fu, W., Qi, N., Soriano, F., Davies, I.W., and Flanagan, W.M. (2012). siRNA-optimized Modifications for Enhanced In Vivo Activity. Mol Ther Nucleic Acids *1*, e5.

Kikuchi, Y., Tamai, K., and Kaneda, Y. (2008). Cutaneous gene delivery. J Dermatol Sci *50*, 87-98.

Kim, B.J., Kim, Y.J., Yoo, K.H., Park, K.Y., Kim, M.N., Song, K.Y., and Mun, S.K. (2008). Keratitis-ichthyosis-deafness syndrome with unusual hypopigmentation. The Journal of dermatology *35*, 798-800.

Kim, K.H., Kim, J.S., Piao, Y.J., Kim, Y.C., Shur, K.B., Lee, J.H., and Park, J.K. (2002). Keratitis, ichthyosis and deafness syndrome with development of multiple hair follicle tumours. The British journal of dermatology *147*, 139-143.

Koppelhus, U., Tranebjaerg, L., Esberg, G., Ramsing, M., Lodahl, M., Rendtorff, N.D., Olesen, H.V., and Sommerlund, M. (2011). A novel mutation in the connexin 26 gene (GJB2) in a child with clinical and histological features of keratitis-ichthyosis-deafness (KID) syndrome. Clin Exp Dermatol *36*, 142-148.

Koval, M., Molina, S.A., and Burt, J.M. (2014). Mix and match: investigating heteromeric and heterotypic gap junction channels in model systems and native tissues. FEBS Lett *588*, 1193-1204.

Kramer, A., Green, J., Pollard, J., Jr., and Tugendreich, S. (2014). Causal analysis approaches in Ingenuity Pathway Analysis. Bioinformatics *30*, 523-530.

Krampert, M., Bloch, W., Sasaki, T., Bugnon, P., Rulicke, T., Wolf, E., Aumailley, M., Parks, W.C., and Werner, S. (2004). Activities of the matrix metalloproteinase stromelysin-2 (MMP-10) in matrix degradation and keratinocyte organization in wounded skin. Mol Biol Cell *15*, 5242-5254.

Kretz, M., Euwens, C., Hombach, S., Eckardt, D., Teubner, B., Traub, O., Willecke, K., and Ott, T. (2003). Altered connexin expression and wound healing in the epidermis of connexin-deficient mice. J Cell Sci *116*, 3443-3452.

Kruger, O., Plum, A., Kim, J.S., Winterhager, E., Maxeiner, S., Hallas, G., Kirchhoff, S., Traub, O., Lamers, W.H., and Willecke, K. (2000). Defective vascular development in connexin 45-deficient mice. Development *127*, 4179-4193.

Krutovskikh, V.A., Piccoli, C., and Yamasaki, H. (2002). Gap junction intercellular communication propagates cell death in cancerous cells. Oncogene *21*, 1989-1999.

Kumar, N.M., and Gilula, N.B. (1992). Molecular biology and genetics of gap junction channels. Semin Cell Biol *3*, 3-16.

Kumar, S.A., Lester, M.R., and Bratton, D.L. (1996). KID syndrome associated with elevated sweat chloride. Pediatric pulmonology *21*, 192-194.

Kurjiaka, D.T., Steele, T.D., Olsen, M.V., and Burt, J.M. (1998). Gap junction permeability is diminished in proliferating vascular smooth muscle cells. Am J Physiol *275*, C1674-1682.

Labarthe, M.P., Bosco, D., Saurat, J.H., Meda, P., and Salomon, D. (1998). Upregulation of connexin 26 between keratinocytes of psoriatic lesions. J Invest Dermatol *111*, 72-76.

Laird, D.W. (2006). Life cycle of connexins in health and disease. Biochem J *394*, 527-543.

Laird, D.W. (2014). Syndromic and non-syndromic disease-linked Cx43 mutations. FEBS Lett *588*, 1339-1348.

Laird, D.W., Castillo, M., and Kasprzak, L. (1995). Gap junction turnover, intracellular trafficking, and phosphorylation of connexin43 in brefeldin A-treated rat mammary tumor cells. The Journal of cell biology *131*, 1193-1203.

Lamartine, J., Munhoz Essenfelder, G., Kibar, Z., Lanneluc, I., Callouet, E., Laoudj, D., Lemaitre, G., Hand, C., Hayflick, S.J., Zonana, J., *et al.* (2000). Mutations in GJB6 cause hidrotic ectodermal dysplasia. Nat Genet *26*, 142-144.

Lawrence, T.S., Beers, W.H., and Gilula, N.B. (1978). Transmission of hormonal stimulation by cell-to-cell communication. Nature *272*, 501-506.

Lazic, T., Horii, K.A., Richard, G., Wasserman, D.I., and Antaya, R.J. (2008). A report of GJB2 (N14K) Connexin 26 mutation in two patients--a new subtype of KID syndrome? Pediatric dermatology *25*, 535-540.

Lazic, T., Li, Q., Frank, M., Uitto, J., and Zhou, L.H. (2012). Extending the phenotypic spectrum of keratitis-ichthyosis-deafness syndrome: report of a patient with GJB2 (G12R) Connexin 26 mutation and unusual clinical findings. Pediatric dermatology *29*, 349-357.

Leachman, S.A., Hickerson, R.P., Schwartz, M.E., Bullough, E.E., Hutcherson, S.L., Boucher, K.M., Hansen, C.D., Eliason, M.J., Srivatsa, G.S., Kornbrust, D.J., *et al.* (2010). First-in-human mutation-targeted siRNA phase Ib trial of an inherited skin disorder. Mol Ther *18*, 442-446.

Lee, J.R., Derosa, A.M., and White, T.W. (2009). Connexin mutations causing skin disease and deafness increase hemichannel activity and cell death when expressed in Xenopus oocytes. J Invest Dermatol *129*, 870-878.

Lee, J.R., and White, T.W. (2009). Connexin-26 mutations in deafness and skin disease. Expert reviews in molecular medicine *11*, e35.

Leithe, E. (2016). Regulation of connexins by the ubiquitin system: Implications for intercellular communication and cancer. Biochim Biophys Acta *1865*, 133-146.

Leonard, N.J., Krol, A.L., Bleoo, S., and Somerville, M.J. (2005). Sensorineural hearing loss, striate palmoplantar hyperkeratosis, and knuckle pads in a patient with a novel connexin 26 (GJB2) mutation. J Med Genet *42*, e2.

Leslie Pedrioli, D.M., Fu, D.J., Gonzalez-Gonzalez, E., Contag, C.H., Kaspar, R.L., Smith, F.J., and McLean, W.H. (2012). Generic and personalized RNAi-based therapeutics for a dominant-negative epidermal fragility disorder. J Invest Dermatol *132*, 1627-1635.

Levit, N.A., Mese, G., Basaly, M.G., and White, T.W. (2012). Pathological hemichannels associated with human Cx26 mutations causing Keratitis-Ichthyosis-Deafness syndrome. Biochim Biophys Acta *1818*, 2014-2019.

Levit, N.A., Sellitto, C., Wang, H.Z., Li, L., Srinivas, M., Brink, P.R., and White, T.W.

(2015). Aberrant connexin26 hemichannels underlying keratitis-ichthyosis-deafness syndrome are potently inhibited by mefloquine. J Invest Dermatol *135*, 1033-1042.

Levit, N.A., and White, T.W. (2015). Connexin hemichannels influence genetically determined inflammatory and hyperproliferative skin diseases. Pharmacological Research *99*, 337-343.

Li, B., Tsoi, L.C., Swindell, W.R., Gudjonsson, J.E., Tejasvi, T., Johnston, A., Ding, J., Stuart, P.E., Xing, X., Kochkodan, J.J., *et al.* (2014). Transcriptome analysis of psoriasis in a large case-control sample: RNA-seq provides insights into disease mechanisms. J Invest Dermatol *134*, 1828-1838.

Li, Y., and Cassone, V.M. (2015). A simple, specific high-throughput enzyme-linked immunosorbent assay (ELISA) for quantitative determination of melatonin in cell culture medium. Int Immunopharmacol *28*, 230-234.

Lilly, E., Sellitto, C., Milstone, L.M., and White, T.W. (2016). Connexin channels in congenital skin disorders. Semin Cell Dev Biol *50*, 4-12.

Liu, J., Fang, S., Ding, Q., Wang, Y., Ye, T., Zhu, H., Zhang, X., Li, B., Xu, Y., and Li, Z. (2016a). Mutations of connexin 26 (GJB2) gene in a Chinese keratitis-ichthyosis-deafness syndrome patient with squamous cell carcinoma. The Journal of dermatology *43*, 104-106.

Liu, Y., Snedecor, E.R., Zhang, X., Xu, Y., Huang, L., Jones, E.C., Zhang, L., Clark, R.A., Roop, D.R., Qin, C., *et al.* (2016b). Correction of Hair Shaft Defects through Allele-Specific Silencing of Mutant Krt75. J Invest Dermatol *136*, 45-51.

Loewenstein, W.R., and Kanno, Y. (1966). Intercellular communication and the control of tissue growth: lack of communication between cancer cells. Nature *209*, 1248-1249.

Lohman, A.W., Billaud, M., and Isakson, B.E. (2012). Mechanisms of ATP release and signalling in the blood vessel wall. Cardiovasc Res *95*, 269-280.

Lohman, A.W., and Isakson, B.E. (2014). Differentiating connexin hemichannels and pannexin channels in cellular ATP release. FEBS Lett *588*, 1379-1388.

Lopez, W., Gonzalez, J., Liu, Y., Harris, A.L., and Contreras, J.E. (2013). Insights on the mechanisms of Ca(2+) regulation of connexin26 hemichannels revealed by human pathogenic mutations (D50N/Y). J Gen Physiol *142*, 23-35.

Love, M.I., Anders, S., Kim, V., and Huber, W. (2015). RNA-Seq workflow: gene-level exploratory analysis and differential expression. F1000Res *4*, 1070.

Lucke, T., Choudhry, R., Thom, R., Selmer, I.S., Burden, A.D., and Hodgins, M.B. (1999). Upregulation of connexin 26 is a feature of keratinocyte differentiation in hyperproliferative epidermis, vaginal epithelium, and buccal epithelium. J Invest Dermatol *112*, 354-361.

Ma, H., Liang, P., Chen, J., Feng, P., and Lai, W. (2017). Keratitis-ichthyosis-deafness syndrome accompanied by disseminated cutaneous fungal infection. The Journal of dermatology.

Maass, K., Ghanem, A., Kim, J.S., Saathoff, M., Urschel, S., Kirfel, G., Grummer, R., Kretz, M., Lewalter, T., Tiemann, K., *et al.* (2004). Defective epidermal barrier in neonatal mice lacking the C-terminal region of connexin43. Mol Biol Cell *15*, 4597-4608.

Macari, F., Landau, M., Cousin, P., Mevorah, B., Brenner, S., Panizzon, R., Schorderet, D.F., Hohl, D., and Huber, M. (2000). Mutation in the gene for connexin 30.3 in a family with erythrokeratodermia variabilis. American journal of human genetics *67*, 1296-1301.

Maeda, S., Nakagawa, S., Suga, M., Yamashita, E., Oshima, A., Fujiyoshi, Y., and Tsukihara, T. (2009). Structure of the connexin 26 gap junction channel at 3.5 A resolution. Nature *458*, 597-602.

Maeda, Y., Fukushima, K., Nishizaki, K., and Smith, R.J. (2005). In vitro and in vivo suppression of GJB2 expression by RNA interference. Hum Mol Genet *14*, 1641-1650.

Maestrini, E., Korge, B.P., Ocana-Sierra, J., Calzolari, E., Cambiaghi, S., Scudder, P.M., Hovnanian, A., Monaco, A.P., and Munro, C.S. (1999). A missense mutation in connexin26, D66H, causes mutilating keratoderma with sensorineural deafness (Vohwinkel's syndrome) in three unrelated families. Hum Mol Genet *8*, 1237-1243.

Maintz, L., Betz, R.C., Allam, J.P., Wenzel, J., Jaksche, A., Friedrichs, N., Bieber, T., and Novak, N. (2005). Keratitis-ichthyosis-deafness syndrome in association with follicular occlusion triad. European journal of dermatology : EJD *15*, 347-352.

Malchow, R.P., Qian, H., and Ripps, H. (1993). Evidence for hemi-gap junctional channels in isolated horizontal cells of the skate retina. J Neurosci Res *35*, 237-245.

Man, Y.K., Trolove, C., Tattersall, D., Thomas, A.C., Papakonstantinopoulou, A., Patel, D., Scott, C., Chong, J., Jagger, D.J., O'Toole, E.A., *et al.* (2007). A deafness-associated mutant human connexin 26 improves the epithelial barrier in vitro. J Membr Biol *218*, 29-37.

Mani, R.S., Ganapathy, A., Jalvi, R., Srikumari Srisailapathy, C.R., Malhotra, V., Chadha, S., Agarwal, A., Ramesh, A., Rangasayee, R.R., and Anand, A. (2009). Functional consequences of novel connexin 26 mutations associated with hereditary hearing loss. Eur J Hum Genet *17*, 502-509.

Martin, P.E., Easton, J.A., Hodgins, M.B., and Wright, C.S. (2014). Connexins: sensors of epidermal integrity that are therapeutic targets. FEBS Lett *588*, 1304-1314.

Martin, P.E., and van Steensel, M. (2015). Connexins and skin disease: insights into the role of beta connexins in skin homeostasis. Cell Tissue Res *360*, 645-658.

Martinez, A.D., Acuna, R., Figueroa, V., Maripillan, J., and Nicholson, B. (2009). Gap-junction channels dysfunction in deafness and hearing loss. Antioxid Redox Signal *11*, 309-322.

Martinez, L.A., Naguibneva, I., Lehrmann, H., Vervisch, A., Tchenio, T., Lozano, G., and Harel-Bellan, A. (2002). Synthetic small inhibiting RNAs: efficient tools to inactivate oncogenic mutations and restore p53 pathways. Proc Natl Acad Sci U S A *99*, 14849-14854.

Maruyama, T., Dougan, S.K., Truttmann, M.C., Bilate, A.M., Ingram, J.R., and Ploegh, H.L. (2015). Increasing the efficiency of precise genome editing with CRISPR-Cas9 by inhibition of nonhomologous end joining. Nat Biotechnol *33*, 538-542.

Marziano, N.K., Casalotti, S.O., Portelli, A.E., Becker, D.L., and Forge, A. (2003). Mutations in the gene for connexin 26 (GJB2) that cause hearing loss have a dominant negative effect on connexin 30. Hum Mol Genet *12*, 805-812.

Masgrau-Peya, E., Salomon, D., Saurat, J.H., and Meda, P. (1997). In vivo modulation

of connexins 43 and 26 of human epidermis by topical retinoic acid treatment. The journal of histochemistry and cytochemistry : official journal of the Histochemistry Society *45*, 1207-1215.

Matic, M., Evans, W.H., Brink, P.R., and Simon, M. (2002). Epidermal stem cells do not communicate through gap junctions. J Invest Dermatol *118*, 110-116.

Matranga, C., Tomari, Y., Shin, C., Bartel, D.P., and Zamore, P.D. (2005). Passenger-strand cleavage facilitates assembly of siRNA into Ago2-containing RNAi enzyme complexes. Cell *123*, 607-620.

Mauro, V.P., and Chappell, S.A. (2014). A critical analysis of codon optimization in human therapeutics. Trends Mol Med *20*, 604-613.

Mayama, H., Fujimura, T., Asano, M., Kambayashi, Y., Numata, Y., and Aiba, S. (2013). Squamous cell carcinoma arising from Keratitis-ichthyosis-deafness syndrome. Acta dermato-venereologica *93*, 583-584.

Mazereeuw-Hautier, J., Bitoun, E., Chevrant-Breton, J., Man, S.Y., Bodemer, C., Prins, C., Antille, C., Saurat, J.H., Atherton, D., Harper, J.I., *et al.* (2007). Keratitis-ichthyosis-deafness syndrome: disease expression and spectrum of connexin 26 (GJB2) mutations in 14 patients. The British journal of dermatology *156*, 1015-1019.

McCaffrey, A.P., Meuse, L., Pham, T.T., Conklin, D.S., Hannon, G.J., and Kay, M.A. (2002). RNA interference in adult mice. Nature *418*, 38-39.

McCarty, M.F., Bielenberg, D.R., Nilsson, M.B., Gershenwald, J.E., Barnhill, R.L., Ahearne, P., Bucana, C.D., and Fidler, I.J. (2003). Epidermal hyperplasia overlying human melanoma correlates with tumour depth and angiogenesis. Melanoma Res *13*, 379-387.

McGrath, J.A., McMillan, J.R., Shemanko, C.S., Runswick, S.K., Leigh, I.M., Lane, E.B., Garrod, D.R., and Eady, R.A. (1997). Mutations in the plakophilin 1 gene result in ectodermal dysplasia/skin fragility syndrome. Nat Genet *17*, 240-244.

McLachlan, E., Shao, Q., Wang, H.L., Langlois, S., and Laird, D.W. (2006). Connexins act as tumor suppressors in three-dimensional mammary cell organoids by regulating differentiation and angiogenesis. Cancer Res *66*, 9886-9894.

McNutt, N.S., and Weinstein, R.S. (1969). Carcinoma of the cervix: deficiency of nexus intercellular junctions. Science *165*, 597-599.

Meigh, L., Hussain, N., Mulkey, D.K., and Dale, N. (2014). Connexin26 hemichannels with a mutation that causes KID syndrome in humans lack sensitivity to CO2. Elife *3*, e04249.

Menon, G.K., and Elias, P.M. (1991). Ultrastructural localization of calcium in psoriatic and normal human epidermis. Archives of dermatology *127*, 57-63.

Mese, G., Richard, G., and White, T.W. (2007). Gap junctions: basic structure and function. J Invest Dermatol *127*, 2516-2524.

Mese, G., Sellitto, C., Li, L., Wang, H.Z., Valiunas, V., Richard, G., Brink, P.R., and White, T.W. (2011). The Cx26-G45E mutation displays increased hemichannel activity in a mouse model of the lethal form of keratitis-ichthyosis-deafness syndrome. Mol Biol Cell *22*, 4776-4786.

Messmer, E.M., Kenyon, K.R., Rittinger, O., Janecke, A.R., and Kampik, A. (2005). Ocular manifestations of keratitis-ichthyosis-deafness (KID) syndrome.

Ophthalmology *112*, e1-6.

Meyer, C.G., Amedofu, G.K., Brandner, J.M., Pohland, D., Timmann, C., and Horstmann, R.D. (2002). Selection for deafness? Nat Med *8*, 1332-1333.

Mhaske, P.V., Levit, N.A., Li, L., Wang, H.Z., Lee, J.R., Shuja, Z., Brink, P.R., and White, T.W. (2013). The human Cx26-D50A and Cx26-A88V mutations causing keratitis-ichthyosis-deafness syndrome display increased hemichannel activity. Am J Physiol Cell Physiol *304*, C1150-1158.

Michon, L., Nlend Nlend, R., Bavamian, S., Bischoff, L., Boucard, N., Caille, D., Cancela, J., Charollais, A., Charpantier, E., Klee, P., *et al.* (2005). Involvement of gap junctional communication in secretion. Biochim Biophys Acta *1719*, 82-101.

Miele, E., Spinelli, G.P., Miele, E., Di Fabrizio, E., Ferretti, E., Tomao, S., and Gulino, A. (2012). Nanoparticle-based delivery of small interfering RNA: challenges for cancer therapy. Int J Nanomedicine *7*, 3637-3657.

Montgomery, J.R., White, T.W., Martin, B.L., Turner, M.L., and Holland, S.M. (2004). A novel connexin 26 gene mutation associated with features of the keratitis-ichthyosis-deafness syndrome and the follicular occlusion triad. Journal of the American Academy of Dermatology *51*, 377-382.

Mori, R., Power, K.T., Wang, C.M., Martin, P., and Becker, D.L. (2006). Acute downregulation of connexin43 at wound sites leads to a reduced inflammatory response, enhanced keratinocyte proliferation and wound fibroblast migration. J Cell Sci *119*, 5193-5203.

Nagy, J.I., Li, X., Rempel, J., Stelmack, G., Patel, D., Staines, W.A., Yasumura, T., and Rash, J.E. (2001). Connexin26 in adult rodent central nervous system: demonstration at astrocytic gap junctions and colocalization with connexin30 and connexin43. J Comp Neurol *441*, 302-323.

Natsuga, K., Akiyama, M., and Shimizu, H. (2011). Malignant skin tumours in patients with inherited ichthyosis. The British journal of dermatology *165*, 263-268.

Naus, C.C., Elisevich, K., Zhu, D., Belliveau, D.J., and Del Maestro, R.F. (1992). In vivo growth of C6 glioma cells transfected with connexin43 cDNA. Cancer Res *52*, 4208-4213.

Naus, C.C., and Laird, D.W. (2010). Implications and challenges of connexin connections to cancer. Nature reviews Cancer *10*, 435-441.

Neoh, C.Y., Chen, H., Ng, S.K., Lane, E.B., and Common, J.E. (2009). A rare connexin 26 mutation in a patient with a forme fruste of keratitis-ichthyosis-deafness (KID) syndrome. International journal of dermatology *48*, 1078-1081.

Nestle, F.O., Di Meglio, P., Qin, J.Z., and Nickoloff, B.J. (2009). Skin immune sentinels in health and disease. Nat Rev Immunol *9*, 679-691.

Neyton, J., and Trautmann, A. (1985). Single-channel currents of an intercellular junction. Nature *317*, 331-335.

Nicolas, J.F., Jakob, H., and Jacob, F. (1978). Metabolic cooperation between mouse embryonal carcinoma cells and their differentiated derivatives. Proc Natl Acad Sci U S A *75*, 3292-3296.

Niessen, H., Harz, H., Bedner, P., Kramer, K., and Willecke, K. (2000). Selective permeability of different connexin channels to the second messenger inositol 1,4,5-

trisphosphate. J Cell Sci *113 (Pt 8)*, 1365-1372.

Nissinen, L., and Kahari, V.M. (2014). Matrix metalloproteinases in inflammation. Biochim Biophys Acta *1840*, 2571-2580.

Nyquist, G.G., Mumm, C., Grau, R., Crowson, A.N., Shurman, D.L., Benedetto, P., Allen, P., Lovelace, K., Smith, D.W., Frieden, I., *et al.* (2007). Malignant proliferating pilar tumors arising in KID syndrome: a report of two patients. American journal of medical genetics Part A *143A*, 734-741.

Ogawa, Y., Takeichi, T., Kono, M., Hamajima, N., Yamamoto, T., Sugiura, K., and Akiyama, M. (2014). Revertant mutation releases confined lethal mutation, opening Pandora's box: a novel genetic pathogenesis. PLoS genetics *10*, e1004276.

Paquet, D., Kwart, D., Chen, A., Sproul, A., Jacob, S., Teo, S., Olsen, K.M., Gregg, A., Noggle, S., and Tessier-Lavigne, M. (2016). Efficient introduction of specific homozygous and heterozygous mutations using CRISPR/Cas9. Nature *533*, 125-129.

Patel, V., Sun, G., Dickman, M., Khuu, P., and Teng, J.M. (2015). Treatment of keratitis-ichthyosis- deafness (KID) syndrome in children: a case report and review of the literature. Dermatologic therapy *28*, 89-93.

Paul, D.L., Ebihara, L., Takemoto, L.J., Swenson, K.I., and Goodenough, D.A. (1991). Connexin46, a novel lens gap junction protein, induces voltage-gated currents in nonjunctional plasma membrane of Xenopus oocytes. The Journal of cell biology *115*, 1077-1089.

Payton, B.W., Bennett, M.V., and Pappas, G.D. (1969). Permeability and structure of junctional membranes at an electrotonic synapse. Science *166*, 1641-1643.

Pendaries, V., Gasc, G., Titeux, M., Tonasso, L., Mejia, J.E., and Hovnanian, A. (2012). siRNA-mediated allele-specific inhibition of mutant type VII collagen in dominant dystrophic epidermolysis bullosa. J Invest Dermatol *132*, 1741-1743.

Petit, C., Levilliers, J., and Hardelin, J.P. (2001). Molecular genetics of hearing loss. Annu Rev Genet *35*, 589-646.

Pollmann, M.A., Shao, Q., Laird, D.W., and Sandig, M. (2005). Connexin 43 mediated gap junctional communication enhances breast tumor cell diapedesis in culture. Breast Cancer Res *7*, R522-534.

Pollok, S., Pfeiffer, A.C., Lobmann, R., Wright, C.S., Moll, I., Martin, P.E., and Brandner, J.M. (2011). Connexin 43 mimetic peptide Gap27 reveals potential differences in the role of Cx43 in wound repair between diabetic and non-diabetic cells. Journal of cellular and molecular medicine *15*, 861-873.

Polusani, S.R., Kalmykov, E.A., Chandrasekhar, A., Zucker, S.N., and Nicholson, B.J. (2016). Cell coupling mediated by connexin 26 selectively contributes to reduced adhesivity and increased migration. J Cell Sci *129*, 4399-4410.

Press, E., Alaga, K.C., Barr, K., Shao, Q., Bosen, F., Willecke, K., and Laird, D.W. (2017a). Disease-linked connexin26 S17F promotes volar skin abnormalities and mild wound healing defects in mice. Cell Death Dis *8*, e2845.

Press, E.R., Shao, Q., Kelly, J.J., Chin, K., Alaga, A., and Laird, D.W. (2017b). Induction of cell death and gain-of-function properties of connexin26 mutants predict severity of skin disorders and hearing loss. J Biol Chem *292*, 9721-9732.

Proksch, E., Brandner, J.M., and Jensen, J.M. (2008). The skin: an indispensable

barrier. Exp Dermatol *17*, 1063-1072.

Ran, F.A., Hsu, P.D., Wright, J., Agarwala, V., Scott, D.A., and Zhang, F. (2013). Genome engineering using the CRISPR-Cas9 system. Nature protocols *8*, 2281-2308.

Rand, T.A., Ginalski, K., Grishin, N.V., and Wang, X. (2004). Biochemical identification of Argonaute 2 as the sole protein required for RNA-induced silencing complex activity. Proc Natl Acad Sci U S A *101*, 14385-14389.

Rand, T.A., Petersen, S., Du, F., and Wang, X. (2005). Argonaute2 cleaves the anti-guide strand of siRNA during RISC activation. Cell *123*, 621-629.

Raptis, L.H., Brownell, H.L., Firth, K.L., and Mackenzie, L.W. (1994). A novel technique for the study of intercellular, junctional communication: electroporation of adherent cells on a partly conductive slide. DNA Cell Biol *13*, 963-975.

Rath, E.C., Pitman, S., Cho, K.H., and Bai, Y. (2017). Identification of streptococcal small RNAs that are putative targets of RNase III through bioinformatics analysis of RNA sequencing data. BMC Bioinformatics *18*, 540.

Reaume, A.G., de Sousa, P.A., Kulkarni, S., Langille, B.L., Zhu, D., Davies, T.C., Juneja, S.C., Kidder, G.M., and Rossant, J. (1995). Cardiac malformation in neonatal mice lacking connexin43. Science *267*, 1831-1834.

Reese, M.G., Eeckman, F.H., Kulp, D., and Haussler, D. (1997). Improved splice site detection in Genie. J Comput Biol *4*, 311-323.

Ren, J., Pan, X., Li, L., Huang, Y., Huang, H., Gao, Y., Xu, H., Qu, F., Chen, L., Wang, L., *et al.* (2016). Knockdown of GPR137,G Protein-coupled receptor 137, Inhibits the Proliferation and Migration of Human Prostate Cancer Cells. Chem Biol Drug Des *87*, 704-713.

Retamal, M.A., Reyes, E.P., Garcia, I.E., Pinto, B., Martinez, A.D., and Gonzalez, C. (2015). Diseases associated with leaky hemichannels. Front Cell Neurosci *9*, 267.

Revel, J.P., and Karnovsky, M.J. (1967). Hexagonal array of subunits in intercellular junctions of the mouse heart and liver. The Journal of cell biology *33*, C7-C12.

Rezze, G.G., Fregnani, J.H., Duprat, J., and Landman, G. (2011). Cell adhesion and communication proteins are differentially expressed in melanoma progression model. Hum Pathol *42*, 409-418.

Richard, G., Brown, N., Ishida-Yamamoto, A., and Krol, A. (2004). Expanding the phenotypic spectrum of Cx26 disorders: Bart-Pumphrey syndrome is caused by a novel missense mutation in GJB2. J Invest Dermatol *123*, 856-863.

Richard, G., Rouan, F., Willoughby, C.E., Brown, N., Chung, P., Ryynanen, M., Jabs, E.W., Bale, S.J., DiGiovanna, J.J., Uitto, J., *et al.* (2002). Missense mutations in GJB2 encoding connexin-26 cause the ectodermal dysplasia keratitis-ichthyosis-deafness syndrome. American journal of human genetics *70*, 1341-1348.

Richard, G., Smith, L.E., Bailey, R.A., Itin, P., Hohl, D., Epstein, E.H., Jr., DiGiovanna, J.J., Compton, J.G., and Bale, S.J. (1998). Mutations in the human connexin gene GJB3 cause erythrokeratodermia variabilis. Nat Genet *20*, 366-369.

Richardson, R.J., Joss, S., Tomkin, S., Ahmed, M., Sheridan, E., and Dixon, M.J. (2006). A nonsense mutation in the first transmembrane domain of connexin 43 underlies autosomal recessive oculodentodigital syndrome. J Med Genet *43*, e37.

Rodriguez-Paris, J., Waldhaus, J., Gordhandas, J.A., Pique, L., and Schrijver, I. (2016). Comparative functional characterization of novel non-syndromic GJB2 gene variant p.Gly45Arg and lethal syndromic variant p.Gly45Glu. PeerJ *4*, e2494.

Rorth, P., Szabo, K., Bailey, A., Laverty, T., Rehm, J., Rubin, G.M., Weigmann, K., Milan, M., Benes, V., Ansorge, W., *et al.* (1998). Systematic gain-of-function genetics in Drosophila. Development *125*, 1049-1057.

Rouan, F., White, T.W., Brown, N., Taylor, A.M., Lucke, T.W., Paul, D.L., Munro, C.S., Uitto, J., Hodgins, M.B., and Richard, G. (2001). trans-dominant inhibition of connexin-43 by mutant connexin-26: implications for dominant connexin disorders affecting epidermal differentiation. J Cell Sci *114*, 2105-2113.

Ruan, R., Chen, M., Sun, S., Wei, P., Zou, L., Liu, J., Gao, D., Wen, L., and Ding, W. (2016). Topical and Targeted Delivery of siRNAs to Melanoma Cells Using a Fusion Peptide Carrier. Sci Rep *6*, 29159.

Saez, J.C., Connor, J.A., Spray, D.C., and Bennett, M.V. (1989). Hepatocyte gap junctions are permeable to the second messenger, inositol 1,4,5-trisphosphate, and to calcium ions. Proc Natl Acad Sci U S A *86*, 2708-2712.

Saez, J.C., Schalper, K.A., Retamal, M.A., Orellana, J.A., Shoji, K.F., and Bennett, M.V. (2010). Cell membrane permeabilization via connexin hemichannels in living and dying cells. Exp Cell Res *316*, 2377-2389.

Sahoo, B., Handa, S., Kaur, I., Radotra, B.D., and Kumar, B. (2002). KID syndrome: response to acitretin. The Journal of dermatology *29*, 499-502.

Saito-Katsuragi, M., Asada, H., Niizeki, H., Katoh, F., Masuzawa, M., Tsutsumi, M., Kuniyasu, H., Ito, A., Nojima, H., and Miyagawa, S. (2007). Role for connexin 26 in metastasis of human malignant melanoma: communication between melanoma and endothelial cells via connexin 26. Cancer *110*, 1162-1172.

Saitoh, M., Oyamada, M., Oyamada, Y., Kaku, T., and Mori, M. (1997). Changes in the expression of gap junction proteins (connexins) in hamster tongue epithelium during wound healing and carcinogenesis. Carcinogenesis *18*, 1319-1328.

Sakabe, J., Yoshiki, R., Sugita, K., Haruyama, S., Sawada, Y., Kabashima, R., Bito, T., Nakamura, M., and Tokura, Y. (2012). Connexin 26 (GJB2) mutations in keratitis-ichthyosis-deafness syndrome presenting with squamous cell carcinoma. The Journal of dermatology *39*, 814-815.

Salomon, D., Masgrau, E., Vischer, S., Ullrich, S., Dupont, E., Sappino, P., Saurat, J.H., and Meda, P. (1994). Topography of mammalian connexins in human skin. J Invest Dermatol *103*, 240-247.

Salomon, D., Saurat, J.H., and Meda, P. (1988). Cell-to-cell communication within intact human skin. J Clin Invest *82*, 248-254.

Sanchez, H.A., Bienkowski, R., Slavi, N., Srinivas, M., and Verselis, V.K. (2014). Altered inhibition of Cx26 hemichannels by pH and Zn2+ in the A40V mutation associated with keratitis-ichthyosis-deafness syndrome. J Biol Chem *289*, 21519-21532.

Sanchez, H.A., Slavi, N., Srinivas, M., and Verselis, V.K. (2016). Syndromic deafness mutations at Asn 14 differentially alter the open stability of Cx26 hemichannels. J Gen Physiol *148*, 25-42.

Sanchez, H.A., and Verselis, V.K. (2014). Aberrant Cx26 hemichannels and keratitis-ichthyosis-deafness syndrome: insights into syndromic hearing loss. Front Cell Neurosci *8*, 354.

Sanchez, H.A., Villone, K., Srinivas, M., and Verselis, V.K. (2013). The D50N mutation and syndromic deafness: altered Cx26 hemichannel properties caused by effects on the pore and intersubunit interactions. J Gen Physiol *142*, 3-22.

Sargen, M.R., Gormley, R.H., Pasha, T.L., Yum, S., Acs, G., Xu, X., and Zhang, P.J. (2013). Melanocytic tumors express connexin 43 but not 26: immunohistochemical analysis with potential significance in melanocytic oncogenesis. Am J Dermatopathol *35*, 813-817.

Sbidian, E., Feldmann, D., Bengoa, J., Fraitag, S., Abadie, V., de Prost, Y., Bodemer, C., and Hadj-Rabia, S. (2010). Germline mosaicism in keratitis-ichthyosis-deafness syndrome: pre-natal diagnosis in a familial lethal form. Clinical genetics *77*, 587-592.

Schalper, K.A., Palacios-Prado, N., Orellana, J.A., and Saez, J.C. (2008). Currently used methods for identification and characterization of hemichannels. Cell communication & adhesion *15*, 207-218.

Schutz, M., Auth, T., Gehrt, A., Bosen, F., Korber, I., Strenzke, N., Moser, T., and Willecke, K. (2011). The connexin26 S17F mouse mutant represents a model for the human hereditary keratitis-ichthyosis-deafness syndrome. Hum Mol Genet *20*, 28-39.

Schwarz, D.S., Ding, H., Kennington, L., Moore, J.T., Schelter, J., Burchard, J., Linsley, P.S., Aronin, N., Xu, Z., and Zamore, P.D. (2006). Designing siRNA that distinguish between genes that differ by a single nucleotide. PLoS genetics *2*, e140.

Seok, H., Lee, H., Jang, E.S., and Chi, S.W. (2017). Evaluation and control of miRNA-like off-target repression for RNA interference. Cell Mol Life Sci.

Serrano-Ahumada, A.S., Cortes-Gonzalez, V., Gonzalez-Huerta, L.M., Cuevas, S., Aguilar-Lozano, L., and Villanueva-Mendoza, C. (2017). Severe Phenotype of Keratitis-Ichthyosis-Deafness Syndrome With Presumed Ocular Surface Squamous Neoplasia. Cornea.

Shang, R., Zhang, F., Xu, B., Xi, H., Zhang, X., Wang, W., and Wu, L. (2015). Ribozyme-enhanced single-stranded Ago2-processed interfering RNA triggers efficient gene silencing with fewer off-target effects. Nat Commun *6*, 8430.

Shuja, Z., Li, L., Gupta, S., Mese, G., and White, T.W. (2016). Connexin26 Mutations Causing Palmoplantar Keratoderma and Deafness Interact with Connexin43, Modifying Gap Junction and Hemichannel Properties. J Invest Dermatol *136*, 225-235.

Shurman, D.L., Glazewski, L., Gumpert, A., Zieske, J.D., and Richard, G. (2005). In vivo and in vitro expression of connexins in the human corneal epithelium. Investigative ophthalmology & visual science *46*, 1957-1965.

Shwin, K.W., Lee, C.R., and Goldbach-Mansky, R. (2017). Dermatologic Manifestations of Monogenic Autoinflammatory Diseases. Dermatol Clin *35*, 21-38.

Smith, F.J., Hickerson, R.P., Sayers, J.M., Reeves, R.E., Contag, C.H., Leake, D., Kaspar, R.L., and McLean, W.H. (2008). Development of therapeutic siRNAs for pachyonychia congenita. J Invest Dermatol *128*, 50-58.

Smyth, C.M., Sinnathuray, A.R., Hughes, A.E., and Toner, J.G. (2012). Cochlear implantation in keratitis-ichthyosis-deafness syndrome: 10-year follow-up of two

patients. Cochlear implants international *13*, 54-59.

Sohl, G., and Willecke, K. (2004). Gap junctions and the connexin protein family. Cardiovasc Res *62*, 228-232.

Sonoda, S., Uchino, E., Sonoda, K.H., Yotsumoto, S., Uchio, E., Isashiki, Y., and Sakamoto, T. (2004). Two patients with severe corneal disease in KID syndrome. American journal of ophthalmology *137*, 181-183.

Speranza, E., Altamura, L.A., Kulcsar, K., Bixler, S.L., Rossi, C.A., Schoepp, R.J., Nagle, E., Aguilar, W., Douglas, C.E., Delp, K.L., *et al.* (2017). Comparison of Transcriptomic Platforms for Analysis of Whole Blood from Ebola-Infected Cynomolgus Macaques. Sci Rep *7*, 14756.

Spray, D.C., Ye, Z.C., and Ransom, B.R. (2006). Functional connexin "hemichannels": a critical appraisal. Glia *54*, 758-773.

Srinivas, M., Verselis, V.K., and White, T.W. (2017). Human diseases associated with connexin mutations. Biochimica et Biophysica Acta (BBA) - Biomembranes.

Stong, B.C., Chang, Q., Ahmad, S., and Lin, X. (2006). A novel mechanism for connexin 26 mutation linked deafness: cell death caused by leaky gap junction hemichannels. The Laryngoscope *116*, 2205-2210.

Stout, C.E., Costantin, J.L., Naus, C.C., and Charles, A.C. (2002). Intercellular calcium signaling in astrocytes via ATP release through connexin hemichannels. J Biol Chem *277*, 10482-10488.

Su, C.C., Li, S.Y., Su, M.C., Chen, W.C., and Yang, J.J. (2010). Mutation R184Q of connexin 26 in hearing loss patients has a dominant-negative effect on connexin 26 and connexin 30. Eur J Hum Genet *18*, 1061-1064.

Su, Y.A., Bittner, M.L., Chen, Y., Tao, L., Jiang, Y., Zhang, Y., Stephan, D.A., and Trent, J.M. (2000). Identification of tumor-suppressor genes using human melanoma cell lines UACC903, UACC903(+6), and SRS3 by comparison of expression profiles. Mol Carcinog *28*, 119-127.

Sun, L.D., Cheng, H., Wang, Z.X., Zhang, A.P., Wang, P.G., Xu, J.H., Zhu, Q.X., Zhou, H.S., Ellinghaus, E., Zhang, F.R., *et al.* (2010). Association analyses identify six new psoriasis susceptibility loci in the Chinese population. Nat Genet *42*, 1005-1009.

Szklarczyk, D., Franceschini, A., Wyder, S., Forslund, K., Heller, D., Huerta-Cepas, J., Simonovic, M., Roth, A., Santos, A., Tsafou, K.P., *et al.* (2015). STRING v10: protein-protein interaction networks, integrated over the tree of life. Nucleic acids research *43*, D447-452.

Szymko-Bennett, Y.M., Russell, L.J., Bale, S.J., and Griffith, A.J. (2002). Auditory manifestations of Keratitis-Ichthyosis-Deafness (KID) syndrome. The Laryngoscope *112*, 272-280.

Tada, J., and Hashimoto, K. (1997). Ultrastructural localization of gap junction protein connexin 43 in normal human skin, basal cell carcinoma, and squamous cell carcinoma. J Cutan Pathol *24*, 628-635.

Tagalakis, A.D., Munye, M.M., Ivanova, R., Chen, H., Smith, C.M., Aldossary, A.M., Rosa, L.Z., Moulding, D., Barnes, J.L., Kafetzis, K.N., *et al.* (2018). Effective silencing of ENaC by siRNA delivered with epithelial-targeted nanocomplexes in

human cystic fibrosis cells and in mouse lung. Thorax.

Takada, H., Furuya, K., and Sokabe, M. (2014). Mechanosensitive ATP release from hemichannels and Ca(2)(+) influx through TRPC6 accelerate wound closure in keratinocytes. J Cell Sci *127*, 4159-4171.

Takahashi, R., Nagayama, S., Furu, M., Kajita, Y., Jin, Y., Kato, T., Imoto, S., Sakai, Y., and Toguchida, J. (2014). AFAP1L1, a novel associating partner with vinculin, modulates cellular morphology and motility, and promotes the progression of colorectal cancers. Cancer Med *3*, 759-774.

Tang, F., Barbacioru, C., Nordman, E., Li, B., Xu, N., Bashkirov, V.I., Lao, K., and Surani, M.A. (2010). RNA-Seq analysis to capture the transcriptome landscape of a single cell. Nature protocols *5*, 516-535.

Tarzemany, R., Jiang, G., Jiang, J.X., Larjava, H., and Hakkinen, L. (2017). Connexin 43 Hemichannels Regulate the Expression of Wound Healing-Associated Genes in Human Gingival Fibroblasts. Sci Rep *7*, 14157.

Tattersall, D., Scott, C.A., Gray, C., Zicha, D., and Kelsell, D.P. (2009). EKV mutant connexin 31 associated cell death is mediated by ER stress. Hum Mol Genet *18*, 4734-4745.

Terrinoni, A., Codispoti, A., Serra, V., Didona, B., Bruno, E., Nistico, R., Giustizieri, M., Alessandrini, M., Campione, E., and Melino, G. (2010). Connexin 26 (GJB2) mutations, causing KID Syndrome, are associated with cell death due to calcium gating deregulation. Biochem Biophys Res Commun *394*, 909-914.

Thiagarajan, P.S., Sinyuk, M., Turaga, S.M., Mulkearns-Hubert, E.E., Hale, J.S., Rao, V., Demelash, A., Saygin, C., China, A., Alban, T.J., *et al.* (2018). Cx26 drives self-renewal in triple-negative breast cancer via interaction with NANOG and focal adhesion kinase. Nat Commun *9*, 578.

Thomas, T., Jordan, K., Simek, J., Shao, Q., Jedeszko, C., Walton, P., and Laird, D.W. (2005). Mechanisms of Cx43 and Cx26 transport to the plasma membrane and gap junction regeneration. J Cell Sci *118*, 4451-4462.

Thomas, T., Telford, D., and Laird, D.W. (2004). Functional domain mapping and selective trans-dominant effects exhibited by Cx26 disease-causing mutations. J Biol Chem *279*, 19157-19168.

Tittarelli, A., Guerrero, I., Tempio, F., Gleisner, M.A., Avalos, I., Sabanegh, S., Ortiz, C., Michea, L., Lopez, M.N., Mendoza-Naranjo, A., *et al.* (2015). Overexpression of connexin 43 reduces melanoma proliferative and metastatic capacity. Br J Cancer *113*, 259-267.

Traub, O., Look, J., Dermietzel, R., Brummer, F., Hulser, D., and Willecke, K. (1989). Comparative characterization of the 21-kD and 26-kD gap junction proteins in murine liver and cultured hepatocytes. The Journal of cell biology *108*, 1039-1051.

Trochet, D., Prudhon, B., Beuvin, M., Peccate, C., Lorain, S., Julien, L., Benkhelifa-Ziyyat, S., Rabai, A., Mamchaoui, K., Ferry, A., *et al.* (2018). Allele-specific silencing therapy for Dynamin 2-related dominant centronuclear myopathy. EMBO Mol Med *10*, 239-253.

Trochet, D., Prudhon, B., Vassilopoulos, S., and Bitoun, M. (2015). Therapy for dominant inherited diseases by allele-specific RNA interference: successes and pitfalls. Current gene therapy *15*, 503-510.

Tsuzuku, T., Kaga, K., Kanematsu, S., Shibata, A., and Ohde, S. (1992). Temporal bone findings in keratitis, ichthyosis, and deafness syndrome. Case report. The Annals of otology, rhinology, and laryngology *101*, 413-416.

Tu, C.L., and Bikle, D.D. (2013). Role of the calcium-sensing receptor in calcium regulation of epidermal differentiation and function. Best Pract Res Clin Endocrinol Metab *27*, 415-427.

Uhlen, M., Fagerberg, L., Hallstrom, B.M., Lindskog, C., Oksvold, P., Mardinoglu, A., Sivertsson, A., Kampf, C., Sjostedt, E., Asplund, A., *et al.* (2015). Proteomics. Tissue-based map of the human proteome. Science *347*, 1260419.

Valiunas, V., Cohen, I.S., and Brink, P.R. (2018). Defining the factors that affect solute permeation of gap junction channels. Biochim Biophys Acta *1860*, 96-101.

van Geel, M., van Steensel, M.A., Kuster, W., Hennies, H.C., Happle, R., Steijlen, P.M., and Konig, A. (2002). HID and KID syndromes are associated with the same connexin 26 mutation. The British journal of dermatology *146*, 938-942.

van Steensel, M.A., Spruijt, L., van der Burgt, I., Bladergroen, R.S., Vermeer, M., Steijlen, P.M., and van Geel, M. (2005). A 2-bp deletion in the GJA1 gene is associated with oculo-dento-digital dysplasia with palmoplantar keratoderma. American journal of medical genetics Part A *132A*, 171-174.

van Steensel, M.A., van Geel, M., Nahuys, M., Smitt, J.H., and Steijlen, P.M. (2002). A novel connexin 26 mutation in a patient diagnosed with keratitis-ichthyosis-deafness syndrome. J Invest Dermatol *118*, 724-727.

Verselis, V.K., and Srinivas, M. (2008). Divalent cations regulate connexin hemichannels by modulating intrinsic voltage-dependent gating. J Gen Physiol *132*, 315-327.

Verselis, V.K., and Srinivas, M. (2013). Connexin channel modulators and their mechanisms of action. Neuropharmacology *75*, 517-524.

Vreeburg, M., de Zwart-Storm, E.A., Schouten, M.I., Nellen, R.G., Marcus-Soekarman, D., Devies, M., van Geel, M., and van Steensel, M.A. (2007). Skin changes in oculo-dento-digital dysplasia are correlated with C-terminal truncations of connexin 43. American journal of medical genetics Part A *143*, 360-363.

Wade, M.H., Trosko, J.E., and Schindler, M. (1986). A fluorescence photobleaching assay of gap junction-mediated communication between human cells. Science *232*, 525-528.

Walcott, B., Moore, L.C., Birzgalis, A., Claros, N., Valiunas, V., Ott, T., Willecke, K., and Brink, P.R. (2002). Role of gap junctions in fluid secretion of lacrimal glands. Am J Physiol Cell Physiol *282*, C501-507.

Wang, C.M., Lincoln, J., Cook, J.E., and Becker, D.L. (2007a). Abnormal connexin expression underlies delayed wound healing in diabetic skin. Diabetes *56*, 2809-2817.

Wang, H., Cao, X., Lin, Z., Lee, M., Jia, X., Ren, Y., Dai, L., Guan, L., Zhang, J., Lin, X., *et al.* (2015). Exome sequencing reveals mutation in GJA1 as a cause of keratoderma-hypotrichosis-leukonychia totalis syndrome. Hum Mol Genet *24*, 243-250.

Wang, M., Berthoud, V.M., and Beyer, E.C. (2007b). Connexin43 increases the sensitivity of prostate cancer cells to TNFalpha-induced apoptosis. J Cell Sci *120*, 320-

329.

Wang, N., De Bock, M., Antoons, G., Gadicherla, A.K., Bol, M., Decrock, E., Evans, W.H., Sipido, K.R., Bukauskas, F.F., and Leybaert, L. (2012). Connexin mimetic peptides inhibit Cx43 hemichannel opening triggered by voltage and intracellular Ca2+ elevation. Basic Res Cardiol *107*, 304.

Wang, Z., Gerstein, M., and Snyder, M. (2009). RNA-Seq: a revolutionary tool for transcriptomics. Nat Rev Genet *10*, 57-63.

Watanabe, D., Zako, M., Tamada, Y., and Matsumoto, Y. (2007). A case of keratitis-ichthyosis-deafness (KID) syndrome. International journal of dermatology *46*, 400-402.

Watts, J.K., and Corey, D.R. (2012). Silencing disease genes in the laboratory and the clinic. J Pathol *226*, 365-379.

Werchau, S., Toberer, F., Enk, A., and Helmbold, P. (2011). Keratitis-ichthyosis-deafness syndrome: response to alitretinoin and review of literature. Archives of dermatology *147*, 993-995.

White, T.W., Goodenough, D.A., and Paul, D.L. (1998). Targeted ablation of connexin50 in mice results in microphthalmia and zonular pulverulent cataracts. The Journal of cell biology *143*, 815-825.

White, T.W., and Paul, D.L. (1999). Genetic diseases and gene knockouts reveal diverse connexin functions. Annu Rev Physiol *61*, 283-310.

Whitehead, K.A., Langer, R., and Anderson, D.G. (2009). Knocking down barriers: advances in siRNA delivery. Nat Rev Drug Discov *8*, 129-138.

Willecke, K., and Nielsen, M.S. (2007). Synopsis of the International Gap Junction Conference in Elsinore, Denmark August 5-9, 2007. Cell communication & adhesion *14*, 251-257.

Wilson, F.M., 2nd, Grayson, M., and Pieroni, D. (1973). Corneal changes in ectodermal dysplasia. Case report, histopathology, and differential diagnosis. American journal of ophthalmology *75*, 17-27.

Wolfe, C.M., Davis, A., Shaath, T.S., and Cohen, G.F. (2017). Visual impairment reversal with oral acitretin therapy in keratitis-ichthyosis-deafness (KID) syndrome. JAAD Case Rep *3*, 556-558.

Wong, P., Tan, T., Chan, C., Laxton, V., Chan, Y.W., Liu, T., Wong, W.T., and Tse, G. (2016). The Role of Connexins in Wound Healing and Repair: Novel Therapeutic Approaches. Front Physiol *7*, 596.

Wright, C.S., Pollok, S., Flint, D.J., Brandner, J.M., and Martin, P.E. (2012). The connexin mimetic peptide Gap27 increases human dermal fibroblast migration in hyperglycemic and hyperinsulinemic conditions in vitro. Journal of cellular physiology *227*, 77-87.

Wright, C.S., van Steensel, M.A., Hodgins, M.B., and Martin, P.E. (2009). Connexin mimetic peptides improve cell migration rates of human epidermal keratinocytes and dermal fibroblasts in vitro. Wound repair and regeneration : official publication of the Wound Healing Society [and] the European Tissue Repair Society *17*, 240-249.

Wu, S.Y., Yang, X., Gharpure, K.M., Hatakeyama, H., Egli, M., McGuire, M.H., Nagaraja, A.S., Miyake, T.M., Rupaimoole, R., Pecot, C.V., *et al.* (2014). 2'-OMe-

phosphorodithioate-modified siRNAs show increased loading into the RISC complex and enhanced anti-tumour activity. Nat Commun *5*, 3459.

Xu, J., and Nicholson, B.J. (2013). The role of connexins in ear and skin physiology - functional insights from disease-associated mutations. Biochim Biophys Acta *1828*, 167-178.

Xu, L., Carrer, A., Zonta, F., Qu, Z., Ma, P., Li, S., Ceriani, F., Buratto, D., Crispino, G., Zorzi, V., *et al.* (2017). Design and Characterization of a Human Monoclonal Antibody that Modulates Mutant Connexin 26 Hemichannels Implicated in Deafness and Skin Disorders. Front Mol Neurosci *10*, 298.

Yang, J., Qin, G., Luo, M., Chen, J., Zhang, Q., Li, L., Pan, L., and Qin, S. (2015). Reciprocal positive regulation between Cx26 and PI3K/Akt pathway confers acquired gefitinib resistance in NSCLC cells via GJIC-independent induction of EMT. Cell Death Dis *6*, e1829.

Yano, T., and Yamasaki, H. (2001). Regulation of cellular invasion and matrix metalloproteinase activity in HepG2 cell by connexin 26 transfection. Mol Carcinog *31*, 101-109.

Yilmazel, B., Hu, Y., Sigoillot, F., Smith, J.A., Shamu, C.E., Perrimon, N., and Mohr, S.E. (2014). Online GESS: prediction of miRNA-like off-target effects in large-scale RNAi screen data by seed region analysis. BMC Bioinformatics *15*, 192.

Yu, M., Zhang, C., Li, L., Dong, S., Zhang, N., and Tong, X. (2014). Cx43 reverses the resistance of A549 lung adenocarcinoma cells to cisplatin by inhibiting EMT. Oncol Rep *31*, 2751-2758.

Yum, S.W., Zhang, J., Valiunas, V., Kanaporis, G., Brink, P.R., White, T.W., and Scherer, S.S. (2007). Human connexin26 and connexin30 form functional heteromeric and heterotypic channels. Am J Physiol Cell Physiol *293*, C1032-1048.

Zhang, A., Hitomi, M., Bar-Shain, N., Dalimov, Z., Ellis, L., Velpula, K.K., Fraizer, G.C., Gourdie, R.G., and Lathia, J.D. (2015a). Connexin 43 expression is associated with increased malignancy in prostate cancer cell lines and functions to promote migration. Oncotarget *6*, 11640-11651.

Zhang, H., Ma, X., Shi, T., Song, Q., Zhao, H., and Ma, D. (2010). NSA2, a novel nucleolus protein regulates cell proliferation and cell cycle. Biochem Biophys Res Commun *391*, 651-658.

Zhang, J., O'Carroll, S.J., Henare, K., Ching, L.M., Ormonde, S., Nicholson, L.F., Danesh-Meyer, H.V., and Green, C.R. (2014). Connexin hemichannel induced vascular leak suggests a new paradigm for cancer therapy. FEBS Lett *588*, 1365-1371.

Zhang, J., Scherer, S.S., and Yum, S.W. (2011). Dominant Cx26 mutants associated with hearing loss have dominant-negative effects on wild type Cx26. Mol Cell Neurosci *47*, 71-78.

Zhang, X., Huang, L., Wu, T., Feng, Y., Ding, Y., Ye, P., and Yin, Z. (2015b). Transcriptomic Analysis of Ovaries from Pigs with High And Low Litter Size. PLoS One *10*, e0139514.

Zhang, Y., Tang, W., Ahmad, S., Sipp, J.A., Chen, P., and Lin, X. (2005). Gap junction-mediated intercellular biochemical coupling in cochlear supporting cells is required for normal cochlear functions. Proc Natl Acad Sci U S A *102*, 15201-15206.

Zhao, H.B., Yu, N., and Fleming, C.R. (2005). Gap junctional hemichannel-mediated ATP release and hearing controls in the inner ear. Proc Natl Acad Sci U S A *102*, 18724-18729.

Zheng, D., Giljohann, D.A., Chen, D.L., Massich, M.D., Wang, X.Q., Iordanov, H., Mirkin, C.A., and Paller, A.S. (2012). Topical delivery of siRNA-based spherical nucleic acid nanoparticle conjugates for gene regulation. Proc Natl Acad Sci U S A *109*, 11975-11980.

Zhu, D., Caveney, S., Kidder, G.M., and Naus, C.C. (1991). Transfection of C6 glioma cells with connexin 43 cDNA: analysis of expression, intercellular coupling, and cell proliferation. Proc Natl Acad Sci U S A *88*, 1883-1887.

Zoidl, G., Kremer, M., Zoidl, C., Bunse, S., and Dermietzel, R. (2008). Molecular diversity of connexin and pannexin genes in the retina of the zebrafish Danio rerio. Cell communication & adhesion *15*, 169-183.

Zong, G., Wang, H., Li, J., Xie, Y., Bian, E., and Zhao, B. (2014). Inhibition of GPR137 expression reduces the proliferation and colony formation of malignant glioma cells. Neurol Sci *35*, 1707-1714.

Zucker, S.N., Bancroft, T.A., Place, D.E., Des Soye, B., Bagati, A., and Berezney, R. (2013). A dominant negative Cx43 mutant differentially affects tumorigenic and invasive properties in human metastatic melanoma cells. Journal of cellular physiology *228*, 853-859.